



HAL
open science

High resolution of fast-rotating stars across the H-R diagram

Armando Domiciano de Souza

► **To cite this version:**

Armando Domiciano de Souza. High resolution of fast-rotating stars across the H-R diagram: photosphere and circumstellar environment. Solar and Stellar Astrophysics [astro-ph.SR]. Université de Nice Sophia Antipolis; Université Côte d'Azur, 2014. tel-01581110

HAL Id: tel-01581110

<https://theses.hal.science/tel-01581110>

Submitted on 4 Sep 2017

HAL is a multi-disciplinary open access archive for the deposit and dissemination of scientific research documents, whether they are published or not. The documents may come from teaching and research institutions in France or abroad, or from public or private research centers.

L'archive ouverte pluridisciplinaire **HAL**, est destinée au dépôt et à la diffusion de documents scientifiques de niveau recherche, publiés ou non, émanant des établissements d'enseignement et de recherche français ou étrangers, des laboratoires publics ou privés.



Distributed under a Creative Commons Attribution - NonCommercial - NoDerivatives 4.0 International License



Observatoire
de la CÔTE d'AZUR



UNIVERSITÉ
CÔTE D'AZUR



Observatoire de la Côte d'Azur (OCA)
Université de Nice Sophia Antipolis (UNS) - UFR Sciences

Laboratoire J. L. Lagrange (UMR 7293 CNRS)
Université Côte d'Azur (UCA)

HABILITATION À DIRIGER DES RECHERCHES

HABILITATION THESIS

Haute résolution d'étoiles en rotation rapide à travers le diagramme H-R:

photosphère et environnement circumstellaire

High resolution of fast-rotating stars across the H-R diagram:

photosphere and circumstellar environment

ARMANDO DOMICIANO DE SOUZA JR.

Soutenue publiquement le 5 décembre 2014 devant le jury composé de :

M. Farrokh VAKILI	OCA, UNS, Lab. Lagrange	Président
M. Georges MEYNET	Observatoire de Genève	Rapporteur
M. Guy PERRIN	Observatoire de Paris	Rapporteur
M. Bruno LOPEZ	OCA, UNS, Lab. Lagrange	Rapporteur
M. Michel RIEUTORD	Université de Toulouse	Examineur
M. Philippe STEE	OCA, UNS, Lab. Lagrange	Examineur



ACKNOWLEDGEMENTS

To Júlia, Irani, Lucas, and Rodrigo.

ACKNOWLEDGEMENTS

CONTENTS

	Page
List of Figures	vii
Achronyms	x
1 Introduction	1
1.1 Rotation: a key ingredient in stellar physics	1
1.2 OLBI : a key technique in stellar physics	6
2 Photosphere and circumstellar environment (CSE) of fast rotators	11
2.1 Basic hydrodynamical equations	11
2.2 Equilibrium structure of fast-rotating stars	12
2.2.1 Roche model	12
2.2.2 Gravity darkening	17
2.2.3 Examples of photospheric intensity-maps	24
2.2.4 Eddington limit and anisotropic CSE	30
2.3 Circumstellar disks of Be stars	33
2.4 Gas and dust CSE of supergiant B[e] stars	36
2.4.1 Grid of supergiant B[e] models	39
2.5 Numerical models	44
2.5.1 CHARRON (Code for High Angular Resolution of Rotating Objects in Nature)	44
2.5.2 FRACS (Fast Ray-tracing Algorithm for Circumstellar Structures)	45
2.5.3 HDUST, a Monte Carlo NLTE radiative-transfer code in gas-dust CSE	62
3 High spectro-spatial resolution observations of fast rotators in the H-R diagram	65
3.1 The main sequence A-type star Altair (α Aquilae)	65
3.2 The Be star Achernar (α Eridani)	78
3.2.1 Photospheric parameters of Achernar	78
3.2.2 The close CSE of Achernar: wind and residual disk	95
3.2.3 The binary companion of Achernar: detection and characterization	108
3.2.4 Beyond the diffraction limit of optical/IR interferometers: angular diameter and rotation parameters of Achernar from differential phases	118
3.3 The supergiant B[e] star CPD-57° 2874	129
4 Perspectives	147

CONTENTS

A Roche surface	151
Bibliography	153

List of Figures

1.1	Time evolution of surface rotation velocity of massive stars.	3
1.2	Distribution of average stellar projected rotation velocities $v_{\text{eq}} \sin i$	4
1.3	Best-fit models or reconstructed images of 7 fast-rotating stars obtained between 2001 and 2011 with the interferometers PTI, NPOI, CHARA, and VLTI.	5
2.1	Reference frame and some parameters of the Roche model.	14
2.2	Stellar surface and $R_{\text{eq}}/R_{\text{p}}$ of the Roche model for several rotation rates.	16
2.3	Equatorial to polar effective temperatures for the ELR and von Zeipel gravity-darkening models.	21
2.4	Gravity darkening coefficient β obtained from models and from interferometric observations as a function of rotation flattening and the local T_{eff}	23
2.5	CHARRON specific intensity I_{λ} (V, H, and K bands) and T_{eff} maps at different inclinations i	26
2.6	CHARRON specific intensity I_{λ} (V, H, and K bands) and T_{eff} maps at different inclinations v_{eq}	27
2.7	CHARRON specific intensity I_{λ} and equivalent width maps for FeI 5169.	28
2.8	CHARRON specific intensity I_{λ} and equivalent width maps at spectral lines MgII-SiII 6347.	28
2.9	CHARRON specific intensity I_{λ} and equivalent width maps for H α	28
2.10	CHARRON specific intensity I_{λ} and equivalent width maps for HeI 6678.	29
2.11	CHARRON specific intensity I_{λ} and equivalent width maps for OI 7772.	29
2.12	CHARRON specific intensity I_{λ} and equivalent width maps for Br γ	29
2.13	Schematic model for sgB[e] stars.	37
2.14	Examples of model intensity maps of sgB[e] stars computed with the Monte Carlo radiative transfer code HDUST.	38

LIST OF FIGURES

ACRONYMS

A&A Astronomy & Astrophysics. [24](#), [65](#), [78](#), [79](#), [95](#), [108](#), [118](#), [129](#)

AMBER Astronomical Multi-BEam combineR. [8](#), [45](#), [79](#), [118](#), [129](#), [147–149](#)

CHARA Center for High Angular Resolution Astronomy. [5](#)

CHARRON Code for High Angular Resolution of Rotating Objects in Nature. [24](#), [26](#), [28](#), [44](#), [62](#), [65](#), [78](#), [79](#), [149](#)

CSE Circumstellar environment. [2](#), [11](#), [30](#), [32–34](#), [36–38](#), [45](#), [62](#), [63](#), [79](#), [95](#), [108](#), [129](#), [148](#), [149](#)

ESO European Southern Observatory. [3](#), [129](#)

ESTER Evolution STellaire en Rotation Rapide. [148](#)

FRACS Fast Ray-tracing Algorithm for Circumstellar Structures. [45](#), [129](#), [148](#), [149](#)

FT Fourier transform. [7](#), [8](#), [44](#)

GTO Guaranteed Time Observations. [118](#), [147](#), [148](#)

H-R Hertzsprung-Russell. [1](#), [2](#), [4](#)

IAU International Astronomical Union. [2](#)

IR Infrared. [2](#), [7](#), [38](#), [108](#), [129](#)

JMMC Jean-Marie Mariotti Center. [6](#)

MATISSE Multi AperTure mid-Infrared SpectroScopic Experiment. [45](#), [148](#), [149](#)

MCMC Markov Chain Monte Carlo. [78](#), [79](#), [149](#)

MS Main Sequence. [1](#), [2](#)

NPOI Kenneth J. Johnston Navy Precision Optical Interferometer. [5](#), [65](#)

OCA Observatoire de la Côte d'Azur. [38](#), [39](#), [148](#)

OLBI Optical/IR Long-Baseline Interferometry. [2](#), [3](#), [6](#), [7](#), [9](#), [65](#), [78](#), [129](#)

PTI Palomar Testbed Interferometer. [3](#), [5](#), [65](#)

RVZ Roche-von Zeipel. [44](#)

SED Spectral Energy Distribution. [44](#)

sgB[e] Supergiant B[e]. [36–39](#), [45](#), [62](#), [63](#), [129](#), [148](#), [149](#)

SI International system of units (French: *Système International d'unités*). [11](#)

SIGAMM Simulations Intensives en Géophysique, Astronomie, Mécanique et Mathématiques.
[38](#)

VDD Viscous decretion disk. [33](#), [35](#), [37](#)

VLT Very Large Telescope. [108](#), [148](#)

VLTI Very Large Telescope Interferometer. [3](#), [5](#), [8](#), [45](#), [65](#), [78](#), [79](#), [95](#), [118](#), [129](#), [147–149](#)

CHAPTER 1

INTRODUCTION

1.1 Rotation: a key ingredient in stellar physics

Rotation is present everywhere in astrophysics, from the smallest bodies of the solar system to the largest scale structures in the Universe. In stars, rotation is present since their formation from the interstellar molecular clouds, during all the protoplanetary phase, main sequence (MS), formation of planetary systems, and up to the final stages of stellar evolution, playing a crucial role for example in supernovae explosions, formation of pulsars and rotating black holes, possible origin of some gamma-ray bursts.

The first evidences proving that stars rotate date back to the XVII century thanks to the Galilei Galileo observations of mysterious dark features moving in front of the visual image of the Sun. After some debates, these features were correctly interpreted as dark spots on the solar surface, with their movement being caused by the rotation of the Sun. Since then, this field encountered a initially slow development, probably due to the lack of realistic physical models and precise observational data.

Already in the XIX century, Captain W. de W. Abney was probably the first to suggest that (1) spectral absorption lines from stellar surfaces can be Doppler-broadened by rotation and (2) that these lines could allow us to calculate the stellar rotation velocity (Abney, 1877).

The first observations and theoretical works concerning spectral line broadening by rotation were performed by Schlesinger (1911, and references therein) and Shajn & Struve (1929), respectively. Struve (1931a) included rotation as one of the major factors defining the stellar absorption spectrum. Subsequent important works showed that the B type stars (in particular B stars with emission lines, i.e., Be stars) are amongst the fastest rotators (e.g. Struve, 1931b; Slettebak, 1976). In parallel, crucial results were achieved in the modeling of the physical structure of rotation stars (e.g. von Zeipel, 1924; James, 1964; Bodenheimer & Ostriker, 1973).

Thanks to these and numerous other theoretical and observational results obtained over the XX century until nowadays, rotation is considered a fundamental stellar parameter that, together with the stellar mass and metallicity, governs the structure and evolution of stars across the Hertzsprung-Russell (H-R) diagram.

The recognition of the crucial role of rotation in stellar physics is endorsed for example by two international conferences specially dedicated to this topic and that took place in the beginning of

the XXI century: (1) the IAU Symposium 215 *Stellar Rotation*¹, and (2) the workshop *400 Years of Stellar Rotation*². In addition, several reviews and books on stellar rotation were written in the past few decades, such as [Strittmatter \(1969\)](#), [Roxburgh \(1970\)](#), [Maeder & Meynet \(2000b\)](#), [Maeder \(2009\)](#), [Maeder & Meynet \(2012\)](#), among many others.

As expected, the effects of rotation on stars are stronger for high rotation velocities. In the present work, we study the physical structure of the external layers (photosphere in particular) and circumstellar environment (CSE) of fast-rotating stars across the H-R diagram. The presented results concern in particular massive, hot stars, such as Be and supergiant B[e] stars (emission line B stars; described in the next chapters). During the MS phase, the surface rotation velocity varies as a consequence of transport processes, contraction, expansion, and mass loss. Figure 1.1 shows the time evolution of the surface rotation velocity of massive stars (figure from [Meynet & Maeder, 2000](#)). For MS stars of masses $M \lesssim 15 M_{\odot}$, the surface rotation velocity approaches, and even reaches, the critical or breakup limit, where the surface gravity is balanced by the centrifugal acceleration (formal definition given in Chapter 2). After the MS phase, the critical velocity of stars of similar masses can again be reached during a blue loop after a red supergiant phase ([Meynet & Maeder, 2006](#)). Reaching or closely approaching the critical velocity may induce important episodes of mass ejection leading to the formation of CSE, such as those detected around Be and supergiant B[e] stars. The relation between rotation, photosphere, and CSE of massive stars is further discussed in Chapter 2.

From the observational point of view, several works show that fast rotation is indeed a general characteristic of massive, hot stars. The velocity distributions in Fig. 1.2 are examples showing that the average rotation velocity is significantly higher in massive stars compared to lower mass stars. Among these fast-rotating stars, the O and B stars, and in particular the Be stars, are those exhibiting the highest rotation velocities.

As presented in Sect. 2.2, the most apparent effects of fast rotation on the stellar surface are (1) the deformation of the outer layers of the star (rotation flattening), and (2) the latitudinal dependent emitted flux (gravity darkening), both consequences of the balance between centrifugal and gravitational forces within the star. Depending on the rotation rate, these two effects can lead to significant modifications in the apparent specific intensity distribution of the star as seen by a distant observer (intensity map). Thus, fast rotators cannot be assumed to be spherical stars with a unique photospheric effective temperature and gravity.

Such important modifications in the intensity maps can be directly probed by Optical/IR Long-Baseline Interferometry (OLBI) or stellar interferometry (briefly described in Sect. 1.2). The first attempts to measure the flattening of a fast-rotator (Altair) were performed by Hanbury Brown, with the Narrabri Intensity Interferometer ([Hanbury Brown et al., 1967](#)). However, the quality of the observations and the available baselines did not allow to discriminate between different models for Altair describing a possible geometrical deformation of its photosphere. Since these initial attempts from Hanbury Brown, the first conclusive measurements of rotational flattening were obtained in the beginning of the XXI century, followed by several others since then. Figure 1.3 summarizes the OLBI results on rapid rotators from 2001 to 2011 as given by the recent review paper from [van Belle \(2012\)](#).

The first successful direct measurement of the photospheric flattening of a fast-rotator (Al-

¹2001 - Cancun, Mexico; <http://www.astro.ugto.mx/~eenens/iau215/>

²2013 - Natal (RN), Brazil; <http://www.dfte.ufrn.br/400rotation/>

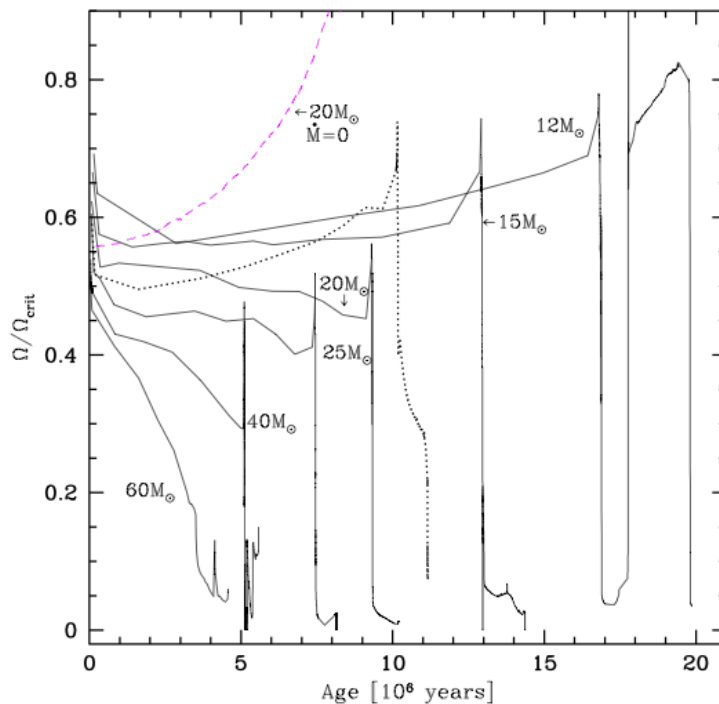


Figure 1.1 – Time evolution during MS of surface rotation angular velocity Ω of massive stars relative to the critical one Ω_c (see definitions in Chapter 2). Stars of masses $M \lesssim 15 M_{\odot}$ approach critical velocity, which may lead to important mass-ejection episodes during their evolution. It is interesting to note that this is not the case for more massive stars ($M \gtrsim 20 M_{\odot}$), where the surface rotation velocity and Ω/Ω_c decrease significantly because of the high mass loss of these stars, which removes a lot of angular momentum during MS. Indeed, the dashed curve, corresponding to a $20 M_{\odot}$ without mass loss, shows that for this hypothetical star the critical velocity is reached well before the end of the MS phase. Figure from [Meynet & Maeder \(2000\)](#).

tair) was performed by [van Belle et al. \(2001\)](#) using the Palomar Testbed Interferometer (PTI). Two years later our team measured the rotational flattening of the Be star Achernar using VINCI, the commissioning instrument of the ESO-VLTI ([Domiciano de Souza et al., 2003](#)). The strong flattening measured on Achernar in 2002-2003 could not be explained by the Roche model (described in Sect. 2.2.1), commonly adopted to explain the rotational deformation in fast rotators. This result motivated several theoretical and observational works on fast-rotating stars, differential rotation, and Be stars (e.g. [Zorec et al., 2011](#); [Carciofi et al., 2008](#); [Vinicius et al., 2006](#); [Jackson et al., 2004](#)). The recent status of the interferometric observations and physical interpretation of Achernar performed by our team is presented in Sect. 3.2.

Moreover, the determination of gravity darkening of single, fast-rotating stars is a delicate task, and only quite recently (beginning of the XXI century) the OLBI observations (including closure phases and several baselines) allowed to directly measure this effect. The question of gravity darkening is crucial to understand for example the structure and evolution of fast rotators, and the mass-loss mechanisms in massive stars. It is discussed in this work in the context of OLBI observations and compared to recent theoretical results.

1. Introduction

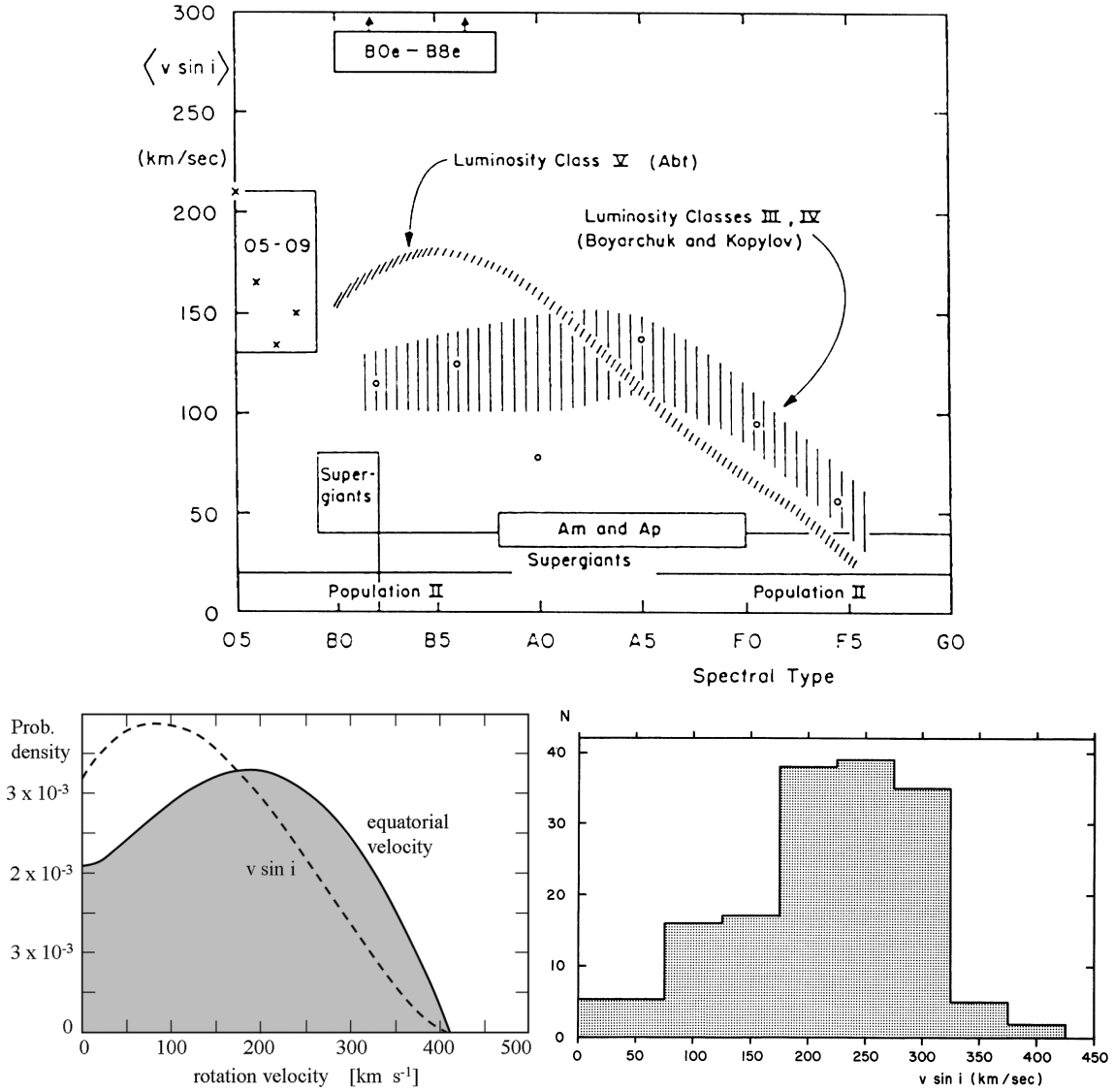


Figure 1.2 – *Top*: Distribution of average projected rotation velocities ($v_{\text{eq}} \sin i$) for different spectral types and luminosity classes. *Bottom left*: Distribution of projected ($v_{\text{eq}} \sin i$) and equatorial (v_{eq}) rotation velocities of 496 stars between spectral types O9.5 and B8. *Bottom right*: Distribution of $v_{\text{eq}} \sin i$ for 166 Be stars with spectral types between B0 and B9.5. These plots show that for non-degenerate stars, the O and B stars have the highest rotation velocities (a few hundred km s^{-1}) in the H-R diagram and, among them, the Be stars are the fastest rotators, with velocities up to $\simeq 400 \text{ km s}^{-1}$. Figures from Slettebak (1970), Slettebak (1982), Huang & Gies (2006), and Maeder & Meynet (2012).

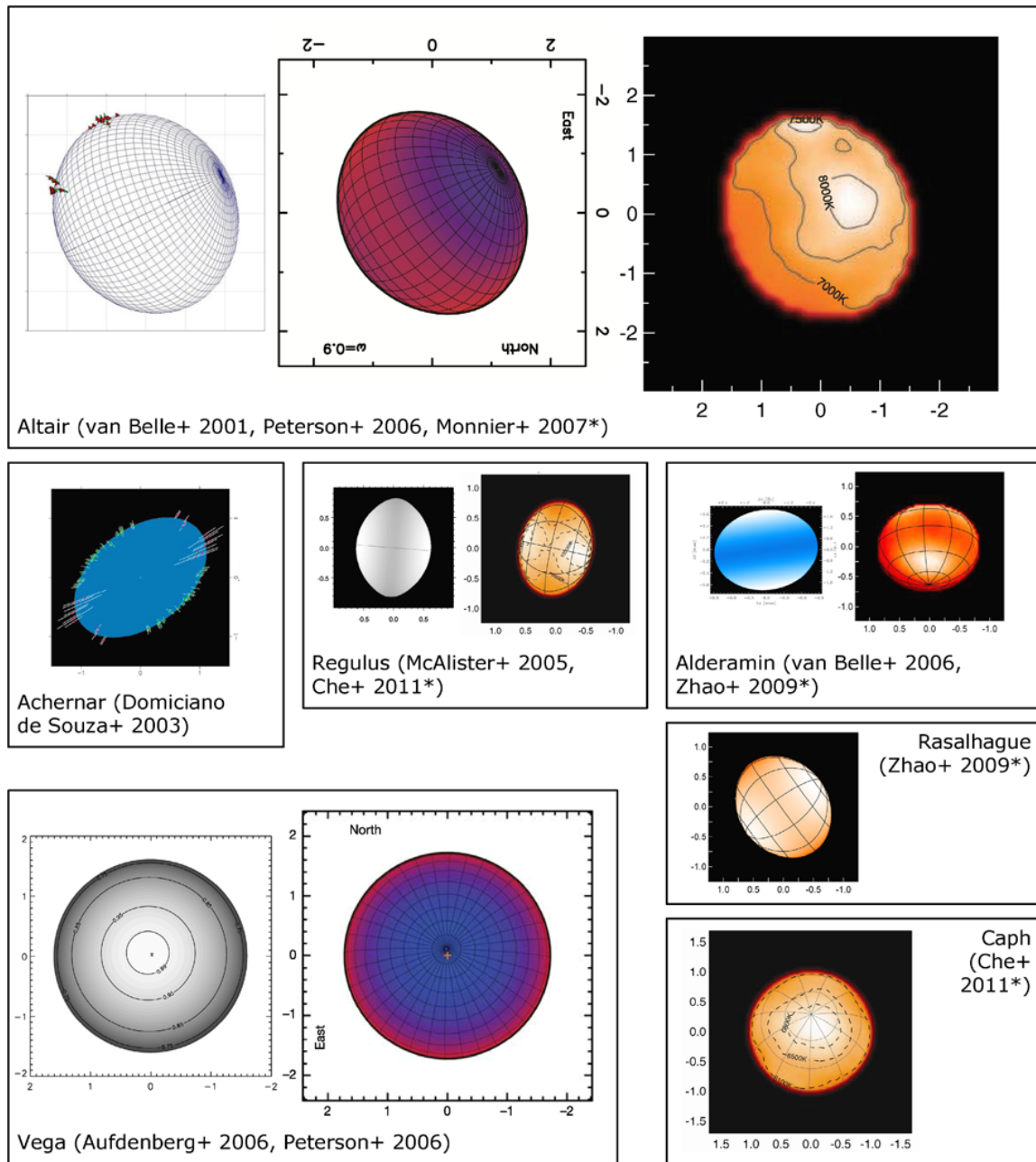


Figure 1.3 – Best-fit models or reconstructed images (references marked with * when an image reconstruction has been achieved) of 7 fast-rotating stars obtained between 2001 and 2011 with the interferometers PTI, NPOI, CHARA, and VLTI (see papers cited below for references). Images of the stellar photospheres were scaled in order to correctly represent the measured relative apparent sizes. The names of the 7 fast-rotators and corresponding main references are (from from the hottest to the coolest): Achernar (α Eri, B3-6Vpe; Domiciano de Souza et al., 2003; Kervella & Domiciano de Souza, 2006; Domiciano de Souza et al., 2014), Regulus (α Leo, B8IVn; McAlister et al., 2005; Che et al., 2011), Vega (α Lyr, A0V; Aufdenberg et al., 2006; Peterson et al., 2006b; Monnier et al., 2012), Rasalhague (α Oph, A5III; Zhao et al., 2009), Altair (α Aql, A7IV-V; van Belle et al., 2001; Domiciano de Souza et al., 2005; Peterson et al., 2006a; Monnier et al., 2007), Alderamin (α Cep, A7IV; Zhao et al., 2009; van Belle et al., 2006), and Caph (β Cas, F2IV; Che et al., 2011). Figure adapted from van Belle (2012).

1.2 OLBI : a key technique in stellar physics

In the last few decades, Optical/IR Long-Baseline Interferometry (OLBI) became a key observing technique in stellar physics. In particular, the combination of high-angular and high-spectral resolutions provides unprecedented details on the intensity distribution and velocity fields of stars (photosphere and close circumstellar environment). Thanks to OLBI, several physical processes in the photosphere or within a few stellar radii can be directly probed in stars other than the Sun, for the first time in a regular basis.

Some basic concepts of OLBI used in the present work are shortly presented in this section. Several books, conferences, and papers exist on this subject for the interested reader. For example, recent results, basic references, and useful tools on OLBI are available at the web pages of the JMMC³ and the IAU Commission 54⁴.

Modern OLBI instruments combine light from a given sky target collected by two or more telescopes separated by distances reaching hundreds of meters. Different additional devices (not detailed here) are required in order to make sure to combine the light collected by each telescope within a coherence volume where interference fringes exist. Indeed, stellar light shows partial coherence, both spatial/transversal and temporal/longitudinal, because stars have a finite size and are formed by gas emitting nearly as a blackbody.

For a given wavelength λ and a star of typical angular size θ , the 2D spatial/transversal coherence is of the order of

$$S_c = \left(\frac{\lambda}{\theta}\right)^2 = B_{\text{res}}^2 . \quad (1.1)$$

where B_{res} is the telescope separation (baseline) allowing to resolve the star. The temporal/longitudinal coherence depends on the spectral bandwidth $\Delta\lambda$ (or frequency bandwidth $\Delta\nu$) used for observations, so that interference fringes will be present only if the optical paths followed by the light collected by each telescope differ by less than a typical longitudinal coherence length,

$$\Lambda_c = \frac{c}{\Delta\nu} = c\tau_c = \frac{\lambda^2}{\Delta\lambda} = \lambda R_{\text{spec}} , \quad (1.2)$$

where c is the vacuum light speed, τ_c is the coherence time, and R_{spec} is the spectral resolution ($= \lambda/\Delta\lambda$). The order of magnitude of the coherence volume V_c is thus

$$V_c = S_c \Lambda_c = \frac{\lambda^4}{\theta^2 \Delta\lambda} = B_{\text{res}}^2 \lambda R_{\text{spec}} . \quad (1.3)$$

The coherence volume thus depends on the wavelength and spectral bandwidth of the observations, and on the typical target's size at this spectral domain. OLBI takes advantage of this dependence to extract information on the studied target.

Most of the technical difficulties in OLBI come from the necessity to have the interferometer working in a stable way within the coherence volume, i.e., with optical path differences between the different telescopes smaller than Λ_c during the time where fringes are recorded and with baselines $B \sim B_{\text{res}} = \sqrt{S_c}$. To have an idea of these strong technical constraints consider the typical values of $\theta = 1$ mas, $\lambda = 1 \mu\text{m}$, and $\Delta\lambda = 0.01 \mu\text{m}$, which results in $S_c \simeq 40000 \text{ m}^2$ ($B \sim B_{\text{res}} \simeq 200 \text{ m}$), $\Lambda_c = 100 \mu\text{m}$, and $V_c \simeq 4 \text{ m}^3$.

³Jean-Marie Mariotti Center (JMMC) for optical and infrared interferometry (<http://www.jmmc.fr/>).

⁴IAU/IAI Commission 54: optical & infrared interferometry (<http://iau-c54.wikispaces.com/home>).

Even inside the coherence volume, instrumental effects and, in particular, turbulence from Earth's atmosphere tend to vary the different optical paths in an unpredictable and fast manner. Earth-atmosphere turbulence can affect interference fringes on time scales typically as small as a few milliseconds in the visible to a few tens of milliseconds in the near- and mid-IR. Turbulence also degrades the quality of the images recorded by the telescope (seeing effect) diminishing significantly the number of photons available to form interference fringes. Different devices and observing strategies (e.g. adaptive optics, fringe tracking, short individual exposure times) exist to try to overcome, at least partially, these effects that degrade the quality and signal-to-noise ratio of the recorded fringes.

If the interferometer is able to work in a stable manner within Λ_c , it can then be used to measure the spatial coherence of a sky target. This is achieved by measuring, for several telescope separations (called baselines), the contrasts and positions of interference fringes, which correspond, respectively, to the amplitudes and phases of the *complex degree of coherence* or, alternatively, the *complex visibility* V .

For a given sky-projected monochromatic brightness distribution I_λ (also called intensity map), the Van Cittert-Zernike theorem (e.g. [Born & Wolf, 1980](#)) relates the observed complex visibility to the Fourier transform (FT) of I_λ , normalized by its value at the origin, i.e.,

$$V(u, v, \lambda) = |V(u, v, \lambda)| e^{i\phi(u, v, \lambda)} = \frac{\tilde{I}_\lambda(u, v)}{\tilde{I}_\lambda(0, 0)}, \quad (1.4)$$

where \tilde{I}_λ is the FT of I_λ , given explicitly by

$$\tilde{I}_\lambda(u, v) = \iint I_\lambda(x, y) e^{-i2\pi(xu+yv)} dx dy. \quad (1.5)$$

Note that the normalization term $\tilde{I}_\lambda(0, 0)$ is the stellar flux. The spatial (angular) coordinates x and y describe the position of the intensity map on the sky-plane and are generally chosen to follow the coordinates of right ascension (α) and declination (δ). They are defined by the actual (linear) position on the visible stellar surface projected onto the sky-plane, divided by the distance d to the star. Of course, OLBI does not provide observations at all spatial (or Fourier) frequencies, u and v , but only at values corresponding to the separations of telescopes, i.e.,

$$(u, v) = \frac{\vec{B}_{\text{proj}}}{\lambda} = \frac{B_{\text{proj}}}{\lambda} (\sin \text{PA}, \cos \text{PA}), \quad (1.6)$$

where B_{proj} is the projected baseline (distance between two telescopes projected onto the target's direction), and PA is the position angle of the baseline (from north to east). Observations with different baselines and/or at different times (technique of Earth-rotation synthesis) are often used to increase the number of observed points in the uv -plane, i.e., the uv -coverage.

As mentioned above, the instrument (telescopes, optics, detectors, etc) and the Earth's atmosphere alter the recorded target's light in different ways that cannot be completely compensated. As a consequence, the observed complex visibility is given by

$$V_{\text{obs}}(u, v, \lambda, t) = V_{\text{obs}} e^{i\phi_{\text{obs}}} = V(u, v, \lambda) OTF(u, v, \lambda, t), \quad (1.7)$$

where OTF is the time-dependent optical transfer function, which is the FT of the combined point spread function (PSF) of the instrument and of the Earth atmosphere. Note that the target can also vary in time, but we are interested here only in the temporal variations of the OTF and its effects on the interferometric observables.

Visibility amplitudes

The visibility amplitude is the first first to be used and probably the most common interferometric observable. It is a measure of the interferometric fringe contrast, and it is formally given by the modulus of V_{obs} (Eq. 1.7)

$$|V_{\text{obs}}(u, v, \lambda)| = |V(u, v, \lambda)| |\langle OTF \rangle_{\Delta t}| = |V(u, v, \lambda)| T, \quad (1.8)$$

where the proportionality factor T (with $0 \leq T \leq 1$) is called (modulus) transfer function (also represented as MTF), which is the modulus of the OTF averaged over the time span Δt of the observations.

To measure the target's visibility amplitude $|V(u, v, \lambda)|$ it is often necessary to combine the observations of the target with those of one or more calibrators, which are stars of known size (and thus known theoretical fringe contrast). The use of calibrators of known sizes allows thus to estimate T from their observed and theoretical visibility amplitudes.

The observations of target and calibrator thus need to be performed close in time and with the same instrumental conditions, so that T estimated from the calibrator(s) can be applied to the target, preferably interpolating between observations of calibrators performed immediately before and after the target. This calibration procedure compensates most of the effects that corrupt the measurements of interference fringes, diminishing the fringe contrast.

Differential and closure phases

Because of instrumental instabilities and optics imperfections, and the fast and unpredictable phase variations introduced in the light path by the turbulence of Earth atmosphere, interferometers cannot measure directly the target's FT phase $\phi(u, v, \lambda)$ (Eq. 1.4). At least part of the phase information can be recovered from two observable quantities related to $\phi(u, v, \lambda)$, namely, the *differential phase* and the *closure phase*.

The *differential phase* is essentially $\phi(u, v, \lambda)$ as a function of wavelength from which a reference phase calculated at a chosen wavelength value (or wavelength range) has been subtracted. Somewhat different ways of estimating the differential phase from observations exist, depending on the instrument used and on the assumptions made for the calculations. Since most of the results using differential phases in this work are based on the observations from the VLT/AMBER beam combiner (Petrov et al., 2007), the formalism adopted here for the differential phase estimations is similar to the one adopted by Millour et al. (2011, 2006) for this instrument.

The time-average of the FT of the intercorrelations (cross-correlation spectrum) between observed fringes in the reference (λ_{ref}) and considered (λ) wavelengths is given by,

$$\begin{aligned} C(u, v, u_{\text{ref}}, v_{\text{ref}}, \lambda, \lambda_{\text{ref}}) &= \langle V_{\text{obs}}(u, v, \lambda, t) V_{\text{obs}}^*(u_{\text{ref}}, v_{\text{ref}}, \lambda_{\text{ref}}, t) \rangle_t \\ &= |C(u, v, u_{\text{ref}}, v_{\text{ref}}, \lambda, \lambda_{\text{ref}})| e^{i\phi_{\text{diff}}(u, v, u_{\text{ref}}, v_{\text{ref}}, \lambda, \lambda_{\text{ref}})}, \end{aligned} \quad (1.9)$$

where ϕ_{diff} is the observed differential phase that can be approximated in a first order by

$$\phi_{\text{diff}} = \phi - \left(a + \frac{b}{\lambda} \right), \quad (1.10)$$

where ϕ is defined in Eq. 1.4, the parameter a corresponds to a global phase offset, and b is a slope representing an overall residual piston term.

In the optical/IR, the term $(a + b/\lambda)$ that is subtracted from ϕ represents a weak dependence of the phase with λ . It contains not only the influence of the instrument and Earth atmosphere but also any phase term from the object that is slowly varying with λ . Consequently, only strong variations of ϕ with λ remain in the differential phase ϕ_{diff} . Fortunately, this is typically what happens in spectral lines where the phase can strongly depend on the wavelength, while being nearly constant in the adjacent continuum.

The *closure phase* is an observable now commonly delivered by OLBI instruments operating simultaneously with three or more telescopes. From the fringes recorded with three telescopes, T_i , T_j , and T_k , the phases observed at each baseline are given by (c.f. Eq. 1.7)

$$\begin{aligned}\phi_{\text{obs}}(u_{ij}, v_{ij}) &= \phi(u_{ij}, v_{ij}) + [\varphi(T_i) - \varphi(T_j)] , \\ \phi_{\text{obs}}(u_{jk}, v_{jk}) &= \phi(u_{jk}, v_{jk}) + [\varphi(T_j) - \varphi(T_k)] , \\ \phi_{\text{obs}}(u_{ki}, v_{ki}) &= \phi(u_{ki}, v_{ki}) + [\varphi(T_k) - \varphi(T_i)] ,\end{aligned}\tag{1.11}$$

where only the dependence on the spatial frequencies are written explicitly for simplicity. The last term represents the phase shifts (e.g. $\varphi(T_i)$) introduced by the instrument and Earth atmosphere on the path of the light collected by each telescope (e.g. T_i). From the equation above it is possible to combine the three ϕ_{obs} to form the quantity called closure phase, in which the phase shifts φ are canceled out and only the sum of the phase information from the target at each baseline remains, i.e.,

$$\begin{aligned}\Phi_{ijk} &= \phi_{\text{obs}}(u_{ij}, v_{ij}) + \phi_{\text{obs}}(u_{jk}, v_{jk}) + \phi_{\text{obs}}(u_{ki}, v_{ki}) \\ &= \phi(u_{ij}, v_{ij}) + \phi(u_{jk}, v_{jk}) + \phi(u_{ki}, v_{ki})\end{aligned}\tag{1.12}$$

Several astrophysical results on fast-rotating stars that use visibility amplitudes, differential phases, and closure phases are presented in Chapter 3.

CHAPTER 2

PHOTOSPHERE AND CIRCUMSTELLAR ENVIRONMENT (CSE) OF FAST ROTATORS

2.1 Basic hydrodynamical equations

The mechanical equilibrium structure of stars and their circumstellar environment (CSE) is governed by the following two basic hydrodynamical equations (see for example [Rieutord, 2015](#)),

Equation of continuity (mass conservation)

$$\frac{\partial \rho}{\partial t} + \vec{\nabla} \cdot (\rho \vec{v}) = \frac{\partial \rho}{\partial t} + (\vec{v} \cdot \vec{\nabla}) \rho + \rho \vec{\nabla} \cdot \vec{v} = 0, \text{ and} \quad (2.1)$$

Equation of Navier-Stokes (equation of motion)

$$\frac{d\vec{v}}{dt} = \frac{\partial \vec{v}}{\partial t} + (\vec{v} \cdot \vec{\nabla}) \vec{v} = -\frac{\vec{\nabla} P}{\rho} + \vec{\nabla} (\vec{v} \cdot \vec{\nabla} \nu) + \vec{\nabla} \wedge (\vec{v} \wedge \vec{\nabla} \nu) + \nu \Delta \vec{v} - \vec{v} \Delta \nu + \vec{\nabla} \left(\frac{\nu}{3} \vec{\nabla} \cdot \vec{v} \right) + \vec{a},$$

or its simplified form (equation of Navier),

$$\frac{d\vec{v}}{dt} = \frac{\partial \vec{v}}{\partial t} + (\vec{v} \cdot \vec{\nabla}) \vec{v} = -\frac{\vec{\nabla} P}{\rho} + \nu \Delta \vec{v} + \vec{a}, \quad (2.2)$$

where the symbols have their usual meanings in equations describing a medium with mass density ρ , pressure P , velocity \vec{v} , and acceleration \vec{a} due to external forces. Viscous effects are accounted for in the terms containing the kinematic viscosity¹ ν , which is given by the ratio of the dynamic (shear) viscosity μ to the density ρ . The volume (or bulk) viscosity is neglected

¹Also called momentum diffusivity; units of $\text{m}^2 \text{s}^{-1}$ in the SI.

(Stokes hypothesis), which is convenient for monoatomic gazes. The simplified Navier equation describes a fluid with constant ρ ($\Rightarrow \vec{\nabla} \cdot \vec{v} = 0$) and viscosity.

It is worth noting that the demonstration of some general properties of the solutions of the Navier-Stokes equation is one of the seven **Millennium Prize problems** in mathematics that were stated by the Clay Mathematics Institute in 2000.

2.2 Equilibrium structure of fast-rotating stars

We shortly describe here some important concepts and equations defining the physical structure of fast-rotating stars. These concepts and equations are described and developed by a large number of works and authors. As one example we mention the recent book of [Maeder \(2009\)](#) that covers many aspects of the physical structure and evolution of rotating stars, and also provides a large (and still non-exhaustive) number of references on this subject.

In most stars, any perturbation on their physical structure is compensated within a dynamical timescale

$$\tau_{\text{dyn}} \sim \sqrt{\frac{R^3}{GM}} \sim \frac{R}{\bar{c}_s}, \quad (2.3)$$

where G is the gravitation constant, R and M are the stellar radius and mass, and \bar{c}_s is the average sound speed. Depending on the spectral type and evolutionary status of the star, τ_{dyn} varies from ~ 1 s (white dwarfs) to ~ 10 d (red supergiants), which is in any case much shorter than the stellar lifetime. Most stars are thus in steady-state, hydrostatic equilibrium, which allows to rewrite the Navier equation (Eq. 2.2) in a simpler form,

$$\frac{\vec{\nabla} P}{\rho} = \vec{g} - (\vec{v} \cdot \vec{\nabla}) \vec{v} \equiv \vec{g}_{\text{eff}}, \quad (2.4)$$

where viscosity is neglected. The effective gravity \vec{g}_{eff} is composed by the stellar gravity \vec{g} (only external force considered here) and the advection term $(\vec{v} \cdot \vec{\nabla}) \vec{v}$. Depending on \vec{v} , it is possible to express \vec{g}_{eff} as the gradient of a potential Ψ (conservative forces), so that,

$$\frac{\vec{\nabla} P}{\rho} = \vec{g}_{\text{eff}} = -\vec{\nabla} \Psi. \quad (2.5)$$

The identity above implies that $P = P(\Psi)$ and $\rho = \rho(\Psi)$, i.e., the isobars, isodensities, and equipotentials coincide. If the equation of state of the stellar gas follows the relation $P = P(\rho, T)$ (as an ideal gas for instance), then the isobars, isodensities, isothermals, and equipotentials are identical. P , ρ , and T are functions of Ψ only and the star is said to be barotropic. Although this is a good first approximation in general, the "iso" surfaces do not coincide exactly in reality, and the stars are baroclinic.

2.2.1 Roche model

Several works on rotating stars, in particular those based on stellar interferometry, show that the Roche model provides a realistic representation of the distribution of mass and angular momentum throughout the massive stars (masses above a few M_{\odot}).

The Roche model is based on two main approximations: (1) uniform (or solid) rotation with constant angular velocity Ω and (2) all mass M concentrated in the stellar center. The term Roche model is sometimes used when differential rotation is considered, where only the second assumption is adopted. A third, implicit assumption, is that the star is in a steady-state, hydrostatic equilibrium configuration.

Roche's effective gravity and potential

Consider a non-inertial reference frame rotating at an angular velocity Ω identical to the stellar rotation. Under the Roche approximation the stellar particles are thus subjected to a radial (direction \hat{r}) inward point-like gravitational acceleration \vec{g} and to a centrifugal acceleration \vec{a}_{cent} perpendicular to the rotation axis (direction $\hat{\omega}$). In this case, the effective gravity defined in Eq. 2.4 can be explicitly expressed as,

$$\begin{aligned}\vec{g}_{\text{eff}} &= \vec{g} + \vec{a}_{\text{cent}} \\ &= -\frac{GM}{r^2}\hat{r} + \Omega^2\varpi\hat{\omega} \\ &= -\frac{GM}{r^2}\hat{r} + \Omega^2r\sin\theta\hat{\omega} \\ &= -\frac{GM}{r^2}\hat{r} + \frac{v_\phi^2}{\varpi}\hat{\omega},\end{aligned}\tag{2.6}$$

or, in spherical coordinates (unit vectors $\hat{r}, \hat{\theta}, \hat{\phi}$),

$$\vec{g}_{\text{eff}}(r, \theta) = \left(-\frac{GM}{r^2} + \Omega^2r\sin^2\theta, \Omega^2r\sin\theta\cos\theta, 0 \right),\tag{2.7}$$

where $\varpi(= r\sin\theta)$ is the distance to the rotation axis, and $v_\phi(= \Omega\varpi)$ is the azimuthal (ϕ) component of the velocity, which is the total rotation velocity in this case. Figure 2.1 illustrates the adopted reference frame, and some of the parameters and physical quantities of the Roche model. Note that, contrarily to a non-rotating spherical star, \vec{g}_{eff} does not follow the radial direction, forming an angle ε with \hat{r} .

For uniform rotation (or differential rotation with $\Omega = \Omega(\varpi)$), we have the conservative case of Eq. 2.5, where \vec{g}_{eff} can be expressed as the gradient of a potential,

$$\vec{g}_{\text{eff}} = -\vec{\nabla}\Psi,\tag{2.8}$$

where Ψ is now the so called Roche potential, which is given by the sum of the point-like gravitational potential and the centrifugal potential for uniform rotation,

$$\begin{aligned}\Psi(r, \theta) &= \Psi_{\text{grav}}(r) + \Psi_{\text{cent}}(r, \theta) \\ &= -\frac{GM}{r} - \frac{\Omega^2(r\sin\theta)^2}{2}.\end{aligned}\tag{2.9}$$

Poisson's equation

When dealing with equations of rotating stars it is often useful to consider the Poisson's equation, relating the gravitational potential to the mass density distribution. In the framework of the Roche

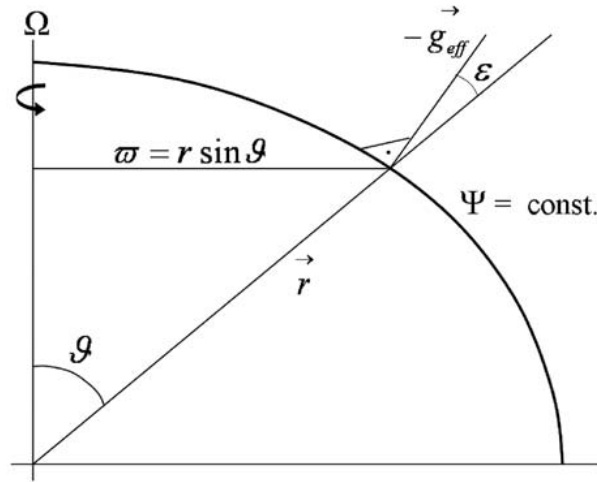


Figure 2.1 – Reference frame and some parameters of the Roche model (see text for details and definitions of symbols). Figure from [Maeder \(2009\)](#).

model it can be written as

$$\Delta\Psi = \Delta\Psi_{\text{grav}} + \Delta\Psi_{\text{cent}} = -\vec{\nabla} \cdot \vec{g}_{\text{eff}} = \begin{cases} 4\pi G\rho - 2\Omega^2, & \text{for } r = 0 \\ -2\Omega^2, & \text{for } r > 0 \end{cases} \quad (2.10)$$

Recall that the mass is concentrated at the stellar center so that $\rho \neq 0$ only at $r = 0$.

Some works solve the Poisson's equation for the gravitational potential in order to model rotating stars with more sophisticated densities and rotation laws (e.g. [Ostriker & Mark, 1968](#); [Clement, 1974](#); [Jackson et al., 2005](#), and references therein).

Surface shape and critical velocity

The stellar surface shape is obtained from the Roche potential (Eq. 2.9). It follows an equipotential (Ψ constant), satisfying the more general condition that no work is required nor provided for any displacement $d\vec{l}$ on the surface,

$$\vec{g}_{\text{eff}} \cdot d\vec{l} = -\vec{\nabla}\Psi \cdot d\vec{l} = 0. \quad (2.11)$$

As already indicated in Eq. 2.9, the surface shape of a Roche star is nonspherical since Ψ is a function of both r and θ . The stellar surface is thus defined by the points $r(\equiv R(\theta))$ that follow the equipotential,

$$\Psi = -\frac{GM}{R(\theta)} - \frac{\Omega^2 R^2(\theta) \sin^2 \theta}{2} = -\frac{GM}{R_p} = -\frac{GM}{R_{\text{eq}}} - \frac{(\Omega R_{\text{eq}})^2}{2} = \text{constant}, \quad (2.12)$$

where the term ΩR_{eq} is the equatorial rotation velocity $v_{\text{eq}} (= v_{\phi}(\pi/2))$. The constant value setting the surface equipotential is chosen as a reference point on this surface. In the equation above we give values at two possible reference points that are often adopted, namely, equipotential in terms of the radius at the pole R_p or at the equator R_{eq} .

The polar radius is used as reference mostly in works dealing with stellar evolution and/or for comparisons with models without rotation since it is almost insensitive to rotation ([Ekström](#)

et al., 2008). For example, rotation leads to a decrease of R_p of less than $\sim 2\%$ compared to the case without rotation (at solar metallicity and masses between 3 and 20 M_\odot). It is thus common to consider R_p independent on the rotation velocity.

In works dealing with interferometric observations it is preferable to express the surface equipotential in terms of the equatorial radius R_{eq} since the equatorial angular diameter ($2R_{\text{eq}}/d$, where d is the distance to the star) is the quantity more directly related to the observations. Indeed, R_p cannot be directly measured for an arbitrary inclination angle i of the rotation axis, unless the star is seen exactly equator-on. Before deriving the complete form of the Roche surface, the ratio between the equatorial and polar radii can already be obtained directly from Eq. 2.12,

$$\frac{R_{\text{eq}}}{R_p} = \left(1 - \frac{v_{\text{eq}}^2 R_p}{2GM}\right)^{-1} = 1 + \frac{v_{\text{eq}}^2 R_{\text{eq}}}{2GM}$$

or

(2.13)

$$\epsilon \equiv 1 - \frac{R_p}{R_{\text{eq}}} = \frac{v_{\text{eq}}^2 R_p}{2GM},$$

where ϵ is the flattening parameter, ranging from 0 (spherical star where $r = R_p$ at all latitudes) to a maximum (critical) flattening ϵ_c , attained when gravity is totally compensated by the centrifugal force at some point on the stellar surface. For uniform rotation, this condition is satisfied first at the stellar equator where the centrifugal force is highest, so the equatorial radius attains its maximum critical value R_c . By imposing that $g_{\text{eff}}(r = \varpi = R_{\text{eq}} = R_c) = 0$ in Eq 2.6, and solving for the equatorial velocity, one can thus define the critical equatorial rotation velocity $v_c (= v_\phi = v_{\text{eq}})$ and the critical angular rotation velocity Ω_c as

$$v_c = \Omega_c R_c = \sqrt{\frac{GM}{R_c}},$$

and

(2.14)

$$\Omega_c = \sqrt{\frac{GM}{R_c^3}}.$$

In the Roche model, R_c , and the strongest allowed flattening ϵ_c , can be expressed as a function of R_p from Eq. 2.12 (or Eq. 2.13), by substituting R_{eq} by R_c and v_{eq} by v_c from Eq. 2.14 above,

$$\frac{R_c}{R_p} = \frac{3}{2}$$

or

(2.15)

$$\epsilon_c = 1 - \frac{R_p}{R_c} = \frac{1}{3}.$$

It is sometimes useful to consider a different definition of critical velocity, valid beyond the frame of the Roche approximation, whenever the star rotates at an equatorial (critical) velocity corresponding to the circular Keplerian orbital velocity at the stellar equator. Thus, for any given equatorial radius R_{eq} , the Keplerian (subscript "k") or orbital (subscript "orb"), linear and angular,

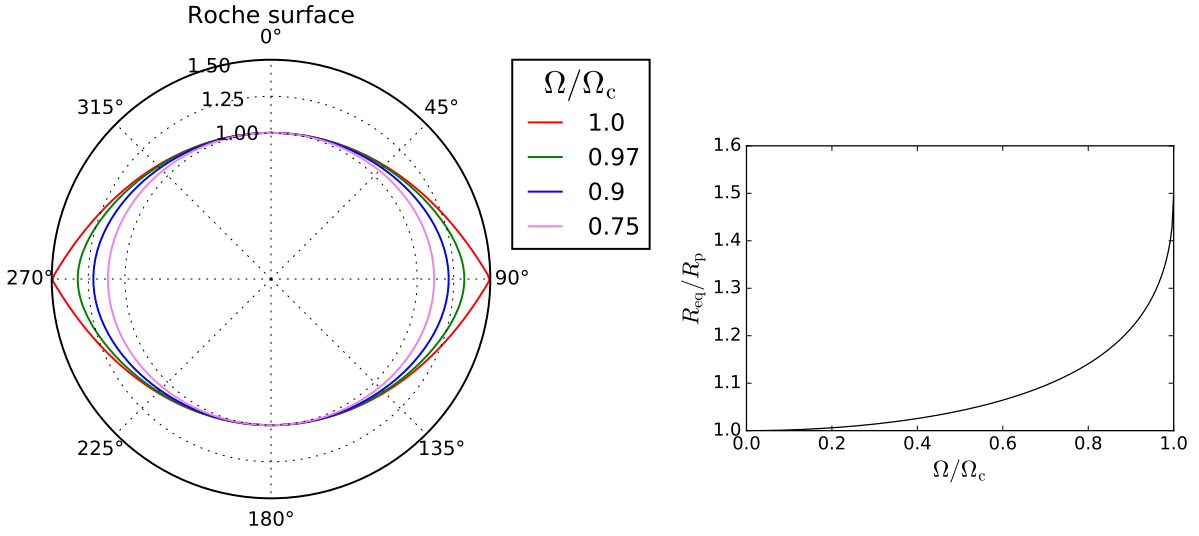


Figure 2.2 – *Left*: Meridional cut of the Roche stellar surface ($R(\theta)/R_p$ in polar coordinates) for several rotation rates (Ω/Ω_c) as given by Eq. 2.18. *Right*: $R_{\text{eq}}/R_p (= R(90^\circ)/R(0^\circ))$ as a function of Ω/Ω_c .

critical velocities are defined, respectively, as

$$v_k = v_{\text{orb}} = \Omega_k R_{\text{eq}} = \sqrt{\frac{GM}{R_{\text{eq}}}},$$

and

$$\Omega_k = \Omega_{\text{orb}} = \frac{v_k}{R_{\text{eq}}} = \sqrt{\frac{GM}{R_{\text{eq}}^3}}.$$
(2.16)

Another quantity often used is the angular velocity relative to Ω_k , i.e.,

$$\omega = \frac{\Omega}{\Omega_k} = v_{\text{eq}} \sqrt{\frac{R_{\text{eq}}}{GM}} = \sqrt{\frac{2\epsilon}{1-\epsilon}}$$
(2.17)

The stellar surface of the Roche model is obtained by solving Eq. 2.12, which is a (depressed) cubic equation on R as a function of θ . Different formulations of $R(\theta)$ exist in the literature, depending also on the chosen normalizations of physical quantities. For example, in Appendix A we show that $R(\theta)$ can be expressed in terms of trigonometric functions as,

$$R(\theta) = R_p \frac{\sin \left[\frac{1}{3} \arcsin \left(\frac{\Omega}{\Omega_c} \sin \theta \right) \right]}{\frac{1}{3} \left(\frac{\Omega}{\Omega_c} \sin \theta \right)} = R_p \frac{\cos \left[\frac{1}{3} \arccos \left(-\frac{\Omega}{\Omega_c} \sin \theta \right) + \frac{4\pi}{3} \right]}{\frac{1}{3} \left(\frac{\Omega}{\Omega_c} \sin \theta \right)}.$$
(2.18)

These formulations are similar to those given by Kopal (1987), van Belle et al. (2001), and Domiciano de Souza et al. (2002). Figure 2.2 shows examples of the Roche stellar surface and of the ratio R_{eq}/R_p as given by the equation above for different values of Ω/Ω_c .

Note that the surface (local) effective gravity is directly obtained from Eq. 2.6 (or Eq. 2.7) with $r = R(\theta)$. In particular, the modulus of the surface effective gravity $g_{\text{eff}}(\theta) (= |\vec{g}_{\text{eff}}(R(\theta))|)$

at the stellar equator g_{eq} is given by the difference between the gravitational and centrifugal accelerations at this point, i.e.,

$$g_{\text{eq}} = g_{\text{eff}}\left(\frac{\pi}{2}\right) = \frac{GM}{R_{\text{eq}}^2} - \frac{v_{\text{eq}}^2}{R_{\text{eq}}}. \quad (2.19)$$

The modulus of the surface polar effective gravity g_{p} is simply given by the polar gravitational acceleration, since there is no centrifugal force at the poles,

$$g_{\text{p}} = g_{\text{eff}}(0) = g_{\text{eff}}(\pi) = \frac{GM}{R_{\text{p}}^2}. \quad (2.20)$$

The ratio between g_{eq} and g_{p} can be expressed as

$$\frac{g_{\text{eq}}}{g_{\text{p}}} = (1 - \epsilon)(1 - 3\epsilon) = \left(\frac{R_{\text{p}}}{R_{\text{eq}}}\right)^2 (1 - \omega^2) = \frac{1 - \omega^2}{(1 + \omega^2/2)^2}, \quad (2.21)$$

where ϵ and ω are defined in Eqs. 2.13 and 2.17.

2.2.2 Gravity darkening

Gravity darkening is an important effect in stellar physics resulting from a local surface radiative flux dependent on the local effective gravity. In a seminal paper, [von Zeipel \(1924\)](#) showed that under some equilibrium conditions the radiative flux F is proportional to the local effective gravity g_{eff} , i.e.,

$$\begin{aligned} F &= \sigma T_{\text{eff}}^4 = C g_{\text{eff}} \\ \text{or} & \\ T_{\text{eff}} &= \left(\frac{C}{\sigma}\right)^{0.25} g_{\text{eff}}^{0.25}, \end{aligned} \quad (2.22)$$

where C is a proportionality constant composed of several physical quantities (see below), σ is the Stefan-Boltzmann constant, and T_{eff} is the local effective temperature.

We note that, because of gravity darkening, the star does not have a unique effective temperature over the photosphere and thus presents a different aspect depending on the viewing angle. Moreover, gravity darkening is responsible by internal circulations of matter, energy, and angular momentum, and by non-spherical mass and angular momentum losses. All these physical processes have a direct impact on the structure and evolution of the star. A precise formulation of the gravity darkening effect is thus crucial for a more profound understanding of stellar physics.

Indeed, since the beginning of the XXth Century, the gravity darkening effect (also called von Zeipel effect) has been discussed, improved, and computed by several authors: [von Zeipel \(1924\)](#), [Eddington \(1925\)](#), [Lucy \(1967\)](#), [Connon Smith & Worley \(1974\)](#), [Kippenhahn \(1977\)](#), [Claret \(1998, 2000, 2012\)](#), [Maeder \(1999\)](#), [Rieutord \(2006\)](#), [Espinosa Lara & Rieutord \(2011\)](#), and many others. The results from this work concerning gravity darkening are presented in Chapter 3.

On the other hand, observational proof or direct measurement of gravity darkening in fast-rotating single stars have been provided only quite recently, thanks to the high spatial resolution power from stellar interferometers: [Ohishi et al. \(2004\)](#), [Domiciano de Souza et al. \(2005\)](#),

Sect. 3.1), Peterson et al. (2006b), Monnier et al. (2007), Che et al. (2011), Domiciano de Souza et al. (2014, Sect. 3.2), and others.

We present below a quick review of some of the basic equations and recent theoretical developments and observations on the gravity darkening effect.

The von Zeipel theorem

In radiative regions of the star, in particular atmospheres of hot stars, the local radiative flux vector is proportional and antiparallel to the gradient of local temperature gas T (diffusion of photons approximation),

$$\vec{F} = -\chi \vec{\nabla} T = -\frac{4acT^3}{3\kappa\rho} \vec{\nabla} T, \quad (2.23)$$

where χ is the coefficient of radiative conductivity, which is a function of the radiation constant a , the vacuum light speed c , the local total mean opacity κ (generally the Rosseland mean opacity), the local density ρ , and the local temperature T .

Under the assumption that the star is barotropic and in mechanical equilibrium, the isodensities, isobars, and isotherms coincide with the equipotential surfaces (e.g. Rieutord, 2006; Espinosa Lara & Rieutord, 2011): density ρ , temperature T , and pressure P are functions of the potential Ψ only. This corresponds also to the fundamental hypothesis adopted by von Zeipel (1924)². This hypothesis also implies that κ is constant on an equipotential, so that χ is a function of the potential Ψ only in Eq. 2.23. In this case, using Eq. 2.8, we obtain the von Zeipel theorem or law (von Zeipel, 1924)

$$\vec{F} = -\chi(\Psi) \frac{dT(\Psi)}{d\Psi} \vec{\nabla} \Psi = \chi(\Psi) \frac{dT(\Psi)}{d\Psi} \vec{g}_{\text{eff}} \equiv -C(\Psi) \vec{g}_{\text{eff}}, \quad (2.24)$$

which is identical to Eq. 2.22 when the absolute values are considered. This equation shows that the radiative flux vector is also antiparallel to the effective gravity in the von Zeipel law, with a proportionality term C , which is constant on an equipotential. The proportionality constant C can be obtained by integrating Eq. 2.24 over the surface equipotential such that

$$C = -\chi \frac{dT}{d\Psi} = -\frac{\int \vec{F} \cdot \vec{d}s}{\int \vec{g}_{\text{eff}} \cdot \vec{d}s} = \frac{L}{\int g_{\text{eff}} ds} = \frac{L}{\int \vec{\nabla} \Psi \cdot \vec{d}s} = \frac{L}{\int \Delta \Psi dV} = \frac{L}{4\pi GM_{\Omega}}, \quad (2.25)$$

where we used the definition of stellar luminosity $L (= \int \vec{F} \cdot \vec{d}s)$, the Poisson equation (Eq. 2.10), the divergence (or Gauss) theorem, and the fact that \vec{g}_{eff} is antiparallel to the stellar surface vector $\vec{d}s$. M_{Ω} is the modified mass, defined below in Eq. 2.28.

When dealing with observations it is often useful to relate C and L in the foregoing equations to the local effective temperature T_{eff} and to a mean effective temperature \bar{T}_{eff} , averaged over the whole stellar surface (equipotential) S_{\star} ,

$$L = \int \vec{F} \cdot \vec{d}s = C \int g_{\text{eff}} ds = \sigma \int T_{\text{eff}}^4 ds = \sigma \bar{T}_{\text{eff}}^4 S_{\star}. \quad (2.26)$$

Note that the above equation recovers the relation between g_{eff} and T_{eff} given in Eq. 2.22.

²"...the nature of the gas is constant over every level surface, but may change from one level surface to another"

It is also sometimes necessary to consider the stellar bolometric flux

$$F_{\text{bol}} = \frac{L}{4\pi d^2} = \sigma \bar{T}_{\text{eff}}^4 \frac{S_{\star}}{4\pi d^2} = \sigma \bar{T}_{\text{eff}}^4 \frac{\bar{\varnothing}^2}{4}, \quad (2.27)$$

where $\bar{\varnothing}$ is the mean angular diameter of a spherical star having a surface area S_{\star} , and d is the distance to the star.

The modified mass M_{Ω} in Eq. 2.25 is a consequence of the Poisson equation (Eq. 2.10), and is given by

$$M_{\Omega} = M \left(1 - \frac{\Omega^2}{2\pi G \bar{\rho}} \right) \leq M, \quad (2.28)$$

where M is the stellar mass and $\bar{\rho}$ ($= M/V$) is the average density inside the equipotential surface of volume V . Values for the term $\Omega^2/2\pi G \bar{\rho}$ at different Ω in the Roche approximation are given by Maeder (2009). It ranges from 0 to a maximum value corresponding to the Roche critical velocity (Eq. 2.14),

$$\frac{\Omega_c^2}{2\pi G \bar{\rho}_c} = \frac{V_c}{2\pi R_c^3} = 0.361, \quad (2.29)$$

where $V_c (= 2.2666 R_c^3)$ and $\bar{\rho}_c (= M/V_c)$ are the critical volume and critical average density of the Roche model (cf. Kopal, 1987).

Generalizations of the von Zeipel theorem

The physical conditions assumed to deduce to the gravity darkening law proposed by (von Zeipel, 1924) are not strictly valid (diffusion approximation, uniform rotation, barotropicity). Several other researchers proposed generalizations of the von Zeipel theorem. For example, Lucy (1967) showed, by averaging from various stellar 1D atmosphere numerical models, that the relation $T_{\text{eff}} \propto g_{\text{eff}}^{0.08}$ reproduces better the gravity darkening in cooler stars with convective atmospheres than Eq. 2.22. However, as in the case of the von Zeipel theorem, the computations and results from Lucy also contain important approximations, assuming small deviations from sphericity (slow rotation).

In practice, in order to account for departures from the results of von Zeipel and Lucy, it is usual to express the gravity darkening in terms of an *ad hoc* parameter β (gravity darkening coefficient) relating the local F , T_{eff} , and g_{eff} :

$$\begin{aligned} F &= \sigma T_{\text{eff}}^4 = C_{\beta} g_{\text{eff}}^{4\beta} \\ \text{or} & \\ T_{\text{eff}} &= \left(\frac{C_{\beta}}{\sigma} \right)^{0.25} g_{\text{eff}}^{\beta}, \end{aligned} \quad (2.30)$$

where C_{β} is a proportionality constant obtained as in Eq. 2.25, but replacing g_{eff} par $g_{\text{eff}}^{4\beta}$. It is sometimes useful to write this gravity darkening β -law in terms of T_{eff} and g_{eff} at a given point of the stellar surface, such as

$$T_{\text{eff}} = T_p \left(\frac{g_{\text{eff}}}{g_p} \right)^{\beta}, \quad (2.31)$$

where, in this case, the subscript "p" denotes the polar effective temperature and gravity. Note that $\beta = 0.08$ and $\beta = 0.25$, respectively, in the Lucy's and von Zeipel's formulations of the gravity darkening.

Similarly to Lucy's work, Claret (1998, 2000, 2012) used 1D stellar atmosphere models to compute β values for different physical conditions. The gravity darkening parameter varies continuously from radiative ($\beta \lesssim 0.25$) to convective ($\beta \lesssim 0.1$) atmospheres. The exact behavior of these numerically deduced β depends on the stellar mass, atmosphere model used, and atmospheric optical depth considered. Espinosa Lara & Rieutord (2012) discuss the results from Lucy and Claret, arguing that 1D models should be avoided when computing gravity darkening exponents.

By adopting a different approach, Espinosa Lara & Rieutord (2011) propose an alternative gravity darkening law that is independent on convective or radiative nature of the stellar atmosphere. Their gravity darkening model is based on three hypothesis, which are generally valid on stellar atmospheres:

- Flux conservation, i.e., there are no heat sources or sinks on the stellar atmosphere, which is expressed as a divergence-free vector flux,

$$\vec{\nabla} \cdot \vec{F} = 0 . \quad (2.32)$$

- Flux antiparallel to the local effective gravity \vec{g}_{eff} . This hypothesis is valid both for convective (heat transport is parallel to \vec{g}_{eff}) and radiative (\vec{F} can be considered antiparallel to \vec{g}_{eff} within $\simeq 10^{-2}$ rad), so that,

$$\vec{F} = -f(r, \theta) \vec{g}_{\text{eff}} . \quad (2.33)$$

where $f(r, \theta)$ is a function of the position on the star. Note the difference with respect to the von Zeipel law (Eq. 2.24) where $f(r, \theta) = C$, a constant term.

- The stellar surface and \vec{g}_{eff} are given by the Roche model with uniform angular velocity Ω (cf. Sect. 2.2.1).

Based on these hypothesis, Espinosa Lara & Rieutord (2011) derived an alternative gravity darkening law (ELR model hereafter) with the following effective temperature profile

$$T_{\text{eff}}(\theta) = \left(\frac{F}{\sigma}\right)^{0.25} = \left(\frac{L}{4\pi\sigma GM}\right)^{0.25} \sqrt{\frac{\tan \vartheta(R(\theta), \theta)}{\tan \theta}} g_{\text{eff}}^{0.25} , \quad (2.34)$$

where $R(\theta)$ is given by Eq. 2.18 and ϑ is the solution of

$$\cos \vartheta + \ln \tan \frac{\vartheta}{2} = \frac{1}{3} \omega^2 \left(\frac{R(\theta)}{R_{\text{eq}}} \cos \theta\right)^3 + \cos \theta + \ln \tan \frac{\theta}{2} , \quad (2.35)$$

where ω is defined in Eq. 2.17. ϑ can be determined for each θ for example applying Newton's interactive method to the equation above. Thus, the ELR gravity darkening law is completely defined by L , M , R_{eq} , and Ω (or any equivalent combination of parameters).

The equatorial to polar effective temperatures ratio is given by

$$\begin{aligned} \frac{T_{\text{eq}}}{T_{\text{p}}} &= \sqrt{1 - \epsilon} \left(\frac{1 - 3\epsilon}{1 - \epsilon}\right)^{1/12} \exp\left(-\frac{\epsilon(1 - \epsilon)^2}{3}\right) \\ &= \sqrt{\frac{2}{2 + \omega^2}} (1 - \omega^2)^{1/12} \exp\left(-\frac{4}{3} \frac{\omega^2}{(2 + \omega^2)^3}\right) , \end{aligned} \quad (2.36)$$

2.2. Equilibrium structure of fast-rotating stars

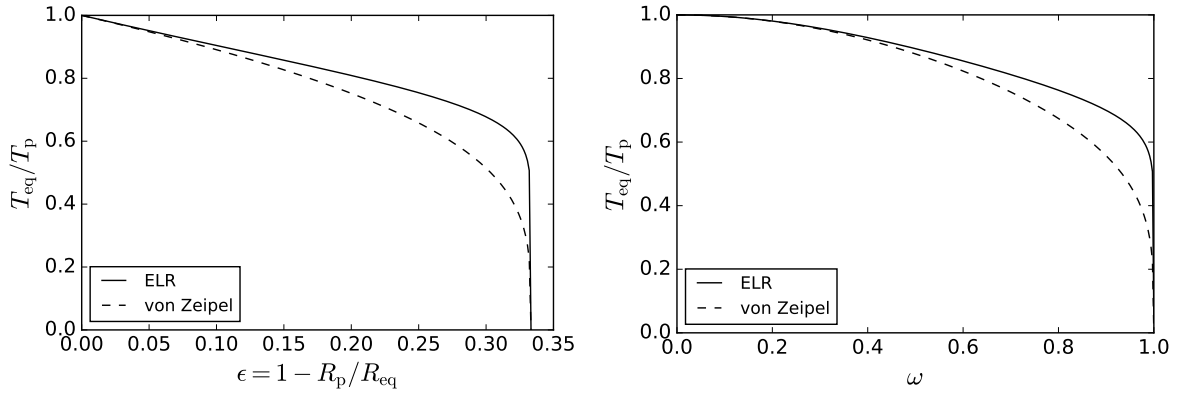


Figure 2.3 – Equatorial to polar effective temperatures for the ELR and von Zeipel gravity-darkening models, under the Roche approximation, as a function of ϵ (*left*) and ω (*right*). The ratio $T_{\text{eq}}/T_{\text{p}}$ for the von Zeipel model is directly obtained from Eqs. 2.21 and 2.31 with $\beta = 0.25$. Gravity darkening at high rotation rates leads to stellar equatorial regions with effective temperatures significantly lower than the poles.

where ϵ and ω are defined in Eqs. 2.13 and 2.17. Figure 2.3 shows $T_{\text{eq}}/T_{\text{p}}$ given by Eq. 2.36 compared to the values expected for the von Zeipel model.

It is important to note that the coefficient β appearing in β -law models is not an input parameter of the ELR gravity-darkening model and that it is not required to describe the relation between T_{eff} and g_{eff} . Indeed, the dependence of $\ln T_{\text{eff}}$ with $\ln g_{\text{eff}}$ does not necessarily follow a straight line with a constant slope as is the case for example in Eq. 2.31, so that a unique β value cannot be defined for the whole photosphere in the ELR model. However, it is sometimes useful or necessary to derive an equivalent β in order to compare the ELR model to predictions from other β -law models and/or to β values estimated from observations.

An equivalent β value can be estimated for example from a fit to $\ln T_{\text{eff}}$ *versus* $\ln g_{\text{eff}}$ over all latitudes following the curve defined by Eq. 2.34. An equivalent β can be straightforwardly derived from the equatorial and polar ratios of T_{eff} and g_{eff} (Eqs. 2.21 and 2.36) leading to the following analytical relation

$$\begin{aligned} \beta &= \frac{\ln T_{\text{eq}}/T_{\text{p}}}{\ln g_{\text{eq}}/g_{\text{p}}} \\ &= \frac{1}{4} - \frac{1}{6} \frac{\ln \frac{1-3\epsilon}{1-\epsilon} + 2\epsilon(1-\epsilon)^2}{\ln(1-\epsilon)(1-3\epsilon)} \\ &= \frac{1}{4} - \frac{1}{6} \frac{\ln(1-\omega^2) + \omega^2(1+\omega^2/2)^{-3}}{\ln(1-\omega^2) - 2\ln(1+\omega^2/2)} \end{aligned} \quad (2.37)$$

The first-order polynomial expansion of the above relation for β gives

$$\begin{aligned} \beta &= \frac{1}{4} - \frac{1}{3}\epsilon + \mathcal{O}(\epsilon^2) \\ &= \frac{1}{4} - \frac{1}{6}\omega^2 + \mathcal{O}(\omega^4), \end{aligned} \quad (2.38)$$

with $\omega^2 \rightarrow 2\epsilon$ for $\epsilon \rightarrow 0$. Note that the ELR model predicts an equivalent $\beta < 0.25$ for $\epsilon > 0$ (or $\omega^2 > 0$), contrarily to the von Zeipel gravity darkening that has $\beta = 0.25$, independently on ϵ .

Predictions of gravity darkening models compared to observations

Several recent works based on interferometric observations of fast-rotating stars measured values of β ranging from ~ 0.15 to ~ 0.23 . These observational results show in particular that the von Zeipel law ($\beta = 0.25$) is not generally valid and overestimates the dependence of T_{eff} with g_{eff} . Figure 2.4 compares the alternative gravity darkening models from Claret (1998, 2000, 2012) and Espinosa Lara & Rieutord (2011) with recent values of β measured from interferometric observations of six single fast-rotating stars.

Depending on the adopted optical depth for a given stellar atmosphere model, Claret's gravity darkening is able to explain the β measured on the four colder stars, or on Regulus (and marginally on Achernar), but not all stars (cold and hot) at once. It seems thus difficult to recover the β values measured on both cold and hot stars with Claret's model without adjusting several parameters in order to match the observations. In particular, considering different optical depths seems to be necessary to account for all measured β , but it is not clear why and/or which value should be adopted in each case.

The ELR model, relying on few input parameters and hypothesis, reproduces five out of the six measured β (marginal agreement for α Cep), with a significant disagreement only for the colder star in the list, β Cas (F2IV), which is motivating. Two possibilities exist to explain this discrepancy, namely, (1) the measured β presents an observational bias, that could be caused by the low inclination of β Cas ($i = 19.9^\circ \pm 1.9^\circ$; Che et al., 2011) or (2) the presence of convection in colder stars indeed leads to lower β values (as suggested by the results of Claret and Lucy) and should then be included in the model of Espinosa Lara & Rieutord (2011).

One way to decide between these two possibilities is to perform additional interferometric observations covering a broader range of flattening, in particular on cold stars (with convective atmospheres). These observations consist in an interesting research program that can contribute to determine if gravity darkening is as function mainly of rotation flattening alone or if convection (and/or T_{eff}) plays an important role as well.

Before finishing this discussion concerning gravity darkening, we would like to mention that other generalizations of the von Zeipel theorem exist, but they consider slow rotation in many cases. Caution should thus be taken when confronting these models to observations and results of fast rotators. For example, by considering slow differential rotation, alternative gravity darkening laws were derived by Kippenhahn (1977) for $\Omega = \Omega(r, \theta)$, and by Maeder (1999) for $\Omega = \Omega(r)$, known as "shellular" rotation (c.f. Zahn, 1992). For these angular velocities, \vec{g}_{eff} cannot be expressed as the gradient of a potential in general so that Eq. 2.8 does not apply and Eq. 2.24 (von Zeipel theorem) is not strictly valid, leading to other alternative expressions of gravity darkening.

2.2. Equilibrium structure of fast-rotating stars

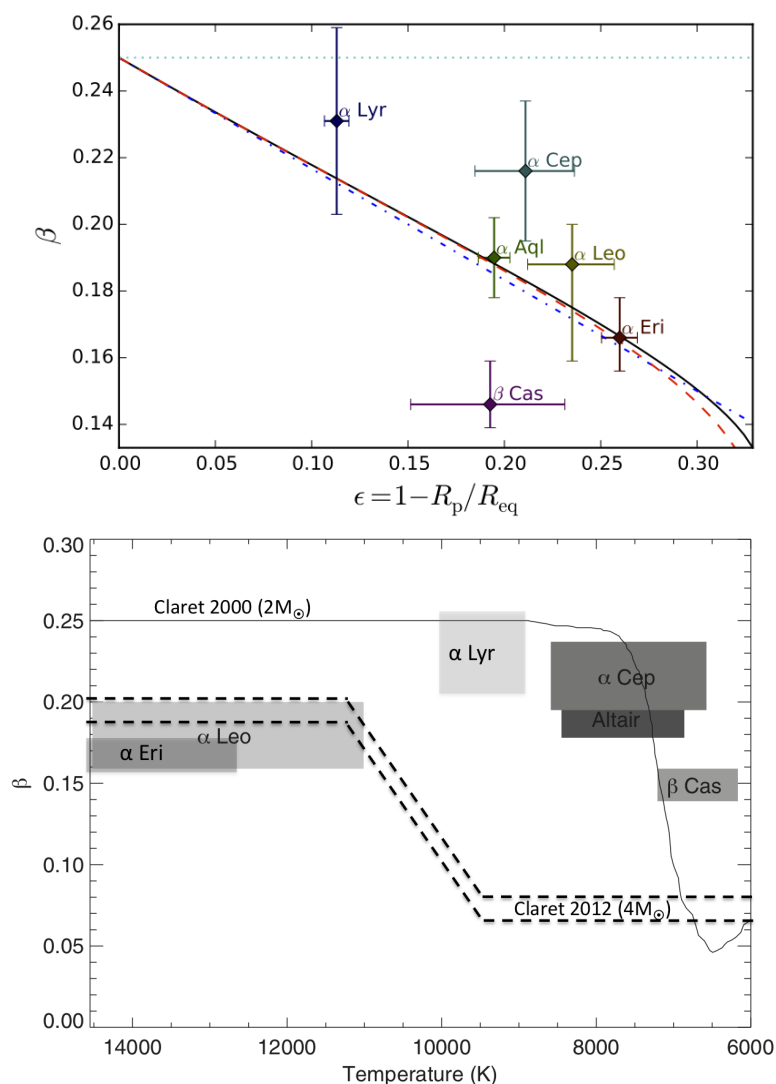


Figure 2.4 – Gravity darkening coefficient β as a function of the rotation flattening $\epsilon = 1 - R_p/R_{eq}$ (*top*) and as a function of the local T_{eff} over the stellar surface (*bottom*). The top and bottom solid curves correspond, respectively, to gravity darkening models from [Espinosa Lara & Rieutord \(2011\)](#) (ELR model; equivalent β from a fit to the $\log T_{\text{eff}}$ versus $\log g_{\text{eff}}$ curve using Eqs. 2.21 and 2.36) and [Claret \(2000\)](#) (β for a $2 M_{\odot}$ star extrapolated to higher T_{eff} at the von Zeipel value 0.25). The dashed and dot-dashed curves in the top panel are the equivalent β values estimated for the ELR model from the analytical Eqs. 2.37 and 2.38; the horizontal dotted line at $\beta = 0.25$ is the von Zeipel value. The region between the dashed lines in the bottom roughly reproduce the β values for a $4 M_{\odot}$ star calculated by [Claret \(2012\)](#) using gray and ATLAS (Kurucz) model atmospheres. Compared to the solid line curve, this model has globally a lower β since it was computed for low optical depth regions ($\tau \simeq 1$), i.e., where the diffusion approximation for the flux is not strictly valid. For high optical depths the von Zeipel $\beta = 0.25$ is recovered. All these β -law curves slightly shift to lower T_{eff} with increasing masses ([Claret, 2000](#)). The most recent and precise values of β measured from interferometric observations of six single fast-rotating stars are also plotted on both panels. From hotter to colder star, the observed fast rotators are: α Eri (Achernar, B3-6Vpe; Sect. 3.2; [Domiciano de Souza et al., 2014](#)), α Leo (Regulus, B8IVn; [Che et al., 2011](#)), α Lyr (Vega, A0V; [Monnier et al., 2012](#)), α Aql (Altair, A7IV-V; [Monnier et al., 2007](#)), α Cep (Alderamin, A7IV; [Zhao et al., 2009](#)), β Cas (Caph, F2IV; [Che et al., 2011](#)). The plots in this figure are similar to those presented by [Domiciano de Souza et al. \(2014\)](#), [Espinosa Lara & Rieutord \(2011\)](#), and [Che et al. \(2011\)](#), with updates to include additional observations and models.

2.2.3 Examples of photospheric intensity-maps

Figures 2.5 to 2.12 show several examples illustrating some of the fast-rotation effects on the stellar surface structure and emitted flux (rotational deformation and gravity darkening) presented previously in this section. These simulated images were created with the numerical model CHARRON described in Sect. 2.5.1. The local specific intensity profiles I_λ over the stellar surface are computed using the spectral synthesis code `Synspec`³ (e.g. Hubeny & Lanz, 2011) with input stellar atmosphere models from the ATLAS9 code with solar abundance⁴ (e.g. Kurucz, 1979). The physical parameters adopted to compute these CHARRON models are given in Table 2.1.

Figure 2.5 shows CHARRON models of sky-projected maps of I_λ (in the V, H, and K photometric bands) and effective temperature T_{eff} maps, computed at different inclinations i . The apparent flattening changes with i and for each spectral band the influence of gravity and limb darkening also varies (stronger effect at shorter wavelengths). For the I_λ and T_{eff} maps at intermediate inclinations ($i = 45^\circ$ and 60°) the brighter apparent regions are not exactly located at the hot poles, but are somewhat closer to the center of the maps. This is caused by a combination of gravity darkening (influencing I_λ and T_{eff}) and flattening/limb darkening (influencing I_λ only).

Figure 2.6 shows the I_λ and T_{eff} maps as in Fig. 2.5, but for two different rotation rates ($v_{\text{eq}} = 250 \text{ km s}^{-1} = 0.832v_c$ and $v_{\text{eq}} = 290 \text{ km s}^{-1} = 0.929v_c$). This figure illustrates the changing of surface flattening and distribution of flux and temperature with the the rotation velocity.

Figures 2.7 to 2.12 show selected specific intensities I_λ and equivalent width EW maps in the vicinity of several spectral lines from the visible to the near-IR, namely, FeI 5169, MgII-SiII 6347, H α , HeI 6678, OI 7772, and Br γ . The chosen wavelengths for the maps around each spectral line correspond to the immediate continuum, line center (zero Doppler shift), and line center plus a Doppler shift of $0.5v_{\text{eq}} \sin i$. The rightmost columns of Figs. 2.7 to 2.12, show the equivalent width EW maps, which are calculated as

$$EW(x, y) = \int \left(1 - \frac{I_\lambda(x, y)}{I_c(x, y)} \right) d\lambda, \quad (2.39)$$

where I_c is the specific intensity in the continuum close to the spectral line and the integration is performed at each point (x, y) on the apparent stellar surface. $EW(x, y)$ will thus be higher at regions of the stellar surface where the corresponding spectral absorption line is stronger (deeper).

These non-uniform I_λ and EW maps show clearly that different atoms and/or transitions have different dependence on $g_{\text{eff}}(\theta)$ and $T_{\text{eff}}(\theta)$ so that the line intensity changes over the stellar surface. For example, in these models the HeI 6678 line (Fig. 2.10) is stronger (deeper) at the hot poles than at the equatorial regions, while the opposite happens for the other lines shown. From these examples it is clear that, contrarily to a non-rotating spherical star, different lines can be mainly formed at different regions of the stellar surface of a rotating star.

Some of these figures and others similar to them were provided to Rivinius et al. (2013) to illustrate fast-rotation effects in an A&A review paper dedicated to Be stars.

³<http://nova.astro.umd.edu/Synspec49/synspec.html>

⁴Web page of grid models: <http://kurucz.harvard.edu/grids.html>

Table 2.1 – Stellar parameters adopted to create the CHARRON models of the images shown in Figs. 2.5 to 2.12. Most physical parameters are defined in Chapter 2. The adopted parameter values roughly correspond to a fast-rotating B type star.

Model parameter	Value
Stellar mass M	$6 M_{\odot}$
Inclination angle of rotation axis i	$0^{\circ}, 45^{\circ}, 60^{\circ}, 90^{\circ}$
Equatorial radius R_{eq}	$11 R_{\odot}$
Polar radius R_{p}	$8.46, 7.83 R_{\odot}$
Flattening parameter ϵ	$0.231, 0.288$
Equatorial rotation velocity v_{eq}	$250, 290 \text{ km s}^{-1}$
$v_{\text{eq}}/v_{\text{c}}$	$0.832, 0.929$
Ω/Ω_{c}	$0.960, 0.993$
$v_{\text{eq}}/v_{\text{k}}$ (or Ω/Ω_{k})	$0.775, 0.899$
Equatorial eff. gravity (log) $\log g_{\text{eq}}$	$2.734, 2.416 \text{ dex}$
Polar eff. gravity (log) $\log g_{\text{p}}$	$3.361, 3.428 \text{ dex}$
Gravity-darkening coefficient β	0.20
Surface averaged mean temperature \bar{T}_{eff}	$15\,000 \text{ K}$
Polar eff. temperature T_{p}	$17\,214 \text{ K}, 17\,819 \text{ K}$
Equatorial eff. temperature T_{eq}	$12\,898 \text{ K}, 11\,180 \text{ K}$

2. Photosphere and circumstellar environment (CSE) of fast rotators

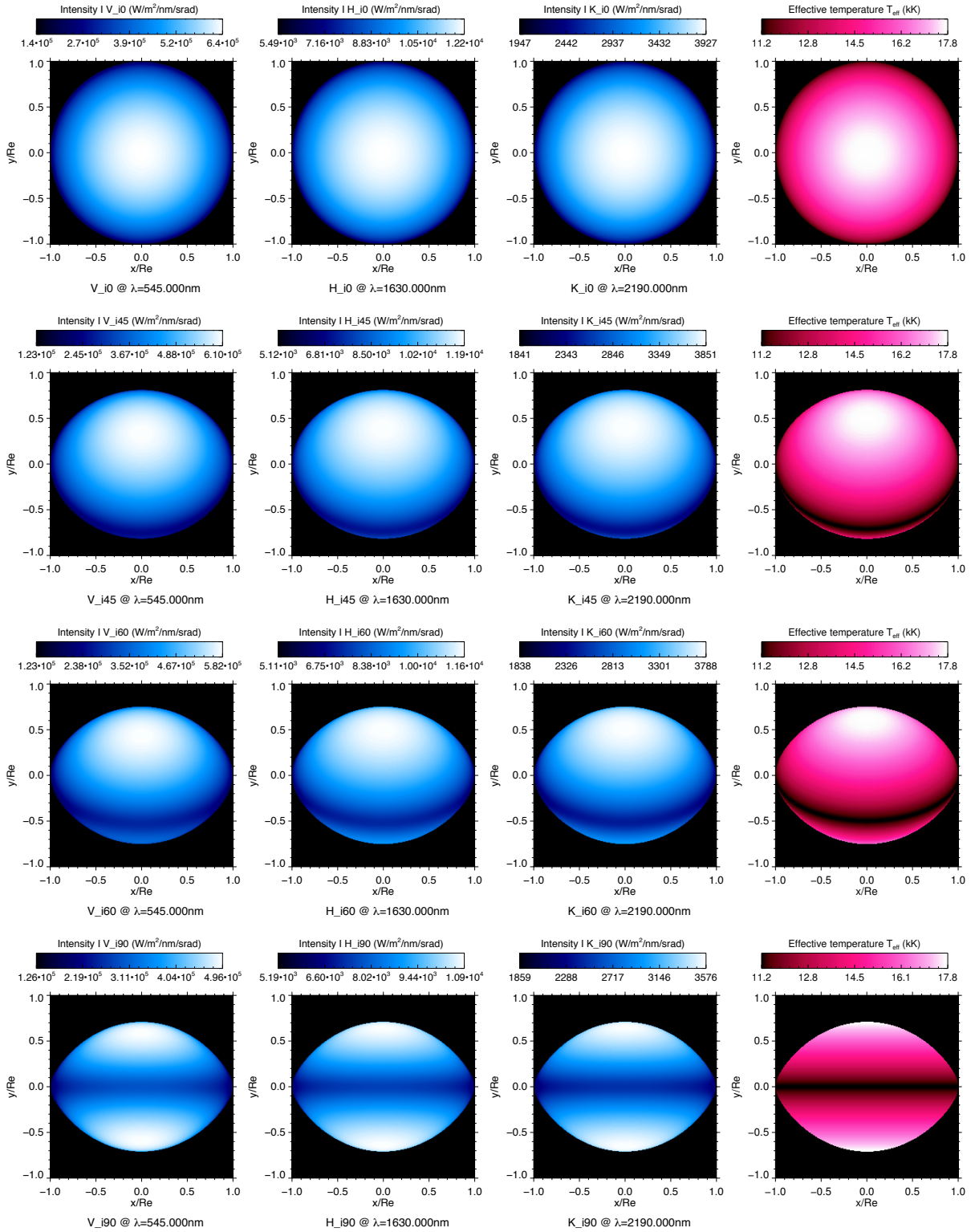


Figure 2.5 – Specific intensity I_λ (V, H, and K photometric bands starting from the left column) and T_{eff} (right column) maps for a fast-rotating B type star computed with CHARRON (Sect. 2.5.1). Models were created for $\beta = 0.20$ and $v_{\text{eq}} = 290 \text{ km s}^{-1} = 0.929v_c$ at different inclinations $i = 0^\circ, 45^\circ, 60^\circ, 90^\circ$, plotted in each row. Horizontal and vertical spatial scales are normalized by the equatorial radius R_{eq} . Further parameters of the models are given in Table 2.1.

2.2. Equilibrium structure of fast-rotating stars

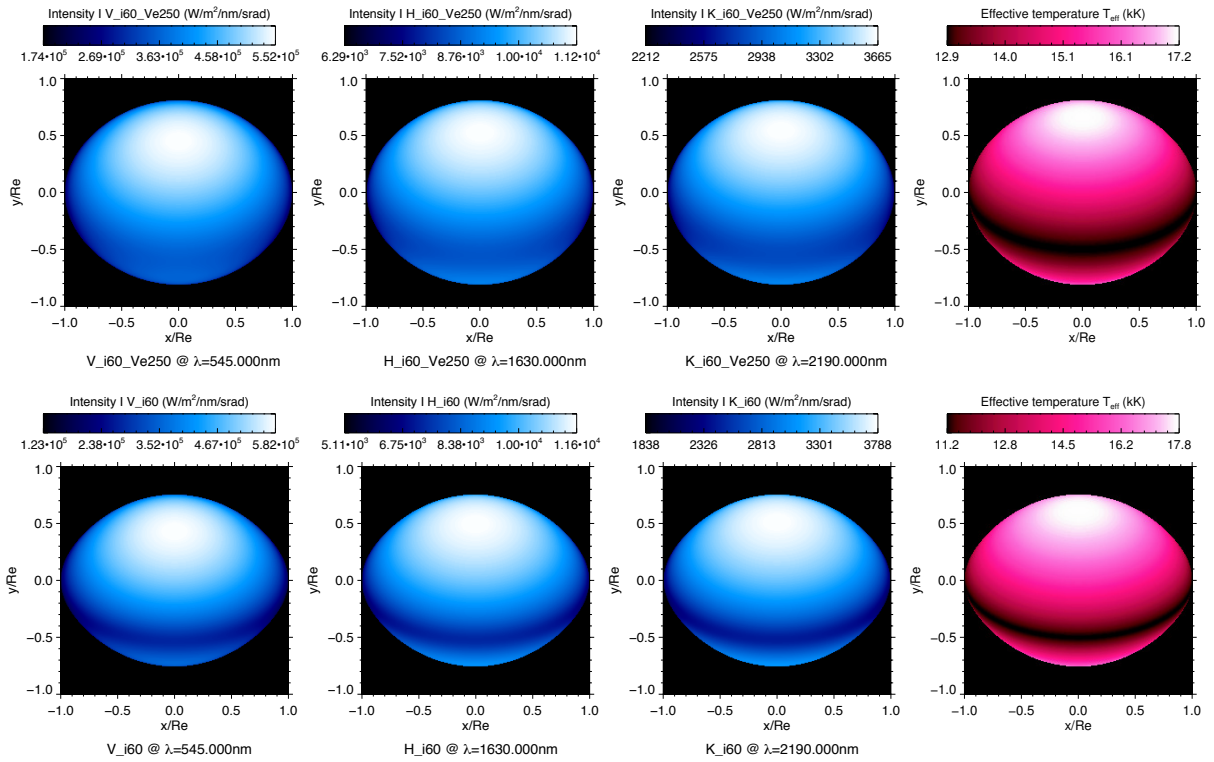


Figure 2.6 – Similar to Fig. 2.5, with I_λ (V, H, and K bands) and T_{eff} maps for two different rotation rates: $v_{\text{eq}} = 250 \text{ km s}^{-1} = 0.832 v_c$ (top row) and $v_{\text{eq}} = 290 \text{ km s}^{-1} = 0.929 v_c$ (bottom row). Models shown correspond to $\beta = 0.20$ and $i = 60^\circ$; further parameters of the models are given in Table 2.1.

2. Photosphere and circumstellar environment (CSE) of fast rotators

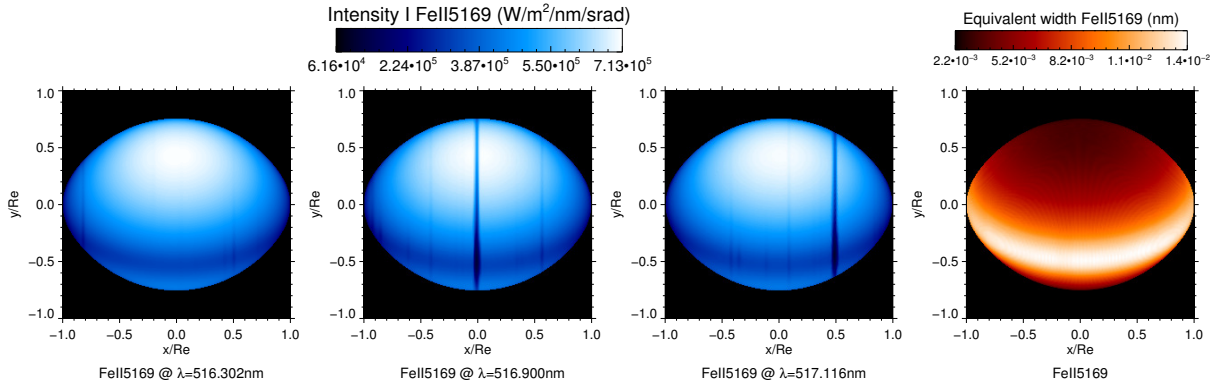


Figure 2.7 – Specific intensity I_λ (continuum, line center, and line center plus $0.5v_{\text{eq}} \sin i$ starting from the left column) and equivalent width EW (right column; Eq. 2.39) maps in the vicinity of the spectral line Fe I 5169. Models were created with CHARRON (Sect. 2.5.1) for a fast-rotating B type star with $\beta = 0.20$, $i = 60^\circ$, and $v_{\text{eq}} = 290 \text{ km s}^{-1} = 0.929v_c$. Further parameters of the model are given in Table 2.1.

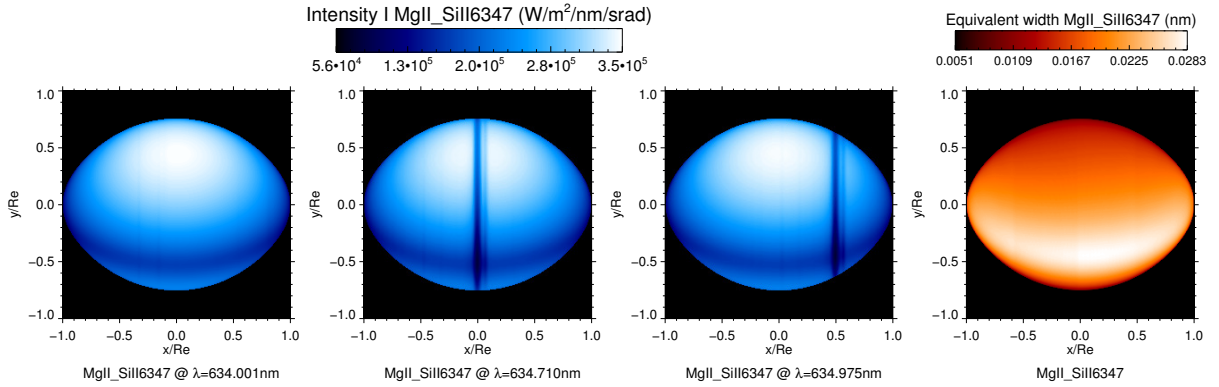


Figure 2.8 – Similar to Fig. 2.7, with I_λ (continuum, line center, and line center plus $0.5v_{\text{eq}} \sin i$) and equivalent width maps in the vicinity of the spectral lines Mg II-Si III 6347.

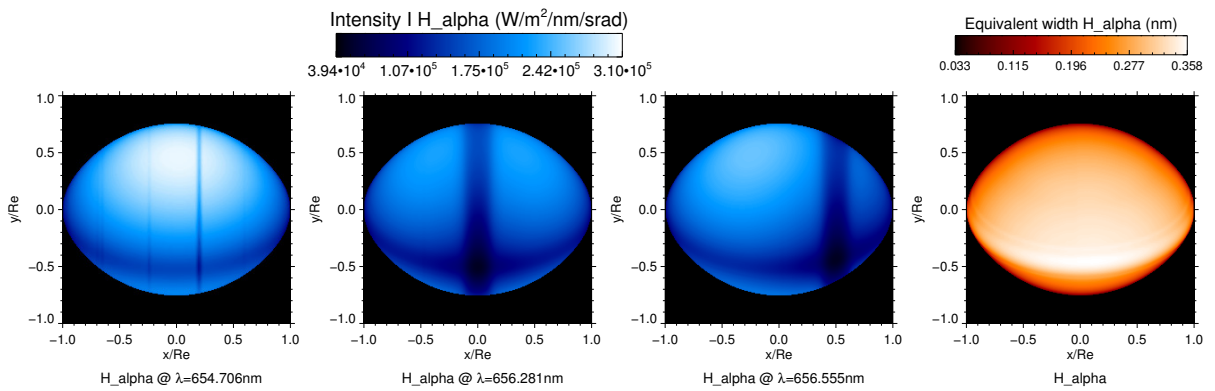


Figure 2.9 – Similar to Fig. 2.7, with I_λ (continuum, line center, and line center plus $0.5v_{\text{eq}} \sin i$) and equivalent width maps in the vicinity of the spectral line $\text{H}\alpha$ (6563\AA).

2.2. Equilibrium structure of fast-rotating stars

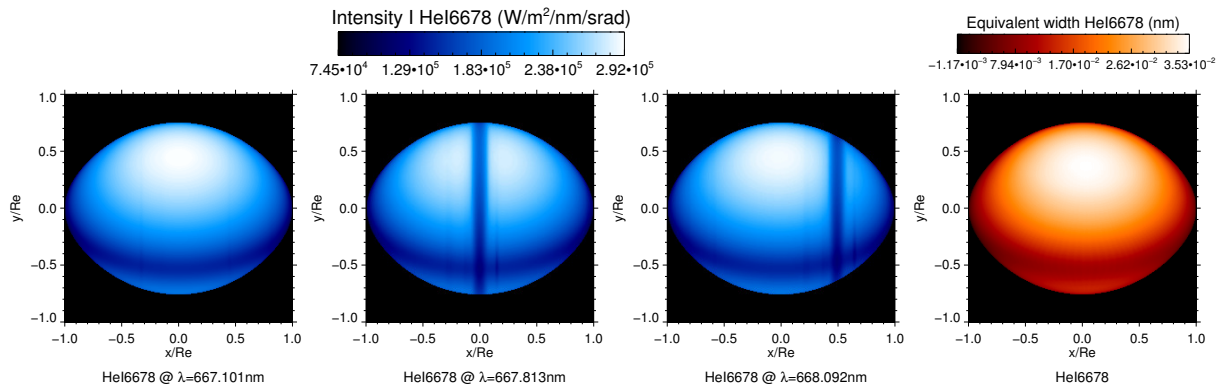


Figure 2.10 – Similar to Fig. 2.7, with I_λ (continuum, line center, and line center plus $0.5v_{\text{eq}} \sin i$) and equivalent width maps in the vicinity of the spectral line He I 6678.

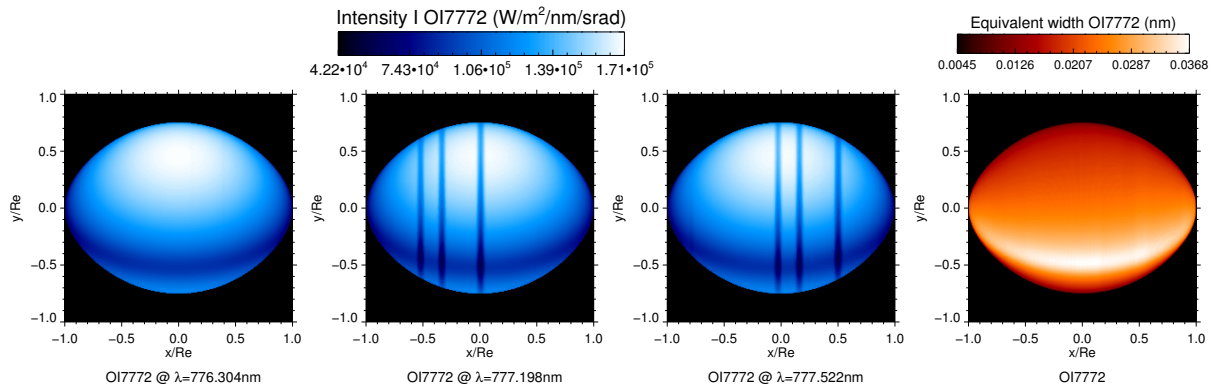


Figure 2.11 – Similar to Fig. 2.7, with I_λ (continuum, line center, and line center plus $0.5v_{\text{eq}} \sin i$) and equivalent width maps in the vicinity of the spectral line triplet O I 7772.

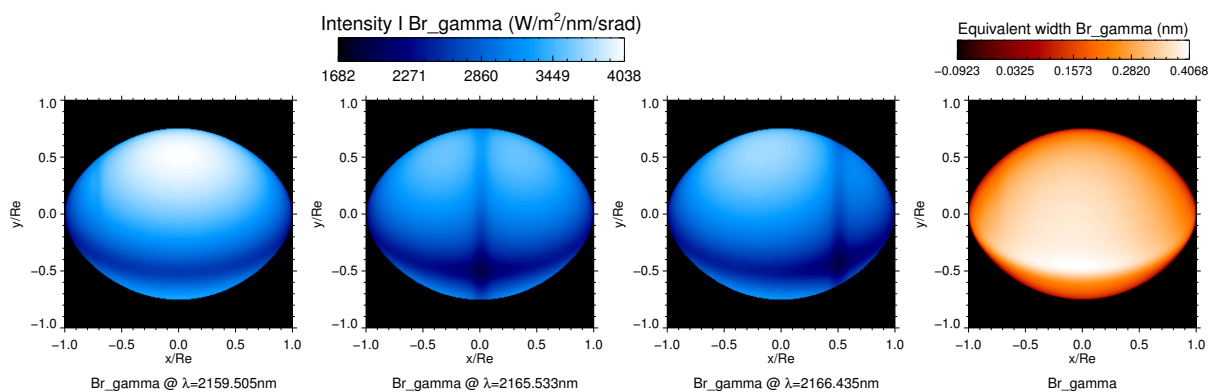


Figure 2.12 – Similar to Fig. 2.7, with I_λ (continuum, line center, and line center plus $0.5v_{\text{eq}} \sin i$) and equivalent width maps in the vicinity of the spectral line Br γ ($2.166 \mu\text{m}$).

2.2.4 Eddington limit and anisotropic CSE

In the next sections we consider the anisotropic (latitudinal-dependent) circumstellar environment (CSE) of the fast-rotating Be and supergiant B[e] stars (described in Sects. 2.3 and 2.4). The anisotropic CSE is a direct result of mass ejections from the luminous, hot, and massive central star. Although the mechanism(s) leading to these mass ejections is(are) still not completely understood, fast-rotation of the central star certainly provides most of the energy required for the material to overcome the stellar gravity and to be ejected into the CSE. In addition to rotation, radiation pressure P_{rad} can also contribute to the formation of the CSE around massive stars.

We shortly present in this section some basic concepts providing clues to understand the link between the strong radiation from the photosphere of massive, fast-rotating stars and the mass and angular momentum losses events. Important references on this topic are, for example, Lamers & Pauldrach (1991), Langer (1997), Glatzel (1998), Maeder (1999), Maeder & Meynet (2000a), Maeder (2009), among others.

In a luminous star, where photon density and radiation pressure are important, the total acceleration \vec{g}_{tot} at the photosphere is the sum of the effective \vec{g}_{eff} and radiation \vec{a}_{rad} accelerations,

$$\vec{g}_{\text{tot}} = \vec{g}_{\text{eff}} + \vec{a}_{\text{rad}} = \vec{g} + \vec{a}_{\text{cent}} + \vec{a}_{\text{rad}} , \quad (2.40)$$

with

$$\vec{a}_{\text{rad}} = -\frac{\vec{\nabla} P_{\text{rad}}}{\rho} = \frac{\kappa(\theta)\vec{F}}{c} . \quad (2.41)$$

The outward radiative acceleration \vec{a}_{rad} is the result of the outward flux \vec{F} or, equivalently, the inward gradient of the radiative pressure $\vec{\nabla} P_{\text{rad}}$, related to each other in the theory of radiative transfer. The remaining quantities in the above relation are the vacuum light speed c , the local mass density ρ , and the local total mean opacity $\kappa(\theta)$, which in general depends on the co-latitude θ in rotating stars because of geometrical deformation and gravity darkening. Note that to derive the von Zeipel's gravity darkening law (Sect. 2.2.2) it is assumed that κ is constant over the stellar surface (equipotential). This assumption is not adopted in the ELR model.

Let us consider that \vec{F} is related to \vec{g}_{eff} as in Eq. 2.33 (ELR model). As discussed in Sect. 2.2.2, this assumption is more general than the original one from von Zeipel (Eq. 2.24) and is adopted in more recent studies of gravity darkening (e.g. Espinosa Lara & Rieutord, 2011; Maeder, 1999).

These equations show that \vec{F} , \vec{g}_{eff} , and \vec{a}_{rad} have all the same direction and are functions of the co-latitude θ over the stellar surface. This allows to express the total surface acceleration \vec{g}_{tot} as a function of \vec{g}_{eff} only,

$$\begin{aligned} \vec{g}_{\text{tot}} &= -\frac{\vec{F}}{f} + \frac{\kappa\vec{F}}{c} \\ &= \vec{g}_{\text{eff}} \left(1 - \frac{\kappa f}{c} \right) \\ &\equiv \vec{g}_{\text{eff}} (1 - \Gamma(\theta)) , \end{aligned} \quad (2.42)$$

where $\Gamma(\theta) (= \kappa(\theta)f/c)$ is the local Eddington factor (ranging from 0 to 1), which depends on the choice of the proportionality function f in Eq. 2.33. Explicit expressions for f are given for example by (1) Espinosa Lara & Rieutord (2011) for the ELR gravity-darkening model, and

by (2) [Maeder \(1999\)](#) for "shellular" differential rotation (cf. [Zahn, 1992](#)); we note that in these examples f is a function of θ over the stellar surface. In any case, the main contribution to $\Gamma(\theta)$ comes from the proportionality constant from the von Zeipel theorem (Eq. 2.25), so that $\Gamma(\theta)$ is essentially given by

$$\Gamma(\theta) \sim \frac{\kappa(\theta)L}{4\pi cGM_\Omega} \equiv \frac{F(\theta)}{F_{\text{Edd}}(\theta)}, \quad (2.43)$$

where F_{Edd} is the limit (or Eddington) flux ([Eddington, 1926](#)). The commonly known constant Eddington factor Γ_0 and limit (or Eddington) luminosity L_{Edd} are a special case of the above relation valid for non-rotating spherical stars with constant κ , i.e.,

$$\begin{aligned} \Gamma_0 &= \frac{\kappa L}{4\pi cGM} \equiv \frac{L}{L_{\text{Edd}}}, \\ \text{and} \\ \frac{L_{\text{Edd}}}{L_\odot} &= \frac{4\pi cGM}{\kappa L_\odot} \simeq \frac{1.3 \times 10^3 M}{\kappa M_\odot}, \end{aligned} \quad (2.44)$$

with κ given in m^2kg^{-1} in the last expression. The limiting (Eddington) flux F_{Edd} (or L_{Edd} for non-rotating spherical stars) corresponds to a condition (locally or globally) on the photosphere where radiation acceleration totally compensates the effective gravity ($\vec{g}_{\text{rad}} = -\vec{g}_{\text{eff}}$), which implies $\vec{g}_{\text{tot}} = \vec{0}$. Very massive and luminous stars can closely approach or even bypass this condition, leading to extreme mass losses episodes, such as those observed in Luminous Blue Variable (LBV) stars. However, the majority of stars do not present such high luminosities so that $F(\theta) \ll F_{\text{Edd}}(\theta)$ or, equivalently, $\Gamma(\theta) \ll 1$.

As a rough estimate of Γ_0 in Eq. 2.44, let us consider a non-rotating, spherical, main-sequence (MS) star of mass M and luminosity L . For hot, massive MS stars we adopt the mass-luminosity relation (in terms of solar values) $L/L_\odot = (M/M_\odot)^3$, and consider a constant opacity from Thomson (electron) scattering ($\kappa_{\text{es}} \simeq 0.02 - 0.04 \text{ m}^2\text{kg}^{-1}$)⁵ as the main opacity source. Under these assumptions we obtain

$$\Gamma_0 \simeq 7.7 \times 10^{-4} \kappa_{\text{es}} \left(\frac{M}{M_\odot} \right)^2 \simeq 1.5 - 3.1 \times 10^{-5} \left(\frac{M}{M_\odot} \right)^2. \quad (2.45)$$

From this estimation it is clear that for massive MS stars of masses below $M \sim 30 M_\odot$ (colder than late O type stars) the Eddington factor has a globally negligible value: $\Gamma_0 < 10^{-2}$. A more detailed discussion and estimation of the Eddington factor is given for example by [Maeder \(2009\)](#).

Of course electron scattering is not the only source of opacity in stellar photospheres. In particular, for massive stars some important opacity sources are bound-free (κ_{bf}), free-free (κ_{ff}), and bound-bound (κ_{bb}) transitions. Contrarily to the constant electron scattering opacity κ_{es} , these additional opacities are highly dependent on the temperature, presenting even some discontinuities in certain conditions. Consequently, although a global Eddington factor, considering electron scattering, is only important in the most luminous and massive stars as discussed above, Γ can increase significantly in some regions of the photosphere because of additional latitudinal-dependent opacities. For example, κ_{bf} and κ_{ff} , which are important on MS B type stars, can be described by a temperature-dependent Kramers opacity law, i.e., $\kappa \propto \rho/T^{3.5}$.

⁵Following [Maeder \(2009\)](#) who gives $\kappa_{\text{es}} = 0.02(1 + X) \text{ m}^2\text{kg}^{-1}$, where X is the hydrogen mass fraction.

Thus, in the context of fast-rotating stars, the presence of gravity-darkening (poles hotter than the equator) can lead to important variations of $\kappa(\theta)$, and thus $\Gamma(\theta)$, across the stellar photosphere.

These combined effects of rotation, gravity-darkening, and opacity induce an anisotropic radiation pressure (flux) and, consequently, anisotropic mass and angular momentum losses. Indeed, from radiative wind theory the mass and angular momentum losses increase with $\vec{g}_{\text{eff}}(\theta)$, $\kappa(\theta)$, and $\Gamma(\theta)$ (see for example [Maeder, 1999](#)). These functional dependences lead to what [Maeder \(1999\)](#) calls the " g_{eff} -effect" and the " κ -effect" (or "opacity-effect"), which offer important clues to explain the strong latitudinal-dependent mass-loss in rotating stars, in particular the formation of equatorial disks in Be stars (Sect. 2.3) and the CSE (polar wind and equatorial disk) of supergiant B[e] stars (Sect. 2.4).

Many other works on the formation of anisotropic CSE in the context of fast-rotation exist, for example [Lamers & Pauldrach \(1991\)](#) discuss CSE formation caused by a bi-stability mechanism (abrupt changes in $\kappa(\theta)$ on the photosphere as a result of gravity darkening), and [Meynet & Maeder \(2006\)](#) discuss the links between critical rotation and the Be and supergiant B[e] stars.

Before proceeding to the next section we would like to note that, independently on the importance of the radiation pressure, the critical velocity defined in Eq. 2.14 is valid. Recalling that it corresponds to the condition $\vec{g}_{\text{eff}} = \vec{0}$, one can directly see that it leads to $\vec{g}_{\text{tot}} = \vec{0}$ in Eq. 2.42, regardless of the value of $\Gamma(\theta)$. This result comes from the fact that, because of gravity darkening, \vec{a}_{rad} is proportional to \vec{g}_{eff} , so the radiation pressure is smaller in the regions of lower effective gravity and thus lower effective temperature ([Glatzel, 1998](#); [Maeder & Meynet, 2000a](#)).

Equation 2.42 has a second root corresponding to $\vec{g}_{\text{tot}} = \vec{0}$, namely $\Gamma(\theta) = 1$. This solution corresponds to cases where radiation pressure is very high. Using Eqs. 2.28 and 2.43, this condition is given by (cf. [Maeder & Meynet, 2000a](#); [Meynet & Maeder, 2006](#)),

$$\Gamma_{\text{max}} \equiv \frac{\kappa_{\text{max}} L}{4\pi c G M} = 1 - \frac{\Omega^2}{2\pi G \bar{\rho}}, \quad (2.46)$$

where the subscript "max" indicates that this equation is fulfilled first in the region(s) of maximum opacity. Recalling that $\Omega^2/2\pi G \bar{\rho} \leq 0.361$ in the Roche approximation (cf. Eq. 2.29), the solution of Eq. 2.46 will depend on the value of Γ_{max} , i.e.,

- $\Gamma_{\text{max}} < 0.639 (= 1 - 0.361)$: no solution exists;
- $\Gamma_{\text{max}} = 0.639$: the only solution corresponds to Ω_c (cf. Eqs. 2.14 and 2.29);
- $\Gamma_{\text{max}} > 0.639$: solutions can exist corresponding to a different critical rotation velocity $\Omega_c^\Gamma < \Omega_c$ (or $v_c^\Gamma < v_c$). Using Eqs. 2.14, 2.29, and 2.46, Ω_c^Γ can be expressed as (cf. [Maeder & Meynet, 2000a](#); [Meynet & Maeder, 2006](#)),

$$\Omega_c^\Gamma = \frac{9}{4} \sqrt{\frac{4\pi R_p^3}{3V}} \sqrt{\frac{GM}{R_c^3}} \sqrt{1 - \Gamma_{\text{max}}} = \frac{9}{4} \sqrt{\frac{4\pi R_p^3}{3V}} \Omega_c \sqrt{1 - \Gamma_{\text{max}}}. \quad (2.47)$$

This solution means that for very luminous stars ($\Gamma \gtrsim 0.639$), a critical limit can be attained for rotation velocities below the usual Ω_c (or, equivalently, v_c). This is caused by the fact that fast rotation diminishes the Eddington limit (Eq. 2.43) by reducing the modified mass (Eq. 2.28). Finally, it is important to note that the, sometimes adopted, critical velocity given by $\Omega_c \sqrt{1 - \Gamma_0}$, is not the correct expression for gravity-darkened, fast-rotating stars (compare with Eq. 2.47 above), being valid only in the particular case of a spherical star with uniform brightness.

2.3 Circumstellar disks of Be stars

Discovered almost 150 years ago by Father [Secchi \(1866\)](#), Be stars are currently defined as "a non-supergiant B star whose spectrum has, or had at some time, one or more Balmer lines in emission" (reason for the suffix "e" in their name). The cyclic appearance of these emission lines (a $B \leftrightarrow Be$ cycle known as the Be-phenomenon) is thought to be connected to ejected material from the stellar photosphere forming a circumstellar disk. Rapid rotation leading to surface instabilities has been proposed by [Struve \(1931b\)](#) to explain the ejection of material from the central star. As proposed by Struve, rapid rotation is indeed the key ingredient in the Be-phenomenon, providing most of the energy required to overcome the surface gravitational potential. However, centrifugal force from rotation does not seem to be able to totally overcome the surface gravity, and other physical mechanisms could also play a non-negligible role, such as non-radial pulsations, radiation pressure, and binarity. These physical effects give rise to temporal variabilities (not necessarily periodic) ranging from hours to decades. The study of the links between the Be-phenomenon and these physical processes is an important topic of research in the domain of massive stars.

In particular, since Be stars are the most rapidly rotating, non-degenerate stars on average (cf. [Fig. 1.2](#)), they constitute ideal laboratories for a deeper understanding of the role of rotation in stellar physics. Indeed, Be stars provide crucial tests for modern models of stellar structure and evolution that include rotation, pushing them to limits of high rotation rates (rotation velocities above $\sim 80\%$ of the breakup limit). Recent reviews covering observational and theoretical aspects of Be stars are presented by [Carciofi \(2011\)](#), [Stee & Meilland \(2012\)](#), [Rivinius et al. \(2013\)](#), among others.

Any complete and self-consistent study of Be stars requires to consider both (1) the fast rotation of the B star (e.g. using models such as the one presented in [Sect. 2.2](#)), and (2) a circumstellar disk (eventually variable in time) giving rise to emission lines.

A physical model for fast-rotating stars was described in [Sect. 2.2](#), while in this section we summarize the probably most accepted and successful model of Be star's disks: the **viscous decretion disk (VDD) model** in Keplerian rotation ([Lee et al., 1991](#)). More recent descriptions of the VDD model, including quantitative comparisons to observations, are given for example by [Porter \(1999\)](#), [Bjorkman & Carciofi \(2005\)](#), and [Carciofi \(2011\)](#).

The VDD model can be derived directly from the equations of continuity ([Eq. 2.1](#)) and Navier-Stokes ([Eq. 2.2](#)). From these equations, a simplified but realistic description of the VDD model is obtained by assuming a steady-state, cylindrically symmetric disk. Cylindrical coordinates (ϖ, ϕ, z) are the more natural reference frame to be adopted. The axis of symmetry is considered to be parallel to the angular momentum vector of the central rotating star. Let us also assume that the CSE material follows circular orbits, which are the least energy orbits for a given local angular momentum (cf. [Pringle, 1981](#)). Additionally, we assume that the gravity from the central star is the only force acting on the CSE, neglecting viscous forces in particular.

From these assumptions, we have that the physical quantities are not dependent on ϕ , and that only the azimuthal velocity component v_ϕ is non zero. [Equation 2.1](#) and the ϕ -component of

Eq. 2.2 are thus trivially satisfied, while the ϖ - and z -component can be expressed simply as,

$$\begin{aligned} \frac{1}{\rho} \frac{\partial P}{\partial \varpi} &= \frac{v_\phi^2}{\varpi} - \frac{GM\varpi}{(\varpi^2 + z^2)^{3/2}} \\ &\simeq \frac{v_\phi^2}{\varpi} - \frac{GM}{\varpi^2}, \end{aligned} \quad (2.48)$$

and

$$\begin{aligned} \frac{1}{\rho} \frac{\partial P}{\partial z} &= -\frac{GMz}{(\varpi^2 + z^2)^{3/2}} \\ &\simeq -\frac{GMz}{\varpi^3}. \end{aligned} \quad (2.49)$$

The last equalities above assume that the disk is thin ($z \ll \varpi$), which is in agreement with observations of Be disks (e.g. Rivinius et al., 2013). The pressure P and the density ρ can be related considering the equation of state of an ideal gas,

$$P = c_s^2 \rho, \quad (2.50)$$

where c_s is the local sound speed given by,

$$c_s = \sqrt{\frac{kT}{\mu m_H}}, \quad (2.51)$$

where k is the Boltzmann constant, T is the gas temperature, μ is the mean molecular weight, and m_H the hydrogen mass. Note that $c_s \sim 10 \text{ km s}^{-1}$ for $T \sim 10^4 \text{ K}$, i.e., much smaller than the orbital velocity v_ϕ , which is of the order of the stellar equatorial rotation velocity ($\sim 100 \text{ km s}^{-1}$).

Keplerian rotation

Consequently, the term depending on P and ρ (and thus c_s) in Eq. 2.48 can be neglected compared to the term on v_ϕ . This implies that the azimuthal velocity of the CSE is approximately given by a Keplerian rotation law,

$$v_\phi = v_\phi(\varpi) = \sqrt{\frac{GM}{\varpi}} = v_k \sqrt{\frac{R_{\text{eq}}}{\varpi}}, \quad (2.52)$$

where Eq. 2.16 was used in the last equality. Other rotation laws for Be disks were proposed, such as angular momentum conservation ($v_\phi \propto \varpi^{-1}$) obtained in radiatively driven outflows. However, an increasing number of observational results (mostly from spectro-interferometry) suggest that Be disks rotate at Keplerian orbital speeds (e.g. Meilland et al., 2007; Kraus et al., 2012; Meilland et al., 2012, and others).

Density structure of the (isothermal) disk

Equation 2.49 shows that the disk is hydrostatically supported in the vertical direction (balance between vertical pressure gradient and vertical component of stellar gravity). A simple expression for the vertical density structure of the disk can be obtained by solving Eq. 2.49 for ρ . Using

Eqs. 2.50 and 2.51 and assuming that the disk is vertically isothermal (T independent on z) one obtains,

$$\rho(\varpi, z) = \rho_0(\varpi) \exp \left[-\frac{1}{2} \left(\frac{z}{H(\varpi)} \right)^2 \right], \quad (2.53)$$

where ρ_0 is the density at the disk mid-plane ($z = 0$) and $H(\varpi)$ is the disk scale height given by,

$$H(\varpi) = \frac{c_s(\varpi)}{v_\phi(\varpi)} \varpi = \sqrt{\frac{kT(\varpi)\varpi^3}{\mu m_H GM}}. \quad (2.54)$$

We note that $H \propto \varpi^{1.5}$ (flared) if the disk is completely isothermal. Moreover, the condition $c_s \ll v_\phi$ implies that $H \ll \varpi$, which is in agreement with the thin-disk hypothesis.

The radial dependence of $\rho_0(\varpi)$ is not determined in the formulation above. It can be set for example by considering mass loss from the central star and viscous outflow of the ejected material through the disk. It is sometimes useful to consider also the surface density $\Sigma(\varpi)$ by integrating $\rho(\varpi, z)$ over z , so that

$$\rho_0(\varpi) = \frac{\Sigma(\varpi)}{\sqrt{2\pi}H(\varpi)}. \quad (2.55)$$

When studying Be disks it is often assumed that $T(\varpi)$ and $\rho_0(\varpi)$ decrease as power laws of ϖ (e.g. Bjorkman & Carciofi, 2005; Carciofi, 2011).

Viscosity and mass loss

The commonly adopted prescription for viscous (accretion and decretion) disks is the eddy (or turbulent) viscosity proposed by Shakura & Sunyaev (1973), where turbulence is composed of vortices (eddies) of typical turnover velocity v_t with size scale of the largest eddies l . This allows the kinematic viscosity (see Eq. 2.2) to be expressed as,

$$\nu = v_t l = \alpha c_s H \quad (0 < \alpha < 1), \quad (2.56)$$

where the last equality, with the viscosity parameter α ranging from 0 to 1, is based on the reasonable assumptions that $l < H$ and that $v_t < c_s$.

Adding viscosity does not change the foregoing equations and assumptions adopted for the VDD model. The main difference introduced by the addition of viscosity is the fact that the ϖ -component of the velocity is no longer zero, i.e., $v_\varpi \neq 0$. In this case, the continuity equation is no longer trivially satisfied, and can now be expressed as,

$$\frac{\partial}{\partial \varpi} (2\pi \varpi \Sigma v_\varpi) \equiv \frac{\partial \dot{M}}{\partial \varpi} = 0 \Rightarrow v_\varpi = \frac{\dot{M}}{2\pi \varpi \Sigma}. \quad (2.57)$$

where Σ is defined in Eq. 2.55 and the mass loss rate $\dot{M} (= 2\pi \varpi \Sigma v_\varpi)$ is a constant (independent on ϖ). In Be disks, v_ϖ is called outflow velocity, which is much smaller than c_s for typical values of \dot{M} , preventing any direct measurement of this velocity. It can be shown that for a given \dot{M} and for large (old) isothermal disks $\Sigma \propto \varpi^{-2}$ (e.g. Carciofi, 2011), so that $\rho_0 \propto \varpi^{-3.5}$ (cf. Eqs. 2.54 and 2.55).

Although this steep density profile is in qualitative agreement with observations, real Be disks do not exactly follow this density power law and they are not isothermal. A self-consistent

treatment of radiative transfer and physical equilibrium structure of the disk is required to more realistically determine the density and temperature distributions. This can be achieved for example with the HDUST code described in Sect. 2.5.3, as shown by Carciofi & Bjorkman (2006).

The use of such radiative transfer models also allows to estimate α and \dot{M} by studying the temporal evolution of the disk (Carciofi et al., 2012). We intend to apply a similar analysis to study the Be star Achernar (cf. Chapter 4), in a research work that will be performed mostly by D. Moser Faes in the frame of his PhD thesis⁶.

2.4 Gas and dust CSE of supergiant B[e] stars

Supergiant B[e] (sgB[e]) stars are evolved, luminous, and massive stars ($\log(L/L_{\odot}) > 4.0$), presenting the so-called B[e] phenomenon (e.g. Lamers et al., 1998): (1) strong hydrogen emission lines; (2) narrow permitted and forbidden low-excitation emission lines of for example FeII, [FeII], and [OI]; (3) strong IR excess, mostly from free-free, free-bound, and hot circumstellar dust emission. A non-spherical circumstellar envelope (CSE) is another common property of sgB[e] stars. The origin of this non-spherical CSE is believed to be intimately linked to the fast-rotation of the central star and/or to binarity, but the question is still under debate and the details of the underlying physical processes are still not well understood.

One possible picture for the sgB[e] stars, proposed by Zickgraf et al. (1985, see Fig. 2.13), consists of a fast-rotating, massive central B type star with (1) a fast and hot radiation-driven wind in the polar directions, where lines of highly ionized metals form, and (2) a slow, much cooler and denser (by a factor $10^2 - 10^3$) wind in the equatorial direction, probably as a consequence of rotation and opacity effects, which forms a disk-like structure with physical conditions allowing the existence of dust and molecules. A brief discussion of the combined effects of mass loss, rotation, and Eddington limit is given in Sect. 2.2.4.

Carciofi et al. (2010) propose a physical prescription of this picture of sgB[e] stars, which is in agreement with several observations (cf. results in Sect. 3.3 for example). In this section, we briefly describe the main equations of this prescription that is adopted in the present work. A more detailed description of this model is given by Carciofi et al. (2010) and in Sect. 2.5.2.

The sgB[e] models (central star and CSE) are assumed to be axis-symmetric and are described in spherical coordinates: r (radius) and θ (colatitude). The central star is described by a photospheric radius R (assumed spherical), an effective temperature T_{eff} , and a luminosity L . The density and velocity structure of the CSE are derived from a mass-loss \dot{M} per solid angle enhanced at the equator,

$$\frac{d\dot{M}(\theta)}{d\Omega} = \frac{d\dot{M}(0)}{d\Omega} [1 + A_1 \sin^m(\theta)] \quad (\text{mass-loss rate per unit solid angle}), \quad (2.58)$$

and from a standard β -law velocity for radiatively driven winds (purely radial gas motion),

$$v(r, \theta) = v_r(r, \theta) = v_0 + [v_{\infty}(\theta) - v_0](1 - R/r)^{\beta} \quad (\text{wind radial velocity}), \quad (2.59)$$

with

$$v_{\infty}(\theta) = v_{\infty}(0) [1 + A_2 \sin^m(\theta)] \quad (\text{wind terminal velocity}). \quad (2.60)$$

⁶Double thesis IAG/USP (Brazil) and OCA/UNS (France); thesis co-supervisors: A. C. Carciofi and A. Domiciano de Souza.

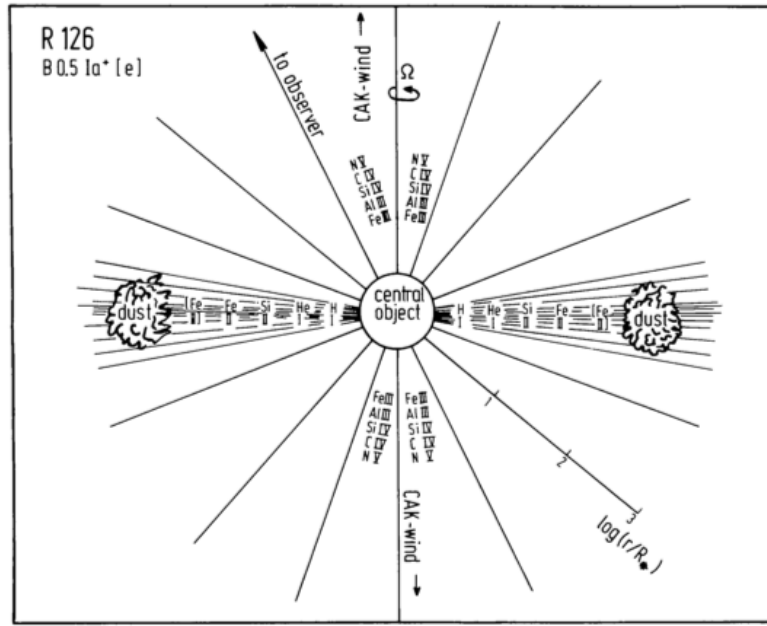


Figure 2.13 – Schematic model for sgB[e] stars proposed by Zickgraf et al. (1985). Its composed by a fast-rotating, massive central star and by a bimodal CSE. See text for further details.

The parameters $A_1 (> 0)$ and $A_2 (< 0)$ control the relative differences between the values of $\frac{d\dot{M}(\theta)}{d\Omega}$ and $v_\infty(\theta)$ at the equator ($\theta = \pi/2$) and at the poles ($\theta = 0$ or π). In particular $\frac{d\dot{M}(\theta=0)}{d\Omega} < \frac{d\dot{M}(\theta=\pi/2)}{d\Omega}$ and $v_\infty(\theta = 0) > v_\infty(\theta = \pi/2)$.

The CSE density of this radial outflow is obtained from the mass continuity equation (Eq. 2.1) and from Eqs. 2.58 and 2.59:

$$\rho(r, \theta) = \frac{1}{r^2 v(r, \theta)} \frac{d\dot{M}(\theta)}{d\Omega}, \quad (2.61)$$

Note that $\rho(r, \theta)$ is high in the equatorial regions because $\frac{d\dot{M}(\theta)}{d\Omega}$ is high in these regions while $v(r, \theta)$ is low. The opposite behavior occurs at the poles. Thus, $\rho(r, \theta = 0) < \rho(r, \theta = \pi/2)$.

In addition, dust is allowed to exist only in the denser equatorial regions ($\pi/2 - \Delta\theta_{\text{dust}} \leq \theta \leq \pi/2 + \Delta\theta_{\text{dust}}$). The dust opening angle $\Delta\theta_{\text{dust}}$ is determined by the parameters m and A_1 as,

$$\Delta\theta_{\text{dust}} = \cos^{-1} \left[\left(\frac{A_1 - 1}{2A_1} \right)^{1/m} \right] \quad (\text{dust opening angle}), \quad (2.62)$$

corresponding to the colatitudes above ($\theta = \pi/2 - \Delta\theta_{\text{dust}}$) and below ($\theta = \pi/2 + \Delta\theta_{\text{dust}}$) the equator at which $\frac{d\dot{M}(\theta)}{d\Omega}$ is half the equatorial value.

This two-component wind description thus reproduces the main characteristics of the bimodal CSE view proposed by Zickgraf et al. (1985).

It is however important to note the existence of an alternative model, which considers Keplerian rotation of the sgB[e] CSE (e.g. Kraus et al., 2013), similar to the VDD model for Be stars presented in Sect. 2.3. Neither of these two models seem to completely explain all observations. In addition, binarity could also play an important role in sgB[e] stars. Some recent results and discussions on these important topics are presented in the review papers from Chesneau (2009), Millour et al. (2013), de Wit et al. (2014), and their references.

Examples of intensity maps of supergiant B[e] stars

To illustrate the sgB[e] CSE described above we present in Fig. 2.14 examples of intensity maps showing the central star and bimodal CSE composed of gas and dust. These intensity maps were computed with the 3-D Monte Carlo NLTE radiative transfer code HDUST (described in Sect. 2.5.3) running on the massive parallel computing facility *Mésocentre SIGAMM*⁷ installed at OCA. These images are part of our grid of sgB[e] models as presented in Sect. 2.4.1.

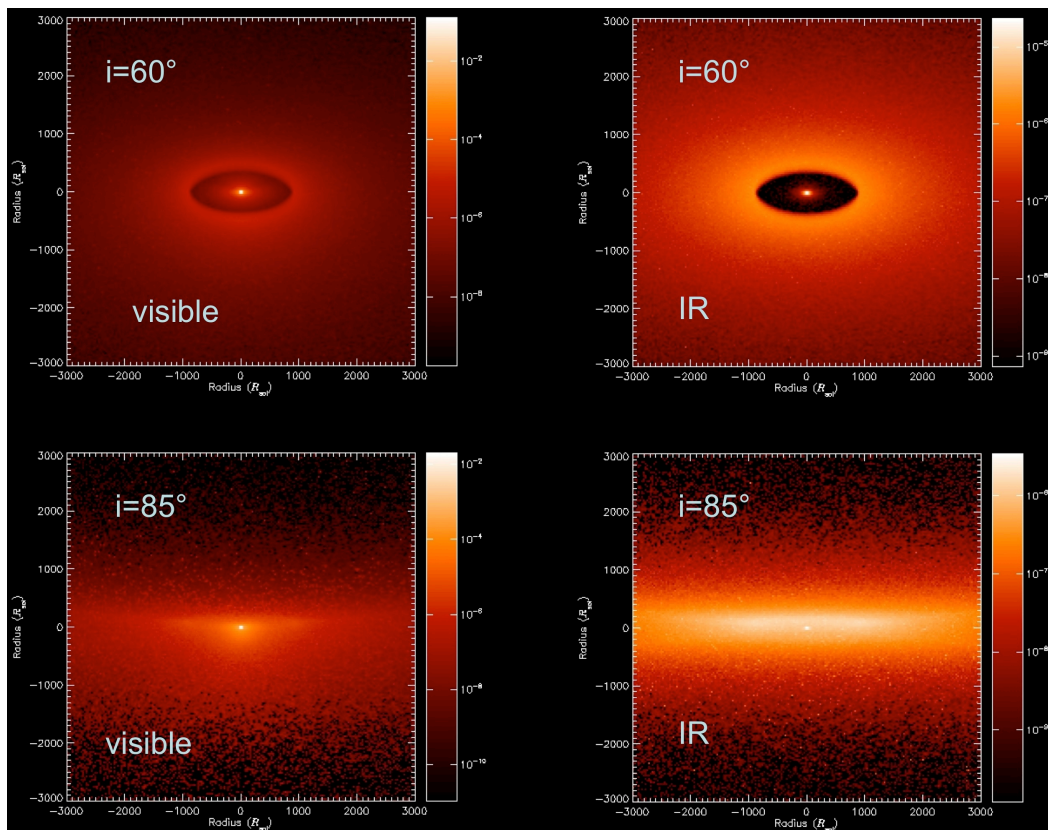


Figure 2.14 – Examples of model intensity maps of sgB[e] stars computed with the Monte Carlo radiative transfer code HDUST mainly developed by A. C. Carciofi (Sect. 2.5.3). The models include a hot central B type star ($T_{\text{eff}} = 20\,000\text{ K}$) surrounded by a non-spherical CSE composed by gas (hydrogen) and dust (silicates with a power law distribution of sizes ranging from 1 to 50 μm). The intensity maps are given for two inclinations ($i = 60^\circ$ and 85°) both in the visible/near IR (0.6 to 1.2 μm) and in thermal IR (10 to 11 μm) spectral domains. Spatial scales (horizontal and vertical) are given in solar radii. The differences in the images are due to effects of projection (distinct i) as well as physical effects governed by the relative contributions from the central B star, the continuum emission from ionized gas in the central parts (free-free, free-bound), and from the dust thermal continuum emission. Gas contribution is important in the visible and close to the central star while the dust, concentrated in the equatorial region, dominates the thermal IR emission. As seen in the images, dust particles can survive only beyond the sublimation radius defined by the distance where the temperature of dust particles is equal to the sublimation temperature ($\simeq 1\,500\text{ K}$ in this case). Sect. 2.4.1 gives further details on the central star, gas and dust CSE, dust composition and distribution.

⁷Simulations Intensives en Géophysique, Astronomie, Mécanique et Mathématiques.

2.4.1 Grid of supergiant B[e] models

As described in Sect. 2.5.3, physically-consistent Monte Carlo radiative transfer codes, such as HDUST, are very time consuming, generally requiring high performance parallel computing. This prevents a practical use of this type of code in model-fitting procedures that require many computations ($\sim 10^3$ to $\sim 10^5$ depending on the problem to be handled) of the model for different combination of values of the free parameters being fitted.

One possibility to partially overcome this limitation is to create a grid of pre-calculated models, covering a chosen range of the parameter space, which can be subsequently compared to the data. Following this strategy, we have built a grid of Supergiant B[e] (sgB[e]) HDUST models, covering several different values of selected physical parameters, namely, effective temperature of the central star, mass-loss rate, dust grains density and size, disk opening angle, and inclination angle.

The details of the grid are given in the paper below, published in the proceedings of the 2012 ESO Workshop (*Circumstellar Dynamics at High Resolution*; Domiciano de Souza & Carciofi, 2012).

The sgB[e] HDUST grid was created using the massive parallel computing facility *Mésocentre SIGAMM* installed and hosted by the Observatoire de la Côte d'Azur (OCA), France (*hdust project*; PI: A. Domiciano de Souza). This work was partially supported by a franco-brazilian PICS-CNRS program⁸.

As a next step, and in collaboration with M. Borges Fernandes and A. C. Carciofi, we intend to expand this grid to include additional luminosities, temperatures, densities, rotation laws, among other parameters.

⁸Title: *Multi-technique study of stellar environments*; P.I.: A. Domiciano de Souza; program held from 2009 to 2012.

Circumstellar Dynamics at High Resolution
ASP Conference Series, Vol. 464
A. C. Carciofi and Th. Rivinius, eds.
©2012 Astronomical Society of the Pacific

Grid of Supergiant B[e] Models from HDUST Radiative Transfer

A. Domiciano de Souza¹ and A. C. Carciofi²

¹*Lab, J.-L. Lagrange, Observatoire de la Côte d'Azur, Univ. de Nice-Sophia Antipolis, CNRS, Nice, France*

²*Instituto de Astronomia, Geofísica e Ciências Atmosféricas, Univ. de São Paulo, Brazil*

Abstract. By using the Monte Carlo radiative transfer code HDUST (developed by A. C. Carciofi and J. E. Bjorkman) we have built a grid of models for stars presenting the B[e] phenomenon and a bimodal outflowing envelope. The models are particularly adapted to the study of B[e] supergiants and FS CMA type stars. The adopted physical parameters of the calculated models make the grid well adapted to interpret high angular and high spectral observations, in particular spectro-interferometric data from ESO-VLTI instruments AMBER (near-IR at low and medium spectral resolution) and MIDI (mid-IR at low spectral resolution). The grid models include, for example, a central B star with different effective temperatures, a gas (hydrogen) and silicate dust circumstellar envelope with a bimodal mass loss presenting dust in the denser equatorial regions. The HDUST grid models were pre-calculated using the high performance parallel computing facility Mésocentre SIGAMM, located at OCA, France.

1. Introduction

Supergiant B[e] stars (sgB[e]) are evolved and luminous stars ($\log(L/L_{\odot}) > 4.0$), presenting the so-called B[e] phenomenon (e.g., Lamers et al. 1998): (1) strong hydrogen emission lines; (2) narrow permitted and forbidden low-excitation emission lines of Fe II, [Fe II], and [O I]; (3) strong IR excess mostly from free-free, free-bound, and hot circumstellar dust emission. A non-spherical circumstellar envelope (CSE) is another common property of sgB[e] stars. Many questions remain unclear concerning the origin, size, geometry, and physical structure (e.g. density and temperature distribution) of these CSE. The commonly accepted picture for the sgB[e] stars (Zickgraf et al. 1985) consists of a massive central star with (1) a fast and hot radiation-driven wind in the polar directions and (2) a slow, much cooler and denser (by a factor $10^2 - 10^3$) wind in the equatorial direction, which might form a disk-like structure with physical conditions allowing the existence of dust and molecules. The origin of the non-spherical CSE is believed to be caused by binarity and/or fast rotation of the central star, but the question is still under debate. The FS CMA stars are another class of B[e] stars proposed by Miroshnichenko (2007), which are similar but somewhat less luminous than the sgB[e] ($2.5 > \log(L/L_{\odot}) > 4.5$) and for which the binarity is confirmed.

High angular and high spectral resolution (HASR) instruments nowadays available (e.g., adaptive optics, long baseline interferometry), allow to directly study these relatively complex CSE. In particular, the ESO-VLTI beam combiners AMBER (near-

Table 1. Stellar and wind parameters of HDUST grid of B[e] models

Parameter	Value
Stellar parameters	
R	$10 R_{\odot}$
T_{eff}	15 000, 20 000, 25 000 K
L ($\Rightarrow \log(L/L_{\odot})$)	$12\,000 L_{\odot}$ ($\Rightarrow 4.08$)
Wind parameters	
$d\dot{M}(0^{\circ})/d\Omega$	$50, 100 \times 10^{-9} M_{\odot} \text{ yr}^{-1} \text{ sr}^{-1}$
v_0	10 km s^{-1}
$v_{\infty}(0^{\circ})$	600 km s^{-1}
β, A_1, A_2	2, 49, -0.7
m ($\Rightarrow \Delta\theta_{\text{dust}}$)	182, 92, 20 ($\Rightarrow 5^{\circ}, 7^{\circ}, 15^{\circ}$)

IR) and MIDI (mid-IR) have provided many important results in the study of B[e] stars in the past decade (e.g., Borges Fernandes et al. 2009; Domiciano de Souza et al. 2008, 2011). Based on the experience acquired from these and other works, it became clear that it is very important to use realistic physical models to interpret modern HASR observations. Such physical models are quite demanding in terms of computing time, generally requiring high performance parallel computing.

In order to facilitate future HASR studies of sgB[e] and FS CMa stars we have pre-calculated a grid of models using the Monte Carlo radiative transfer code HDUST (Carciofi & Bjorkman 2006). HDUST is a 3-D Monte Carlo code that combines the full NLTE treatment of the radiative transfer in gaseous media with a very general treatment for CSE dust grains. The HDUST grid models were pre-calculated using the parallel computing facility Mésocentre SIGAMM, located at OCA, France.

2. B[e] Model Adopted

The physical properties of the grid models are identical to those described by Carciofi et al. (2010), but we give here a succinct description of the main equations. The models are axi-symmetric with coordinates r and θ (colatitude). The central star is described by its radius R , effective temperature T_{eff} , and luminosity L . The density and velocity structure of the bimodal CSE are derived from a mass-loss enhanced at the equator

$$\frac{d\dot{M}(\theta)}{d\Omega} = \frac{d\dot{M}(0)}{d\Omega} [1 + A_1 \sin^m(\theta)] \quad (\text{mass-loss rate per unit solid angle}), \quad (1)$$

and from a standard β -law velocity for radiatively driven winds

$$v_r(r, \theta) = v_0 + [v_{\infty}(\theta) - v_0](1 - R/r)^{\beta} \quad (\text{wind radial velocity}), \quad (2)$$

with

$$v_{\infty}(\theta) = v_{\infty}(0) [1 + A_2 \sin^m(\theta)] \quad (\text{wind terminal velocity}). \quad (3)$$

A_1 and $A_2 (< 0)$ control the ratio between the values of each quantity at the equator and at the pole. Dust is allowed to exist around the equator, between the latitudes $\pm\Delta\theta_{\text{dust}}$,

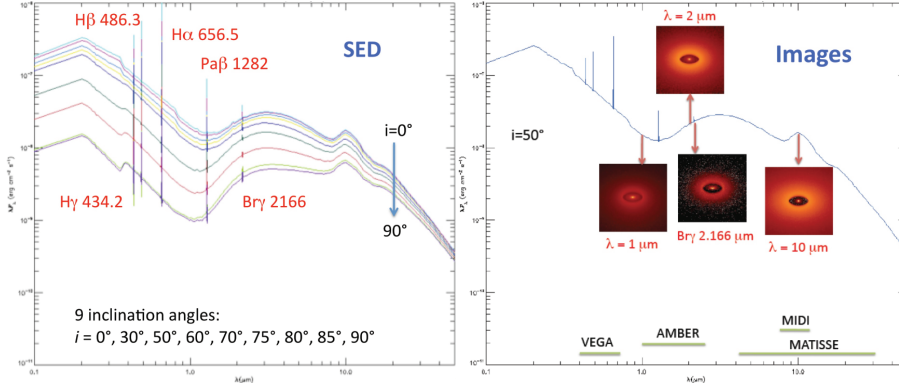


Figure 1. *Left*: SED for a typical HDUST B[e] model of the grid shown at all 9 inclination angles. Hydrogen lines chosen to be present in the SED are written in the figure. Wavelengths range from UV to mid-IR and SED fluxes are given in λF_{λ} . *Right*: Examples of grid intensity maps at 4 selected wavelengths (near- to mid-IR) corresponding to a chosen model SED. These images can be used to compute HASR quantities, such as spectro-interferometric visibilities and differential phases, that can be directly compared to observations performed with present (CHARA/VEGA, VLTI/AMBER, VLTI/MIDI) and near-future (VLTI/MATISSE) beam-combiners. The operating wavelength range these spectro-interferometers are indicated. The relative influences of the central star and the gas+dust CSE are clearly seen in the SED and the images at different wavelengths. For example, note that, compared to the dust disk emission, the central gas disk has a stronger contribution in the Br γ image than in the image at 2 μm (close continuum).

obtained from the parameter m :

$$\Delta\theta_{\text{dust}} = \cos^{-1} \left[\left(\frac{A_1 - 1}{2A_1} \right)^{1/m} \right] \quad (\text{dust opening angle}). \quad (4)$$

3. The HDUST Grid of B[e] Models

Tables 1 and 2 show parameter fixed and variable values for the central star, wind, and CSE composition of the HDUST grid models. In addition, the models are calculated at 9 different inclination angles i (see Fig. 1) and 2 different spatial scales, which are adapted to the field of view and spatial resolution of VEGA and AMBER (images $6000 R_{\odot} \times 6000 R_{\odot}$), and MIDI and MATISSE (images $30\,000 R_{\odot} \times 30\,000 R_{\odot}$). This amounts to $3 (T_{\text{eff}}) \times 2 (dM(0^{\circ})/d\Omega) \times 3 (m) \times 4$ (grain size and density) $\times 9 (i) \times 2$ (spatial scale) models, corresponding to a *total of 1296 models*.

For each model we computed an spectral energy distribution (SED), ranging from the UV (0.1 μm) to the mid-IR (50 μm), and intensity maps at 34 wavelength bins covering the visible, near- and mid-IR. Spectro-interferometric observations can be directly obtained (via Fourier transform) from these intensity maps. The wavelength bins are particularly optimized to interpret observations from VLTI/AMBER (LR-JHK and MR-K bands) and VLTI/MIDI (LR N band). The models are available upon request.

Table 2. Gas and dust parameters of HDUST grid of B[e] models

Parameter	Value	
Gas parameters		
Composition	Hydrogen	
Number of levels	25	
Common dust parameters		
Composition	Amorphous silicate	
Dust distribution index n	-3.5	(MRN law; Mathis et al. 1977)
$T_{\text{destruction}}$	1500 K	
Gas to dust ratio	200	
	Dust model 1	Dust model 2
Grain size $a_{\text{min}}-a_{\text{max}}$	1–50 μm	0.05–50 μm
Grain density ρ_{dust}	0.1, 1.0 g cm^{-3}	0.1, 1.0 g cm^{-3}

Acknowledgments. The authors acknowledge the Observatoire de la Côte d’Azur from allowing the use of the Mésocentre SIGAMM, where the simulations were performed. We also thank the CNRS (PICS program) for financial support. A.C.C. acknowledges support from CNPq (grant 308985/2009-5) and Fapesp (grant 2010/19029-0).

References

Borges Fernandes, M., Kraus, M., Chesneau, O., et al. 2009, A&A, 508, 309.
 Carciofi, A. C., Miroshnichenko, A. S., & Bjorkman, J. E. 2010, ApJ, 721, 1079.
 Carciofi, A. C. & Bjorkman, J. E. 2006, ApJ, 639, 1081
 Domiciano de Souza, A., Bendjoya, P., Niccolini, G., et al. 2011, A&A, 525, A22.
 Domiciano de Souza, A., Kervella, P., Bendjoya, P., et al. 2008, A&A, 480, L29
 Lamers, H. J. G. L. M., Zickgraf, F.-J., de Winter, D., et al. 1998, A&A, 340, 117
 Mathis, J. S., Rumpl, W., & Nordsieck, K. H. 1977, ApJ, 217, 425
 Miroshnichenko, A. S. 2007, ApJ, 667, 497
 Zickgraf, F.-J., Wolf, B., Stahl, O., et al. 1985, A&A, 143, 421

2.5 Numerical models

2.5.1 CHARRON (Code for High Angular Resolution of Rotating Objects in Nature)

Different codes on fast-rotating stars exist, and are generally based on the physical model presented in Sect. 2.2, hereafter called the RVZ (Roche-von Zeipel) model for simplicity. We shortly present here the numerical model CHARRON⁹ (Code for High Angular Resolution of Rotating Objects in Nature), which is an IDL¹⁰-based numerical implementation of the RVZ model. Further details are given by Domiciano de Souza et al. (2002).

CHARRON is oriented to deal with spectro-interferometric data, which means that, from the input physical parameters, it computes a series of monochromatic intensity maps of the stellar photosphere. From the Fourier transform (FT) of these maps one can obtain spectro-interferometric observables, such as those described in Sect. 1.2, namely, visibility amplitudes, differential phases, closure phases, among others. Stellar spectra, magnitudes (or fluxes), spectral energy distributions (SED) can also be directly computed from the intensity maps.

To compute the CHARRON models, the stellar surface is divided in a predefined grid with nearly identical surface area elements (typically $\sim 50\,000$). From the RVZ equations in Sect. 2.2 it is possible to assign different physical quantities to each surface grid element j : radius R_j , rotation velocity $v_j (= \Omega R_j)$, effective gravity $g_{\text{eff},j}$, and effective temperature $T_{\text{eff},j}$. This numerical treatment is similar to the one adopted by Townsend (1997) in the BRUCE code.

A local specific intensity from a plane-parallel atmosphere $I_j (= I_j(g_{\text{eff},j}, T_{\text{eff},j}, \lambda(v_{\text{proj},j}), \mu_j)$ is then associated to each surface element. The wavelength $\lambda(v_{\text{proj},j})$ corresponding to the local specific intensity is Doppler-shifted to the local rotation velocity projected onto the observer's direction $v_{\text{proj},j}$. The parameter μ_j is the cosine between the normal to the surface grid element and the line-of-sight (limb darkening is thus automatically included in the model). Both $v_{\text{proj},j}$ and μ_j depend on the chosen inclination i of the rotation axis.

The local I_j can be given by an analytical equation (including for example continuum flux, line profiles, and limb darkening) or as an output of stellar atmosphere models calculated with radiative transfer codes. The results presented in this work are mainly based on I_j interpolated on a pre-calculated grid of specific intensities, which were obtained from the spectral synthesis code SYNSPEC (Hubeny & Lanz, 2011) and the ATLAS9 stellar atmosphere models (Kurucz, 1979). The total intensity map of the star I_λ is obtained from the juxtaposition of each I_j for the apparent surface grid elements. Examples of intensity maps calculated with CHARRON are given in Sect. 2.2.3.

Model fluxes, SED, magnitudes, and spectro-interferometric quantities are obtained directly from the intensity maps. The stellar distance d and position angle of its sky-projected rotation axis PA_{rot} are also needed to compute these observables.

The optimal input parameters required by CHARRON to compute the different observables for a given model of fast-rotating star may depend on the specific problem studied. Generally, for the RVZ model, the main input parameters are M , R_{eq} (or R_p), v_{eq} (or Ω), β , and \bar{T}_{eff} (or L), to define the stellar structure and intrinsic brightness, plus the parameters i , PA_{rot} , and d , which are needed to compute the observable (apparent) quantities.

⁹In french, *charron* is an ancient metier, it is a *spécialiste du bois, maître de tout ce qui tourne et roule*.

¹⁰Interactive Data Language.

2.5.2 FRACS (Fast Ray-tracing Algorithm for Circumstellar Structures)

Different approaches exist to compute model observables of stellar CSE, ranging from simple analytical and geometrical models to full hydrodynamic-radiative transfer models. The choice of a given modeling approach depends essentially on the available data and on the physical output sought. Of course, more complete and complex models are also more demanding in terms of computing time.

In studies of Be and sgB[e] stars it is common to consider models given by a set of equations that describe a CSE physical structure in stationary physical equilibrium, such as those presented in Sects. 2.3 and 2.4. Even in this case, the complete and self-consistent radiative-transfer solution of the problem can be highly demanding in terms of computing time. This prevents such models to be used both in a full model-fitting procedure (for example a χ^2 minimization requiring several computations of the model) and in estimations of uncertainties on the measured parameters. On the other hand, geometrical models have the advantage of being very fast to calculate, but have a narrower domain on applicability and deliver less physical information than radiative transfer models. In an attempt to create a model that is based on the physics of CSE without being too much time consuming we (G. Niccolini, Ph. Bendjoya, and myself) have developed a *fast ray-tracing algorithm for circumstellar structures* (FRACS¹¹).

FRACS is based on a parametrized CSE composed of dust, combined to a simplified radiative transfer approach (ray-tracing without scattering). This allows a fast computation of intensity maps from a straightforward integration of the radiative transfer equation. Because it is fast, FRACS can be used for model-fitting, which requires the exploration of a wide domain of the parameter space and the computation of a large number of models; the estimation of uncertainties on the fitted parameters is also possible. If necessary, the physical parameters constrained from a model fitting using FRACS can then be used as input for a more self-consistent radiative-transfer model, such as the HDUST code presented in Sect. 2.5.3.

A full description of the FRACS code is presented in the A&A paper hereafter (Niccolini et al., 2011). A second A&A paper (Domiciano de Souza et al., 2011) is given in Sect. 3.3, where we use FRACS to interpret VLT/MIDI observations of the sgB[e] star CPD-57° 2874.

As described in Chapter 4, we plan to develop a second version of FRACS including atomic and molecular lines, other sources of continuum gas emission (free-free, free-bound), and different parametric prescriptions for the CSE (e.g. Keplerian disks). This upgrade will allow FRACS to be used also to interpret sgB[e] and Be observations from spectro-interferometers able to resolve lines (e.g. VLT/AMBER, VLT/MATISSE, VLT/GRAVITY, CHARA/VEGA, ALMA).

¹¹Name inspired from BSG.

Fast ray-tracing algorithm for circumstellar structures (FRACS)

I. Algorithm description and parameter-space study for mid-IR interferometry of B[e] stars

G. Niccolini, P. Bendjoya, and A. Domiciano de Souza

UMR 6525 CNRS, H. FIZEAU-Université de Nice Sophia-Antipolis, Observatoire de la Côte d'Azur, Campus Valrose,
06108 Nice Cedex 2, France
e-mail: nicolin@unice.fr

Received 26 March 2010 / Accepted 9 September 2010

ABSTRACT

Aims. The physical interpretation of spectro-interferometric data is strongly model-dependent. On one hand, models involving elaborate radiative transfer solvers are too time consuming in general to perform an automatic fitting procedure and derive astrophysical quantities and their related errors. On the other hand, using simple geometrical models does not give sufficient insights into the physics of the object. We propose to stand in between these two extreme approaches by using a physical but still simple parameterised model for the object under consideration. Based on this philosophy, we developed a numerical tool optimised for mid-infrared (mid-IR) interferometry, the fast ray-tracing algorithm for circumstellar structures (FRACS), which can be used as a stand-alone model, or as an aid for a more advanced physical description or even for elaborating observation strategies.

Methods. FRACS is based on the ray-tracing technique without scattering, but supplemented with the use of quadtree meshes and the full symmetries of the axisymmetrical problem to significantly decrease the necessary computing time to obtain e.g. monochromatic images and visibilities. We applied FRACS in a theoretical study of the dusty circumstellar environments (CSEs) of B[e] supergiants (sgB[e]) in order to determine which information (physical parameters) can be retrieved from present mid-IR interferometry (flux and visibility).

Results. From a set of selected dusty CSE models typical of sgB[e] stars we show that together with the geometrical parameters (position angle, inclination, inner radius), the temperature structure (inner dust temperature and gradient) can be well constrained by the mid-IR data alone. Our results also indicate that the determination of the parameters characterising the CSE density structure is more challenging but, in some cases, upper limits as well as correlations on the parameters characterising the mass loss can be obtained. Good constraints for the sgB[e] central continuum emission (central star and inner gas emissions) can be obtained whenever its contribution to the total mid-IR flux is only as high as a few percents. Ray-tracing parameterised models such as FRACS are thus well adapted to prepare and/or interpret long wavelengths (from mid-IR to radio) observations at present (e.g. VLTI/MIDI) and near-future (e.g. VLTI/MATISSE, ALMA) interferometers.

Key words. methods: numerical – methods: observational – techniques: high angular resolution – techniques: interferometric – stars: mass loss – stars: emission-line, Be

1. Introduction

When dealing with optical/IR interferometric data, one needs to invoke a model for the understanding of the astrophysical object under consideration. This is because of (1) the low coverage of the uv -plane and most of the time because of the lack of the visibility phase; and (2) because our aim is to extract physical parameters from the data. This is particularly true for the Mid-Infrared Interferometric Instrument (MIDI, [Leinert et al. 2003](#)) at the Very Large Telescope Interferometer (VLTI), on which our considerations will be focused. Some pure geometrical information can be recovered through a simple toy model such as Gaussians (see e.g. [Leinert et al. 2004](#); [Domiciano de Souza et al. 2007](#)).

However, this approach does not give any insights into the physical nature of the object. One would dream of having a fully consistent model to characterise the object under inspection. In many cases, if not all, a fully consistent model is out of reach and one uses at least a consistent treatment of the radiative transfer. Models based for instance on the Monte Carlo method are very popular (see e.g. [Ohnaka et al. 2006](#); [Niccolini & Alcolea 2006](#); [Wolf et al. 1999](#)) for this purpose. Still, the

medium density needs to be parameterised and it is not determined in a self-consistent way. For massive stars for instance, it would be necessary to take into account non-LTE effects including both gas and dust emission of the circumstellar material as well as a full treatment of radiation hydrodynamics. Fitting interferometric data this way is as yet impossible because of computing time limitations.

Of course, solving at least the radiative transfer in a self-consistent way is already very demanding for the computational resources. Consequently, model parameters cannot be determined in a fully automatic way and the model fitting process must be carried out mostly *by hand*, or automatised by systematically exploring the parameter-space, the “chi-by-eye” approach mentioned in [Press et al. \(1992\)](#). The followers of this approach consider the “best fitting” model as their best attempt: a model that is compatible with the data. It is admittedly not perfect, but it is in most of the cases the best that can be done given the difficulty of the task. It is remarkable that a thorough χ^2 analysis of VLTI/MIDI data of the Herbig Ae star AB Aurigae has been performed by [di Folco et al. \(2009\)](#) which remains to date one of the most achieved studies of this kind. From the χ^2 analysis,

formal errors can be derived and at least the information concerning the constraints for the physical parameters can be quantified. Qualitative information about the correlation of parameters can be pointed out.

The next step after the toy models for the physical characterisation of the astrophysical objects can be made from the pure geometrical model towards the self-consistency by including and parameterising the object emissivity in the analysis. For instance, Lachaume et al. (2007) and Malbet et al. (2005) use optically thick (i.e. emitting as black bodies) and infinitely thin discs to model the circumstellar environment of pre-main-sequence and B[e] stars. Of course this approach has some restriction when modelling a disc: for instance it cannot handle nearly edge-on disc and an optically thin situation.

We propose an intermediate approach: between the use of simple geometrical models and sophisticated radiative transfer solvers. Indeed, it is a step backwards from the “self-consistent” radiative transfer treatment, which is in most cases too advanced with regard to the information provided by the interferometric data. For this intermediary approach, we assume a prescribed and parameterised emissivity for the medium. Our purpose is to derive the physical parameters that characterise this emissivity. In the process, we compute intensity maps and most particularly visibility curves from the knowledge of the medium emissivity with a fast ray-tracing technique (a few seconds depending on map resolution), taking into account the particular symmetries of a disc configuration. Then, the model fitting process can be undertaken in an automatic way with standard methods (see e.g. Levenberg 1944; Marquardt 1963). The techniques we present are designed to be quite general and not tailored to any particular emissivity except for the assumed axisymmetry of the problem under consideration.

Our purpose is twofold. On one hand – as already mentioned – we aim to estimate physical parameters and their errors characterising the circumstellar dusty medium under consideration with as few restrictive assumptions as possible; at least within the obvious limitations of the present model. On the other hand our purpose is to provide the user of a more detailed model, such as a Monte Carlo radiative transfer code, with a first characterisation of the circumstellar matter to start with.

In Sect. 2 we describe the general framework of the proposed ray tracing technique. In particular how to derive the observable from the astrophysical object emissivity. In Sect. 3 we describe the numerical aspects that are specific to the present ray-tracing technique. In particular, the use of a quadtree mesh and the symmetries that allow us to speed up the computation are detailed. In Sect. 4 we focus our attention on the circumstellar disc of B[e] stars and describe a parametric model of the circumstellar environment. In Sect. 5 we analyse artificial interferometric data generated both from the parametric model itself and from a Monte Carlo radiative transfer code (Niccolini & Alcolea 2006). Our purpose is not to fit any particular object, but to present our guideline to the following question: which physical information can we get from the data? A discussion of our results and the conclusions of our work are given in Sects. 6 and 7 respectively.

2. The ray-tracing technique

We describe here the FRACS algorithm, developed to study stars with CSEs from mid-IR interferometric observables (e.g. visibilities, fluxes, closure phases). Although FRACS could be extended to investigate any 3D CSE structures, we focus here on the particular case of axisymmetrical dusty CSEs. This

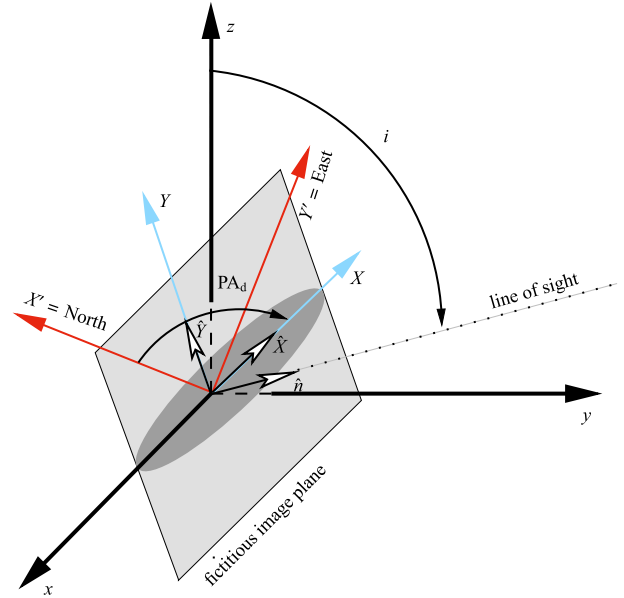


Fig. 1. Coordinate systems. The shaded ellipse represents a disc viewed by the observer.

study is motivated by the typical data one can obtain from disc-like CSE observed with MIDI, the mid-IR 2-telescope beam-combiner instrument of ESO’s VLTI (Leinert et al. 2003).

2.1. Intensity map

Intensity maps of the object are the primary outputs of the model that we need to compute the visibilities and fluxes that are directly compared to the observations. For this purpose, we integrate the radiation transfer equation along a set of rays (ray-tracing technique) making use of the symmetries of the problem (see Sect. 3 for details).

The unit vector along the line of sight is given by $\hat{n} = \hat{y} \sin i + \hat{z} \cos i$, i being the inclination between the z -axis and the line of sight and \hat{x} , \hat{y} the unit vector along the x et y -axis of a cartesian system of coordinates (see Fig. 1), referred to as the “model system” below. The problem is assumed to be invariant by rotation around the z -axis. We define a fictitious image plane by giving two unit vectors $\hat{Y} = -\hat{y} \cos i + \hat{z} \sin i$ and $\hat{X} = -\hat{x}$. This particular choice is made making use of the axisymmetry of the problem. Note that for this particular coordinate system (X, Y) the disc position angle (whenever $i \neq 0$) is *always* defined as 90° . The actual image plane, with the Y' and X' axis corresponding respectively to North and East, is obtained by rotating the axis of our fictitious image plane by an angle $PA_d - \frac{\pi}{2}$, where PA_d is the position angle of the disc with respect to North.

The dust thermal emissivity at wavelength λ and position vector \mathbf{r} is given by

$$\eta_\lambda(\mathbf{r}) = \kappa_\lambda^{\text{abs}}(\mathbf{r}) B_\lambda(T(\mathbf{r})), \quad (1)$$

where $\kappa_\lambda^{\text{abs}}(\mathbf{r})$ is the absorption coefficient and $B_\lambda(T(\mathbf{r}))$ the Planck function at the medium temperature $T(\mathbf{r})$ at \mathbf{r} . $\kappa_\lambda^{\text{abs}}$ is defined as $n(\mathbf{r}) C_\lambda^{\text{abs}}$, where C_λ^{abs} is the absorption cross section and $n(\mathbf{r})$ the number density of dust grains at \mathbf{r} .

We neglect the scattering of the radiation by dust grains, optimising our approach to long wavelengths (from mid-IR to radio).

2. Photosphere and circumstellar environment (CSE) of fast rotators

G. Niccolini et al.: Fast ray-tracing algorithm for circumstellar structures (FRACS). I.

This assumption simplifies the radiative transfer equation by removing the scattering term.

We obtain the intensity map at position (X, Y) in the image plane (inclined by i) and at wavelength λ by integrating the transfer equation along the particular ray that passes through the considered point of the image plane. Defining $\mathbf{r}_s(X, Y, i)$ (simply \mathbf{r}_s for short) as the position vector along a ray, given in the model system of coordinates by

$$\mathbf{r}_s(X, Y, i) = \begin{pmatrix} -X \\ -Y \cos i + s \sin i \\ Y \sin i + s \cos i \end{pmatrix}, \quad (2)$$

and by introducing the optical depth at wavelength λ and position s along the ray by

$$\tau_\lambda(X, Y, i; s) = \int_s^{\sqrt{R_{\text{out}}^2 - R^2}} \kappa_\lambda^{\text{ext}}(\mathbf{r}_{s'}) ds', \quad (3)$$

we obtain

$$I_\lambda(X, Y, i) = \int_{-\sqrt{R_{\text{out}}^2 - R^2}}^{\sqrt{R_{\text{out}}^2 - R^2}} \kappa_\lambda^{\text{abs}}(\mathbf{r}_s) B_\lambda [T(\mathbf{r}_s)] e^{-\tau_\lambda(X, Y, i; s)} ds, \quad (4)$$

where the extinction coefficient $\kappa_\lambda^{\text{ext}}(\mathbf{r}) \approx \kappa_\lambda^{\text{abs}}(\mathbf{r})$ because scattering is neglected.

We assume that the CSE is confined within a sphere of radius R_{out} , s varies consequently from $-\sqrt{R_{\text{out}}^2 - R^2}$ to $\sqrt{R_{\text{out}}^2 - R^2}$ ($R^2 = X^2 + Y^2$) in Eq. (4) and in the definition of a ray Eq. (2). This hypothesis can be relaxed without altering the present considerations and the domain of integration of Eq. (4) suitably chosen.

If some radiation sources (e.g. black body spheres) are included in the analysis, an additional term must be added in Eq. (4) whenever a particular ray intersect a source. For a source with specific intensity I_λ^s this additional term is given by $I_\lambda^s e^{-\tau_\lambda(X, Y, i; s^{(s)})}$, $s^{(s)}$ being the distance at which the ray given by X, Y and i (see Eq. (2)) intersects the outermost (along the ray) source boundary. In that case the lower integration limit in Eq. (4), that is $-\sqrt{R_{\text{out}}^2 - R^2}$, must also be replaced by $s^{(s)}$.

2.2. Interferometric observables

From the monochromatic intensity maps at wavelength λ (Eq. (4)) we obtain both the observed fluxes F_λ and visibilities V_λ for an object at distance d ,

$$F_\lambda(i) = \frac{1}{d^2} \int_{-\infty-\infty}^{\infty} \int_{-\infty-\infty}^{\infty} I_\lambda(X, Y, i) dXdY, \quad (5)$$

and

$$V_\lambda(B, \text{PA}) = \frac{1}{d^2 F_\lambda(i)} \int_{-\infty-\infty}^{\infty} \int_{-\infty-\infty}^{\infty} I_\lambda(X, Y, i) \times e^{-2j\pi \frac{B}{\lambda} [\frac{X}{\lambda} \cos(\Delta) + \frac{Y}{\lambda} \sin(\Delta)]} dXdY, \quad (6)$$

where V_λ is obtained for a given baseline specified by its projected length B (on the sky, i.e. (X', Y') coordinates) and its polar angle PA from North to East (direction of the Y' axis). Δ and j represent, respectively, $\text{PA}_d - \text{PA}$ and $\sqrt{-1}$.

3. Numerical considerations

We seek to produce intensity maps within seconds¹ and we aim for our numerical method to be sufficiently general in order to deal with a large range of density and temperature structures. Given these two relatively tight constraints, the numerical integration of Eq. (4) is not straightforward.

For example we have tested that the 5th order Runge-Kutta integrators of Press et al. (1992) with adaptive step-size (as discussed in Steinacker et al. 2006) does not suit our constraints. Indeed, the step adaption leads to difficulties if sharp edges (e.g. inner cavities) are present in the medium emissivity.

3.1. Mesh generation

Regarding the above mentioned constraints and the different numerical approaches tested, we found that Eq. (4) is more efficiently computed with an adaptive mesh based on a tree data structure (quadtrees/octrees). The mesh purpose is twofold: first, it must guide the computation of Eq. (4) and distribute the integration points along the rays according to the variations of the medium emissivity; second, within the restriction of axis-symmetrical situations, the mesh must handle any kind of emissivity. Quad/octree meshes are extensively used in Monte Carlo radiative transfer codes (e.g. see Bianchi 2008; Niccolini & Alcolea 2006; Jonsson 2006; Wolf et al. 1999); the mesh generation algorithm is thoroughly described in Kurosawa & Hillier (2001).

The mesh we use is a *cartesian* quadtree. *Cartesian* refers here to the mesh type and not to the system of coordinates we use. Indeed, the mesh is implemented as a nested squared domain (cells) in the $\rho - |z|$ plane ($\rho = \sqrt{x^2 + y^2}$). The whole mesh is enclosed by the largest cell (the root cell in the tree hierarchy) of size R_{out} in ρ and $|z|$. The underlying *physical* coordinate system is cylindrical (with $z > 0$) and the mesh cells correspond to a set of two (for $z > 0$ and $z < 0$) tori, which are the actual *physical* volumes.

The mesh generation algorithm consists in recursively dividing each cell in four child cells until the following conditions are simultaneously fulfilled for each cell in the mesh (see Kurosawa & Hillier 2001, for more details):

$$\frac{\iiint_{V_\xi} [\kappa_\lambda^{\text{abs}}(\mathbf{r})]^\alpha d^3\mathbf{r}}{\iiint_{V_{\text{tot}}} [\kappa_\lambda^{\text{abs}}(\mathbf{r})]^\alpha d^3\mathbf{r}} < \eta \quad \text{and} \quad (7)$$

$$\frac{\iiint_{V_\xi} [T(\mathbf{r})]^\beta d^3\mathbf{r}}{\iiint_{V_{\text{tot}}} [T(\mathbf{r})]^\beta d^3\mathbf{r}} < \eta, \quad (8)$$

where V_ξ is the volume of cell ξ , V_{tot} is the volume of the root cell and α, β and η are parameters controlling the mesh refinement.

In the present work α and β have been fixed to 1, but higher values can be useful for some particular situations where the generated mesh must be tighter than the mesh generated directly from the $\kappa_\lambda^{\text{abs}}$ and T variations. Typically, these situations show up for high optical depths (in this paper, optical depth values do not exceed ≈ 1 at $10 \mu\text{m}$ along the rays). The practical choice of α, β and η is obtained from a compromise between execution speed and numerical accuracy of the Eq. (4) integration

¹ The actual computation time reached is less than 10 s for a 10^4 pixel map on an Intel T2400 1.83 GHz CPU.

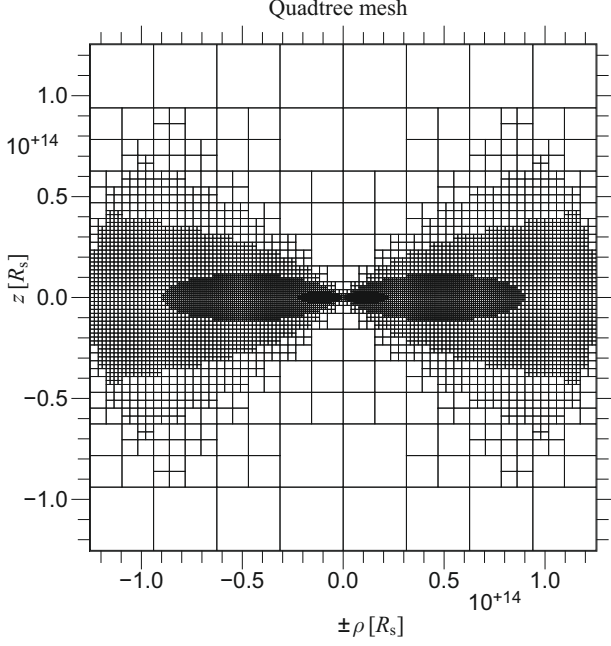


Fig. 2. Quadtree mesh for a disc configuration. The disc parameters are those of model (b) described in Sect. 5.2 (see also Tables 2 and 4). The mesh refinement parameter η (Eqs. (7) and (8)) has been set to the high value 10^{-3} in order to obtain a coarse mesh more easily represented.

(e.g. typical values of η range from 10^{-5} to 10^{-4}). When dealing with optically thick situations, a supplementary conditions can be added to Eqs. (7) and (8) in order to prescribe an upper limit to the cell optical depth. For instance, making use of the computation of the integral in Eq. (7), one can add the following criterion for cell ξ (whose centre is (ρ_ξ, z_ξ) and size Δ_ξ)

$$\frac{1}{2\pi\rho_\xi\Delta_\xi} \iiint_{V_\xi} \kappa_\lambda^{\text{ext}}(\mathbf{r}) d^3\mathbf{r} \leq \Delta\tau_{\text{lim}}, \quad (9)$$

where $\Delta\tau_{\text{lim}}$ is the prescribed upper limit to the cell optical depth.

For the moderate optical depths reached in this work, with values of η down to 10^{-5} and $\Delta\tau_{\text{lim}}$ set to 10^{-2} , the criteria of Eqs. (7) and (8) are the leading conditions to the mesh refinement.

Figure 2 shows the mesh obtained in the particular case of a B[e] circumstellar disc (see Sect. 4) for models whose parameters are given in Table 2 (see caption for more details).

The volume integrals in Eqs. (7) and (8) are estimated by Monte Carlo integration. For a quantity $f(\mathbf{r})$ and for the cell ξ the integral $\iiint_{V_\xi} f(\mathbf{r}) d^3\mathbf{r}$ is approximated by

$$2\pi \int_{z_\xi - \frac{\Delta_\xi}{2}}^{z_\xi + \frac{\Delta_\xi}{2}} \int_{\rho_\xi - \frac{\Delta_\xi}{2}}^{\rho_\xi + \frac{\Delta_\xi}{2}} \rho f(\rho, z) dz d\rho \approx \frac{2\pi\Delta_\xi^2}{N} \sum_{k=1}^N \rho_k f(\rho_k, z_k), \quad (10)$$

where we made explicit use of the mesh coordinates and where (ρ_k, z_k) with $k = 1, \dots, N$ are chosen randomly and uniformly within the cell domain.

3.2. Symmetries

We can make use of the CSE symmetries to reduce the computation domain of an intensity map from Eq. (4) to only a fourth of it and consequently reduce the computation time.

Recalling the definition of a ray (Eq. (2)), we have two noticeable identities for any disc physical quantity Φ (e.g. $\kappa_\lambda^{\text{abs}}$, $\kappa_\lambda^{\text{ext}}$, T , n , ...) depending on \mathbf{r}

$$\Phi(\mathbf{r}_s(X, Y, i)) = \Phi(\mathbf{r}_s(-X, Y, i)) \quad \text{and} \quad (11)$$

$$\Phi(\mathbf{r}_s(X, Y, i)) = \Phi(\mathbf{r}_{-s}(X, -Y, i)), \quad (12)$$

where Eq. (11) expresses the disc symmetry with respect to the $y-z$ plane and Eq. (12) the point symmetry with respect to the origin of the model system of coordinates.

From the above identities it is straightforward to deduce their counterpart for the intensity map

$$I_\lambda(X, Y, i) = I_\lambda(-X, Y, i) \quad \text{and} \quad (13)$$

$$I_\lambda(X, Y, i) = I_\lambda(X, -Y, i) e^{-\int_{-s_{\text{max}}}^{+s_{\text{max}}} \kappa_\lambda^{\text{ext}}(\mathbf{r}_{s'}) ds'}, \quad (14)$$

where $s_{\text{max}} = \sqrt{R_{\text{out}}^2 - R^2}$. Note that the exponential factor in Eq. (14) has to be evaluated when computing $I_\lambda(X, Y, i)$ anyway; no extra effort is required to derive $I_\lambda(X, Y, i)$ from $I_\lambda(X, -Y, i)$ except for the multiplication of $I_\lambda(X, -Y, i)$ by this factor.

3.3. Intensity map

The fictitious image plane is split into a set of pixels whose positions X_j and Y_k are given by

$$X_j = \Delta_X \times \left(j + \frac{1}{2} - \frac{N}{2} \right), \quad (15)$$

$$Y_k = \Delta_Y \times \left(k + \frac{1}{2} - \frac{N}{2} \right), \quad (16)$$

where $\Delta_X = \Delta_Y$ is the pixel size in X and Y , and N is the number of pixels in X and Y , and where

$$0 \leq j, k \leq (N \div 2) + \delta, \quad (17)$$

where $\delta = -1$ for N even and $\delta = 0$ otherwise and “ \div ” stands for the integer division. Taking into account the symmetries mentioned in Sect. 3.2 only a fourth of the pixels need to be considered.

The evaluation of the integral in Eq. (4) is carried out for each pixel (X_j, Y_k) and along the ray $\mathbf{r}_s(X_j, Y_k, i)$. The intersection points of the ray with the cell boundaries corresponds to a set of distances along the ray defined as

$$s_0 = 0 \quad (18)$$

$$s_l = s_{l-1} + \Delta s_{l-1} \quad \text{for } 1 \leq l \leq n_{\text{cells}}, \quad (19)$$

where n_{cells} is the number of cells encountered along the ray, and Δs_l the distance crossed within the l th cell.

We estimate numerically the optical depth $\tau_\lambda(X, Y, i; s)$, defined in Eq. (3), via the midpoint rule quadrature by

$$\tau_\lambda(X, Y, i; s_l) \approx \tau_\lambda^{(l)} = \sum_{k=l}^{n_{\text{cells}}-1} \kappa_\lambda^{\text{ext}}(\mathbf{r}_{s_{l+1/2}}) \Delta s_l, \quad (20)$$

where we defined $s_{l+1/2} = s_l + \frac{\Delta s_l}{2}$ for $l = 0, \dots, n_{\text{cells}} - 1$.

2. Photosphere and circumstellar environment (CSE) of fast rotators

G. Niccolini et al.: Fast ray-tracing algorithm for circumstellar structures (FRACS). I.

The numerical estimate of $I_\lambda(X_j, Y_k, i)$ is obtained by

$$I_\lambda(X_j, Y_k, i) \approx \sum_{l=0}^{n_{\text{cells}}-1} \kappa_\lambda^{\text{abs}}(\mathbf{r}_{s_{l+1/2}}) B_\lambda(T(\mathbf{r}_{s_{l+1/2}})) e^{-\tau_\lambda^{(l)}} \Delta s_l. \quad (21)$$

The results for all j and k can then be obtained from the discrete counterpart of the symmetry relations (13) and (14)

$$I_\lambda(X_{N-1-j}, Y_k, i) = I_\lambda(X_j, Y_k, i), \quad (22)$$

$$I_\lambda(X_j, Y_{N-k-1}, i) = I_\lambda(X_j, Y_k, i) e^{-\tau_\lambda^{(0)}}. \quad (23)$$

3.4. Interferometric observables

From the numerical estimate of $I_\lambda(X_j, Y_k, i)$ given above we obtain (similarly to Eqs. (5) and (6)) the numerical fluxes and visibilities, which can be directly compared to the observed data. The numerical estimate of these quantities is again obtained through the mid-point rule.

The numerical flux $F_\lambda(i)$ is computed by

$$F_\lambda(i) \approx \frac{1}{d^2} \sum_{k=0}^{N-1} \sum_{l=0}^{N-1} I_\lambda(X_k, Y_l, i) \Delta X \Delta Y. \quad (24)$$

The complex visibility is approximated numerically by

$$V_\lambda \approx \frac{1}{d^2 F_\lambda(i)} \sum_{k=0}^{N-1} \sum_{l=0}^{N-1} I_\lambda(X_k, Y_l, i) e^{2j\pi \frac{\mathbf{R}_{kl}}{d}} \Delta X \Delta Y, \quad (25)$$

where $\mathbf{B} = (B \cos \Delta, B \sin \Delta)$ and $\mathbf{R}_{kl} = (X_k, Y_l)$.

3.5. Artificial data generation

The procedure described below aims to mimic the observables of the VLTI/MIDI instrument: the flux F_λ (Eq. (24)) and the modulus of the visibility $|V_\lambda|$ (Eq. (25)). The wavelengths and baselines chosen for the artificial data generation correspond to accessible values to VLTI/MIDI with the Unit Telescopes (UTs): $\lambda_j = 7, 8, 9, 10, 11, 12$, and $13 \mu\text{m}$ ($j = 1, \dots, n_\lambda; n_\lambda = 7$), and (B_k, PA_k) as shown in Table 1 ($k = 1, \dots, n_B; n_B = 18$). These values amount to 126 points covering the uv-plane.

For a given intensity map at λ_j , F_{λ_j} and $|V_{\lambda_j}|$ are taken as the expectation values of the simulated data. The observed flux $F_{\lambda_j}^{\text{obs}}$ is then generated assuming a Gaussian noise with an RMS (root mean square) corresponding to 10% relative error $\sigma_F(j) = 0.1 \times F_{\lambda_j}$.

The artificial observed visibility amplitudes $|V_\lambda^{\text{obs}}|$ are obtained as

$$|V_{\lambda_j}^{\text{obs}}(B_k, \text{PA}_k)| = |V_{\lambda_j}(B_k, \text{PA}_k)| + \Delta V_k, \quad (26)$$

where ΔV_k is a wavelength independent shift that mimics the error in the observed visibilities, introduced by the calibration procedure commonly used in optical/IR interferometry. For each (B_k, PA_k) , ΔV_k is computed assuming a Gaussian noise with an RMS corresponding to 10% relative error (typical for VLTI/MIDI) $\sigma_V(k) = 0.1 \times \langle |V_\lambda(B_k, \text{PA}_k)| \rangle$, where $\langle |V_\lambda(B_k, \text{PA}_k)| \rangle$ is the wavelength mean visibility modulus.

3.6. Model fitting and error estimate

We describe here the procedure adopted in order to simultaneously fit observed fluxes and visibilities using FRACS models

Table 1. Projected baselines. These values correspond to the baselines accessible from pairs of Unit Telescopes (UT) at ESO-VLTI.

k	B_k [m]	PA_k [deg]
1	37.8	61.7
2	41.3	53.4
3	43.7	44.8
4	46.2	44.5
5	49.5	37.5
6	51.9	30.0
7	61.7	134.6
8	62.0	111.2
9	62.4	122.5
10	81.3	108.2
11	83.0	52.2
12	86.3	96.0
13	89.0	84.4
14	89.9	44.8
15	94.8	36.7
16	113.6	82.4
17	121.2	73.6
18	126.4	64.9

defined by a given set of input parameters. This procedure is applied to artificial data in the next sections.

In order to quantify the discrepancy between the artificial observations ($|V_{\lambda_j}^{\text{obs}}|$ and $F_{\lambda_j}^{\text{obs}}$) and the visibilities and fluxes from a given model ($|V_{\lambda_j}(B_k, \text{PA}_k)|$ and F_{λ_j}) we use the χ^2 like quantities

$$\chi_{|V|}^2 = \sum_{j=1}^{n_\lambda} \sum_{k=1}^{n_B} \left(\frac{|V_{\lambda_j}^{\text{obs}}(B_k, \text{PA}_k)| - |V_{\lambda_j}(B_k, \text{PA}_k)|}{\sigma_V(k)} \right)^2, \quad (27)$$

and

$$\chi_F^2 = \sum_{j=1}^{n_\lambda} \sum_{k=1}^{n_B} \left(\frac{F_{\lambda_j}^{\text{obs}} - F_{\lambda_j}}{\sigma_F(j)} \right)^2. \quad (28)$$

To take into account both the mid-IR flux and the visibilities on the same level in the fitting process, we minimise the following sum

$$\chi^2 = \chi_{|V|}^2 + \chi_F^2. \quad (29)$$

In the discussion below about the parameter and error determination we use the reduced χ^2 defined by $\chi_r^2 = \chi^2 / (2n_B n_\lambda - n_{\text{free}})$ (for n_{free} free parameters).

From a minimising algorithm the best-fit model parameters can then be found by determining the minimum χ_r^2 : $\chi_{r,\text{min}}^2$. The ‘‘error’’ estimate is obtained from a thorough exploration of the parameter space volume, defined by a contour level $\chi_{r,\text{min}}^2 + \Delta\chi_r^2$, where $\Delta\chi_r^2$ has been chosen equal to 1. This volume can be interpreted as a confidence region. The quantity defined in Eq. (29) is a weighted sum of χ^2 variables whose cumulative distribution function can be approximated by a gamma distribution (see Feiveson & Delaney 1968) with the same mean and variance. It is then possible to obtain a rough estimate of the confidence level associated with the $\Delta\chi_r^2 = 1$ confidence region given approximately by $\approx 2\sigma$.

The size of the confidence region is determined by considering all possible pairs of parameters for a given fitted model and computing χ_r^2 maps for each. The procedure to estimate the errors can be summarised as follows:

- For a given χ_r^2 map, i.e. for a given couple of parameters among the $n_{\text{free}} \times (n_{\text{free}} - 1)/2$ possibilities, we identify the

2.5. Numerical models

A&A 525, A21 (2011)

region bounded by $\Delta\chi_r^2 = 1$ around the minimum of this particular map.

- The boundaries of the projection of these regions on each of the two parameter axis considered are recorded for each map.
- The final errors on a given parameter are taken as the highest boundary values of the projected regions over all maps.

4. Astronomical test case: sgB[e] stars

In the following sections we apply FRACS to a theoretical interferometric study of dusty CSE of B[e] supergiants (sgB[e] in the nomenclature of [Lamers et al. 1998](#)). However, we emphasise that FRACS is in no way restricted to this particular class of objects.

sgB[e] stars reveal in particular a strong near- or mid-IR excess caused by hot dust emission. There is evidence (e.g. [Zickgraf et al. 1985](#)) that the stellar environment, and in particular dust, could be confined within a circumstellar disc. Our purpose is to characterise this class of objects and derive not only geometrical parameters (e.g. inner dust radius, disc position angle and inclination) but also physical parameters such as temperature gradients, dust formation region, material density, ...

The physical description of the CSE chosen for our study is the wind model with equatorial density enhancement. This is a classical CSE model commonly adopted for sgB[e] (e.g. [Porter 2003](#)).

In order to compute the model intensity maps we need to parameterise the emissivity of the disc. Consistently with FRACS assumptions, we consider only dust thermal emission without scattering by dust grains and the gas contribution to the medium emissivity. In the rest of this section we characterise the emissivity by describing the dust density law, the absorption cross section, and the temperature structure of the CSE.

4.1. Mass loss and dust density

Dust is confined between the inner and outer radius R_{in} and R_{out} respectively. We assume a stationary and radial mass loss; physical quantities will consequently depend only on the radial component r and the co-latitude θ . The disc symmetry axis coincides with the z axis of the model cartesian system of coordinates. The mass loss rate and velocity parameterisations are simplifications of the one adopted by [Carciofi et al. \(2010\)](#), and we refer the reader to their work for a complete description (see also [Stee et al. 1995](#), for a similar description).

The mass loss rate per unit solid angle, at co-latitude θ , is parameterised as follows

$$\frac{d\dot{M}}{d\Omega}(\theta) = \frac{d\dot{M}}{d\Omega}(0) (1 + A_1 \sin^m(\theta)), \quad (30)$$

with the help of two dimensionless parameters A_1 and m .

Even though our computations make no explicit use of the radial velocity field $v_r(\theta)$ (assumed to have reached the terminal velocity $v_\infty(\theta)$ in the region under considerations, i.e. $v_r(\theta) \approx v_\infty(\theta)$), the dust density depends on $v_r(\theta)$ parameterised in a similar fashion

$$v_r(\theta) = v_r(0) (1 + A_2 \sin^m \theta), \quad (31)$$

where we have introduced the supplementary dimensionless parameters A_2 . From Eqs. (30) and (31) we see that A_1 and A_2 are

the relative differences of the values of $\frac{d\dot{M}}{d\Omega}(\theta)$ and $v_r(\theta)$ at the equator and the pole (relatively to the pole).

From the mass continuity equation one obtains the number density of dust grains

$$n(r, \theta) = n_{\text{in}} \left(\frac{R_{\text{in}}}{r} \right)^2 \frac{1 + A_2}{1 + A_1} \frac{1 + A_1}{1 + A_2} \frac{(\sin \theta)^m}{(\sin \theta)^m}, \quad (32)$$

where n_{in} is the dust grain number density at R_{in} in the disc equatorial plane. In Eq. (32), the parameter m controls how fast the density drops from the equator to the pole, defining an equatorial density enhancement (disc-like structure).

Consistent with the accepted conditions for dust formation ([Carciofi et al. 2010](#); [Porter 2003](#)) we assume that the dust can survive only in the denser parts of the disc. We thus define a dusty disc opening angle $\Delta\theta_d$ determined by the latitudes for which the mass loss rate has dropped to half of its equatorial value:

$$\Delta\theta_d = 2 \arccos \left(\frac{A_1 - 1}{2A_1} \right)^{\frac{1}{m}}. \quad (33)$$

To summarise, the dust grains only exist (i.e., $n(r, \theta) \neq 0$) in the regions bounded by $R_{\text{in}} \leq r \leq R_{\text{out}}$ and by $\frac{\pi - \Delta\theta_d}{2} \leq \theta \leq \frac{\pi + \Delta\theta_d}{2}$.

4.2. Dust opacities

The absorption cross section C_λ^{abs} for the dust grains is obtained from the [Mie \(1908\)](#) theory. The Mie absorption cross sections are computed from the optical indices of astronomical silicate ([Draine & Lee 1984](#)). Note that since scattering is neglected, $C_\lambda^{\text{abs}} \approx C_\lambda^{\text{ext}}$, with C_λ^{ext} being the extinction cross section.

For a power-law size distribution function according to [Mathis et al. \(1977\)](#) the mean cross sections (e.g. for C_λ^{abs}) are given by

$$C_\lambda^{\text{abs}} = \frac{\int_{a_{\text{min}}}^{a_{\text{max}}} a^{-\beta} C_\lambda^{\text{abs}}(a) da}{\int_{a_{\text{min}}}^{a_{\text{max}}} a^{-\beta} da}, \quad (34)$$

where a_{min} and a_{max} are the minimum and maximum radii for the dust grains under consideration and β is the exponent of the power-law. The computation of the cross section in Eq. (34) was performed with the help of the [Wiscombe \(1980\)](#) algorithm.

4.3. Temperature structure

The dust temperature is assumed to be unique (i.e. independent of grain size) and described by a power-law

$$T(r) = T_{\text{in}} \left(\frac{R_{\text{in}}}{r} \right)^\gamma, \quad (35)$$

where T_{in} is the temperature at the disc inner radius R_{in} . We note that γ is not necessarily a free parameter because in the optically thin regime (large wavelength and radius) the temperature goes as $T(r) \propto r^{-\frac{2}{4+\delta}}$ with $\delta \simeq 1$ (see [Lamers & Cassinelli 1999](#)).

4.4. Central continuum emission

The continuum emission from the central regions is composed by the emission from the star and from the close ionised gas

2. Photosphere and circumstellar environment (CSE) of fast rotators

G. Niccolini et al.: Fast ray-tracing algorithm for circumstellar structures (FRACS). I.

Table 2. Model parameters. This table lists the parameters of 12 different models.

Parameters	Values	Unit
A_1	150	–
A_2	–0.8	–
$\Delta\theta_d$	10/60	deg
R_s	60	R_\odot
R_{in}	30	R_s
R_{out}	3000	R_s
n_{in}	0.015/0.15	m^{-3}
T_{in}	1500	K
γ	0.75	–
$I_{\lambda_0}^s$	6500	$W m^{-2} \mu m^{-1} str^{-1}$
α	3	–
PA_d	125	deg
i	20/50/90	deg
a_{min}	0.5	μm
a_{max}	50	μm
β	–3.5	–

Notes. The parameter values that change ($\Delta\theta_d$, n_{in} and i) from one model to the other have been enclosed in a box and separated by a slash. The values of $\Delta\theta_d = 10^\circ/60^\circ$ given below correspond via Eq. (33) to $m = 183.56/4.86$ respectively.

(free-free and free-bound emission). This central source emission is confined to a small region of radius R_s ($\ll R_{in}$), which is unresolved (angular sizes of a few milliarcseconds) by mid-IR interferometers. Thus, in our modelling R_s is simply a scaling factor of the problem fixed to a typical radius value for massive stars. The specific intensity (in $W m^{-2} \mu m^{-1} str^{-1}$) of this central source is parameterised as follows

$$I_\lambda^s = I_{\lambda_0}^s \left(\frac{\lambda_0}{\lambda} \right)^\alpha, \quad (36)$$

where $I_{\lambda_0}^s$ is the specific intensity at a reference wavelength λ_0 ($=10 \mu m$ in the following), and α gives the spectral dependence of the continuum radiation. In the mid-IR its value is expected to lie between $\alpha = 4$ (pure black body) and $\alpha \approx 2.6$ (free-free emission) for an electron density proportional to r^{-2} (Panagia & Felli 1975; Felli & Panagia 1981).

5. Study of the tested models

Following the description in the last sections we describe here the chosen sgB[e] model parameters used to simulate VLTI/MIDI observations (visibilities and fluxes) and the corresponding analysis, i.e. model fitting, using FRACS. The list of chosen parameters is summarised in Table 2. Two types of numerical tests are presented. Firstly, synthetic mid-IR interferometric data are generated from FRACS itself. In that way, it is possible to determine what information the mid-IR interferometric data contain under the optimistic assumption that we do have the *true* model. Secondly, this study is supplemented by the comparison of FRACS to a Monte Carlo radiative transfer computation. This confirms that FRACS can indeed mimic, under appropriate conditions, the results of a more sophisticated code as seen from the mid-IR interferometric eye.

5.1. Parameter description

The distance to the simulated object has been fixed to $d = 1$ pc, which is a typical distance for Galactic sgB[e].

The inner radius $R_{in} = 30 R_s = 1800 R_\odot$ value was chosen by considering the location of the hottest dust grains (see Lamers & Cassinelli 1999) with a condensation temperature of 1500 K assumed to be the T_{in} value. The value of R_{out} cannot be determined from the mid-IR data and has been fixed to $3000 R_s = 1.8 \times 10^5 R_\odot$. The temperature gradient γ was fixed to 0.75 according to Porter (2003). PA_d was fixed to 125° .

The central source emission is supposed to have a radius $R_s = 60 R_\odot$. We recall that the central region is unresolved by the interferometer and that its radiation describes both the stellar and inner gas contribution to the continuum mid-IR emission. The specific intensity of this central source $I_{\lambda_0}^s$ has been chosen to be $6500 W m^{-2} \mu m^{-1} str^{-1}$. If the central source was a pure blackbody this value would correspond to the $10 \mu m$ emission of a blackbody with an effective temperature around ≈ 8000 K. However, this central emission is not a pure blackbody, and we adopt the spectral dependence of the central source emission to be $\alpha = 3$, which is a compromise between $\alpha = 4$ for a pure blackbody and a value of ≈ 2.6 for free-free emission (Panagia & Felli 1975; Felli & Panagia 1981).

Spectroscopic observations of H α and forbidden line emissions from B[e] CSE (Zickgraf 2003) reveal that typical values for A_2 are expected to range from -0.95 to -0.75 . We adopt the value -0.8 in our models. According to Lamers & Waters (1987), the values of A_1 range from 10^2 to 10^4 in most cases (though values as low as 10 are not excluded). With this high value of A_1 the factor $1 + A_1 (\sin \theta)^{1/m}$ in Eq. (32) of $n(r, \theta)$ is approximately given by $A_1 (\sin \theta)^{1/m}$ for all pertinent values of θ , i.e. those close to $\pi/2$ within the disc. This leads to an evident degeneracy in $n_{in} \times A_1$ in $n(r, \theta)$: we are only sensible to the product of the two parameters as a scaling factor for the density. Therefore, the value of A_1 is assumed to be fixed to 150.

To define the dust opacities the chosen value for β is that of Mathis et al. (1977), i.e. $\beta = -3.5$. Because some sgB[e] show weak $9.7 \mu m$ silicate features in their spectrum (e.g. Porter 2003; Domiciano de Souza et al. 2007) we chose to use large grains in our test models: $a_{min} = 0.5 \mu m$ and $a_{max} = 50 \mu m$. However, with this particular choice of large grains, the average albedo from 7 to $13 \mu m$ is 6.4% , with the highest value reached at $7 \mu m$. We have checked with a Monte Carlo (MC) simulations (see Sect. 5.3) that the effect of scattering on our primary observables, visibilities, and fluxes is indeed negligible by comparing the results obtained by switching the scattering process off and on². The mean relative differences are 3.5% and 3.0% for the visibilities and the fluxes respectively. These values must be compared to the effect of random noise in the MC simulation, estimated to be of the same order and to experimental errors, typically $\sim 10\%$ for the visibilities and fluxes. We underline that whenever the albedo can be neglected, it is theoretically safe to compute visibilities and fluxes from the consideration presented in Sect. 2, in any other situations the effect of scattering on the observable must be carefully tested.

The parameters n_{in} , m and i were set to different values defining 12 test models to be analysed from their corresponding simulated data. Two n_{in} values ($0.015 m^{-3}$ and $0.15 m^{-3}$) have been chosen in order to have an approximate disc-dust optical depth in the equatorial plane (from R_{in} to R_{out}) close to ≈ 0.1 and ≈ 1 in the wavelength range considered (from $7 \mu m$ to $13 \mu m$). These values corresponds to a mass loss rate of $\dot{M} \approx 2.5 \times 10^{-7 \dots -6} M_\odot yr^{-1}$. Two m values were chosen corresponding

² The computation have been done for model b described in Sect. 5.2, the baselines listed in Table 1 and the wavelengths under consideration from 7 to $13 \mu m$.

2.5. Numerical models

A&A 525, A21 (2011)

Table 3. Relative errors (given in %) on the parameters for models (a) et (b) (see text for description of models).

Models\Parameters	A_2	m	R_{in}	n_{in}	T_{in}	γ	$I_{\lambda_0}^s$	α	PA_d	i
(a)	(53)	≥ 100	1.9	46	15	7.1	27	13	4.3	6.2
(b)	(59)	≥ 100	4.5	100	20	12	≥ 100	96	9.4	7.2

Notes. For each of the 10 free parameters considered in the analysis, the values of the relative error corresponding to the 12 different models are given. Indeed, these relative errors are “mean values” for the errors because the error bars are not symmetric with respect to the best-fit values. The parenthesis around the relative error of A_2 recall that this parameter is bounded.

Table 4. Constraints on the model parameters.

Models\parameters				Constraints [%]		
τ	$\Delta\theta_d$ [deg]	i [deg]		≤ 10	$10 \rightarrow 25$	≥ 25
1	0.1	60	20	R_{in}, γ	T_{in}, α	PA_d, i
2	1.	60	20	R_{in}	T_{in}, γ	α, PA_d, i
3	0.1	10	20	–	R_{in}	$T_{in}, \gamma, \alpha, PA_d, i$
4	1.	10	20	R_{in}, γ	T_{in}	α, PA_d, i
(a)	0.1	60	50	R_{in}, γ, PA_d, i	T_{in}, α	
(b)	1.	60	50	R_{in}, PA_d, i	T_{in}, γ	α
5	0.1	10	50	–	R_{in}	$T_{in}, \gamma, \alpha, PA_d, i$
6	1.	10	50	R_{in}, γ, PA_d, i	T_{in}	α
7	0.1	60	90	R_{in}, γ, PA_d	T_{in}, i, α	
8	1.	60	90	R_{in}, PA_d	T_{in}, γ, i	α
9	0.1	10	90	PA_d	R_{in}	$T_{in}, \gamma, \alpha, i$
10	1.	10	90	R_{in}, γ, PA_d, i	T_{in}	α

Notes. For the 12 models considered here (differing in their value of τ , $\Delta\theta_d$ and i), numbered from 1 to 10 (except for model a and b), we classified the parameters into 3 different relative error ranges: below 10%, between 10 and 25% and above 25%. Because $A_2, m, n_{in}, I_{\lambda_0}^s$ are determined for all the models with an error greater than 25% they have been discarded from the table for the sake of clarity.

to a wide and a narrow opening angle, i.e. $\Delta\theta_d = 10^\circ$ and $\Delta\theta_d = 60^\circ$. Three inclinations i were tested (20° , 50° , and 90°) corresponding to discs seen close to pole-on, intermediate inclination, and equator-on. These values of n_{in}, m, i , together with the parameters fixed above, define 12 test models that will be studied below.

From these 12 test models we have generated 12 sets of artificial VLT/MIDI observations (visibilities and fluxes) following the procedure described in Sect. 3.5. We do not aim to present an exhaustive review of all types of sgB[e] CSE. Rather, we focussed on the analysis of the parameter constraints one can hope to obtain from present and near-future mid-IR spectro-interferometry. The quantitative estimate of these constraints is derived from a systematic analysis of the χ_r^2 variations with the parameters.

In our model fitting and χ_r^2 analysis we concentrate on 10 free parameters ($n_{free} = 10$) that can be set into four different groups:

- the *geometrical* parameters: PA_d, i and R_{in} ;
- the parameters related to the *central source*: $I_{\lambda_0}^s$ and α ;
- those describing the *temperature structure*: T_{in} and γ ;
- and the *number density of dust grains*: $A_2, \Delta\theta_d$ (or equivalently m) and n_{in} .

The remaining parameters of the model are in general loosely constrained by mid-IR interferometric observations so that we kept them fixed to the values described above.

5.2. Model fitting and χ_r^2 analysis of the 12 test models

We describe here the data analysis procedure adopted to study our 12 test models. The results of our analysis are summarised

in Tables 3 and 4, and their physical interpretation is presented in Sect. 6.

As a first step we chose 2 of the 12 models, hereafter called models (a) and (b), to be exhaustively studied from a complete model fitting procedure. As an example we show the simulated observed mid-IR fluxes and visibilities for model (a) and (b) in Figs. 3–5. The parameters of models (a) and (b) are those of Table 2 with $\Delta\theta_d = 60^\circ, i = 50^\circ$ and n_{in} fixed to the values 0.015 m^{-3} and 0.15 m^{-3} respectively. These two models are those presenting some of the best constrained model parameters for the dust CSE. On the other hand, the contribution of the central regions to the total flux and visibilities is quite different in models (a) and (b) (see discussion in Sect. 6).

The study of models (a) and (b) have thus been performed as for real interferometric observations. The best-fit values of the parameters have been obtained by the Levenberg-Marquardt algorithm with a stopping criterion corresponding to a relative decrease in χ_r^2 of 10^{-3} .

The errors on each model parameter have been obtained following the methods described in Sect. 3.6. The χ_r^2 maps have been computed with a resolution of 21×21 around the best-fit values of the parameters. The map sizes have been adjusted in order to enclose the $\Delta\chi_r^2 = 1$ contour. This adjustment was performed until an upper limit for the map size of 100% of the best-fit parameter values was reached. This amounts to the computation of 3.969×10^4 different models. The results, namely the mean relative error up to 100%, for these two particular models are summarised in Table 3.

The other ten models (numbered from 1 to 10 in Table 4) have been used in order to get some quantitative (but limited) information about how the uncertainties of the fitted parameters

2. Photosphere and circumstellar environment (CSE) of fast rotators

G. Niccolini et al.: Fast ray-tracing algorithm for circumstellar structures (FRACS). I.

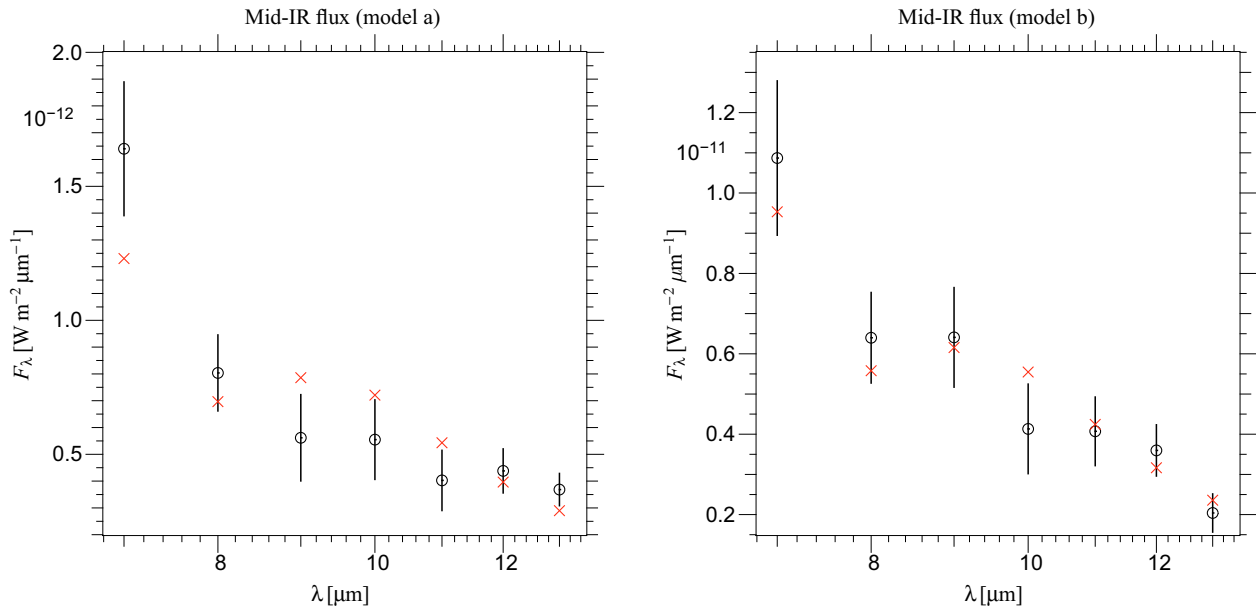


Fig. 3. Simulated VLTI/MIDI mid-IR object flux. The numerically generated data (left model a, right model b) are shown as circles with error bars. The values of the fluxes for the best-fit models are represented as crosses.

evolve as a function of three disc characteristics: its optical depth (τ by means of n_{in} parameter), its inclination (i) and its opening angle ($\Delta\theta_{\text{d}}$, controlled by m). To perform this study we have decided to limit the exploration of the space parameter in a relative range of 25% on both sides from the model parameters. In order to reduce the computation time, the maps were not generated around the best-fit parameters which would have required to compute several thousands models more but around the true parameters themselves. This procedure has the supplementary advantage that we do not rely on any specific minimisation algorithm. We checked that estimating the best-fit parameters from the true ones is reasonable within a few percents using the Levenberg-Marquardt algorithm with a stopping criterion corresponding to a relative decrease in χ_r^2 of 10^{-3} . The resolution of the χ_r^2 maps have been reduced to 15×15 . The total number of models to be computed is as large as 1.0125×10^5 .

5.3. Comparison with a Monte Carlo simulation

We generated synthetic data with the help of a Monte Carlo (MC) radiative transfer code (Niccolini & Alcolea 2006) for model b (see above) for the seven wavelengths considered in the problem and the baselines of Table 1. Again, the adopted procedure to generate the mid-IR interferometric data follows the considerations of Sect. 3.5. In the MC code, the source of photons is described by a blackbody sphere of radius $R_s = 60 R_\odot$ and an effective temperature of $T_{\text{eff}} = 8000$ K. The temperature of the CSE is not prescribed but computed from the Lucy (1999) mean intensity estimator. This choice of T_{eff} gives at the inner radius of model b a dust temperature of ≈ 1150 K lower than the sublimation temperature. In this way, we can test if in the fitting process using FRACS, a spurious effect might not lead the minimisation algorithm to reach the upper limit for T_{in} of 1500 K, corresponding to the adopted dust sublimation temperature.

We obtained the best fitting parameters for the CSE model described in Sect. 4 with FRACS. For a comparison with the MC code, α has been set and fixed to 4 corresponding to the value of

a blackbody. Depending of the disc optical depth, the temperature structure may show two separate regimes corresponding to (1) the inner regions with the strongest temperature gradient, optically thick to the stellar radiation and (2) the outer regions optically thin to the disc radiation with a flatter temperature gradient. In order to determine if mid-IR interferometric data are sensitive to two temperature regimes, we tested the effect of two parameterisations of the temperature structure: the unique power-law of Eq. (35) and a generalisation to two power-laws with a transition radius, R_T , and a second exponent γ'

$$T(r) = T_{\text{in}} \left(\frac{R_{\text{in}}}{R_T} \right)^\gamma \times \left(\frac{R_T}{r} \right)^{\gamma'}, \quad (37)$$

for $r \geq R_T$.

The best-fitting parameters for both parameterisations are shown in Table 5. The images of the disc at $10 \mu\text{m}$ generated with the MC code and their corresponding FRACS counterpart (best-fitting model) are shown in Fig. 6 for comparison.

6. Discussion

We first discuss the uncertainties in the parameters derived for the 12 models studied in Sect. 5.2. For each model we divided the parameters into three groups associated to a given level of constraints expressed by the relative errors: below 10%, between 10% and 25%, and above 25%. This information is summarised in Table 4. The exact relative errors for the two models studied in detail (models a and b) are shown in Table 3. Then, we analyse the results of Sect. 5.3 obtained from the best-fit of the data simulated with the MC radiative transfer code.

6.1. Central source

Table 4 shows that the central source parameters ($J_{\lambda_0}^S$ and α) can only be constrained with relative uncertainties $\geq 10\%$ for all test models. A deeper and more quantitative investigation of

2.5. Numerical models

A&A 525, A21 (2011)

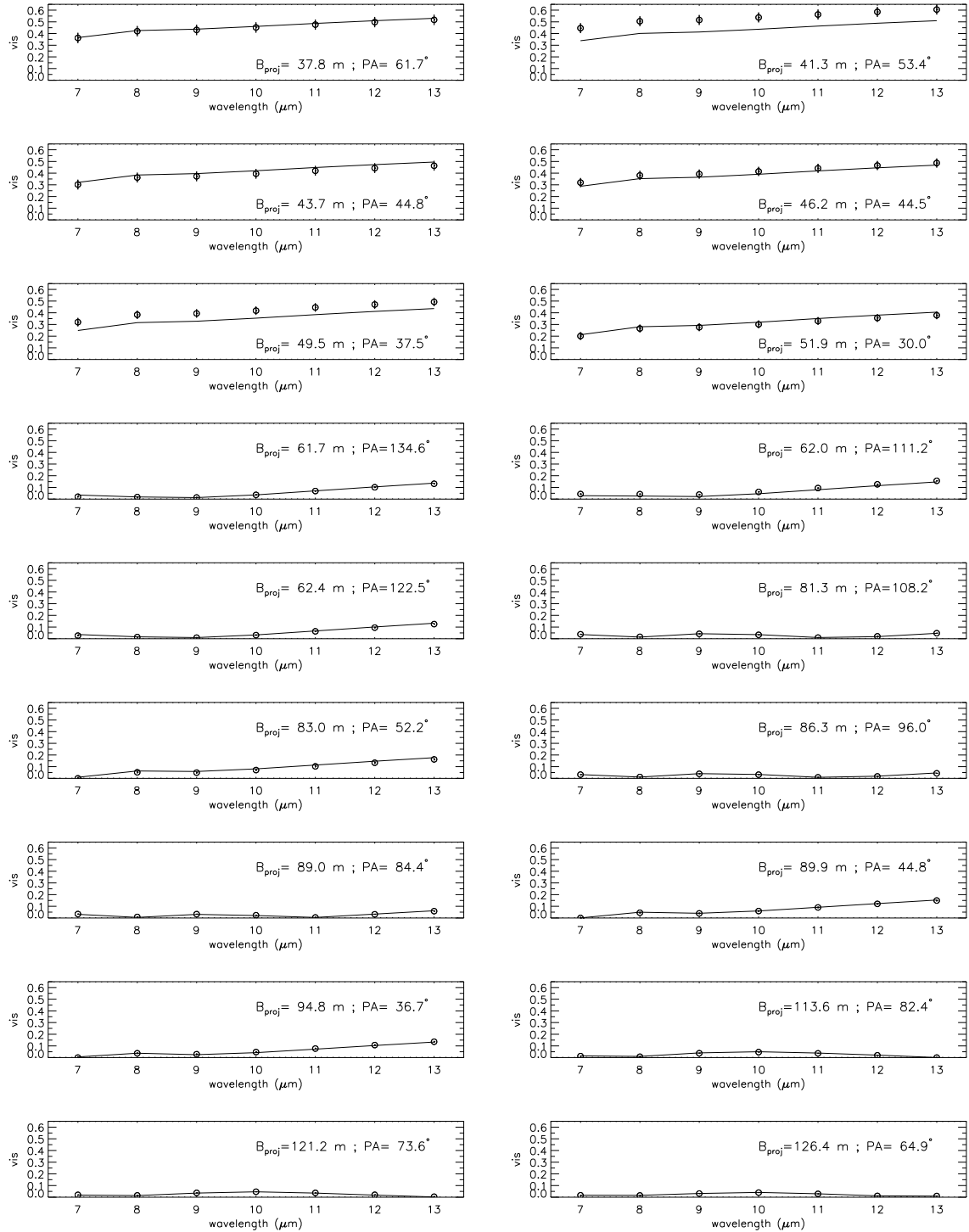


Fig. 4. Visibilities of the artificial sgB[e] circumstellar environment (model a). The visibility variations with the wavelength are shown for each baseline specified by the value of the projected baseline and the position angle on the sky. The circles represent the simulated observations, and the solid curves represent the best-fit model.

these parameters can be obtained from models (a) and (b). From Table 3 it can be seen that $I_{\lambda_0}^s$ and α are much better constrained for model (a) (27% and 13%, resp.) than for model (b) (relative errors $\approx 100\%$).

The key quantity for a good constraint for the central source parameters ($I_{\lambda_0}^s$ and α) is simply the relative contribution of the flux of the central source to the total flux of the object (source and disc). Indeed, the models in Table 3 only differ by this

2. Photosphere and circumstellar environment (CSE) of fast rotators

G. Niccolini et al.: Fast ray-tracing algorithm for circumstellar structures (FRACS). I.

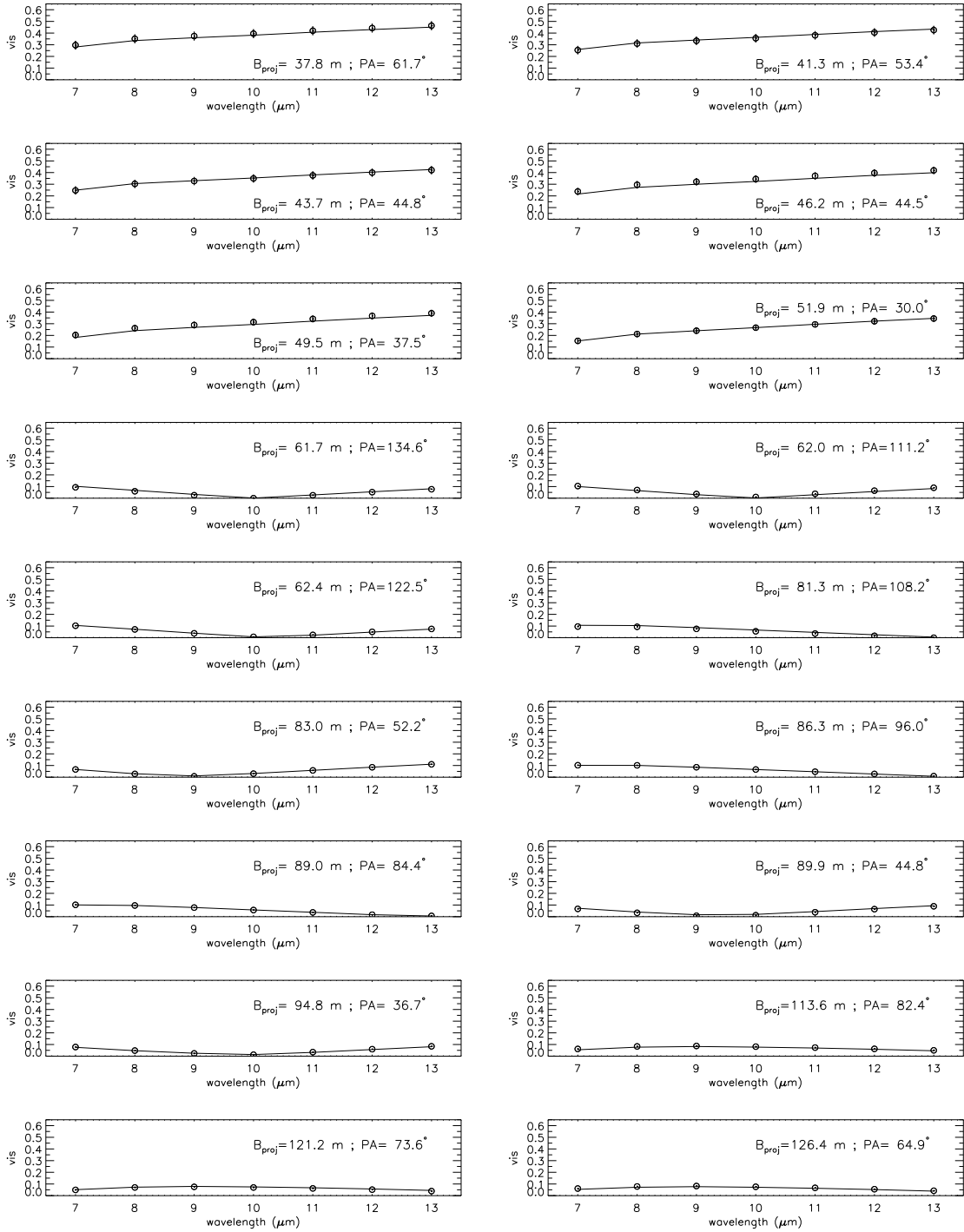


Fig. 5. Visibilities of the artificial sgB[e] circumstellar environment (model b).

relative flux contribution of 5.3% in model (a) ($\tau = 0.1$), while it is only 0.7% in model (b) ($\tau = 1$).

Our analysis thus shows that interferometric data can constrain $I_{\lambda_0}^s$ and α with a relative precision of $\approx 15\text{--}30\%$ even when the central source contributes to (only) a few percent of the total mid-IR flux.

6.2. Geometrical parameters

The parameters PA_d , i , and R_{in} are those usually estimated from simple geometrical models (e.g. ellipses, Gaussians). However, their determination from geometrical models is quite limited, in particular for i , for which only an estimate can be derived from the axis-ratio of an ellipse, for example. In addition, the

2.5. Numerical models

A&A 525, A21 (2011)

Table 5. best-fitting FRACS parameters from artificial data generated with a Monte Carlo code.

Parameters	Units	True values	Two power-law	One power-law
A_2	–	–0.8	–0.791	–0.782
m	–	4.86	5.59	4.74
R_{in}	R_s	30	29.8	29.9
n_{in}	m^{-3}	0.15	0.189	0.169
T_{in}	K	1150 ^(a)	1090	1070
γ/γ'	–	0.725/0.478 ^(a)	0.719/0.613	0.676
R_T	R_{in}	5.24 ^(a)	2.87	–
$I_{\lambda_0}^s$	$\text{W m}^{-2} \mu\text{m}^{-1} \text{str}^{-1}$	6.62×10^3	6.48×10^3	5.04×10^3
PA_d	deg	125	125	124
i	deg	50.0	50.6	50.2

Notes. The column “true values” refers to the MC input parameters, except for T_{in} , γ , and γ' which are determined from the results of the MC simulation. The columns “two power-law” and “one power-law” list the best-fit parameters obtained with FRACS assuming two and one power-law for the temperature respectively. The $\chi^2_{\text{r,min}}$ values are respectively 0.73 and 0.79 for two and one power-law.

^a These values are not prescribed parameters, but are determined from the results of the Monte Carlo simulation. The values reported here are best-fit parameters of the mean disc temperature (see text for more details).

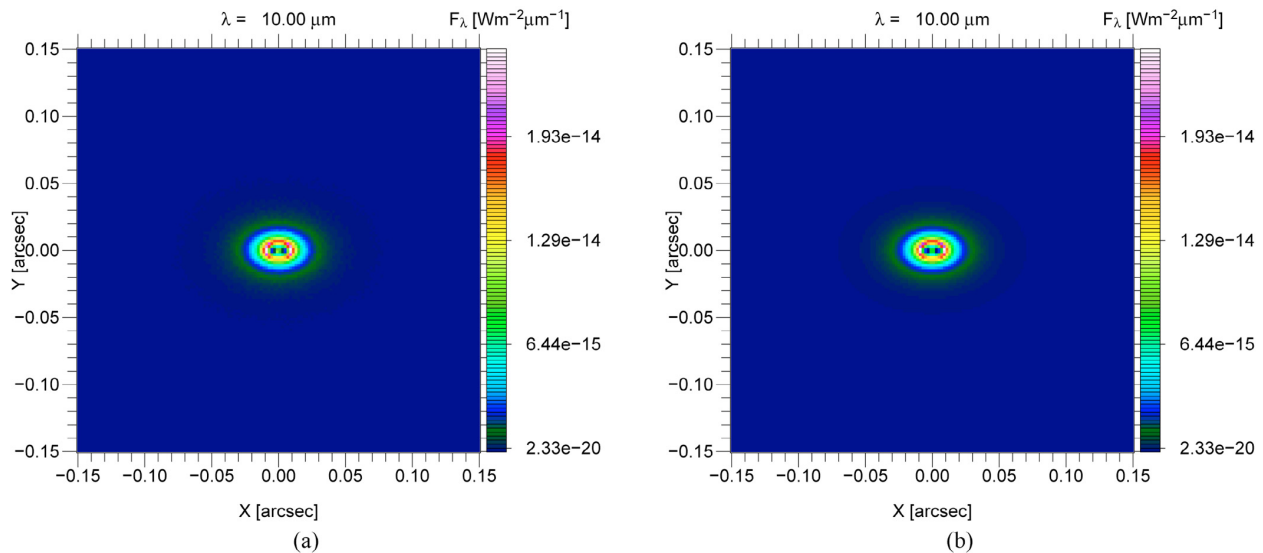


Fig. 6. Disc images at $10 \mu\text{m}$. **a)** Image computed with the help of the Monte Carlo radiative transfer code. **b)** Image of the best-fitting model with two power-laws (parameters of the fourth column in Table 5) obtained with FRACS.

estimate of i from a simple analytical model such as a flat ellipse is only valid for configurations far from the equator (intermediate to low i). The use of a more physical and geometrically consistent model such as FRACS allows us to relax this constraint and makes the determination of i possible for all viewing configurations.

As expected, PA_d and i are better determined if the inclination of the disc with respect to the line of sight is away from pole-on (high i). In Fig. 8 we can clearly see this behaviour from the χ^2_{r} maps involving PA_d and i . Moreover, the uncertainties on PA_d and i do not seem to be strongly dependent on τ (equivalently n_{in}) and $\Delta\theta_d$ (equivalently m) for all models.

The inner dust radius R_{in} is not strongly dependent on any parameter (τ , $\Delta\theta_d$ or i), being very well constrained (better than 10%) for most tested models.

6.3. Temperature

The parameters related to the temperature structure of the CSE, T_{in} and γ , are well constrained in most models, with relative

errors below 20% and 12% for both models (a) and (b). Indeed, γ has a strong impact on the IR emission across the disc, and consequently this parameter has a direct influence on the visibilities (see Figs. 4, 5). T_{in} has a lower influence, compared to γ , on the shape of the monochromatic image (radial dependence of intensity) and can be mainly considered as a scaling factor to it. On the other hand, the mid-IR flux imposes stronger constraints on T_{in} . From Table 4 we see that the CSE’s temperature structure is not highly dependent on τ (n_{in}) and $\Delta\theta_d$ for tested models.

6.4. Number density of dust grains

The parameters related to the density law, that is to say m , n_{in} and A_2 , seems to be rather poorly constrained from the mid-IR data alone. From the results of model (a) and (b) corresponding to an intermediary inclination $i = 50^\circ$, we found that only n_{in} is constrained somewhat moderately with a mean relative error of 46%. For m and A_2 , according to the results of Table 3 it seems that nevertheless, upper limits to their values can be determined. Note that because A_2 is bounded ($-1 \leq A_2 \leq 0$) the mean

2. Photosphere and circumstellar environment (CSE) of fast rotators

G. Niccolini et al.: Fast ray-tracing algorithm for circumstellar structures (FRACS). I.

relative errors, 53% and 59% for model (a) and (b) respectively, correspond approximatively to the limit values of A_2 , which is consequently not constrained.

Table 4 confirms this trend for m , n_{in} and A_2 at least for the situations explored via the models presented here. From all maps computed within $\pm 25\%$ of the true value, we always found that the mean relative error to these parameters is larger than 25% with no hint that it could be close to these limits.

From Fig. 9, comparing the χ_r^2 maps for all pairs of n_{in} , m and A_2 , we can see that the $\Delta\chi_r^2$ contours get sharper around the minimum value for model (a) (corresponding to lower optical depths along the line of sight) than for model (b). Indeed, the constraints on n_{in} and m are improved for lower optical depths, or equivalently for lower disc masses. Indeed, when the disc mass (or optical depth) decreases, the flux (mid-IR flux, intensity maps) emitted by the disc reflects the mass of the disc, while for high optical depths we only probe the regions of the disc very close to the projected surface revealed to the observer. A_2 , however, is unaffected by the change in disc mass and remains undetermined anyway. From Fig. 9 it can be seen that n_{in} , m and A_2 are strongly correlated. This is expected from the expression of the density (see Eq. (32)) depending on these parameters. However, this dependence and the final correlation between these parameters are related through the computation of the visibilities and the mid-IR flux, as well as the comparison to the data and is, therefore, not straightforward.

To improve the situation concerning n_{in} , m and A_2 , the mid-IR data can be supplemented by other types of observations such as for instance spectroscopic data, from which one can better determine A_2 (e.g. see Chesneau et al. 2005). We tested the effect of fixing the value of A_2 , or equivalently of assuming that A_2 is fully determined, in the process of estimating the errors of the other parameters. For model (a), the relative errors on n_{in} and m go down to 33% and 71% respectively while for model (b), n_{in} and m are determined with an accuracy reaching 95% and 78% respectively. The precision to which other parameters are determined is not affected by the determination of A_2 .

We also tested the influence of the determination of n_{in} , m and A_2 on other parameters by fixing their values and estimating the relative errors on the remaining parameters for model (a) and (b). Only $I_{\lambda_0}^s$ and T_{in} are more strongly affected by the determination of n_{in} , m and A_2 : for model (a) (resp. model b) $I_{\lambda_0}^s$ gets determined down to 19% (resp. 80%) and T_{in} down to 9% (resp. 18%). The influence is stronger with lower disc mass (model a compared to model b). This effect can be explained because if we have a good determination of the disc mass because we know n_{in} , m , and A_2 , the determination of the parameters that scale the source and disc fluxes is improved accordingly for the visibility and the mid-IR flux.

n_{in} , m and A_2 shape the density structure of the circumstellar medium. Though they are not well constrained, they certainly have a strong influence on the temperature structure, which in turn is very well constrained. For the particular case of sgB[e] circumstellar discs, a natural evolution of FRACS is to include the direct heating of the medium by the central source of radiation assuming that the disc is optically thin to its own radiation. The temperature structure would not be parameterised, and its good determination would certainly put better constraints on n_{in} , m and A_2 , while keeping an affordable computation time for the model-fitting procedure. This will be the purpose of a subsequent work.

Finally, one can derive a ranking of the parameter constraints according to two criteria: first the parameter must be constrained

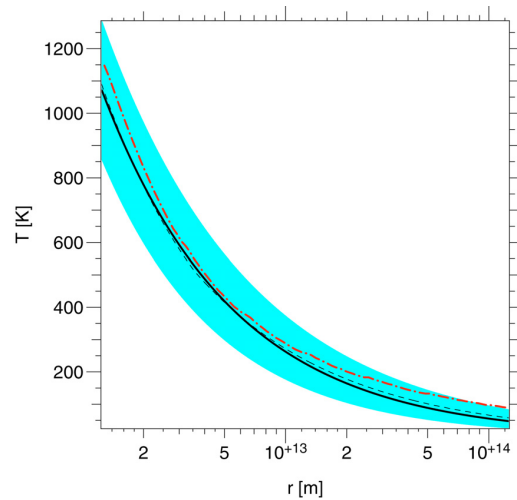


Fig. 7. Temperature of the CSE. The solid line represents the best fit (last column in Table 5) with a unique power-law, the dashed line the best-fit with two power-laws (fourth column in Table 5) and the dot-dashed line the MC results. The shaded region represents the possible domain for a unique power-law by taking into account the errors estimated in Table 3.

within the prescribed limits (100% for model a and b and 25% for model 1 to 10) and second the mean relative error must be as low as possible. The best-fitted parameters, most of the time according to these criteraria are by decreasing order of best determination: R_{in} , PA_d , γ , T_{in} , i , α , $I_{\lambda_0}^s$, n_{in} , m and A_2 . This tendency can be seen in Table 4.

6.5. best-fit to the MC simulation

The $\chi_{r,\text{min}}^2$ values obtained for the two types of temperature parametrisations (one and two power-laws) are quite similar: 0.79 and 0.73 respectively. Regarding the data, both temperature parametrisations are indeed acceptable. In addition, these results show that we can actually obtain very good fits from data sets based on more physically consistent scenarios. A complete error analysis and study of the parameter determination has been presented in the previous sections for data generated from FRACS and will not be repeated here. In particular, parameter confidence intervals, from which errors were derived, have already been estimated. Here, we will instead focus on the *true* errors, i.e. the differences between the true model parameters and the best-fitting values for the parameters (see Table 5). The two types of errors must not be confounded. The *true* errors reflect the capability of FRACS to mimic the mid-IR interferometric data regarding the information it provides. Of course, with the sparse uv-plane coverage inherent to this kind of data as well as the experimental noise, one should not expect a full agreement of the fitted and the true parameters: they are indeed different.

From Table 5, we see that the geometrical parameters, PA_d , i and R_{in} , can be almost exactly recovered as expected. The source specific intensity $I_{\lambda_0}^s$, and the parameters related to the density, A_2 , n_{in} and m can be recovered fairly well and have best-fitting values close to the true parameters.

The values of T_{in} , R_T , γ and γ' reported as “true” in Table 5 are indeed the values of a fit to the average (over the co-latitude for a given r) *computed* temperature in the disc. The true relative differences for T_{in} do not exceed 7% independently of the

2.5. Numerical models

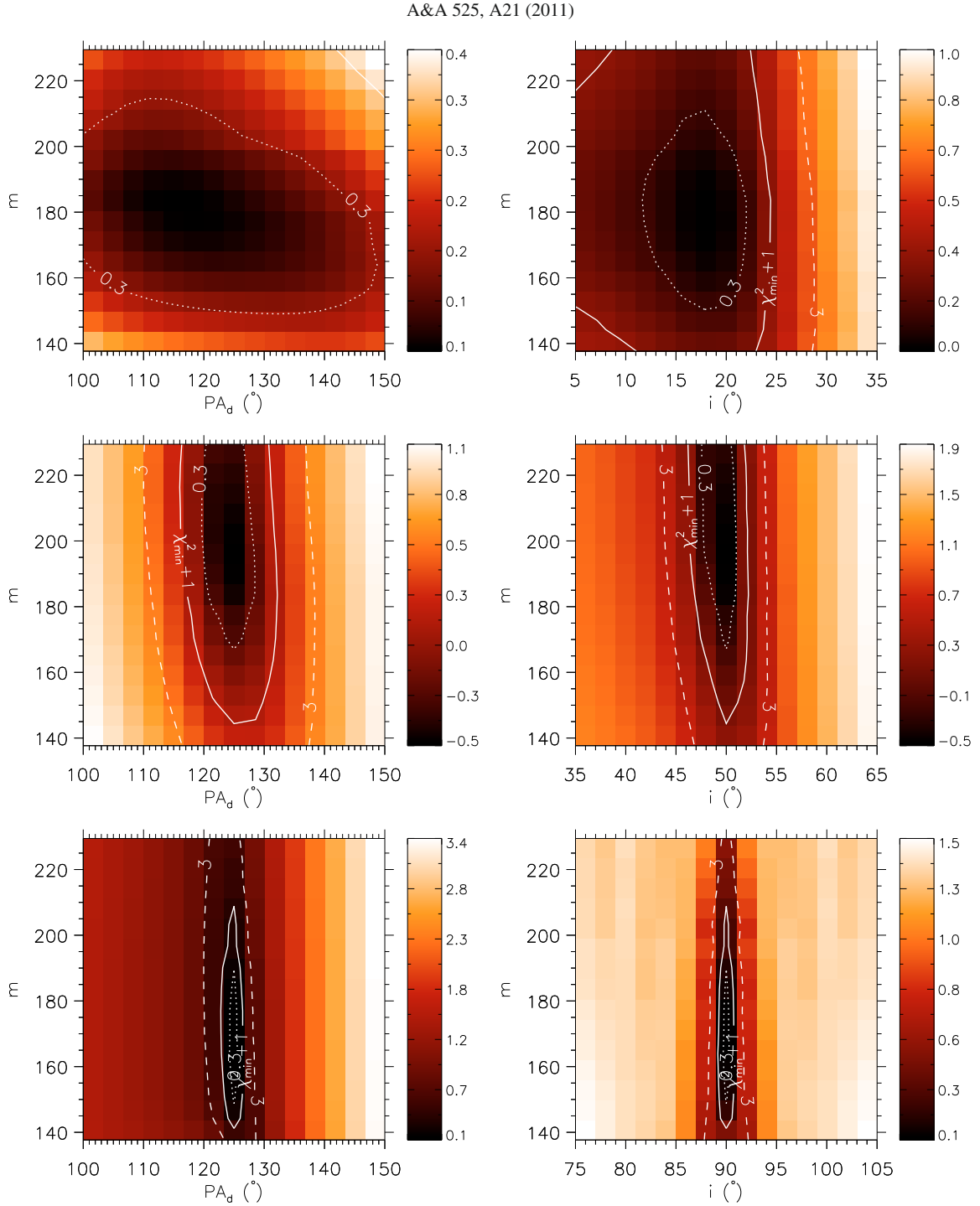


Fig. 8. Evolution of m and PA_d with the inclination i . *Left:* χ_r^2 maps for the couple m and PA_d ; *right:* χ^2 maps for the couple m and i . Contours are drawn for $\chi_{r,\min}^2 + \Delta\chi_r^2$, with $\Delta\chi_r^2 = 0.3, 1, 3$. From top to bottom the inclination i takes the value $20^\circ, 50^\circ$ and 90° . The results correspond to model 4, 6, and 10. The limits of the maps have been set to $\pm 25\%$ of the true values of the parameters.

adopted parameterisation of the temperature (one or two power-laws). The best-fitting values of γ , the inner temperature gradient, obtained with FRACS are very close to the true values with two and one power-law with true relative error of 1% and 7% respectively. This already suggests that the mid-IR data provide information on the inner and *hottest* region of the CSE, in particular on the inner temperature gradient γ .

Fitting the temperature computed with the MC code with a simple power-law, we obtain $\gamma \approx 0.64$. This value is close to those of the best fitting models, especially with a unique power-law (6% relative difference). For comparison, the actual mean temperature gradient as derived from the MC simulation is ≈ 0.60 . For this particular data set, the values of γ' and R_T recovered by FRACS differ by 28% and 45% respectively from

2. Photosphere and circumstellar environment (CSE) of fast rotators

G. Niccolini et al.: Fast ray-tracing algorithm for circumstellar structures (FRACS). I.

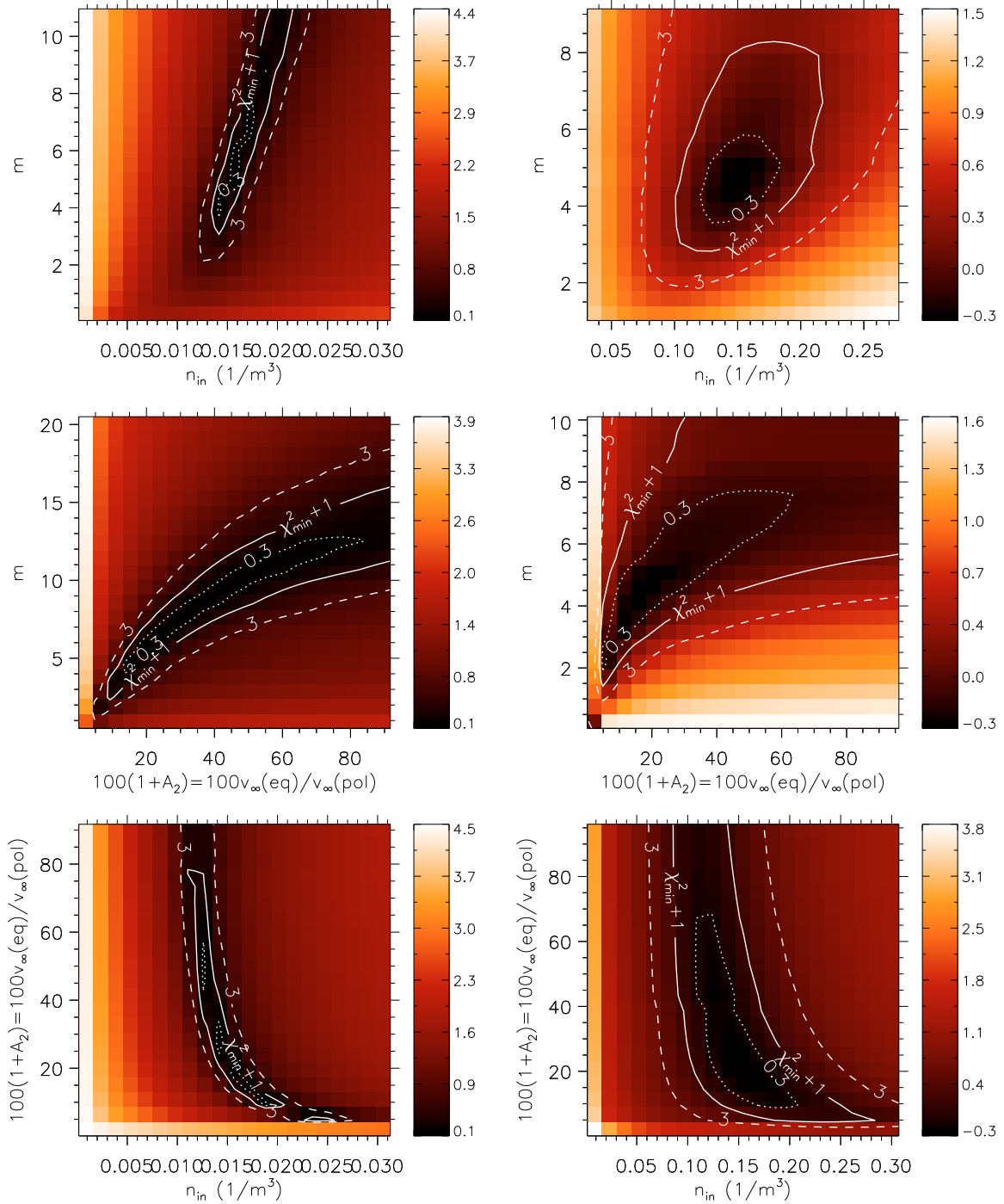


Fig. 9. χ_r^2 maps for the parameters n_{in} , A_2 and m . The results presented here are those of model (a) ($\tau = 0.1$, left part) and model (b) ($\tau = 1$, right part). Contours are drawn for $\chi_{r,min}^2 + \Delta\chi_r^2$, with $\Delta\chi_r^2 = 0.3, 1, 3$. The three possible maps corresponding to the combination of these parameters are represented. These three parameters are better constrained in model (a).

the actual values. This again confirms the sensibility of the interferometric data to the temperature structure mostly in the inner ($r \lesssim R_T$) regions of the disc. The best-fitting models (fourth and last columns in Table 5) as well as the MC results are shown in Fig. 7. Regarding the errors (estimated from the results given in Table 3) shown as a shaded area, we can see that both temperature parameterisations are essentially the same and show a better

agreement with the MC results in the inner than in the outer regions of the disc.

We considered a “truncated” model with two power-laws (with parameter values listed in the third column of Table 5) in which the CSEs emission for $r \geq R_T$, the “outer” regions, has been set to 0. We then compared the visibilities and the fluxes of this truncated model to the same model *including* the outer

2.5. Numerical models

A&A 525, A21 (2011)

region emission. We obtained relative differences, averaged over all considered wavelengths and baselines (Table 1), of 18% and 17% respectively. These relative differences are larger, but are still close to the noise level. For this reason, one cannot expect to obtain much information on the outer temperature gradient γ' , at least for the particular configuration we considered.

7. Conclusion

We proposed and described here a new numerical tool to interpret mid-IR interferometric data. Even though we focussed on the special case of circumstellar disc observations, the numerical techniques have been developed with the aim to be as general as possible. The methods we employ rely on both parameterised physical models and the ray-tracing technique. The need for such a tool is evident because the nature of interferometric data imposes an interpretation through a model of the object to obtain any kind of information. On one hand, Monte-Carlo radiative transfer methods require too much computation time to associate the model-fitting to an automatic minimum search method. On the other hand, purely geometrical function fitting (such as ellipses or Gaussians) are too simple to envisage to obtain physical constraints on the observed disc. Hence, a tool like FRACS fills a blank in the model fitting approach for mid-IR interferometric data interpretation. The main advantages of FRACS are its speed and its flexibility, allowing us to test different physical models. Moreover, an exploration of the parameter space can be performed in different manners and can lead to an estimate of the sensitivity of the fit to the different model parameters, i.e. a realistic error estimate.

We applied these techniques to the special astrophysical case of B[e] star circumstellar environments by generating artificial data in order to analyse beforehand what constraints can be obtained on each parameter of the particular disc model in this work. The techniques will then be applied to real interferometric data of a sgB[e] CSE in a sequel to this paper.

We showed in our analysis that the “geometrical” parameters such as R_{in} , PA_d and i can be determined with an accuracy $\lesssim 15\%$. Mid-IR interferometric data give access to a mean temperature gradient: the temperature structure (T_{in} and γ) can be very well determined (within $\lesssim 20\%$ and $\lesssim 10\%$ respectively). It is possible to have access to the central source emission (with an accuracy $\gtrsim 30\%$) when it has a significant contribution to the total flux of the object (a few % are sufficient). The remaining parameters of our disc model, namely n_{in} , m and A_2 are not very well constrained by MIDI data alone. n_{in} is at best determined with an accuracy of about $\gtrsim 50\%$ in some cases. If A_2 can be estimated through spectroscopic observations, then the picture about the n_{in} and m determination improves somewhat.

FRACS can be used mainly for two purposes. First, it can be used by itself to try and determine physical quantities of the circumstellar matter. Admittedly, it is not a self-consistent model, i.e. the radiative transfer is not solved because the temperature structure is parameterised. From the usual habits in the interpretation of interferometric data it is nevertheless a step beyond the commonly use of toy models or very simple analytical models.

This approach has indeed been very successful in the millimetric wavelength range (e.g. see Guilloteau & Dutrey 1998). Second, it can be viewed as a mean to prepare the work of data fitting with a more elaborate model (such as a Monte Carlo radiative transfer code for instance) and to provide a good starting point.

FRACS is a tool that can help in the process of interpreting and/or preparing observations with second-generation VLTI instruments such as the Multi-AperTure mid-Infrared Spectroscopic Experiment (MATISSE) project (Lopez et al. 2006). In this respect, FRACS is not restricted to the mid-IR, and sub-millimeter interferometric data obtained with the Atacama Large Millimeter Array (ALMA) for instance can be tackled.

Acknowledgements. We thank the anonymous referee for her/his constructive comments that lead to significant improvements of the manuscript. We also would like to thank Alex Carciofi, Olga Suárez Fernández, Andrei and Ivan Belokogne for fruitful discussions and careful proof reading. The Monte Carlo simulations have been carried out on a computer financed by the BQR grant of the Observatoire de la Côte d’Azur. This work is dedicated to Lucien.

References

- Bianchi, S. 2008, A&A, 490, 461
Carciofi, A. C., Miroshnichenko, A. S., & Bjorkman, J. E. 2010, ApJ, 721, 1079
Chesneau, O., Meilland, A., Rivinius, T., et al. 2005, A&A, 435, 275
di Folco, E., Dutrey, A., Chesneau, O., et al. 2009, A&A, 500, 1065
Domiciano de Souza, A., Driebe, T., Chesneau, O., et al. 2007, A&A, 464, 81
Draine, B. T., & Lee, H. M. 1984, ApJ, 285, 89
Feiveson, A. H., & Delaney, F. C. 1968, The distribution and properties of a weighted sum of chi squares, Tech. rep., National Aeronautics and Space Administration
Felli, M., & Panagia, N. 1981, A&A, 102, 424
Guilloteau, S., & Dutrey, A. 1998, A&A, 339, 467
Jonsson, P. 2006, MNRAS, 372, 2
Kurosawa, R., & Hillier, D. J. 2001, A&A, 379, 336
Lachaume, R., Preibisch, T., Driebe, T., & Weigelt, G. 2007, A&A, 469, 587
Lamers, H. J. G. L. M., & Cassinelli, J. P. 1999, Introduction to Stellar Winds, ed. J. P. Lamers, & H. J. G. L. M. Cassinelli
Lamers, H. J. G. L. M., & Waters, L. B. F. M. 1987, A&A, 182, 80
Lamers, H. J. G. L. M., Zickgraf, F., de Winter, D., Houziaux, L., & Zorec, J. 1998, A&A, 340, 117
Leinert, C., Graser, U., Przygodda, F., et al. 2003, Ap&SS, 286, 73
Leinert, C., van Boekel, R., Waters, L. B. F. M., et al. 2004, A&A, 423, 537
Levenberg, K. 1944, The Quarterly of Applied Mathematics, 2, 164
Lopez, B., Wolf, S., Lagarde, S., et al. 2006, in SPIE Conf. Ser., 6268
Lucy, L. B. 1999, A&A, 344, 282
Malbet, F., Lachaume, R., Berger, J., et al. 2005, A&A, 437, 627
Marquardt, D. 1963, SIAM J. Appl. Math., 11, 431
Mathis, J. S., Rumpl, W., & Nordsieck, K. H. 1977, ApJ, 217, 425
Mie, G. 1908, Ann. Phys., 25, 377
Nicolini, G., & Alcolea, J. 2006, A&A, 456, 1
Ohnaka, K., Driebe, T., Hofmann, K., et al. 2006, A&A, 445, 1015
Panagia, N., & Felli, M. 1975, A&A, 39, 1
Porter, J. M. 2003, A&A, 398, 631
Press, W. H., Teukolsky, S. A., Vetterling, W. T., & Flannery, B. P. 1992, Numerical recipes in C. The art of scientific computing (Cambridge: University Press)
Stee, P., de Araujo, F. X., Vakili, F., et al. 1995, A&A, 300, 219
Steinacker, J., Bacmann, A., & Henning, T. 2006, ApJ, 645, 920
Wiscombe, W. J. 1980, Appl. Opt., 19, 1505
Wolf, S., Henning, T., & Stecklum, B. 1999, A&A, 349, 839
Zickgraf, F. 2003, A&A, 408, 257
Zickgraf, F., Wolf, B., Stahl, O., Leitherer, C., & Klare, G. 1985, A&A, 143, 421

2.5.3 HDUST, a Monte Carlo NLTE radiative-transfer code in gas-dust CSE

We shortly describe here the three-dimensional (3-D), non-local thermodynamic equilibrium (NLTE) Monte Carlo radiative transfer code HDUST, developed mainly by A. C. Carciofi, in collaboration with J. E. Bjorkman. The main characteristics (numerical and physical) of HDUST are described in detail by [Carciofi & Bjorkman \(2006\)](#).

HDUST can be used to model the dusty and/or gaseous CSE of young stellar objects (YSO), Be stars, sgB[e] stars, among others. It can provide several observables, both in natural and polarized light, such as, images, spectra, spectral energy distribution, and spectro-interferometric observables. In the following we concentrate in the use of HDUST to model a massive, hot central star with a CSE, in particular, Be and sgB[e] stars. As input, the user thus needs to provide the following information:

- **Central star:** luminosity, effective temperature, radius, rotation velocity. Normally, HDUST considers spherical stars, but we have developed a new version in 2013-2014 that can also consider flattened stars with gravity darkening (cf. Sect. 2.2). For now, the flattened stellar surface is modeled simply with an oblate ellipsoid of revolution where the equatorial-to-polar radii ratio follows Eq. 2.13. Gravity darkening is included either from the generalization of the von Zeipel model or from the ELR model (cf. Sect. 2.2.2). The latitudinal-dependent surface flux is determined, for example, from spectral synthesis codes (e.g. [Synspec](#); [Hubeny & Lanz, 2011](#)) with input stellar atmosphere models from the ATLAS9 code (e.g. [Kurucz, 1979](#)). The implementation of the flattened and gravity-darkened star and comparisons with the CHARRON code were performed in the frame of the double PhD thesis of D. Moser Faes ([Faes, 2015](#)).
- **CSE structure:** HDUST provides predefined CSE structures developed to model Be and sgB[e] stars. The basic equations and main physical parameters of these CSE are detailed in Sects. 2.3 and 2.4.
- **Gas composition** the present version of HDUST only includes hydrogen in the gas component of the CSE, but the new version is expected to include additional chemical elements. This new version is expected to be released in 2017-2018.
- **Dust composition, and spatial and size distributions:** in CSE models containing dust it is necessary to define the kind of dust to be modeled (e.g. amorphous silicate, carbonaceous grains), as well as size distributions (e.g. power law), and grain limiting sizes (minimum and maximum). Normally, the dust density distribution follows the same law as the gas, but with a smaller proportion to be defined by the user (typically $\sim 1\%$). A few pre-defined emission/absorption coefficients can be chosen in the code, but the user can introduce additional ones if necessary. In a physically consistent way, HDUST only allows the dust to exist in regions where the CSE temperature is below the dust sublimation temperature (set by the user).
- **Numerical and output parameters:** number of photons for simulations, numerical grid for the CSE, wavelengths of the output images and spectra, inclination (viewing) angles, among others. All these parameters directly impact on the quality of the final models and on the computation time required to run the code. Because Monte Carlo radiative transfer

requires large amounts of computing time (each photon is treated individually throughout the CSE), it is often necessary to make use of parallel-computing. The HDUST models presented in this work were obtained with the computing facilities (1) of the Mésocentre SIGAMM (hosted by the Observatoire de la Côte d’Azur, France), and (2) of the Laboratory of Astroinformatics LAi (IAG/USP and NAT/Unicsul, Brazil).

Once the input parameters are set, HDUST runs in two main different steps:

1. Iterations on the radiative and statistical equilibrium equations to calculate the atomic level populations, temperatures, and hydrostatic equilibrium density for all grid cells. These calculations include collisional and radiative processes (bound-bound, bound-free, free-free). This step requires several (tens) iterations with $\sim 10^5 - 10^6$ photons for a good convergence of the physical quantities. A final refinement step can be needed. Also, when dust is present, a few additional iterations are required to compute the dust temperature and actual location.
2. Calculations of the emergent spectral flux and images (specific intensity maps) at the required wavelengths. This final step requires a few iterations with $\sim 10^8 - 10^9$ photons for a high signal-to-noise ratio of the final spectra and images.

Examples of HDUST images from sgB[e] models (gas and dust CSE) are given in Fig. 2.14.

CHAPTER 3

HIGH SPECTRO-SPATIAL RESOLUTION OBSERVATIONS OF FAST ROTATORS IN THE H-R DIAGRAM

3.1 The main sequence A-type star Altair (α Aquilae)

Altair (α Aquilae, HD 187642 ; spectral type A7Vn in the [SIMBAD](#) database) is one of the coolest fast-rotating stars among those studied with OLBi techniques. At the same time, because of its high apparent brightness ($V = 0.76$), Altair is probably the most studied fast-rotator, notably from OLBi: [van Belle et al. \(2001\)](#), [Ohishi et al. \(2004\)](#), [Peterson et al. \(2006a\)](#), [Monnier et al. \(2007\)](#).

The results of [Ohishi et al. \(2004\)](#), based on observations from NPOI, suggest a non-uniform surface brightness distribution on Altair, but no physical model was used to constrain Altair's physical parameters from the data. We established a collaboration with the first author in order to interpret their observations with our physical model (CHARRON). In addition, we complemented the NPOI data with additional observations from VLTI/VINCI and PTI, which provided different OLBi observables of Altair, namely, V^2 , triple amplitudes, closure phases.

The results from this work were published on the A&A paper presented hereafter ([Domiciano de Souza et al., 2005](#)). This is one of the first studies of gravity darkening on a single fast-rotating star based on OLBi observations. We investigated two test models corresponding to the theoretical limits for the gravity darkening coefficient β (Eq. 2.30), namely, 0.08 (convective atmospheres) and 0.25 (radiative atmospheres). It is shown in particular that the observations can only be reproduced by the inclusion of gravity darkening, with a significant improvement of the quality of the model fitting. Since this work, where only the classical β values were considered, other results showed different β values exist in fast-rotating stars (cf. Sect. 3.2 for example). This is supported by recent theoretical gravity darkening models (cf. Sect. 2.2.2).

Gravitational-darkening of Altair from interferometry

A. Domiciano de Souza¹, P. Kervella², S. Jankov^{3,4}, F. Vakili³, N. Ohishi⁵, T. E. Nordgren⁶, and L. Abe⁵¹ Max-Planck-Institut für Radioastronomie, Auf dem Hügel 69, 53121 Bonn, Germany
e-mail: adomicia@mpi.fr-bonn.mpg.de² LESIA, UMR 8109, Observatoire de Paris-Meudon, 5 place Jules Janssen, 92195 Meudon Cedex, France³ Lab. Univ. d'Astrophysique de Nice (LUAN), UMR 6525, UNSA, Parc Valrose, 06108 Nice Cedex 02, France⁴ Astronomical Observatory Belgrade, MNTRS 1940, Volgina 7, 11050 Beograd, Serbia and Montenegro⁵ National Astronomical Observatory of Japan, 2-21-1 Osawa, Mitaka, Tokyo 181-8588, Japan⁶ Department of Physics, University of Redlands, 1200 East Colton Avenue, Redlands, CA 92373, USA

Received 3 December 2004 / Accepted 13 June 2005

ABSTRACT

Interferometric observations have revealed that the rapid rotator Altair is a flattened star with a non-centrally symmetric intensity distribution. In this work we perform for the first time a physically consistent analysis of all interferometric data available so far, corresponding to three different interferometers operating in several spectral bands. These observations include new data (squared visibilities in the H and K bands from VLTI-VINCI) as well as previously published data (squared visibilities in the K band from PTI and squared visibilities, triple amplitudes, and closure phases in the visible between 520 nm and 850 nm from NPOI). To analyze these data we perform a χ^2 minimization using an interferometry-oriented model for fast rotators, which includes Roche approximation, limb-darkening, and von Zeipel-like gravity-darkening. Thanks to the rich interferometric data set available and to this physical model, the main uniqueness problems were avoided. As a result, we show that the observations can only be explained if Altair has a gravity-darkening compatible with the expected value for hot stars, i.e., the von Zeipel effect ($T_{\text{eff}} \propto g^{0.25}$).

Key words. techniques: high angular resolution – techniques: interferometric – methods: data analysis – stars: rotation – stars: individual: Altair

1. Introduction

Altair (α Aql, HR 7557, HD 187642) is a bright ($V = 0.77$), rapidly rotating A7IV-V star, which has been studied by many authors. For example, Buzasi et al. (2005) recently detected several oscillating frequencies in Altair and proved that this star is a variable of the δ Scuti type, as expected by its location within the instability strip. Several basic physical parameters of Altair are summarized by Buzasi et al. (2005) in their introduction. One important characteristic of Altair is its fast rotation. Spectroscopic and interferometric observations indicate a $v_{\text{eq}} \sin i$ value between 190 km s^{-1} and 250 km s^{-1} (Abt & Morrell 1995; van Belle et al. 2001; Royer et al. 2002; among others); most recently Reiners & Royer (2004) determined $v_{\text{eq}} \sin i = 227 \pm 11 \text{ km s}^{-1}$ from spectroscopy.

Theories foresee that such a high rotation velocity can lead to many modifications in the physical structure of a star like Altair. In particular, the star is expected (1) to be oblate because of a strong centrifugal force and (2) to exhibit gravity-darkening (after the seminal work of von Zeipel 1924). These theoretically expected modifications are now measured by modern observing techniques, notably those based on long baseline interferometry. See, for example,

Domiciano de Souza et al. (2003) for the case of another rapidly rotating star (Achernar).

For Altair, van Belle et al. (2001) measured the rotational flattening projected onto the sky-plane using the Palomar Testbed Interferometer (PTI, Colavita et al. 1999). By adopting an equivalent limb-darkened ellipse model these authors derived major and minor axes of $2a = 3.461 \pm 0.038 \text{ mas}$ and $2b = 3.037 \pm 0.069 \text{ mas}$, respectively, which means an axial ratio of $a/b = 1.140 \pm 0.029$. van Belle et al. (2001) used a Roche model (solid body rotation and mass M concentrated in a point at the center of the star) without gravity-darkening to analyze their observations of Altair. However, even with this relatively simplified model their analysis encountered several uniqueness problems caused by the limited coverage of spatial frequencies (observations inside the first visibility lobe only) and spectral information (only one broadband near-IR filter used). The important issue of uniqueness problems in interferometric studies of rapidly rotating stars is discussed by Domiciano de Souza et al. (2002).

More recently, Ohishi et al. (2004) used the Navy Prototype Optical Interferometer (NPOI, Armstrong et al. 1998) to observe Altair. In particular, they obtained closure phases and

squared visibilities around the first minimum. These observations suggest that Altair is not only oblate but also that it is a gravity-darkened star with a non-centrally symmetric intensity distribution. The nature of these data largely diminishes the uniqueness problems associated with the analysis of rapid rotators.

Even though the observations indicate that Altair is an oblate and gravity-darkened star, previous works did not adopt physically consistent models including these two effects. In the present work we use our interferometry-oriented model for fast rotators (Domiciano de Souza et al. 2002) to perform a χ^2 minimization including all interferometric data available up-to-date: new squared visibilities in the H and K bands from the Very Large Telescope Interferometer (VLTI, e.g., Glindemann et al. 2003); (2) squared visibilities in the K band from PTI; and (3) squared visibilities, triple amplitudes, and closure phases in the visible from NPOI.

In Sect. 2 we summarize the observations used here, and in Sect. 3 we describe the adopted model, which includes Roche approximation, a limb-darkening law compatible with Altair's effective temperature distribution, and a von Zeipel-like gravity-darkening law. In Sect. 4 we present the main results of our χ^2 analysis of the interferometric data. A critical discussion of our results is given in Sect. 5, while the conclusions of this work are summarized in Sect. 6.

2. Interferometric observations

The first attempt to measure the geometrical deformation of Altair was carried out with the Narrabri intensity interferometer (Hanbury Brown 1974). However, these observations remained too marginal to allow unambiguous conclusions to be drawn by the Australian group. Recent observations by at least three modern interferometers have resulted in several high-quality measurements becoming available. In the following section we briefly describe the three interferometric data sets (one new and two previously published and analyzed) used in this work to constrain a number of unknown physical parameters of Altair.

2.1. VLTI-VINCI near-IR observations

We first describe the new near-IR observations of Altair performed with the VLTI. These new data were obtained with two test siderostats (0.35 m aperture) and the VINCI¹ instrument (Kervella et al. 2000 and Kervella et al. 2003a). The visibility measurements were all recorded on the E0-G1 baseline of the VLTI (ground length of 66 m). We combined the stellar light using a classical fiber-based triple coupler (MONA) for the K band observations, and an integrated optics beam combiner (IONIC, Lebouquin et al. 2004) in the H band. Standard K ($2.0 < \lambda < 2.4 \mu\text{m}$) and H ($1.5 < \lambda < 1.8 \mu\text{m}$) band filters were used for these observations. The effective wavelength of the observations changes slightly depending on the spectral type of the observed target. For Altair, we determined $\lambda_{\text{eff}} = 2.176 \pm 0.003 \mu\text{m}$ and $\lambda_{\text{eff}} = 1.633 \pm 0.003 \mu\text{m}$, respectively in the K and H bands.

¹ V(LT) I(Nterferometer) C(ommissioning) I(nstrument).

The raw data processing has been achieved using a wavelet-based algorithm, integrated in an automated data reduction pipeline (Kervella et al. 2004a). The general principle is similar to the original FLUOR algorithm (Coudé du Foresto et al. 1997), but instead of the classical Fourier analysis, we implemented a wavelet-based time-frequency analysis (Ségransan et al. 1999). The two calibrated output interferograms are subtracted to correct for residual photometric fluctuations. The output of the pipeline is a single value of the squared coherence factor μ^2 for each series of 500 interferograms and the associated bootstrapped error bar. We obtained a total of 5500 interferograms of Altair in the K band and 4500 in the H band, among which 2749 and 1949 were reduced by the pipeline, respectively. All the VINCI data were obtained between July and September 2002. The final normalized squared visibilities V^2 and other observational information are given in Table 1.

We used three stars as calibrators for the K band observations (24 Cap, χ Phe, and 70 Aql) and one for the H band (α Ind). These stars were selected from Cohen et al. (1999) for their stability, and we took their sizes from the Bordé et al. (2002) catalogue. To obtain their equivalent uniform-disk diameters, we applied the broadband limb-darkening corrections provided by Claret (2000a), based on the ATLAS models (Kurucz 1992). In absence of data in the literature, the metallicity of the calibration stars was taken as solar. Note, however, that in the H and K bands the influence of metallicity on the limb-darkening is very weak. The relevant properties of the calibrators used for VINCI observations are listed in Table 2.

The choice of the calibrators is an important step for preparing interferometric observations, since significant departures of their actual visibilities from the expected model can propagate into biases on the calibrated visibilities of the scientific target. Among the possible reasons for such departures, binarity (or multiplicity in general) and deviations from spherical symmetry (due, for instance, to fast rotation or gravitational interaction) are the most critical. All stars in the Cohen et al. (1999) catalogue were carefully scrutinized by these authors for the presence of companions and are currently regarded as single stars. With respect to fast rotation, the value of $v_{\text{eq}} \sin i$ is only available for one star, 70 Aql, which is also the most sensitive star to potential deformations as it is a bright giant. With $v_{\text{eq}} \sin i = 1.9 \text{ km s}^{-1}$, $\log g \approx 1.9$, and a radius of $\approx 200 R_{\odot}$, a first order approximation of its flattening ratio (Roche model) is given by the following relation (e.g. Domiciano de Souza et al. 2002):

$$\frac{R_{\text{eq}}}{R_{\text{p}}} = 1 + \frac{v_{\text{eq}}^2 R_{\text{eq}}}{2GM} < 1 + 10^{-4}. \quad (1)$$

The effect of the rotation on the shape of this star is therefore taken as negligible. Measurements of the projected rotational velocities are not available for the other calibrators of our sample, but as they are giant stars, we assume that they are small enough so that their rotational deformation can be neglected. Our four calibrators are significantly resolved by the interferometer, but the a priori uncertainty on their angular diameters was carefully propagated to the final error bars on the calibrated squared visibilities of Altair. The errors in the calibrated V^2

3. High spectro-spatial resolution observations of fast rotators in the H-R diagram

Table 1. VLTI-VINCI observations of Altair performed in the H and K bands.

H band								
Date (JD)	Projected Baseline (m)	Position Angle ^a (deg)	Calib. V^2	Stat. V^2 error	Syst. V^2 error	Total V^2 error	Uniform disc diameter (mas)	Calibrator
2 452 477.655	62.110	139.77	0.388	± 0.022	± 0.008	± 0.023	3.22 ± 0.09	α Ind
2 452 477.659	61.702	139.97	0.403	± 0.023	± 0.009	± 0.024	3.18 ± 0.10	α Ind
2 452 479.561	65.950	140.66	0.336	± 0.023	± 0.006	± 0.023	3.23 ± 0.09	α Ind
2 452 479.706	55.760	144.48	0.464	± 0.027	± 0.009	± 0.028	3.26 ± 0.12	α Ind
2 452 482.726	52.131	148.77	0.510	± 0.052	± 0.012	± 0.054	3.28 ± 0.24	α Ind
2 452 483.645	61.490	140.08	0.401	± 0.024	± 0.006	± 0.024	3.20 ± 0.10	α Ind
2 452 484.699	54.905	145.37	0.539	± 0.042	± 0.010	± 0.043	2.99 ± 0.18	α Ind
2 452 485.594	64.851	139.08	0.371	± 0.032	± 0.008	± 0.033	3.15 ± 0.13	α Ind
2 452 485.598	64.627	139.07	0.358	± 0.032	± 0.008	± 0.033	3.21 ± 0.13	α Ind
K band								
Date (JD)	Projected Baseline (m)	Position Angle (deg)	Calib. V^2	Stat. V^2 error	Syst. V^2 error	Total V^2 error	Uniform disc diameter (mas)	Calibrator
2 452 469.722	57.285	143.05	0.656	± 0.017	± 0.016	± 0.023	3.18 ± 0.13	24 Cap
2 452 469.755	53.065	147.53	0.685	± 0.015	± 0.017	± 0.023	3.26 ± 0.14	24 Cap
2 452 469.763	51.957	149.02	0.696	± 0.017	± 0.017	± 0.024	3.26 ± 0.15	24 Cap
2 452 531.587	52.790	147.89	0.645	± 0.072	± 0.007	± 0.072	3.52 ± 0.44	χ Phe
2 452 531.592	52.204	148.67	0.632	± 0.076	± 0.007	± 0.076	3.64 ± 0.47	χ Phe
2 452 531.596	51.624	149.49	0.663	± 0.076	± 0.007	± 0.076	3.49 ± 0.48	χ Phe
2 452 536.511	60.454	140.68	0.605	± 0.028	± 0.008	± 0.029	3.28 ± 0.15	70 Aql
2 452 536.543	56.759	143.52	0.636	± 0.031	± 0.008	± 0.032	3.32 ± 0.18	70 Aql
2 452 536.547	56.226	144.03	0.701	± 0.033	± 0.008	± 0.034	2.98 ± 0.20	70 Aql
2 452 536.578	52.212	148.66	0.713	± 0.049	± 0.009	± 0.050	3.14 ± 0.33	70 Aql
2 452 536.582	51.738	149.33	0.643	± 0.043	± 0.008	± 0.043	3.60 ± 0.27	70 Aql

^a 0° is North and 90° is East.

Table 2. Relevant parameters of the calibrators used for VINCI observations of Altair.

Name	24 Cap	χ Phe	70 Aql	α Ind
HD number	HD 200914	HD 12524	HD 196321	HD 196171
m_V	4.5	5.2	4.9	3.1
m_K	0.5	1.3	1.2	0.9
Sp. type	M0.5III	K5III	K5II	K0III
T_{eff} (K) ^a	3630	3780	3780	4720
$\log g^a$	1.4	1.9	1.9	2.6
[Fe/H] ^c	–	–	–	0.0
$v_{\text{eq}} \sin i$ (km s ⁻¹) ^d	–	–	1.9	–
\varnothing_{LD} (mas) ^a	4.43 ± 0.05	2.77 ± 0.03	3.27 ± 0.04	3.28 ± 0.03
\varnothing_{UD} (mas) ^b	4.30 ± 0.05	2.69 ± 0.03	3.17 ± 0.04	3.20 ± 0.03

^a From Cohen et al. (1999).

^b Limb-darkened disc diameters \varnothing_{LD} converted to uniform disc diameters \varnothing_{UD} using the linear limb-darkening coefficients from Claret (2000a).

^c From Cayrel de Strobel et al. (1997, 2001).

^d From Glebocki et al. (2000).

(statistical, systematic, and total) are also listed in Table 1. The uncertainties in V^2 are dominated by the statistical errors.

27 measurements of V^2 on Altair performed in the K band for two distinct baselines (ground lengths of 85 m and 110 m).

2.2. PTI near-IR observations

Another data set used in this paper was obtained with PTI and was previously reported and analyzed by van Belle et al. (2001, hereafter vB2001). This data set corresponds to

2.3. NPOI visible observations

The third data set used in this work, which was previously reported and analyzed by Ohishi et al. (2004, hereafter ONH2004), corresponds to interferometric observations in the

visible obtained with NPOI. These observations of Altair were recorded simultaneously using three baselines forming a triangle (ground lengths of 30, 37, and 64 m), allowing measurements of V^2 , triple amplitudes, and closure phases. In this work we use the NPOI observations of Altair performed on May 25 2001 (see Table 2 of ONH2004), which consist of 7 scans (Hummel et al. 1998). We use 18 spectral channels covering wavelengths from 520 to 850 nm; the data for $\lambda = 633$ nm are not used because they contain light from the metrology laser, and the data for $\lambda = 618$ nm are not used because they are not available for all NPOI observables.

3. Modeling Altair

3.1. Model of a rotating star

Since previous interferometric observations (vB2001 and ONH2004) indicate that Altair's flattening is compatible with uniform rotation, in this paper we adopt the classical Roche model. This model is described in more detail, for example, by Domiciano de Souza et al. (2002), who developed an interferometry-oriented model for rapid rotators. Once the surface equipotential (Ψ) and the corresponding local effective surface gravity ($g(\theta) = |\nabla\Psi|$, where θ is the colatitude) in the Roche approximation are defined, the local effective temperature is given by the following von Zeipel-like gravity-darkening law (e.g. Collins 1965):

$$T_{\text{eff}}(\theta) = T_p \left(\frac{g(\theta)}{g_p} \right)^\beta \quad (2)$$

where T_p and g_p are the polar effective temperature and gravity, respectively. In this paper we adopt two theoretical limits for the gravity-darkening coefficient β , namely, $\beta = 0.25$ for hot stars with radiative external layers (von Zeipel 1924) and $\beta = 0.08$ for cold stars with convective external layers (Lucy 1967).

To compute our models of Altair the code BRUCE (Townsend 1997) is used to obtain a stellar grid ($\approx 25\,500$ visible points) for the local values of effective temperature and gravity, velocity field, projected surface, and surface normal direction.

3.2. Intensity maps

Because of the geometrical deformation and gravity-darkening, the intensity maps are highly dependent on the inclination of the rotation axis i (Domiciano de Souza et al. 2002). In order to evaluate the intensity maps for Altair we first used Kurucz (1992) model atmospheres² as input for the SYNPEC code (Hubeny 1988 and Hubeny & Lanz 1995) to generate a grid of synthetic specific intensities normal to the surface ($I(\mu = 1, \lambda)$, where μ and λ have their usual meanings). This grid corresponds to different values of T_{eff} and $\log g$ in steps of 250 K and 0.5 dex, respectively. To be consistent with recent spectroscopic observations the grids of $I(\mu = 1, \lambda)$ were calculated for microturbulent velocity $v_{\text{micro}} = 2 \text{ km s}^{-1}$ and solar abundance,

² From Dr. R. L. Kurucz model atmospheres and references publicly available at <http://kurucz.harvard.edu/grids/>

except for 14 elements between C and Cu (Erspamer & North 2002, 2003).

Since interferometric observations of Altair were performed within wide spectral bands, we integrated $I(1, \lambda)$ over the corresponding spectral channel/band to obtain a grid of integrated intensities normal to the surface $I(1)$. Before performing this integration we multiply $I(1, \lambda)$ by the atmospheric and instrumental transmissions. Because the computation of $I(1)$ influences the calculations of interferometric observables, we present further details of this integration procedure in Sect. 3.3.

Once $I(1)$ is defined, we can obtain the intensity at every μ ($I(\mu)$) through an appropriate limb-darkening law. Accurate modeling of limb-darkening is crucial to determine precise stellar diameters, in particular for rapidly rotating stars where we expect a non-uniform surface brightness distribution. To model Altair we adopted the four-parameter non-linear limb-darkening law proposed by Claret (2000a,b):

$$\frac{I(\mu)}{I(1)} = 1 - a_1(1 - \mu^{\frac{1}{2}}) - a_2(1 - \mu) - a_3(1 - \mu^{\frac{3}{2}}) - a_4(1 - \mu^2) \quad (3)$$

where tabulated values of a_1 , a_2 , a_3 , and a_4 are given by Claret for 12 commonly used photometric bands. For Altair we used those for the H and K bands to simulate PTI and VLTI-VINCI observations and those for the V (for $\lambda \leq 600$ nm) and R (for $\lambda > 600$ nm) bands to simulate NPOI observations.

Claret (2000a,b) argues that Eq. (3) is valid across the whole HR diagram, which is, in fact, an important requirement for a consistent modeling of Altair since this star could present an effective temperature distribution in the transition range between hot (radiative envelope) and cold (convective envelope) stars (e.g., Panzera et al. 1999).

Finally, we can now define the intensity maps $I(\mathbf{r})$, i.e., the visible stellar surface brightness distribution on the two-dimensional sky-plane at a position \mathbf{r} . To obtain $I(\mathbf{r})$ we thus perform a linear interpolation of the predefined grids of integrated intensities $I(1)$ and the limb-darkening coefficients a_1 , a_2 , a_3 , and a_4 , for each visible point of the stellar grid.

3.3. Complex visibilities

Once the intensity map is defined, the computation of complex visibilities is straightforward. Normalized complex visibilities $V(\mathbf{f})$ are obtained by the numerical counterpart of the following equation (for further details see Domiciano de Souza et al. 2002):

$$V(\mathbf{f}) = |V(\mathbf{f})| e^{i\phi(\mathbf{f})} = \frac{\tilde{I}(\mathbf{f})}{\tilde{I}(\mathbf{0})} \quad (4)$$

where $|V|$ and ϕ are the visibility amplitude and phase, $\tilde{I}(\mathbf{f})$ is the Fourier transform of the intensity map $I(\mathbf{r})$, and \mathbf{f} is the spatial frequency coordinate associated with \mathbf{r} . From Eq. (4) we can directly obtain the interferometric observables: squared visibilities V^2 , triple amplitudes $|V_1||V_2||V_3|$, and closure phases $\phi_1 + \phi_2 + \phi_3$. These observables are functions of the spatial frequency \mathbf{f} , and the indices 1, 2, and 3 denote the three interferometric baselines in a triangular configuration.

For each pair of telescopes, \mathbf{f} is given by the ratio between the vector baseline projected onto the sky \mathbf{B}_{proj} and the

effective wavelength λ_{eff} of the considered spectral channel: $f = \mathbf{B}_{\text{proj}}/\lambda_{\text{eff}}$. This dependence of the spatial frequency on λ_{eff} is responsible for an observational effect known as *bandwidth smearing* (e.g., Kervella et al. 2003b; and Wittkowski et al. 2004). Indeed, the wide spectral coverage in the H ($\approx 0.3 \mu\text{m}$) and K ($\approx 0.4 \mu\text{m}$) bands implies that several spatial frequencies are simultaneously observed by the interferometer (VLTI-VINCI and PTI in our case).

To account for the bandwidth smearing in the near-IR we divided the H and K bands into $N = 20$ spectral sub-channels and computed the stellar intensity distributions I_j integrated over each spectral sub-channel j . The corresponding Fourier transforms \tilde{I}_j are then calculated, and the final normalized squared visibilities in the H and K bands are given by:

$$V_{\text{IR band}}^2 = \frac{\sum_{j=1}^N |\tilde{I}_j(\mathbf{B}_{\text{proj}}/\lambda_{\text{eff},j})|^2}{\sum_{j=1}^N |\tilde{I}_j(\mathbf{0})|^2}. \quad (5)$$

The bandwidth smearing is negligible for the relatively narrow spectral channels of the NPOI observations.

4. Results from the χ^2 analysis

In this section we perform a χ^2 analysis to constrain a number of unknown physical parameters in our model for Altair from the available interferometric observations.

We investigate two test models corresponding to the theoretical limits for the gravity-darkening parameter β , namely, 0.08 (convective atmospheres) and 0.25 (radiative atmospheres). To obtain a mean effective temperature compatible with previous works (between ≈ 7500 K and ≈ 8000 K; see for example Espamer & North 2003, vB2001; and Ferrero et al. 1995) the adopted polar temperatures T_p for the test models are 8000 K and 8500 K, corresponding to $\beta = 0.08$ and 0.25, respectively. The chosen stellar mass $M = 1.8 M_{\odot}$ is given by Malagnini & Morossi (1990). Other slightly different mass estimates exist since determining the mass of a single star, particularly a rapid rotator, is not a simple task, but the main results of this work do not critically depend on this value. We adopted the projected equatorial velocity $v_{\text{eq}} \sin i = 227 \text{ km s}^{-1}$ determined by Reiners & Royer (2004) from high spectral resolution observations. Their value is compatible with other recent measurements of $v_{\text{eq}} \sin i$ within their error bars (e.g. vB2001; and Royer et al. 2002).

In addition to the fixed physical parameters described above, the equatorial radius R_{eq} (or the polar one R_p) is also needed to calculate the models of Altair. However, R_{eq} is related to the equatorial angular diameter \varnothing_{eq} by means of the stellar distance ($d = R_{\text{eq}}/\varnothing_{\text{eq}} = 5.143 \pm 0.025$ pc from Hipparcos; Perryman et al. 1997). Since \varnothing_{eq} is one important output from our interferometric data analysis, R_{eq} has to be updated accordingly to each \varnothing_{eq} value tested during the χ^2 minimization procedure. To avoid calculating a large number of models we performed a preliminary χ^2 minimization using a fixed R_{eq} in order to constraint the range of \varnothing_{eq} close to the

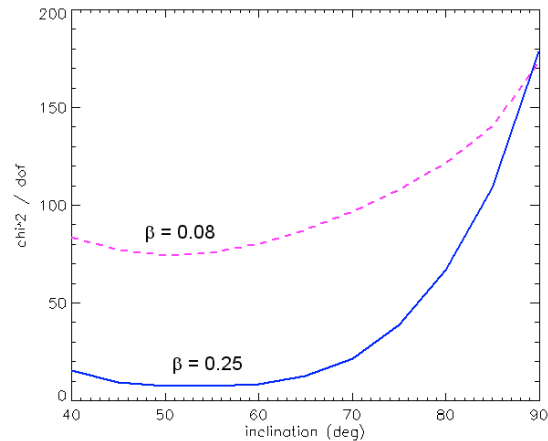


Fig. 1. Reduced χ^2 ($\chi^2/\text{d.o.f.}$) as a function of the stellar inclination i computed from all interferometric observations described in Sect. 2 for the two test models (radiative and convective limits for the gravity-darkening). These values correspond to the best equatorial angular diameter \varnothing_{eq} and major axis orientation η for a given i . Models with $\beta = 0.25$ (solid curve) are preferred compared to models with $\beta = 0.08$ (dashed curve). The minimum $\chi^2/\text{d.o.f.}$ ($\chi_{\text{min}}^2/\text{d.o.f.} = 7.3$) is obtained for $\beta = 0.25$ and $i = 55^\circ$. Further physical parameters for this best model from all data (BMAD) and the corresponding error bars are given in Table 3, together with the results of other χ^2 analyses.

minimum χ^2 . In the final χ^2 analysis, \varnothing_{eq} (and the corresponding R_{eq}) varies with steps of 0.01 mas within a range corresponding to the uncertainty in \varnothing_{eq} . Since this uncertainty is rather small ($\leq 2\%$), R_{eq} could be kept constant without introducing any significant changes in our modeling and results.

Additionally, the major axis orientation (position angle) on the sky-plane η is allowed to vary in steps of 3° . The inclination of the rotation axis i can vary between 40° and 90° (steps of 5°). For $i < 40^\circ$ the equatorial rotation velocity becomes higher than 90% of the critical limit (v_{crit}) leading to unrealistically low equatorial temperatures as a consequence of the von Zeipel effect.

We thus have two test models (corresponding to $\beta = 0.08$ and $\beta = 0.25$) with three free parameters (i , \varnothing_{eq} , and η) for our χ^2 analysis whose results are presented below.

4.1. Analysis of all data

We present the results of our χ^2 analysis applied to all available interferometric data on Altair (cf. Sect. 2). This consists of 47 near-IR V^2 observations (VLTI-VINCI and PTI) together with 630 visible observations (NPOI). Figure 1 shows the reduced χ^2 ($\chi^2/\text{d.o.f.}$, where the degree of freedom (d.o.f.) is 674) as a function of the inclination i computed from all interferometric observations for the two test models. The values in Fig. 1 correspond to the best \varnothing_{eq} and η for a given i .

An important result seen in Fig. 1 is that all models with a gravity-darkening coefficient for hot stars ($\beta = 0.25$) are preferred, i.e., have lower χ^2 in comparison to models with a gravity-darkening coefficient for cold stars ($\beta = 0.08$). This is model-dependent but still the first direct determination of the gravity-darkening coefficient for a rapid rotator, obtained

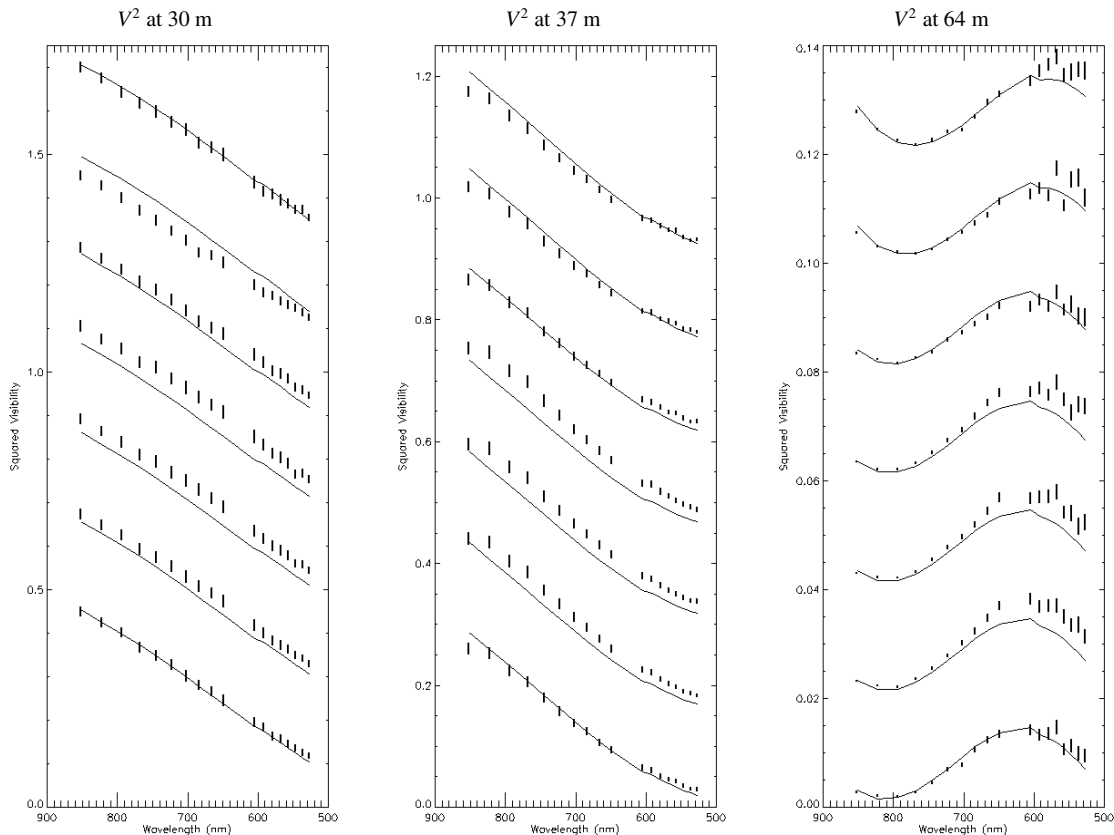


Fig. 2. Squared visibilities V^2 and corresponding errors versus the wavelength for the seven NPOI scans (see Sect. 2). Solid curves correspond to theoretical values obtained from our best model from the χ^2 analysis of all interferometric data (BMAD; see also Fig. 1). Plots for scans 2 to 7 were progressively shifted for better visualization.

thanks to a physically coherent modeling dedicated to stellar interferometry.

The minimum $\chi^2/\text{d.o.f.}$ is $\chi_{\min}^2/\text{d.o.f.} = 7.3$ obtained for an inclination $i = 55^\circ \pm 8^\circ$. This best model obtained from the χ^2 analysis of all data is hereafter referred as BMAD (best model for all data). All free parameters (\varnothing_{eq} , η , and i) and uncertainties corresponding to the BMAD are given in Table 3 together with some selected dependent parameters. In Table 3 we also list the results from additional χ^2 analyses described in the following sections.

In order to avoid an underestimation of the uncertainties on the free parameters, we computed the limits of the confidence domain by searching for the region between $\chi^2/\text{d.o.f.}$ and $\chi^2/\text{d.o.f.} + 1$. We used the reduced χ^2 and not the total χ^2 as we found it difficult to account for possible correlations between the error bars on each measurement, in particular for the NPOI data. By adopting $\chi^2/\text{d.o.f.}$, we chose the conservative approach to consider that all measurements are fully correlated with each other, i.e. that their error bars cannot be diminished by averaging in the fitting process. This means that our derived error bars may be overestimated, but this will avoid an over-interpretation of the data.

In Figs. 2 and 3 we compare the five NPOI observables (V^2 for three baselines, triple amplitudes, and closure phases) with

the corresponding theoretical values derived from the BMAD. We note in particular that, although the uncertainties in the closure phases are quite small (≤ 0.03 rad), there is a rather good agreement between the observed closure phases and those obtained from the BMAD (solid curves). Clearly, models with $\beta = 0.08$ (plotted as dashed curves for comparison) cannot reproduce these data, leading to $\chi^2/\text{d.o.f.} > 75$ in Fig. 1. In Fig. 4 we compare the theoretical squared visibilities V^2 from the BMAD with the observed V^2 and corresponding errors from VLT-VINCI (H and K bands) and PTI (K band), as described in Sect. 2.

Considering all these distinct interferometers, observables, wavelengths, and baselines (lengths and position angles), Figs. 2 to 4 show a good general agreement between observations and the BMAD, particularly for the closure phases. However, some discrepancies between theoretical and observed V^2 exist, leading to a relatively high $\chi_{\min}^2/\text{d.o.f.} (=7.3)$. This issue is discussed hereafter.

4.2. Analysis of selected data subsets

The high $\chi_{\min}^2/\text{d.o.f.}$ obtained in the last section from the analysis of all interferometric data is partially due to an underestimation of long-term errors for the NPOI visibility amplitudes.

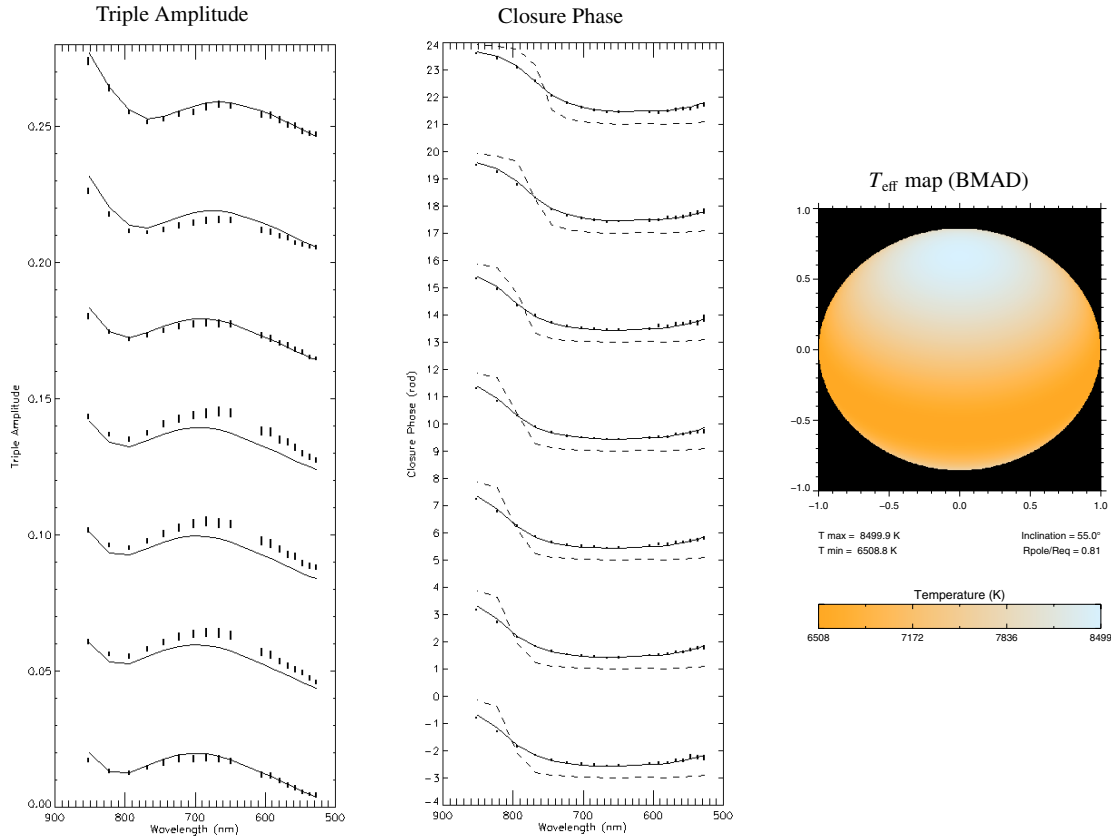


Fig. 3. Triple amplitudes $|V_1||V_2||V_3|$, closure phases $\phi_1 + \phi_2 + \phi_3$, and corresponding errors versus the wavelength for the seven NPOI scans (Sect. 2). Solid curves correspond to theoretical values obtained from our best model from the χ^2 analysis of all interferometric data (BMAD; see also Fig. 1). The closure phase is very sensitive to the stellar intensity distribution. Therefore, a comparison between a strong ($\beta = 0.25$; solid curves) and a weak ($\beta = 0.08$; dashed curves) gravity-darkened model shows that a highly non-uniform surface brightness distribution is mandatory to reproduce the observed closure phases. Note that the closure phases have small error bars ($\lesssim 0.03$ rad). Plots for scans 2 to 7 were progressively shifted for better visualization. The picture in the right is the effective temperature map for the BMAD (Table 3).

This calibration problem is clearly present in Figs. 2 and 3 as a scatter of the observed V^2 and triple amplitudes relative to the model. The observations for a given scan are shifted in the same direction for all wavelengths. On the other hand, the closure phase is a more stable interferometric observable, being unaffected by this calibration problem as shown by the excellent agreement between observation and model in Fig. 3.

We have thus performed another χ^2 analysis including only the (7 scans)*(18 wavelengths) closure phases from NPOI, together with the 47 near-IR V^2 from PTI and VINCI. The $\chi^2/\text{d.o.f.}$ behavior is similar to that seen in Fig. 1, but the minimum reduced χ^2 is now $\gtrsim 2$ times smaller than before, namely, $\chi^2_{\text{min}}/\text{d.o.f.} = 3.2$. In agreement with the analysis of all data presented in the last section, we obtained $\beta = 0.25$ and $i = 55^\circ \pm 14^\circ$. Further physical parameters for this best model determined from the near-IR V^2 and closure phases (BMIRCP) are given in Table 3.

Even though this analysis showed that $\chi^2_{\text{min}}/\text{d.o.f.} (= 3.2)$ diminishes when the NPOI V^2 and triple amplitudes are removed, the value obtained indicates that some non negligible discrepancies between model and observations still exist. Such

discrepancies come from the fact that the near-IR V^2 for the BMAD and the BMIRCP systematically underestimate the observations from PTI and VINCI, as we can see in Fig. 4.

Because these near-IR V^2 include data from two distinct interferometers using different calibrators, one can hardly invoke some kind of calibration problem, such as those found on the NPOI data. These low theoretical near-IR V^2 seem to be due to the rather large equatorial angular diameter deduced from the χ^2 minimization, namely, $\varnothing_{\text{eq}} = 3.83 \pm 0.06$ mas for the BMAD and $\varnothing_{\text{eq}} = 3.88 \pm 0.08$ mas for the BMIRCP (Table 3). To investigate this point we performed two additional χ^2 analyses: one for the (7 scans)*(18 wavelengths) closure phases alone (NPOI data) and another for the 47 near-IR V^2 alone (VLTI-VINCI and PTI data). These results are also summarized in Table 3.

Our analysis result in $\chi^2_{\text{min}}/\text{d.o.f.} = 1.4$ for the best model for the closure phases alone (BMCP). The $\chi^2/\text{d.o.f.}$ behavior is once more similar to that seen in Fig. 1, resulting in $\beta = 0.25$ and $i = 50^\circ \pm 12^\circ$. The derived equatorial diameter ($\varnothing_{\text{eq}} = 3.88 \pm 0.03$ mas) is compatible with those from the two previous analyses (BMAD and BMIRCP).

3.1. The main sequence A-type star Altair (α Aquilae)

574

A. Domiciano de Souza et al.: Gravitational-darkening of Altair from interferometry

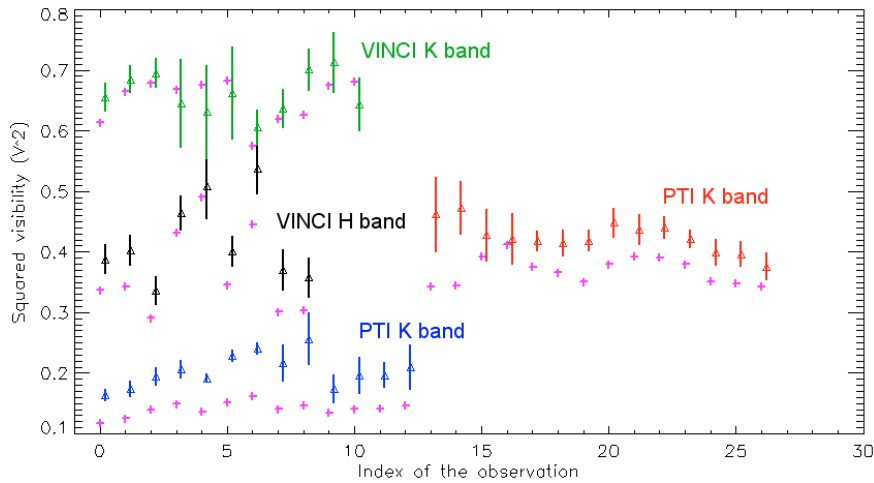


Fig. 4. Squared visibilities V^2 (triangles) and corresponding error bars from VLTI-VINCI (H and K bands) and PTI (K band; baselines 85 m and 110 m) as described in Sect. 2. The abscissa is an index (integer number) to label each group of V^2 data. The crosses correspond to theoretical V^2 obtained from the model with minimum χ^2 (best model; cf. Fig. 1). The abscissas of the V^2 data are slightly shifted to the right compared to those of the theoretical V^2 for better visualization.

Table 3. Input and derived parameters obtained from a χ^2 minimization procedure applied to several data sets: all data (BMAD), near-IR V^2 and closure phases (BMIRCP), closure phases alone (BMCP), and near-IR V^2 alone (BMIR). There is no uncertainty associated to β and T_p because they define two test models based on theoretical limits for the gravity darkening (see text for details). Selected dependent parameters for the best models are also listed.

Fixed input parameters	BMAD	BMIRCP	BMCP	BMIR
$v_{\text{eq}} \sin i$ (km s $^{-1}$)	227	227	227	227
M (M_{\odot})	1.8	1.8	1.8	1.8
i (deg)	–	–	–	50°
(β, T_p) (K)	–	–	–	(0.25, 8500)
Results of the χ^2 analyses	BMAD	BMIRCP	BMCP	BMIR
$\chi^2_{\text{min}}/\text{d.o.f.}$	7.3	3.2	1.5	0.50
(β, T_p) (K) ^a	(0.25, 8500)	(0.25, 8500)	(0.25, 8500)	–
i (deg)	55° ± 8°	55° ± 14°	50° ± 12°	–
$2a = \varnothing_{\text{eq}}$ (mas)	3.83 ± 0.06	3.88 ± 0.08	3.88 ± 0.03	3.44 ± 0.05
R_{eq} ^b (R_{\odot})	2.117 ± 0.035	2.145 ± 0.045	2.145 ± 0.020	1.902 ± 0.029
η (deg)	92° ± 6°	62° ± 17°	95° ± 23°	113° ± 12°
Dependent parameters	BMAD	BMIRCP	BMCP	BMIR
T_{eq} (K)	6509	6483	6171	6453
v_{eq} (km s $^{-1}$)	277	277	296	296
$v_{\text{eq}}/v_{\text{crit}}$ (%)	76%	76%	80%	77%
f_{rot} (cycles/day)	2.585	2.552	2.729	3.077
$2b = \varnothing_{\text{p}}^{\text{max}}$ (mas)	3.29	3.33	3.32	2.99
$a/b = \varnothing_{\text{eq}}/\varnothing_{\text{p}}^{\text{max}}$	1.164	1.165	1.169	1.149
$R_{\text{eq}}/R_{\text{p}}$	1.237	1.240	1.275	1.243

^a Theoretical limit preferred compared to (β, T_p) (K) = (0.08, 8000).

^b From \varnothing_{eq} and Hipparcos distance ($d = 5.143 \pm 0.025$ pc).

Before analyzing the near-IR V^2 alone, we should note that since VLTI-VINCI and PTI data correspond to observations in the first visibility lobe far from the first minimum and in a limited range of baseline position angles, this analysis suffers from a significant uniqueness problem (Domiciano de Souza et al. 2002). This means, in particular, that the stellar inclination cannot be derived from these data. Thus, we fixed $\beta = 0.25$ and

$i = 50^\circ$, compatibly with the values derived for the BMCP. The obtained $\chi^2_{\text{min}}/\text{d.o.f.}$ is 0.50 for the best model for the near-IR V^2 alone (BMIR). As expected, the derived equatorial diameter is significantly smaller ($\varnothing_{\text{eq}} = 3.44 \pm 0.05$ mas) than all previous analyses, which included visible data from NPOI.

Figure 5 shows the fit to the closure phase for the BMCP (solid curves in the left panel) and the fit to the near-IR V^2

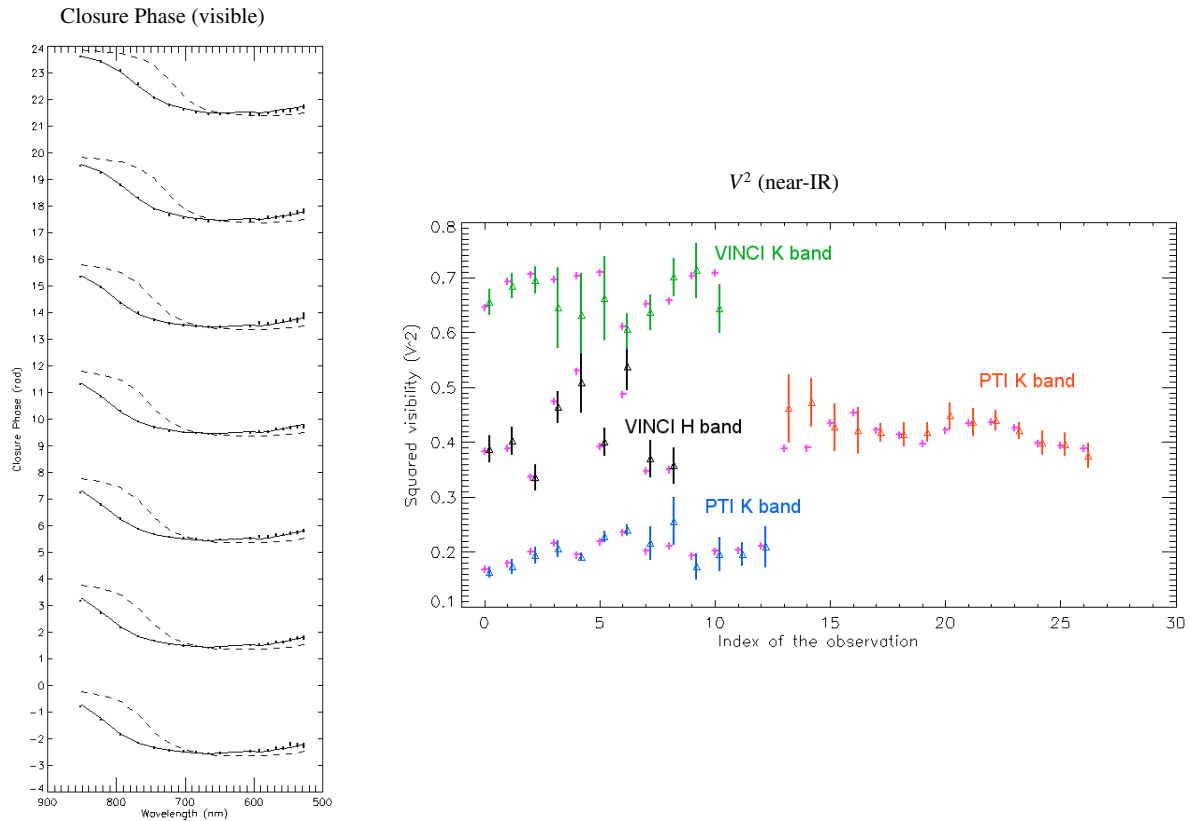


Fig. 5. The left panel shows the closure phases $\phi_1 + \phi_2 + \phi_3$ and corresponding errors versus the wavelength for the seven NPOI scans (Sect. 2). Solid curves correspond to theoretical values obtained from our best model from the χ^2 analysis of closure phases alone (BMCP; see Table 3). Dashed curves correspond to the theoretical closure phases obtained by fixing $i = 50^\circ$, $\varnothing_{\text{eq}} = 3.44$ mas, and $\eta = 113^\circ$. These parameters were derived from the χ^2 analysis of near-IR V^2 alone (BMIR). The solid curves provide a much better fit to the observed closure phases because they correspond to an angular equatorial diameter larger ($\varnothing_{\text{eq}} = 3.88$ mas) than the value for the dashed curves ($\varnothing_{\text{eq}} = 3.44$ mas). On the other hand, a model (BMIR) with $\varnothing_{\text{eq}} = 3.44$ mas nicely fits the near-IR V^2 as shown in the right panel (see also Fig. 4).

for the BMIR (right panel). Individually, these fits are rather good as one can see in Fig. 5 and also as indicated by the corresponding $\chi^2_{\text{min}}/\text{d.o.f.}$ (1.4 for the BMCP and 0.5 for the BMIR). However, it is clear that the large \varnothing_{eq} from the analyses including the closure phases cannot fit the near-IR V^2 (as already shown in Fig. 4).

Conversely, the smaller \varnothing_{eq} derived from the near-IR V^2 alone (BMIR) cannot fit the closure phases. This is shown as dashed curves in Fig. 5 (left panel), where we plotted the theoretical closure phases obtained by a model with fixed $i = 50^\circ$, $\beta = 0.25$, $\varnothing_{\text{eq}} = 3.44$ mas, and $\eta = 113^\circ$ (values from the BMIR). Although this model certainly leads to a high χ^2 , we note that models with $\beta = 0.08$ and free i , \varnothing_{eq} , and η , lead to an even higher χ^2 . Thus, the identification of the von Zeipel effect on Altair ($T_{\text{eff}} \propto g^{0.25}$), which is the main result of this work, is not affected or hampered by this discrepancy between the angular sizes derived from the visible and near-IR data.

In the following section we investigate this discrepancy and discuss some physical consequences of our results, in particular concerning the von Zeipel effect.

5. Discussion

5.1. The size of Altair

The results described in the last section and summarized in Table 3 reveal a discrepancy between the stellar angular diameters required to fit the visible and near-IR interferometric data. This discrepancy also appears when we compare the results obtained in the visible by ONH2004 (NPOI data) and in the K band by vB2001 (PTI data).

To investigate this issue we estimate the angular size of Altair using an independent method: the average surface brightness. Using the surface brightness relations from Kervella et al. (2004b), we can derive the mean equivalent limb-darkened angular diameter of Altair using only its photometric properties (Table 4). We adopted the apparent magnitudes in the visible and near-IR from Hipparcos (Perryman et al. 1997), Morel & Magnetat (1978), Ducati (2002), and the recent infrared catalogue from Kidger & Martín-Luis (2003). The error bars from the original authors on the apparent magnitudes are given for each band, except for the U , R , and I bands, where

3.1. The main sequence A-type star Altair (α Aquilae)

576

A. Domiciano de Souza et al.: Gravitational-darkening of Altair from interferometry

Table 4. Apparent and absolute magnitudes of Altair, using the Hipparcos parallax ($\pi = 194.45 \pm 0.94$ mas).

	<i>U</i>	<i>B</i>	<i>V</i>	<i>R</i>	<i>I</i>	<i>J</i>	<i>H</i>	<i>K</i>	<i>L</i>
m_λ	1.07	0.99	0.77	0.62	0.48	0.327	0.228	0.205	0.20
$\sigma(m_\lambda)$	0.05	0.01	0.01	0.05	0.05	0.009	0.008	0.005	0.01
M_λ	2.51	2.43	2.21	2.06	1.92	1.77	1.67	1.65	1.64

a conservative 0.05 mag error has been assumed. No interstellar extinction is taken into account for this nearby star ($d \simeq 5$ pc).

We obtain consistent limb-darkened disk angular diameters for all the visible-infrared colors, with, for instance, $\varnothing_{\text{LD}}(B, B-L) = 3.258 \pm 0.034$ mas. Considering the Hipparcos parallax of $\pi = 194.45 \pm 0.94$ mas (distance $d = 5.143 \pm 0.025$ pc), this translates into a photometric equivalent linear radius of $1.801 \pm 0.021 R_\odot$. Erspamer & North (2003) obtain an effective temperature of $T_{\text{eff}} = 7550$ K, averaged over the disk of Altair. The $\varnothing_{\text{LD}}(T_{\text{eff}}, m_\lambda)$ relations from Kervella et al. (2004b) give the same LD angular diameter using the *H*, *K*, and *L* apparent magnitudes.

Let us compare the photometric-average angular size derived above ($\varnothing_{\text{LD}}(B, B-L) = 3.258 \pm 0.034$ mas) with an equivalent angular disk diameter leading to the same area of the stellar surface projected onto the sky-plane $\bar{\varnothing}$ obtained from our models. For BMIR we obtain $\bar{\varnothing} = 3.20$ mas, while for BMAD, BMIRCP, and BMCP we obtain $\bar{\varnothing}$ between 3.53 and 3.58 mas. This comparison points towards a smaller size of Altair since there is a better agreement between the sizes estimated by the surface brightness method and by the χ^2 analysis including near-IR V^2 alone, with the latter still being slightly smaller.

From the present data it is not possible to determine whether the discrepancy between the stellar angular diameters in the visible and near-IR has a physical or an instrumental origin. Bias in the wavelength calibration could lead to a larger or smaller size since it affects the spatial frequency. Previous comparisons between stellar angular diameters measured by NPOI and other interferometers show no sign of systematic differences (Nordgren et al. 2001). On the other hand, the large angular size in the visible could also be explained, for example, by an extended emission only seen in the visible. To further investigate the origin of this discrepancy, more precise interferometric observations of Altair are required, preferably in the near-IR at the second visibility lobe and/or with phase closures. These observations should be made in such a way that the quality and the nature of the data in the visible and near-IR are similar and, thus, better comparable. Such observations are expected to be performed with the instrument VLTI-AMBER (e.g., Petrov et al. 2003).

5.2. Rotation and gravity darkening laws

In the present paper we consistently adopted the Roche approximation and a von Zeipel-like gravity-darkening (Eq. (2)). Nevertheless, other more subtle possibilities exist and should be considered in the future when more precise interferometric observations of Altair will be available.

For example, our results indicate that the effective temperature at Altair's equator could be low enough that the star

presents convection in its external equatorial regions ($T_{\text{eq}} \simeq 6500$ K for the models with minimum χ^2). Such low T_{eq} requires a gravity-darkening exponent $\beta \simeq 0.08$ (Lucy 1967; Claret 2000c), so that a latitudinal dependent β parameter should be more convenient for Altair (e.g., a continuous variation from the radiative limit $\beta = 0.25$ to the convective limit $\beta = 0.08$ between the poles and the equator). The hypothesis of a convective equatorial region is supported by several works showing that Altair has a chromosphere and a corona, possibly linked to subphotospheric convective zones (e.g., Ferrero et al. 1995).

Other possibilities for a variable parameter β or even for an alternative gravity-darkening law is the presence of differential rotation (e.g., Connon Smith & Worley 1974; Kippenhahn 1977). Although Reiners & Royer (2004) found no signatures of external latitudinal-dependent differential rotation in Altair, we think that one cannot exclude internal differential rotation and/or external differential rotation not detected by the Fourier transform method used by those authors. In fact, the method used by Reiners & Royer (2004) is not very sensitive to differential rotation laws where polar regions rotate faster than layers closer to the equator (anti solar-like or negative differential rotation; e.g., Reiners & Schmitt 2002).

Interestingly enough, Stoekley (1968) found evidence of an anti-solar-like differential rotation in Altair. The presence of negative surface differential rotation is in fact compatible with the hypothesis of a convective equatorial region. For such cool regions, characteristic of F and later type stars, it is possible that some braking mechanism (magnetic effects and/or viscosity due to the onset of convection) could act preferentially close to Altair's equator, slowing these regions relative to those closer to the poles.

This important issue concerning the presence of differential rotation in Altair, and the corresponding gravity-darkening law, should be investigated in the future by additional studies, preferably with distinct and complementary techniques. For example, Domiciano de Souza et al. (2004) proposed a technique to detect both solar-like and anti-solar-like differential rotation by combining high angular resolution with high spectral resolution (differential interferometry). The forthcoming VLTI-AMBER will be able to operate in a differential interferometry mode in the near-IR (e.g., Petrov et al. 2003).

5.3. Inclination and rotation frequency

The results presented in Sect. 4 suggest an intermediate inclination for Altair (see Table 3). These results seem to disagree with the analysis from Reiners & Royer (2004), which points towards higher inclinations ($i > 68^\circ$ on a 1σ level). However, this discrepancy disappears if we consider 2σ confidence

levels in the results from Reiners & Royer (2004), which implies $i > 45^\circ$. Additionally, Stoeckley (1968) derived an inclination angle between 30° and 50° from the analysis of line profiles of Mg II 4481 and Ca II 3934, which is in agreement with our results as well.

It is important that further studies investigate how subtle effects, such as differential rotation and gravity-darkening, influence the interferometric observables and, in particular, the line profiles. It would thus be possible to consistently combine interferometry and spectroscopy in order to determine the stellar inclination more precisely.

Once i , R_{eq} , and $v_{\text{eq}} \sin i$ are known, the rotation frequency can be determined, in the uniform rotation approximation, by:

$$f_{\text{rot}} = \frac{1}{P_{\text{rot}}} = \frac{(v_{\text{eq}} \sin i)}{2\pi R_{\text{eq}}(\sin i)}. \quad (6)$$

The rotation frequencies computed from the equation above and corresponding to our χ^2 analyses are listed in Table 3. Recently, Buzasi et al. (2005) detected several pulsation modes in WIRE (Wide-field InfraRed Explorer) observations, indicating that Altair is a low-amplitude δ Scuti star. The authors suggest that the two low-frequency modes found ($f_1 = 2.570 \pm 0.020$ cycles/day and $f_2 = 3.526 \pm 0.020$ cycles/day) may be associated with the stellar rotation frequency.

The theoretical f_{rot} values listed in Table 3 suggest that the frequency f_1 measured by Buzasi et al. (2005) is a better candidate for f_{rot} . However, more precise measurements should be acquired before we can unambiguously identify $f_1 = 2.570 \pm 0.020$ cycles/day as the rotation frequency of Altair.

5.4. On the age of Altair

This work, along with previous ones, has proven that long baseline interferometry is a powerful technique for studying rapidly rotating stars. In particular, this technique can provide important clues to the many unanswered questions concerning the structure and evolution of rapid rotators. For example, placing an intermediate-mass star like Altair in its evolutionary history is an interesting but difficult task requiring as much information as possible.

The age of a star can be derived using different indicators. Lachaume et al. (1999) have used five different methods to study main-sequence stars in the solar neighborhood: isochrones in the HR diagram, rotation, calcium emission lines, kinematics in the Galaxy, and iron abundance. Unfortunately, due to Altair's rapid rotation, its spectral lines are very broad, and this prevents the application of the Ca emission line and kinematic methods. The rotational velocity of a hot, fast rotator is not an accurate indicator of its age, because of the uncertainties on the initial rotational velocity and on the braking mechanisms possibly present.

To estimate the age of Altair, we took advantage of the recent models from Girardi et al. (2002). We read the tables of these authors for the following parameters: $[\text{Fe}/\text{H}] = -0.34$, $T_{\text{eff}} = 7550$ K, $\log g = 4.13$ (Erspamer & North 2003), and $Z = 0.008$. We adopted the absolute magnitudes presented in Table 4, derived using the parallax from Hipparcos

(Perryman et al. 1997): $\pi = 194.45 \pm 0.94$ mas. The bolometric magnitude was estimated using the corrections provided by Girardi et al. (2002). The best fit of the models with the observed absolute magnitudes of Altair is obtained for an age between 1.2 and 1.4 Gyr.

The relatively old age of Altair suggests that it has kept a high rotation velocity for a long time, well into its lifetime on the main sequence. It does not seem that an efficient braking mechanism is acting to slow down the rotation velocity of this intermediate-mass star. Altair was searched for the presence of a debris disk by Kuchner et al. (1998) in the mid-infrared, without success. The absence of a disk could be one of the factors that prevented an efficient slow down of the star by magnetic coupling or turbulent friction. In any case we believe that further studies should be performed on the evolution of an intermediate-mass and fast rotating star such as Altair.

6. Summary and conclusions

We performed a physically consistent analysis of all available interferometric data on Altair using our interferometry-oriented model for fast rotators. This model includes Roche approximation, limb-darkening from Claret (2000a,b), and a von Zeipel-like gravity-darkening law, as described in Sect. 3 and also by Domiciano de Souza et al. (2002). The rich observational set analyzed here includes new data from VLTI-VINCI (V^2 in the H and K bands), as well as published data from PTI (V^2 in the K band) and NPOI (V^2 , triple amplitudes, and closure phases in the visible between 520 nm and 850 nm).

In particular, and as already pointed out by ONH2004, the presence of gravity-darkening in Altair is revealed by the NPOI observations showing (1) a non-zero V^2 in the first minimum and (2) a smooth variation of the closure phase between 0 and π rad. Thanks to our interferometry-oriented model we were able, for the first time, to provide a physical interpretation of all observations from NPOI, PTI, and VLTI-VINCI combined. In particular, we could show that Altair exhibits a gravity-darkening compatible with the theoretically expected value for hot stars (von Zeipel effect): $T_{\text{eff}} \propto g^{0.25}$.

Moreover, with the parameters and models considered here we were able to show that the observations of Altair are better reproduced by models with an intermediate inclination (between 40° and 65° including the error bars).

Our analysis also reveals a possible discrepancy between visible and near-IR angular diameters derived from the data that should be further investigated by visible and near-IR observations of high quality, preferably within the second visibility lobe and/or with closure phases.

Further observations should also be performed to investigate the presence of differential rotation on Altair and the corresponding gravity-darkening laws. Precise interferometric observations in the near-IR, allowing us to study differential rotation in particular (Domiciano de Souza et al. 2004), are soon expected for the VLTI spectro-interferometer AMBER (e.g., Petrov et al. 2003).

Acknowledgements. This work has been supported by a postdoctoral fellowship at the Max-Planck-Institut für Radioastronomie

3.1. The main sequence A-type star Altair (α Aquilae)

578

A. Domiciano de Souza et al.: Gravitational-darkening of Altair from interferometry

(Infrared Interferometry Group). We acknowledge Drs. G. Weigelt and T. Driebe for their invaluable suggestions that allowed us to improve the quality of this work.

References

- Abt, H. A., & Morrell, N. I. 1995, *ApJS*, 99, 135
- Armstrong, J. T., Mozurkewich, D., Rickard, L. J., et al. 1998, *ApJ*, 496, 550
- Bordé, P., Coudé du Foresto, V., Chagnon, G., & Perrin, G. 2002, *A&A*, 393, 183
- Buzasi, D. L., Bruntt, H., Bedding, T. R., et al. 2005, *ApJ*, 619, 1072
- Cayrel de Strobel, G., Soubiran, C., Friel, E. D., Ralite, N., & Francois, P. 1997, *A&AS*, 124, 299
- Cayrel de Strobel, G., Soubiran, C., & Ralite, N. 2001, *A&A*, 373, 159
- Claret, A. 2000a, *A&A*, 363, 1081
- Claret, A. 2000b, *VizieR Online Data Catalog*, 336, 31081
- Claret, A. 2000c, *A&A*, 359, 289
- Cohen, M., Walker, R. G., Carter, B., et al. 1999, *AJ*, 117, 1864
- Colavita, M. M., Wallace, J. K., Hines, B. E., et al. 1999, *ApJ*, 510, 505
- Collins, G. W. 1965, *ApJ*, 142, 265
- Connon Smith, R., & Worley, R. 1974, *MNRAS*, 167, 199
- Coudé du Foresto, V., Ridgway, S., & Mariotti, J.-M. 1997, *A&AS*, 121, 379
- Domiciano de Souza, A., Vakili, F., Jankov, S., Janot-Pacheco, E. & Abe, L. 2002, *A&A*, 393, 345
- Domiciano de Souza, A., Kervella, P., Jankov, S., et al. 2003, *A&A*, 407, L47
- Domiciano de Souza, A., Zorec, J., Jankov, S., et al. 2004, *A&A*, 418, 781
- Ducati, J. R. 2002, *NASA Ref. Pub.* 1294
- Erspamer, D., & North, P. 2002, *VizieR Online Data Catalog*, 339, 81121
- Erspamer, D., & North, P. 2003, *A&A*, 398, 1121
- Ferrero, R. F., Gouttebroze, P., Catalano, S., et al. 1995, *ApJ*, 439, 1011
- Girardi, L., Bertelli, G., Bressan, A., et al. 2002, *A&A*, 391, 195
- Glebocki, R., Gnacinski, P., & Stawikowski, A. 2000, *Acta Astron.*, 50, 509
- Glindemann, A., Algomedo, J., Amestica, R., et al. 2003, *Proc. SPIE*, 4838, 89
- Hanbury Brown, R. 1974, in *The Intensity Interferometer* (London: Taylor & Francis LTD), 151
- Hubeny, I. 1988, *Comp. Phys. Comm.*, 52, 103
- Hubeny, I., & Lanz, T. 1995, *ApJ*, 439, 875
- Hummel, C. A., Mozurkewich, D., Armstrong, J. T., et al. 1998, *AJ*, 116, 2536
- Kervella, P., Coudé du Foresto, V., Glindemann, A., & Hofmann, R. 2000, *SPIE*, 4006, 31
- Kervella, P., Gitton, Ph., Ségransan, D., et al. 2003a, *SPIE*, 4838, 858
- Kervella, P., Thévenin, F., Morel, P., Bordé, P., & Di Folco, E. 2003b, *A&A*, 408, 681
- Kervella, P., Ségransan, D., & Coudé du Foresto, V. 2004a, *A&A*, 425, 1171
- Kervella, P., Thévenin, F., Di Folco, E., & Ségransan, D. 2004b, *A&A*, 426, 297
- Kidger, M. R., & Martín-Luis, F. 2003, *AJ*, 125, 3311
- Kippenhahn, R. 1977, *A&A*, 58, 267
- Kuchner, M. J., Brown, M. E., & Koresko, C. D. 1998, *PASP*, 110, 1336
- Kurucz, R. L. 1992, *The Stellar Populations of Galaxies*, IAU Symp. 149, 225
- Lachaume, R., Dominik, C., Lanz, T., & Habing, H. J. 1999, *A&A*, 348, 897
- Lebouquin, J. B., Rousset-Perraut, K., Kern, P., et al. 2004, *A&A*, 424, 719
- Lucy, L. B. 1967, *Z. Astrophys.*, 65, 89
- Malagnini, M. L., & Morossi, C. 1990, *A&AS*, 85, 1015
- Morel, M., & Magnetat, P. 1978, *A&AS*, 34, 477
- Nordgren, T. E., Sudol, J. J., & Mozurkewich, D. 2001, *AJ*, 122, 2707
- Ohishi, N., Nordgren, T. E., & Hutter, D. J. 2004, *ApJ*, 612, 463
- Panzer, M. R., Tagliaferri, G., Pasinetti, L., & Antonello, E. 1999, *A&A*, 348, 161
- Perryman, M. A. C., Lindgren, L., Kovalevsky, J., et al., *The Hipparcos Catalogue*, 1997, *A&A*, 323, 49
- Petrov, R. G., & Amber Consortium, *The 2003, EAS Publications Series, Observing with the VLTI*, ed. G. Perrin and F. Malbet, 6, 111
- Reiners, A., & Schmitt, J. H. M. M. 2002, *A&A*, 384, 155
- Reiners, A., & Royer, F. 2004, *A&A*, 428, 199
- Royer, F., Grenier, S., Baylac, M.-O., Gómez, A. E., & Zorec, J. 2002, *A&A*, 393, 897
- Ségransan, D., Forveille, T., Millan-Gabet, C. P. R., & Traub, W. A. 1999, in *ASP Conf. Ser.* 194, 290
- Stoeckley, T. R. 1968, *MNRAS*, 140, 121
- Townsend, R. H. D. 1997, *MNRAS*, 284, 839
- van Belle, G. T., Ciardi, D. R., Thompson, R. R., Akeson, R. L., & Lada, E. A. 2001, *ApJ*, 559, 1155
- von Zeipel, H. 1924, *MNRAS*, 84, 665
- Wittkowski, M., Aufdenberg, J. P., & Kervella, P. 2004, *A&A*, 413, 711

3.2 The Be star Achernar (α Eridani)

Achernar (α Eridani, HD 10144; spectral type B6Vep in the [SIMBAD](#) database) is the closest ($d = 42.75 \pm 1.04$ pc; [van Leeuwen, 2007](#)) and brightest Be star as seen from Earth. It is easily observable in the southern hemisphere, being the ninth star in the night sky in visible light ($V = 0.46$). It is one of the fastest rotators among the single, non-degenerate stars, with reported projected rotation velocities ranging from 220 up to 410 km s^{-1} .

Some of the most intriguing physical effects observed on Achernar are:

- rotation velocity (e.g. Sects. [3.2.1](#) and [3.2.4](#); [Domiciano de Souza et al., 2014, 2012](#); [Vinicius et al., 2006](#), among others);
- rotational flattening (e.g. Sect. [3.2.1](#); [Domiciano de Souza et al., 2014, 2003](#));
- inclination and/or position angle of the polar axis projected onto the sky plane (e.g. Sects. [3.2.1](#) and [3.2.4](#); [Domiciano de Souza et al., 2014, 2012, 2003](#); [Carciofi et al., 2007](#));
- gravity darkening (Sect. [3.2.1](#); [Domiciano de Souza et al., 2014](#));
- polar wind (Sect. [3.2.2](#); [Kervella & Domiciano de Souza, 2006](#));
- residual equatorial disk (Sect. [3.2.2](#); [Carciofi et al., 2008](#));
- binarity (Sect. [3.2.3](#) [Kervella & Domiciano de Souza, 2007](#); [Kervella et al., 2008](#)).
- variable circumstellar disk ($B \leftrightarrow \text{Be}$ cycle) on time scales of $\sim 14 - 15$ years (e.g. [Vinicius et al., 2006](#));
- non-radial pulsations (e.g. [Goss et al., 2011](#); [Balona et al., 1987](#));

Except for the last two items in the above list, all other effects/parameters were detected/measured by my collaborators and me. One key point that allowed us to achieve these results is the use of physical models to interpret multi-technique observations, including spectroscopy, polarimetry, photometry, and high angular resolution techniques, in particular OLBI. A selection of our main results obtained in the last decade are presented in details in the following sections.

3.2.1 Photospheric parameters of Achernar

In paper below published in A&A ([Domiciano de Souza et al., 2014](#)), we analyze VLT/IRIS observations of Achernar with the model CHARRON (Sect. [2.5.1](#)) to measure several photospheric parameters, in particular, the equatorial radius (equatorial angular diameter), equatorial rotation velocity, polar inclination, position angle of the rotation axis projected on the sky, and the gravity darkening β coefficient (von Zeipel-like law). To our knowledge, it is the first time that these photospheric parameters were simultaneously measured on a Be star. The fit of the CHARRON model to the data was performed using a Python implementation of the Markov Chain Monte Carlo (MCMC) method: the emcee code ([Foreman-Mackey et al., 2013](#); [Goodman & Weare, 2010](#)). The emcee code provides histograms of the model free parameters from which one can directly estimate best-fit values and associate uncertainties.

The interferometric observations analyzed were obtained with VLTI/PIONIER (squared visibilities and phase closures at low spectral resolution in the H band) and with VLTI/AMBER (differential phases at high spectral resolution in the K band around Br γ).

Before considering Achernar as a simple fast-rotator without disk, we performed a physical modeling of its close CSE using the HDUST code to analyze multi-technique observations (spectroscopic, polarimetric, and photometric) in order to show that the VLTI data were recorded during a normal B phase. Our analysis shows that any possible influence of a residual disk can be neglected within $\sim \pm 1\%$ level of intensity. This conclusion is also supported by interferometric image reconstruction.

The combination of (1) high quality interferometric observations of Achernar taken in a normal B phase, (2) physical modeling of fast rotators, and (3) model fitting with an efficient MCMC method, allowed a robust and precise determination of photospheric parameters for this Be star.

In addition, being the most flattened fast-rotating, non-degenerated, single star known to-date, Achernar provides a crucial test to gravity-darkening theories. Indeed, in this work we confronted the gravity-darkening model proposed by [Espinosa Lara & Rieutord \(2011\)](#), ELR model; see discussion in Sect. 2.2.2) to the β coefficient determined from the MCMC fitting of CHARRON to the VLTI data, as well as with values from other fast rotators. The gravity darkening measured on Achernar is compatible with the ELR model providing observational support to this model in the regime of highly flattened stars (flattening $\epsilon = 1 - R_p/R_{\text{eq}} > 0.26$ or, equivalently, $R_{\text{eq}}/R_p > 1.35$; cf. Eq. 2.13). The relative uncertainty on ϵ appearing in Fig. 13 of [Domiciano de Souza et al. \(2014\)](#) corresponds to the relative uncertainty on R_{eq} , i.e. 2.5%.

As shown in the A&A paper below, the ELR model is thus validated by interferometric results obtained on five out of six fast-rotating stars, with flattening ϵ ranging from 0.11 to 0.26 (R_{eq}/R_p from 1.13 to 1.35), Vega being the less flattened star, and Achernar being the flattest one. This agreement between theory and interferometric observations provides a more realistic description of gravity darkening on single stars, significantly improving our view of this important physical effect since the pioneering works of von Zeipel almost a century ago. This more profound understanding of gravity darkening provided by the ELR model also allows to decrease the number of parameters required to model fast rotators, since the surface intensity (effective temperature) distribution is defined without the need of a β coefficient, present in the von Zeipel-like gravity darkening laws currently used.

Finally, we note that this work benefited from important contributions of two PhD students:

- G. Dalla Vedova (thesis supervisors: R. G. Petrov and F. Millour) - image reconstruction with the MIRA¹ code ([Thiébaud, 2008](#));
- D. Moser Faes (thesis supervisors: A. C. Carciofi and A. Domiciano de Souza)² - modeling of the close circumstellar disk with HDUST and comparison to spectroscopic and polarimetric data. Contribution to the creation of plots and interface Python-IDL for the emcee code.

¹Multi-aperture Image Reconstruction Algorithm.

²Ph. Bendjoya is the official co-supervisor in France, since I do not have my HDR.

The environment of the fast rotating star Achernar[★]

III. Photospheric parameters revealed by the VLTI

A. Domiciano de Souza¹, P. Kervella², D. Moser Faes^{2,3}, G. Dalla Vedova¹, A. Mérand⁴, J.-B. Le Bouquin^{5,6}, F. Espinosa Lara^{7,8}, M. Rieutord^{7,8}, P. Bendjoya¹, A. C. Carciofi³, M. Hadjara^{1,9}, F. Millour¹, and F. Vakili¹¹ Laboratoire Lagrange, UMR 7293, Université de Nice-Sophia Antipolis (UNS), CNRS, Observatoire de la Côte d'Azur, 06300 Nice, France

e-mail: Armando.Domiciano@oca.eu

² LESIA, Observatoire de Paris, CNRS UMR 8109, UPMC, Université Paris Diderot, 5 place Jules Janssen, 92195 Meudon, France³ Instituto de Astronomia, Geofísica e Ciências Atmosféricas, Universidade de São Paulo (USP), Rua do Matão 1226, Cidade Universitária, 05508-900 São Paulo, Brazil⁴ European Southern Observatory, Alonso de Córdova 3107, Casilla 19001 Santiago 19, Chile⁵ Univ. Grenoble Alpes, IPAG, 38000 Grenoble, France⁶ CNRS, IPAG, 38000 Grenoble, France⁷ Université de Toulouse, UPS-OMP, IRAP, 31028 Toulouse, France⁸ CNRS, IRAP, 14 avenue Édouard Belin, 31400 Toulouse, France⁹ Centre de Recherche en Astronomie, Astrophysique et Géophysique (CRAAG), Route de l'Observatoire, BP 63, Bouzareah, 16340 Alger, Algérie

Received 6 May 2014 / Accepted 6 July 2014

ABSTRACT

Context. Rotation significantly impacts on the structure and life of stars. In phases of high rotation velocity (close to critical), the photospheric structure can be highly modified, and present in particular geometrical deformation (rotation flattening) and latitudinal-dependent flux (gravity darkening). The fastest known rotators among the nondegenerate stars close to the main sequence, Be stars, are key targets for studying the effects of fast rotation on stellar photospheres.

Aims. We seek to determine the purely photospheric parameters of Achernar based on observations recorded during an emission-free phase (normal B phase).

Methods. Several recent works proved that optical/IR long-baseline interferometry is the only technique able to sufficiently spatially resolve and measure photospheric parameters of fast rotating stars. We thus analyzed ESO-VLTI (PIONIER and AMBER) interferometric observations of Achernar to measure its photospheric parameters by fitting our physical model CHARRON using a Markov chain Monte Carlo method. This analysis was also complemented by spectroscopic, polarimetric, and photometric observations to investigate the status of the circumstellar environment of Achernar during the VLTI observations and to cross-check our model-fitting results.

Results. Based on VLTI observations that partially resolve Achernar, we simultaneously measured five photospheric parameters of a Be star for the first time: equatorial radius (equatorial angular diameter), equatorial rotation velocity, polar inclination, position angle of the rotation axis projected on the sky, and the gravity darkening β coefficient (effective temperature distribution). The close circumstellar environment of Achernar was also investigated based on contemporaneous polarimetry, spectroscopy, and interferometry, including image reconstruction. This analysis did not reveal any important circumstellar contribution, so that Achernar was essentially in a normal B phase at least from mid-2009 to end-2012, and the model parameters derived in this work provide a fair description of its photosphere. Finally, because Achernar is the flattest interferometrically resolved fast rotator to-date, the measured β and flattening, combined with values from previous works, provide a crucial test for a recently proposed gravity darkening model. This model offers a promising explanation to the fact that the measured β parameter decreases with flattening and shows significantly lower values than the classical prediction of von Zeipel.

Key words. stars: rotation – stars: individual: Achernar – methods: observational – methods: numerical – techniques: interferometric – techniques: high angular resolution

1. Introduction

The rapidly rotating Be star Achernar (α Eridani, HD 10144) is a key target in stellar physics for a deeper understanding of

(1) the physical structure and evolution of fast rotators; and (2) the physical mechanism(s) connected with the Be phenomenon (e.g., episodic mass and angular momentum losses, disk formation and dissipation). It is thus crucial to determine a realistic model of Achernar's photosphere by measuring its main relevant physical parameters such as radius, rotation velocity,

[★] Based on observations performed at ESO, Chile under VLTI PIONIER and AMBER programme IDs 087.D-0150 and 084.D-0456.

temperature distribution (gravity darkening), mass, and inclination. Because it is the closest and brightest Be star in the sky, the photosphere of Achernar and its close vicinity can at least be partially resolved by modern high angular resolution instruments that can probe spatial scales ranging from ~ 1 to ~ 100 mas.

In particular, the ESO-Very Large Telescope Interferometer (VLTI; Haguenaer et al. 2010) instruments are well-adapted to this study. Observations performed in 2002 with the commissioning beam-combiner VLTI/VINCI revealed a strong apparent oblateness (rotational flattening) and suggested an extended structure that accounts for a few percent of the photospheric flux (Domiciano de Souza et al. 2003; Kervella & Domiciano de Souza 2006). This strong flattening could not be explained by the commonly adopted stellar rotation models, and two possibilities were proposed to account for it: differential rotation (Jackson et al. 2004), and a residual circumstellar disk (Carciofi et al. 2008). By studying the time variation of $H\alpha$ line profiles, Vinicius et al. (2006) showed that a weak but measurable emission (relative to a reference spectra) was detectable at the epoch of the VLTI/VINCI observations; this supports the hypothesis of a residual disk.

In addition, direct high angular resolution imaging revealed a faint, lower-mass binary companion to the Be star, at angular separations of ~ 50 – 300 mas (Kervella et al., in prep.; Kervella et al. 2008; Kervella & Domiciano de Souza 2007).

These works show that studying Achernar as a simple fast rotator to extract its photospheric parameters is a delicate task, since one has to consider its $B\zeta$ Be cycle as well as the possible influence of the binary companion. In this paper we seek to determine the purely photospheric parameters of Achernar based on a physical model of rapidly rotating stars and on VLTI observations recorded during a quiescent, emission-free phase (normal B phase).

The VLTI observations and data reduction are described in Sect. 2. In Sect. 3 we present a detailed investigation of the possible influence of a circumstellar disk and/or the binary companion on the interferometric observations. The adopted model and the photospheric parameters of Achernar measured from a model-fitting procedure are presented in Sects. 4 and 5. Deviations from the photospheric model and the photosphere vicinity of Achernar possibly revealed by the VLTI observations are investigated in Sect. 6, in particular using interferometric image reconstruction. Finally, the conclusions of this work are given in Sect. 7.

2. Interferometric observations and data reduction

2.1. VLTI/PIONIER

Near-infrared interferometric data of Achernar were obtained in 2011/Aug.-Sep. and 2012/Sep. with the PIONIER beam combiner (Le Bouquin et al. 2011) at the ESO-VLTI (Haguenaer et al. 2010). We used the largest quadruplet available with the Auxiliary Telescopes (AT) at that time (A1-G1-K0-I1) to resolve the stellar photosphere as much as possible. The resulting uv coverage is shown in Fig. 1. Depending on the night, the data were dispersed over three or seven spectral channels across the H band. Table 2 summarizes the log of observations.

The observations of Achernar were interspersed with interferometric calibrator stars to estimate the transfer function of the instrument. We selected these calibrators in the catalog by Cohen et al. (1999), adapted by Bordé et al. (2002), and in the JMMC Stellar Diameters Catalog¹ (JSDC, Lafrasse et al. 2010)

¹ <http://cdsarc.u-strasbg.fr/viz-bin/Cat?II/300>

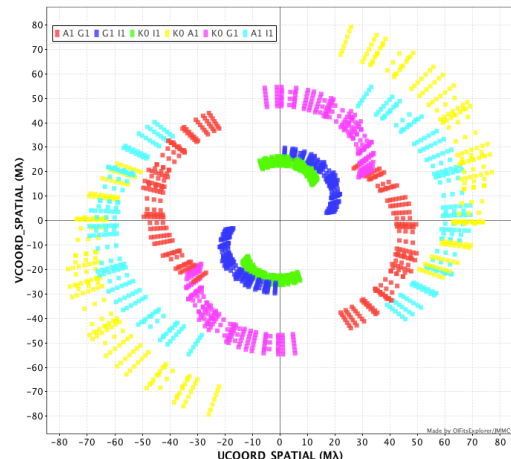


Fig. 1. uv coverage of VLTI/PIONIER observations of Achernar. The AT baselines used are identified with different colors. Image adapted from the OIFITSExplorer/JMMC tool.

using the SearchCal tool developed by the JMMC² (Bonneau et al. 2006). The main properties of the selected stars are listed in Table 1. We chose to use two types of calibrators: bright calibrators (HD 9362 and HD 12524) and fainter calibrators (HD 6793 and HD 187691). The bright calibrators provide a high photometric signal-to-noise ratio (S/N), and a very high precision on the calibration of the visibilities and closure phases. The fainter stars provide a cross-check of the adopted angular size of the bright calibrators and of their measured closure phases. Their small angular diameter results in a high fringe visibility ($V \approx 80\%$) and a very low systematic calibration uncertainty. We observed no deviation of the selected calibrators from central symmetry that might have been caused by binarity, for example.

Data were reduced and calibrated with the package pndrs (Le Bouquin et al. 2011). Each observation provides six squared visibilities V^2 and four closure phases CP. This dataset is available upon request in the standard OIFITS format.

2.2. VLTI/AMBER

Domiciano de Souza et al. (2012a) described and analyzed VLTI/AMBER HR differential phase observations of Achernar around the Bry line. The observations were recorded in 2009 (Oct. 25, Oct. 26, Oct. 30, and Nov. 1) with the high spectral resolution mode and using the FINITO fringe tracker. In this paper we reanalyze these AMBER differential phases together with the PIONIER data, since they were both taken during a diskless phase, as demonstrated in the next section.

3. Disk and companion status during the VLTI observations

The Be and binary nature of Achernar may imply temporal variabilities of observables with possible detectable spectro-interferometric signatures. It is thus important to determine which physical components should be included in the models to interpret VLTI observations from a given epoch. Indeed, Carciofi et al. (2008) showed that the presence of a residual circumstellar disk is a promising explanation of the strong flattening measured

² <http://www.jmmc.fr/>

3. High spectro-spatial resolution observations of fast rotators in the H-R diagram

A. Domiciano de Souza et al.: The environment of the fast rotating star Achernar. III.

Table 1. Interferometric calibrators used for the PIONIER observations of Achernar.

Name	Sp. type	m_V	m_H	m_K	\mathcal{D}_{LD} (mas)	\mathcal{D}_{UD} (mas)	Ref. code
HD 6793	G5III	5.34	3.25	3.24	1.08 ± 0.08	1.06 ± 0.08	B06
HD 9362	K0IIIb	3.95	1.75	1.65	2.24 ± 0.02	2.17 ± 0.02	B02
HD 12524	K5III	5.16	1.69	1.52	2.77 ± 0.03	2.67 ± 0.03	B02
HD 187691	F8V	5.12	3.86	3.90	0.72 ± 0.05	0.70 ± 0.05	B06
HD 216956	A4V	1.16	1.05	1.05	2.22 ± 0.02	2.20 ± 0.03	A09
HD 14641	K5III	5.82	2.19	2.02	2.20 ± 0.03	2.12 ± 0.02	B02

Notes. *VHK* magnitudes are given, as well as limb-darkened (LD) and uniform-disk (UD) angular diameters. The references are B02: [Bordé et al. \(2002\)](#), B06: [Bonneau et al. \(2006\)](#), A09: [Absil et al. \(2009\)](#). The interferometric signature of fast-rotation and debris disk of HD 216956 is significantly below the observational uncertainties so that this star was used as a suitable calibrator.

Table 2. Log of VLTI/PIONIER observations of Achernar.

Date	Nb observations	Nb spec. channels
2011 Aug. 06	4	3
2011 Sep. 22	10	7
2011 Sep. 23	9	7
2012 Sep. 16	9	3
2012 Sep. 17	3	3

in the 2002 VLTI/VINCI observations ([Domiciano de Souza et al. 2003](#)). The presence of this residual disk is supported by a 2002 $H\alpha$ profile that shows a weak but measurable emission superposed on the stronger photospheric absorption ([Vinicius et al. 2006](#)).

Based on our observations of Achernar ([Kervella et al., in prep.](#)), the binary companion was located close to apastron (separation ~ 200 – 300 mas) during the PIONIER observations, which is outside the field of view of this instrument. These observations were performed at the VLT instruments NACO and VISIR and are based on several high angular resolution imaging techniques such as direct imaging, lucky imaging, adaptive optics, and aperture masking. Although the stellar photosphere is not resolved by these observations, they allow one to follow the time evolution of the binary system by resolving both components at different orbital phases.

Concerning the possible influence of a Be circumstellar disk, a more thorough analysis is required as described below.

3.1. Search for polarimetric and spectroscopic signatures of a Be circumstellar disk

To investigate the presence and strength of a possible circumstellar disk during the VLTI (PIONIER and AMBER) observations (Sect. 2), we analyzed contemporaneous broadband polarimetry (B and V) and hydrogen line profiles ($H\alpha$ and $H\beta$). These observations span from 2009 July to 2012 November.

Imaging polarimetry in the B and V bands was obtained using the IAGPOL polarimeter attached to the 0.6 m Boller & Chivens telescope at OPD/LNA³, Brazil. We used a CCD camera with a polarimetric module described by [Magalhães et al. \(1996\)](#), consisting of a rotating half-wave plate and a calcite prism placed in the telescope beam. A typical observation consists of 16 consecutive half-wave plate positions separated by 22.5° . In each observing run at least one polarized standard star HD 41117 or HD 187929 was observed to calibrate the observed position angle. Details of the data reduction can be found in

³ Observatório Pico dos Dias/Laboratório Nacional de Astrofísica.

Table 3. Summary of broadband polarization data that are contemporaneous to the VLTI observations.

Date	Band	Polarization(%)
2009 Sep. 21	B	0.008 ± 0.011
2009 Nov. 18	B	0.014 ± 0.026
2011 Jun. 29	B	0.016 ± 0.038
2011 Sep. 2	B	0.014 ± 0.036
2011 Sep. 2	V	0.025 ± 0.015
2011 Sep. 9	B	0.027 ± 0.018
2011 Sep. 9	V	0.023 ± 0.017
2011 Sep. 29	B	0.008 ± 0.030
2011 Sep. 29	V	0.013 ± 0.018
2011 Oct. 19	B	0.026 ± 0.039
2011 Oct. 19	V	0.013 ± 0.016
2011 Nov. 3	V	0.015 ± 0.036
2012 Jul. 1	V	0.017 ± 0.015
2012 Nov. 21	V	0.035 ± 0.050

Notes. These data are plotted in Fig. 2.

[Magalhães et al. \(1984\)](#). A summary of our polarimetric data is presented in Table 3.

The IAGPOL data, shown in Fig. 2, exhibit values compatible with no intrinsic polarization, having a weighted average polarization of only $0.019 \pm 0.012\%$ during the observed period. This average is used in Sect. 3.2 as an upper limit to the polarization from a possible residual disk. This low polarization level contrasts with the measurements from a period of stellar activity in 2006, where the presence of circumstellar material lead to a polarization 10 times higher (up to 0.19% in B band), as shown by [Carciofi et al. \(2007\)](#). These authors also reported a clear spectroscopic signal with an $H\alpha$ emission-to-continuum (E/C) ratio of ~ 1.06 . The polarization values shown here also suggest no significant contribution from the interstellar medium to this quantity.

In addition to the polarimetric data, $H\alpha$ and $H\beta$ spectra of Achernar contemporaneous to the VLTI observations were also analyzed in search for possible signatures of a circumstellar disk. We obtained seven spectra at OPD/LNA, using the Cassegrain spectrograph (ECass) with 600 groove mm^{-1} grating blazed at 6563 Å in first order, resulting in a reciprocal dispersion of $1.0 \text{ \AA pixel}^{-1}$. FEROS and HARPS spectra were also used to complement the OPD data. The spectroscopic observations are summarized in Table 4.

Following [Rivinius et al. \(2013\)](#), we adopted the FEROS spectra from early 2000 as a reference photospheric spectrum for Achernar. In Fig. 3 we plot the $H\alpha$ and $H\beta$ line profiles (top panels) and the difference profiles, computed as the difference between the observed profiles and the reference FEROS spectrum

3.2. The Be star Achernar (α Eridani)

A&A 569, A10 (2014)

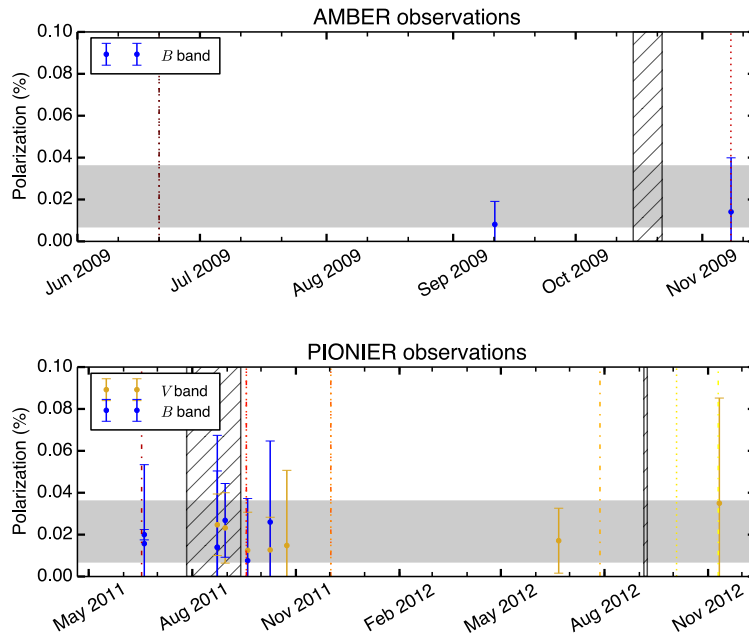


Fig. 2. Polarimetric observations at the epochs of ESO-VLTI AMBER and PIONIER data of Achernar analyzed in this work (vertical hatched bars). All the measurements are compatible with null/negligible polarization. The horizontal gray bars indicate the weighted average of the polarization: $0.019 \pm 0.012\%$. Vertical lines correspond to epochs of $H\alpha$ (dotted) and $H\beta$ (dot-dashed) data observations with colors corresponding to the spectra shown in Fig. 3. The spectroscopic and polarimetric data are thus contemporaneous and embrace the interferometric observations in time.

Table 4. Summary of spectroscopic data of Achernar that are contemporaneous to the VLTI observations.

Date	H line	Instrument	Min. Resolution
2000 Jan. 11	$H\alpha + H\beta$	ESO/FEROS	54 000
2009 Jul. 1	$H\alpha + H\beta$	ECass/OPD	3400
2009 Nov. 18	$H\beta$	ECass/OPD	3400
2011 Jun. 27	$H\alpha$	ECass/OPD	5400
2011 Sep. 28	$H\alpha + H\beta$	ECass/OPD	3400
2011 Dec. 12	$H\alpha + H\beta$	ESO/HARPS	109 000
2012 Aug. 7	$H\alpha$	ECass/OPD	5400
2012 Oct. 14	$H\beta$	ECass/OPD	3400
2012 Nov. 20	$H\alpha$	ECass/OPD	5400

Notes. The typical S/N ratio is 300. The $H\alpha$ and $H\beta$ spectra are shown in Fig. 3.

(bottom panels). All difference profiles are completely featureless, with difference values typically between -0.012 and 0.012 .

Thus, the polarimetric and spectroscopic data above suggest that the presence of a strong Be disk contemporaneous to the interferometric data can be discarded. In the following we quantify this assumption based on physical models of Be disks constrained by the observational limits imposed by the contemporaneous polarimetry (below $0.019 \pm 0.012\%$) and spectroscopy (disk signatures below 0.012 in absolute values relative to a photospheric profile).

3.2. Residual disk

We investigate here whether the presence of a weak residual disk that is hard to detect from non-angularly resolved observations could still affect the interferometric observations of

Achernar. This weak disk is constrained by the limits imposed by contemporaneous polarimetric and spectroscopic data determined in the previous section.

Using radiative transfer simulations from the HDUST code (Carciofi & Bjorkman 2006), we computed a grid of models based on our previous grid used to investigate the 2002 phase of Achernar (Carciofi et al. 2008): a large and dense disk in hydrostatic equilibrium (i.e., geometrically thin) and a smaller and more tenuous disk with enhanced scale height (i.e., geometrically thick). We adopted a power-law radial density profile,

$$\rho(r) = \rho_0 \left(\frac{R_{\text{eq}}}{r} \right)^m, \quad (1)$$

where R_{eq} is the stellar equatorial radius where the disk starts (inner disk radius), ρ_0 is the density of the disk at R_{eq} (density scale), and m is chosen as 3.5 corresponding to the steady-state regime of a viscous decretion disk (VDD) model (cf. Haubois et al. 2012, and references therein). To study the influence of the disk on the different observables we varied ρ_0 considering two sets of disk sizes R_d and scale heights H_0 at the inner disk radius. Table 5 details the parameters of these two sets of VDD models. In addition to these VDD models, we also used HDUST to compute a reference ellipsoidal photospheric model of Achernar compatible with the more physical photospheric model determined in Sect. 4.

The dependence of the polarimetric and spectroscopic observables on the density ρ_0 for the two VDD models are shown in Fig. 4, where the quantities predicted from the models are compared with our observational constraints. By comparing the modeled and observed limits determined in Sect. 3 for the polarization and difference $H\alpha$ spectra, we can set strict upper limits to ρ_0 : $\rho_0 < 0.52 \times 10^{-12} \text{ g cm}^{-3}$ (thin disk) and $\rho_0 < 0.65 \times 10^{-12} \text{ g cm}^{-3}$ (thick disk). As shown in Fig. 4, these limits are mainly imposed by the polarimetric data.

3. High spectro-spatial resolution observations of fast rotators in the H-R diagram

A. Domiciano de Souza et al.: The environment of the fast rotating star Achernar. III.

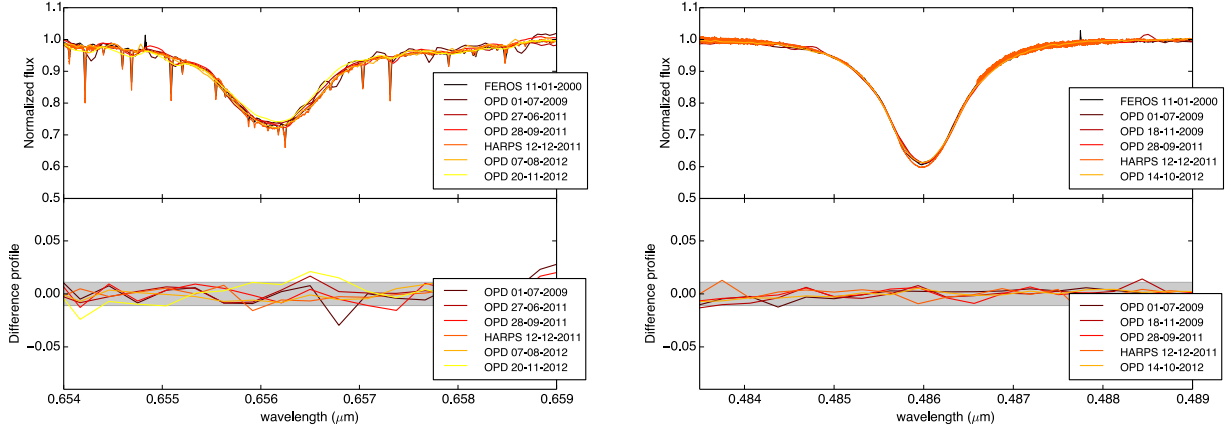


Fig. 3. *Top:* $H\alpha$ (left) and $H\beta$ (right) line profiles of Achernar at the epoch of interferometric observations. *Bottom:* difference in flux of the line profiles with respect to the reference FEROS spectrum from 2000 Jan. 11. This spectrum can be considered as a good approximation to the pure photospheric profile of Achernar (Rivinius et al. 2013). Whenever possible (enough spectral resolution) the telluric lines seen in some spectra have been removed before computing the differences. The horizontal shaded (gray) areas indicate the typical error on the difference profiles and also set a limit to them.

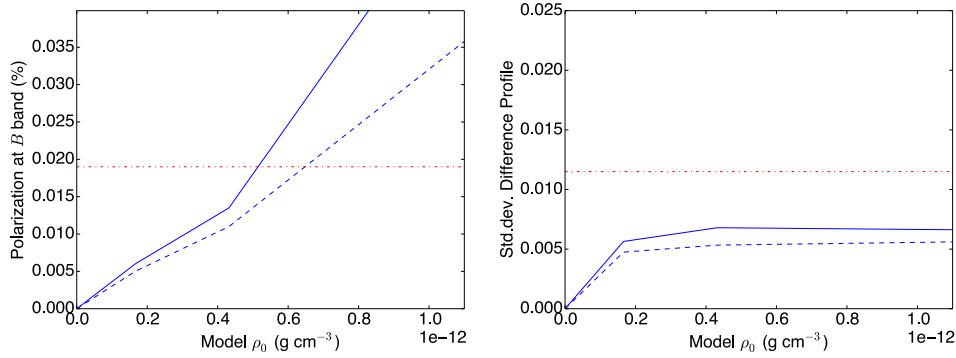


Fig. 4. Polarization in the B band (left) and standard deviation of difference $H\alpha$ profile (right) as a function of disk-base density ρ_0 for the residual disk models from Table 5 (model 1: full line; model 2: dashed line). The standard deviation is the root mean square of the disk model spectrum minus the pure photospheric profile. The horizontal dot-dashed lines represent the observational limits of average polarization and difference profile determined from observations performed at the epoch of interferometric observations, as explained in Sect. 3. While the measured $H\alpha$ difference profile level does not impose a limit to ρ_0 , the measured average polarization sets a strict upper limit to this quantity: $\rho_0 < 0.52 \times 10^{-12} \text{ g cm}^{-3}$ for the thin-disk model and $\rho_0 < 0.65 \times 10^{-12} \text{ g cm}^{-3}$ for the thick-disk model.

Table 5. Parameters of the two geometrical configurations of the residual VDD models.

Disk Model	ρ_0 range ($10^{-12} \text{ g cm}^{-3}$)	R_d (R_\odot)	H_0 (R_\odot)
1 (thin)	0.2–7.5	11.0	0.37
2 (thick)	0.2–7.5	10.1	0.73

Notes. The photospheric parameters are kept constant for the simulations. For a given density ρ_0 the total mass of the disk is the same for both models.

Figure 5 shows detailed a comparison of the VDD modeled $H\alpha$ line profiles for these two ρ_0 limits with the photospheric profile. As expected, the difference profiles have almost everywhere values within the ± 0.012 limit determined from the observed difference profiles (Sect. 3). Only at the wings of the $H\alpha$ profiles the VDD models present some weak signatures differing slightly from the pure photospheric profile. This detailed investigation of $H\alpha$ profiles combined with the results from Fig. 4

thus shows that the limits to ρ_0 imposed by polarimetry are also reliable upper limits to hydrogen spectral lines.

By adopting these limits to ρ_0 we now evaluate the signatures that a possible residual disk might have on our interferometric observations of Achernar. These evaluations are shown in Fig. 6, which compares the H band squared visibilities V^2 , and $\text{Br}\gamma$ differential phases computed with the two VDD models (Table 5) with the expected values for the purely photospheric model. All deviations from the photospheric model are well within the typical observational errors on these interferometric quantities.

Therefore, in the following analysis we can safely rule out any effects of the known companion and of a significant residual disk around Achernar on our interferometric observations.

4. Achernar's photospheric parameters from VLTI observations

Based on the results from the previous section we adopted a model of a fast rotating, single B star without circumstellar

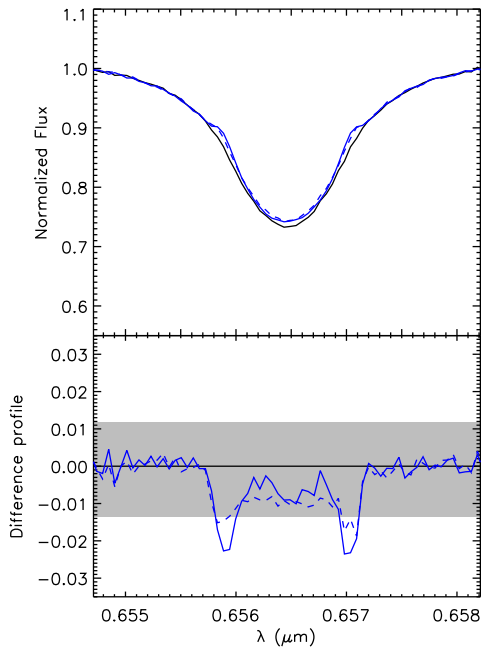


Fig. 5. *Top:* $H\alpha$ line profile for the pure photospheric model (black solid line) and with a residual disk (VDD model) as defined in Table 5 and computed for the upper limit values of ρ_0 (cf. Fig. 4): $0.52 \times 10^{-12} \text{ g cm}^{-3}$ (thin disk; blue solid line) and $0.65 \times 10^{-12} \text{ g cm}^{-3}$ (thick disk; blue dashed line). *Bottom:* the difference between the disk models relative to the photospheric model. The observational limit set to the difference profiles defined in Sect. 3 is indicated by the shaded (gray) region.

environment as a starting point to interpret the interferometric data of Achernar.

4.1. Photospheric model of fast-rotating stars

Most recent works describe the photospheric structure of rapidly rotating, nondegenerate, single stars of intermediate to high masses by adopting a Roche model (rigid rotation and mass concentrated in the stellar center) with a generalized form of the von Zeipel gravity darkening (von Zeipel 1924). We adopted this model since it has proven to well reproduce many distinct observables on rapid rotators (e.g., this work on Achernar and the cited references on other stars). Whether this is the only/best representation for their photospheres could be tested based on future and more precise observations.

Many codes exist that provide similar numerical implementations of this model, hereafter called the RVZ model. The reference numerical code for the RVZ model used here is the IDL-based program CHARRON (Code for High Angular Resolution of Rotating Objects in Nature). We present below a short description of CHARRON in the context of the present work. A more detailed description is given by Domiciano de Souza et al. (2012a,b, 2002).

The stellar photospheric shape follows Roche equipotential (gravitational plus centrifugal),

$$\Psi(\theta) = -\frac{GM}{R(\theta)} - \frac{\Omega^2 R^2(\theta) \sin^2 \theta}{2} = -\frac{GM}{R_{\text{eq}}} - \frac{V_{\text{eq}}^2}{2}, \quad (2)$$

where θ is the colatitude, M is the stellar mass, and R_{eq} and V_{eq} are the equatorial radius and rotation velocity. Solving this cubic equation provides the colatitude-dependent stellar radius $R(\theta)$.

Gravity darkening is considered by relating the local effective gravity $g_{\text{eff}}(\theta) (= |\nabla\Psi(\theta)|)$ to the local effective temperature $T_{\text{eff}}(\theta)$ by,

$$T_{\text{eff}}(\theta) = \left(\frac{C}{\sigma}\right)^{0.25} g_{\text{eff}}^{\beta}(\theta), \quad (3)$$

where σ is the Stefan-Boltzmann constant and β is the gravity-darkening coefficient, which is more general than the $\beta = 0.25$ value from von Zeipel (1924), but which is still assumed to be constant over the stellar surface. We note that for the spectral type of Achernar we can neglect any radiative acceleration effects since it is far from the Eddington limit. The proportionality constant C can be derived from stellar physical parameters such as mass and luminosity (e.g., Maeder & Meynet 2000) or related to a fixed point on the photosphere (the stellar pole, for example). In this work, the constant C and the stellar luminosity L are related to the average effective temperature \bar{T}_{eff} over the total stellar surface S_{\star} (area of the Roche photosphere),

$$L = \sigma \int T_{\text{eff}}^4(\theta) dS = \sigma \bar{T}_{\text{eff}}^4 S_{\star} = C \int g_{\text{eff}}^{4\beta}(\theta) dS. \quad (4)$$

\bar{T}_{eff} can be directly related to the bolometric flux F_{bol} and to the mean angular diameter \overline{D} (diameter of spherical star having a surface area S_{\star}) by,

$$F_{\text{bol}} = \sigma \bar{T}_{\text{eff}}^4 \frac{S_{\star}}{4\pi d^2} = \sigma \bar{T}_{\text{eff}}^4 \frac{\overline{D}^2}{4}, \quad (5)$$

where d is the distance to the star.

In our numerical implementation of the RVZ model the stellar surface is divided into a predefined grid with nearly identical surface area elements (typically $\sim 50\,000$ surface elements). From $T_{\text{eff}}(\theta)$ and $g_{\text{eff}}(\theta)$ defined in the above equations, a local specific intensity from a plane-parallel atmosphere $I = I(g_{\text{eff}}, T_{\text{eff}}, \lambda, \mu)$ is associated with each surface element, where λ is the wavelength and μ is the cosine between the normal to the surface grid element and the line of sight (limb darkening is thus automatically included in the model). The local specific intensities I are interpolated from a grid of specific intensities that are pre-calculated using the spectral synthesis code SYNOPSIS (Hubeny & Lanz 2011) and the ATLAS9 stellar atmosphere models (Kurucz 1979). For Achernar, we adopted atmosphere models with turbulent velocity of 2 km s^{-1} and solar abundance in agreement with its spectral type and short distance.

From the local specific intensities we obtained wavelength-dependent intensity maps of the visible stellar surface at the chosen spectral domain and resolution, such as the image given in Fig. 11. The interferometric observables (e.g., squared visibilities, closure phases, differential phases) are then directly obtained from the Fourier transform of these sky-projected photospheric intensity maps, which for a given star in the sky also depend on its rotation-axis inclination angle i and on the position angle of its sky-projected rotation axis PA_{rot} (counted from north to east until the visible stellar pole).

Thus, the main input parameters of the photospheric RVZ model for fast rotators used to interpret the interferometric observations of Achernar are M , R_{eq} , V_{eq} , β , \bar{T}_{eff} , i , PA_{rot} , and d .

3. High spectro-spatial resolution observations of fast rotators in the H-R diagram

A. Domiciano de Souza et al.: The environment of the fast rotating star Achernar. III.

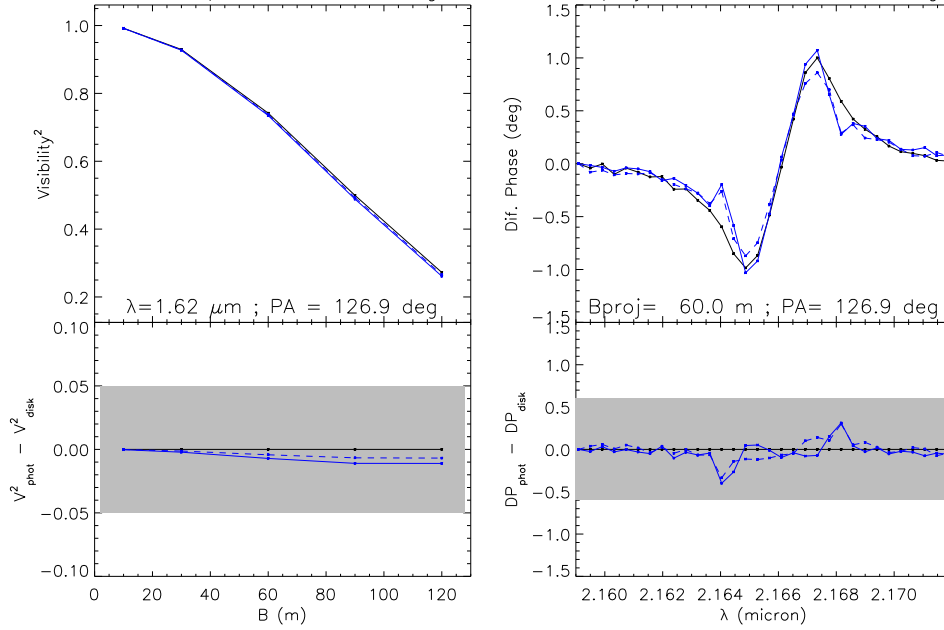


Fig. 6. Interferometric observables, squared visibilities V^2 in the H band (*left*), and $\text{Br}\gamma$ differential phases (*right*), computed for the pure photospheric model (black solid line) and for the two residual-disk models as defined in Table 5 at the upper limit values of ρ_0 (cf. Fig. 4): $0.52 \times 10^{-12} \text{ g cm}^{-3}$ (thin disk; blue solid line) and $0.65 \times 10^{-12} \text{ g cm}^{-3}$ (thick disk; blue dashed line). The baseline position angle PA was chosen to lie along the stellar equator (cf. Sect. 4.2), so that the effects of the residual disk are maximized on these comparisons. The baseline length for the differential phase calculations roughly corresponds to half of the maximum available length. *Bottom*: the difference between the interferometric observables from the disk models relative to the photospheric model. The shaded areas correspond to the typical observational errors from our PIONIER and AMBER observations. These difference plots show that the disk contribution to the interferometric observables is only a small fraction of the observation errors even at the upper limit ρ_0 , discarding any detectable influence of a circumstellar disk on the present interferometric observations of Achernar.

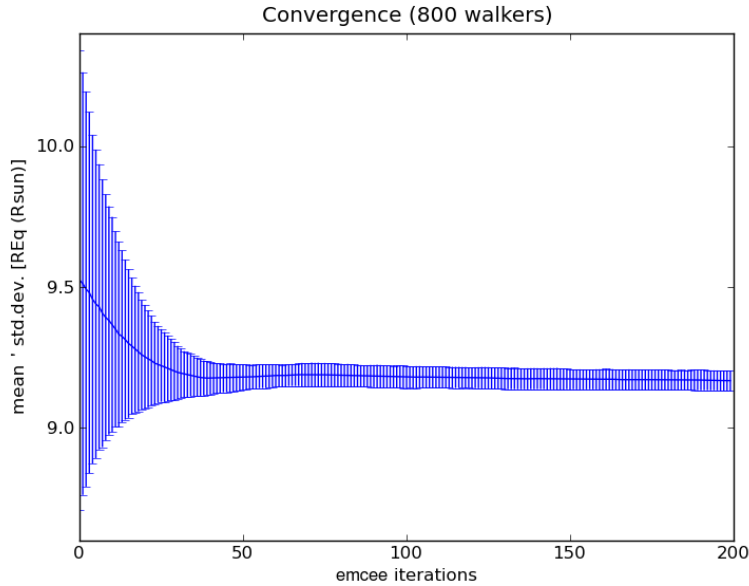


Fig. 7. Convergence of equatorial radius R_{eq} during the burn-in phase of the MCMC fit of the CHARRON RVZ model to the VLTI/PIONIER data using the emcee code (800 walkers and 200 iteration steps).

4.2. Fitting of the CHARRON model to VLTI/PIONIER data with an MCMC method

We used the CHARRON model to constrain several photospheric parameters of Achernar from the PIONIER observations (described in Sect. 2.1), which consists of a homogenous

data set obtained with the same beam-combiner instrument at ESO-VLTI. To be compatible with the observations, the CHARRON intensity maps were calculated over the H band with a spectral resolution of $\sim 20\text{--}40$. We note that in broadband observations, the effect of bandwidth smearing (mixing of different spatial frequencies in a given wavelength bin) can lead to a

3.2. The Be star Achernar (α Eridani)

A&A 569, A10 (2014)

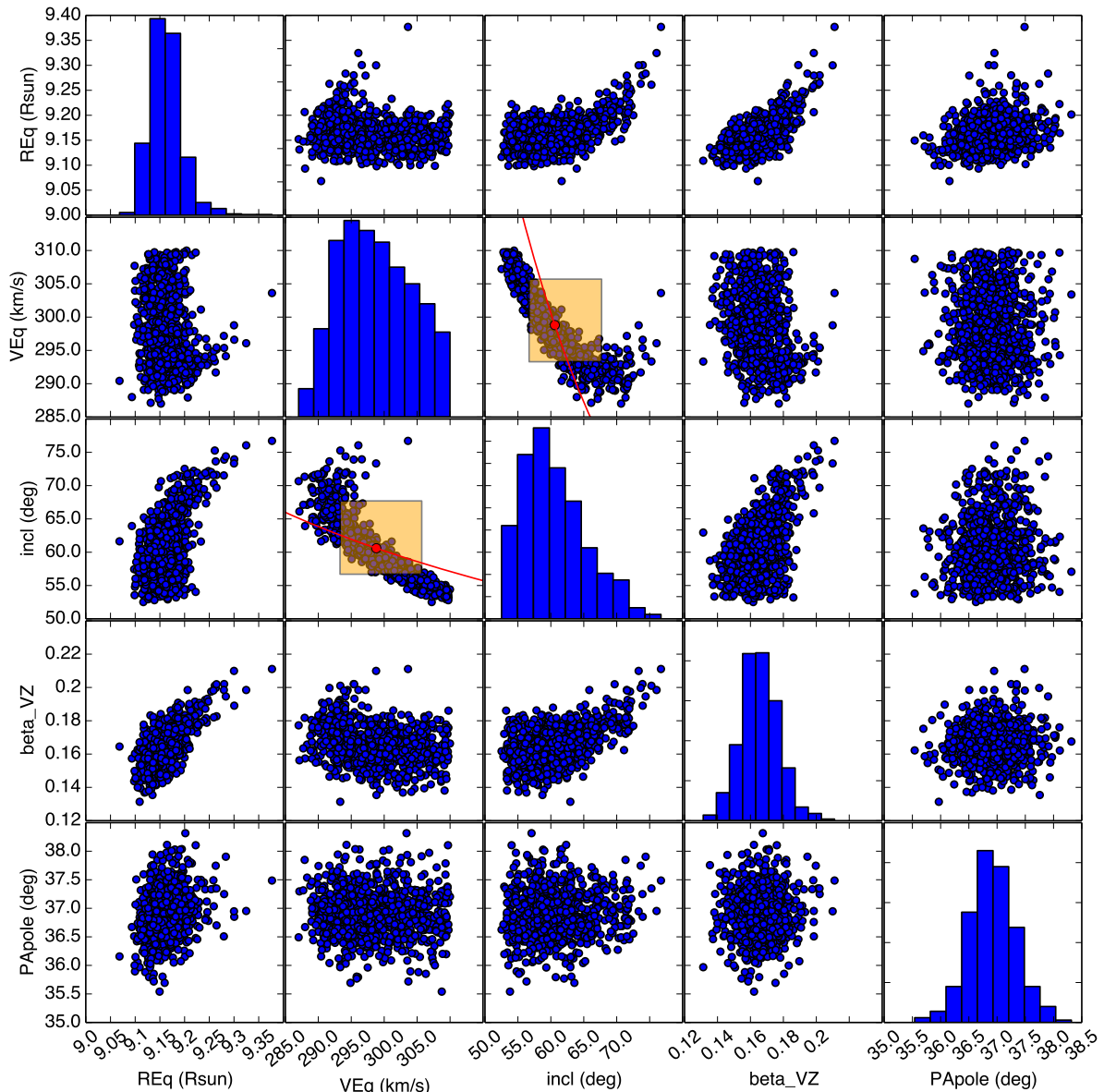


Fig. 8. Histogram distributions and two-by-two correlations for the free parameters (R_{eq} , V_{eq} , i , β , and PA_{rot}) of the best-fit CHARRON RVZ model determined with the emcee code (800 walkers). The mean values and associated uncertainties obtained from these histograms are given in Table 6. The parameters do not show strong correlations in the region defined by the uncertainty around the mean values. The stronger correlation is shown by V_{eq} and i , which roughly follow a curve of constant $V_{\text{eq}} \sin i$ ($\approx 260.3 \text{ km s}^{-1}$), represented by the solid lines, with the circles indicating the mean values in the histograms. The rectangles cover the corresponding uncertainty ranges on V_{eq} and i .

decrease of visibility contrast and should in principle be considered. However, we checked that the bandwidth-smearing effect does not need to be considered in the present analysis because (1) the squared visibilities are higher than 0.3–0.4, which minimizes this effect (Kervella et al. 2003); and (2) the data span a few wavelength bins over the H band so that the range of spatial frequencies mixed is narrow. Based on results from previous works, M , \bar{T}_{eff} , and d were fixed to the following values:

- $M = 6.1 M_{\odot}$. Value from Harmanec (1988), previously adopted by Domiciano de Souza et al. (2012a). This mass also agrees (1) with the estimate from

Jerzykiewicz & Molenda-Zakowicz (2000) ($M = 6.22 \pm 0.16 M_{\odot}$) based on evolutionary tracks; and (2) with the mass estimate from an on-going work on Achernar’s binary system (Kervella et al., in prep.);

- $\bar{T}_{\text{eff}} = 15\,000 \text{ K}$. Value adopted by Domiciano de Souza et al. (2012a) following Vinicius et al. (2006). A critical discussion on this value and comparisons with other works are presented in Sect. 5;
- $d = 42.75 \text{ pc}$. We adopted the updated distance derived from the new reduction of the Hipparcos astrometric data and provided by van Leeuwen (2007).

3. High spectro-spatial resolution observations of fast rotators in the H-R diagram

A. Domiciano de Souza et al.: The environment of the fast rotating star Achernar. III.

Table 6. Physical parameters of Achernar derived from the fit of the RVZ model (CHARRON code) to VLTI/PIONIER H band data using the MCMC method (emcee code).

Free model parameters fitted	Values and uncertainties
Equatorial radius: $R_{\text{eq}} (R_{\odot})^a$	9.16 (+0.23; -0.23)
Equatorial rotation velocity: $V_{\text{eq}} (\text{km s}^{-1})$	298.8 (+6.9; -5.5)
Rotation-axis inclination angle: $i (^{\circ})$	60.6 (+7.1; -3.9)
Gravity-darkening coefficient: β	0.166 (+0.012; -0.010)
Position angle of the visible pole: $\text{PA}_{\text{rot}} (^{\circ})$	216.9 (+0.4; -0.4)
Derived parameters	Values
Equatorial angular diameter: $\mathcal{D}_{\text{eq}} = 2R_{\text{eq}}/d$ (mas)	1.99
Polar radius: $R_{\text{p}} (R_{\odot})$	6.78
$R_{\text{eq}}/R_{\text{p}}; \epsilon \equiv 1 - R_{\text{p}}/R_{\text{eq}}$	1.352; 0.260
Apparent flattening (major to minor axis ratio)	1.30
Mean angular diameter: $\overline{\mathcal{D}}$ (mas)	1.77
$V_{\text{eq}} \sin i$ (km s^{-1})	260.3
Critical rotation rate ^b : $V_{\text{eq}}/V_{\text{c}}; \Omega/\Omega_{\text{c}}$	0.883; 0.980
Keplerian rotation rate ^c : $V_{\text{eq}}/V_{\text{k}}; \Omega/\Omega_{\text{k}}$	0.838; 0.838
Polar temperature: T_{p} (K)	17 124
Equatorial temperature: T_{eq} (K)	12 673
Luminosity: $\log L/L_{\odot}$	3.480
Equatorial gravity: $\log g_{\text{eq}}$	2.772
Polar gravity: $\log g_{\text{p}}$	3.561
Rotation period: P_{rot} (h)	37.25
Rotation frequency: ν_{rot} (d^{-1})	0.644

Notes. Details of the fit are given in Sect. 4.2. ^(a) The uncertainty in the distance d from van Leeuwen (2007) was added quadratically to the fit uncertainty on R_{eq} . ^(b) Critical (Roche model) linear (V_{c}) and angular (Ω_{c}) velocities: $V_{\text{c}} = \Omega_{\text{c}} R_{\text{eq,c}} = \sqrt{GM/R_{\text{eq,c}}}$, with $R_{\text{eq,c}} = 1.5R_{\text{p}}$ (critical Roche equatorial radius). ^(c) Keplerian (orbital) linear (V_{k}) and angular (Ω_{k}) velocities: $V_{\text{k}} = \Omega_{\text{k}} R_{\text{eq}} = \sqrt{GM/R_{\text{eq}}}$.

The free parameters are thus R_{eq} , V_{eq} , i , β , and PA_{rot} .

The model-fitting was performed using the emcee code (Foreman-Mackey et al. 2013), which is a Python implementation of a Markov chain Monte Carlo (MCMC) method proposed by Goodman & Weare (2010). This code has been recently used by Monnier et al. (2012) to interpret interferometric observations.

From a given likelihood function of the parameters, emcee provides histograms of the free model parameters (samplings of the posterior probability) from which one can estimate the best parameter values and associate uncertainties. In the present work, the measurement errors on V^2 and CP are all assumed to be independent and normally distributed so that the likelihood function is proportional to $\exp(-\chi^2)$, where χ^2 has its usual definition and is composed of $\chi^2 = \chi_{V^2}^2 + \chi_{\text{CP}}^2$ (sum of χ^2 from the V^2 and CP data, respectively). To equally explore an homogenous range of initial values, we adopted initial uniform distributions for the five free CHARRON parameters that cover a wide range of physically consistent values.

The emcee algorithm explored the defined parameter space using 800 walkers in a 200 steps initial phase (burn-in) and 150 steps in the final phase, starting from the last state of the burn-in chain (for details of using the code see Foreman-Mackey et al. 2013). Convergence of the parameters distribution was typically attained within $\lesssim 100$ steps during the burn-in phase (an example for R_{eq} is shown in the electronically available Fig. 7).

The final histograms of the five free parameters and their two-by-two correlations are shown in Fig. 8 (available electronically). The best-fit values of the free parameters are the mean of these histograms. The uncertainties on the parameters were defined as corresponding to a range enclosing $\pm 34.15\%$ of the parameter distribution relative to the mean value (this corresponds to the commonly used rule for normal distributions). The

reduced χ^2 of the best-fit model is $\chi_r^2 = 1.9$ (for 1777 degrees of freedom DOF and free free parameters).

Table 6 summarizes the best-fit parameter values and uncertainties measured on Achernar from the MCMC fit of CHARRON RVZ model to the VLTI/PIONIER data. Other derived stellar parameters are also given in the table. The V^2 and CP corresponding to this best-fit model are plotted together with the observations in Figs. 9 and 10. The sky-projected intensity map of the visible stellar photosphere for this model is shown in Fig. 11.

As a completely independent check of the results above, we have also performed a Levenberg-Marquardt fit to the PIONIER data using a different RVZ model developed by one of us (A. Mérand). The best-fit parameter values obtained agree well (within the emcee error bars) with the values derived from the emcee fit of the CHARRON RVZ model.

5. Discussion

5.1. Radius and angular diameter

Long-baseline interferometry is traditionally known to deliver stellar angular diameters (and radii, if distances are available). These size measurements are directly dependent on the chosen photospheric model and on how fairly this model can represent the stellar photosphere. As shown in Sect. 4, the stellar radius is a function of the co-latitude for fast rotators, and the apparent stellar photosphere is dependent on additional parameters such as gravity darkening, effective temperature, rotation velocity, and polar inclination (discussed in the following subsections).

As explained in the previous sections, the equatorial radius R_{eq} determined here (or more generally the photospheric $R(\theta)$) is based on a physical model fitted to observations taken on a normal B phase of Achernar. As expected, the R_{eq} measured

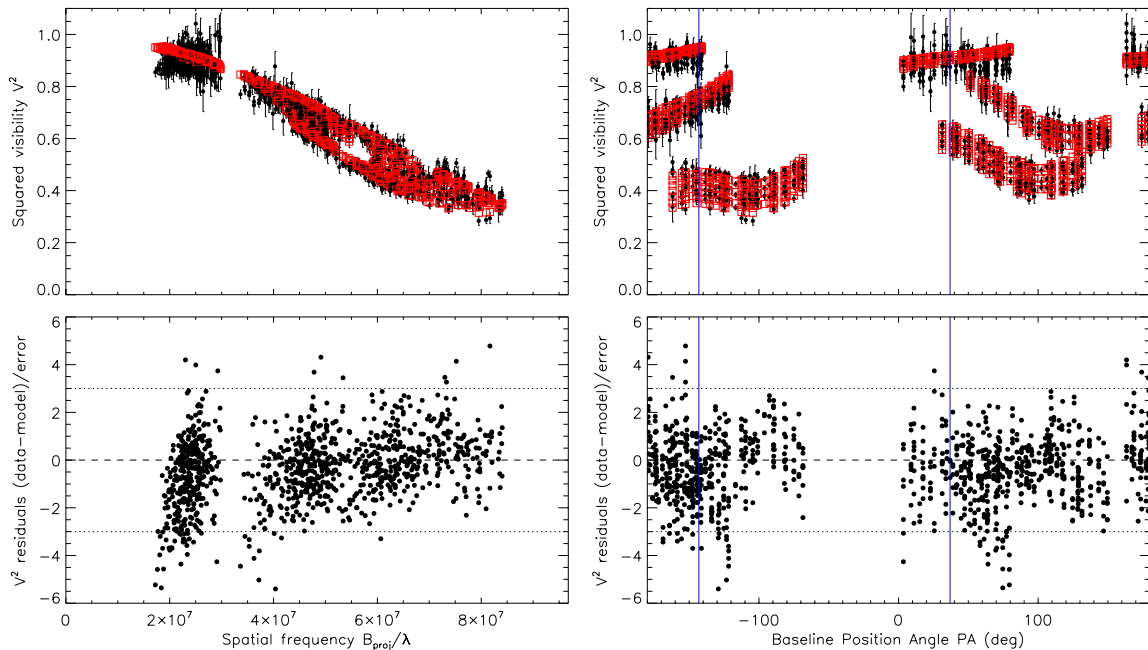


Fig. 9. *Top:* squared visibilities V^2 observed on Achernar (filled circles and error bars) and computed (opened squares) from the best-fit CHARRON model (Table 6) as a function of spatial frequency (*left column*) and baseline PA (*right column*). *Bottom:* V^2 residuals from observations relative to the best-fit model in units of corresponding uncertainties. Vertical solid lines indicate the position angles of the visible ($216.9^\circ \equiv -143.1^\circ$) and hidden ($16.9^\circ = 216.9^\circ - 180^\circ$) stellar poles. The horizontal dotted lines delimit the $\pm 3\sigma$ region around zero (dashed line).

in this work is smaller than the previous results derived from VLTI/VINCI observations, obtained in an epoch with a small, but non-negligible influence of a residual disk (Domiciano de Souza et al. 2003; Kervella & Domiciano de Souza 2006; Carciofi et al. 2008).

We discuss the stellar size derived from the VLTI/AMBER observations by Domiciano de Souza et al. (2012a), we postpone the discussion to Sect. 5.5, where we consider the whole set of model parameters.

Considering the stellar size derived from the VLTI/AMBER observations by Domiciano de Souza et al. (2012a) in Sect. 5.5, where we consider the whole set of model parameters.

5.2. Photometry and effective temperature

The photometric magnitudes in the *UBVJHK* bands and the bolometric flux derived from the CHARRON best-fit model are compared with measurements reported in the literature in Table 7. We first note from the table that these observed magnitudes and bolometric fluxes show uncertainties and/or a dispersion of measured values of about 10%–20%, which are at least partially caused by a combination of instrumental and intrinsic effects from the star. Indeed, Achernar is known to present multiple flux variabilities at time scales from hours to years, which are caused, for example, by pulsations (Goss et al. 2011), binarity (Kervella & Domiciano de Souza 2007), and the B ζ Be cycle (e.g., Vinicius et al. 2006). Thus, the observed magnitudes and bolometric flux should not be considered as tight constraints to the model-fitting, although they provide an important consistency check on the best-fit model parameters. Indeed, the modeled magnitudes and bolometric flux given in Table 7 agree with the observations within their uncertainties and/or dispersion of measured values.

By using Eq. (5) we can cross-check the consistency between the adopted mean effective temperature \bar{T}_{eff} , the measured bolometric flux F_{bol} , and the mean angular diameter $\bar{\vartheta}$ reported in Tables 6 and 7. From the F_{bol} provided by Code et al. (1976) and Nazé (2009) one thus obtains $\bar{T}_{\text{eff}} = 15\,094$ K and $14\,703$ K. We note that the temperature of $14\,510$ K estimated by Code et al. (1976) is somewhat lower than the value estimated here because they considered the higher angular diameter (1.92 mas) reported by Hanbury Brown et al. (1974), based on intensity interferometry observations at the Narrabri Observatory. As expected, this diameter is between the major and minor diameters derived in the present work. However, the measurements from Hanbury Brown did not allow taking into account the angular size variation with the baseline position angle caused by the rotational flattening of Achernar. Thus, recalling that the average effective temperature of $\approx 15\,000$ K reported by Vinicius et al. (2006) was derived from different methods, the adopted $\bar{T}_{\text{eff}} = 15\,000$ K agrees well with several independent measurements (bolometric fluxes, photometry, spectroscopy, and interferometry).

5.3. Inclination and rotation velocity

The inclination angle $i (=60.6^{+7.1}_{-3.9})$ measured in this work is compatible (within $\approx 1.5\sigma$) with the values ($i \sim 65\text{--}70^\circ$) estimated by Vinicius et al. (2006) and Carciofi et al. (2007).

Different values have been previously reported on the projected rotation velocity $V_{\text{eq}} \sin i$ of Achernar, with mainly three distinct range of values: $V_{\text{eq}} \sin i \sim 223\text{--}235$ km s $^{-1}$ (e.g., Slettebak 1982; Chauville et al. 2001; Vinicius et al. 2006), $V_{\text{eq}} \sin i = 292 \pm 10$ km s $^{-1}$ (Domiciano de Souza et al. 2012a), and $V_{\text{eq}} \sin i \sim 410$ km s $^{-1}$ (e.g., Hutchings & Stockley 1977; Jaschek & Egret 1982).

3. High spectro-spatial resolution observations of fast rotators in the H-R diagram

A. Domiciano de Souza et al.: The environment of the fast rotating star Achernar. III.

Table 7. Observed and modeled *UBVJHK* photometry and bolometric flux F_{bol} of Achernar.

Catalogue or reference	<i>U</i>	<i>B</i>	<i>V</i>	<i>J</i>	<i>H</i>	<i>K</i>	F_{bol} (10^{-9} W m $^{-2}$)
2MASS ^a				0.815 ± 0.254	0.865 ± 0.320	0.880 ± 0.330	
NOMAD Tycho-2 ^b		0.473	0.527				
Johnson et al. (1966)		0.32	0.47				
Code et al. (1976)							54.4 ± 4.3
Jaschek & Egret (1982)	-0.36	0.30	0.46				
Nazé (2009)							48.98
CHARRON RVZ model	-0.279	0.339	0.472	0.783	0.828	0.886	53.05
Model in 2012 paper	-0.387	0.215	0.333	0.596	0.631	0.684	62.90

Notes. The model values are based on the parameters given in Table 6 for the best emcee fit of CHARRON RVZ model to PIONIER data. For comparison, we also show the values derived from the model given by Domiciano de Souza et al. (2012a), based on the AMBER differential phases. ^(a) Cutri et al. (2003); Skrutskie et al. (2006). ^(b) Hog et al. (2000); Zacharias et al. (2005).

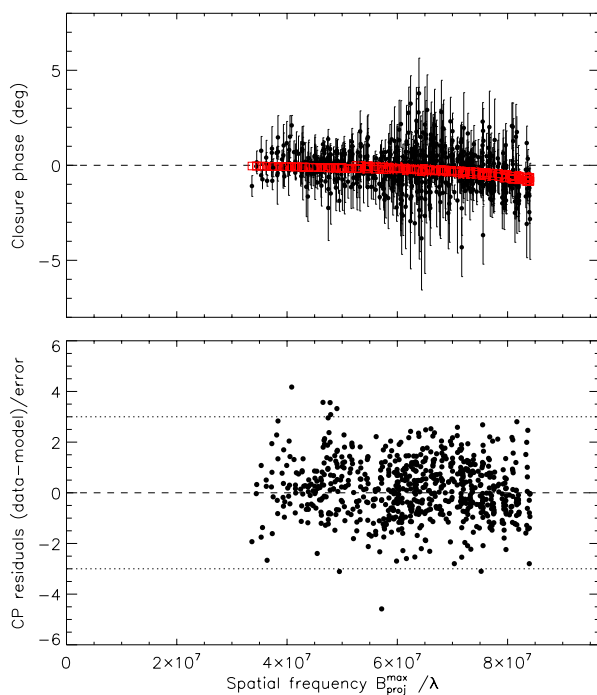


Fig. 10. *Top:* closure phases (CP) observed on Achernar and computed from the best-fit CHARRON model (Table 6) as a function of the spatial frequency (for the longest projected baseline $B_{\text{proj}}^{\text{max}}$ in the corresponding triangle configuration). *Bottom:* CP residuals from observations relative to the best-fit model in units of corresponding uncertainties. The horizontal dotted lines delimit the $\pm 3\sigma$ region around zero (dashed line). Since the photosphere is only partially resolved, the CP signatures of fast rotation are weak (within $\sim \pm 1^\circ$).

In this work we determine $V_{\text{eq}} \sin i = 260.3_{-12}^{+19}$ km s $^{-1}$, where these uncertainties were computed by properly adding the individual uncertainties estimated on i and V_{eq} (cf. Table 6 and Fig. 8). This estimated $V_{\text{eq}} \sin i$ lies between the lower and intermediate values found in the literature, as mentioned above, and it is compatible with them within 2σ to 3σ , i.e., $\approx 30\text{--}40$ km s $^{-1}$.

Some clues for explaining the discrepancies in the measured $V_{\text{eq}} \sin i$ may be given by the fact that different methods for estimating this quantity can lead to different results depending on their sensitivity to the nonuniform photospheric intensity distribution caused by the gravity darkening. For example, it is

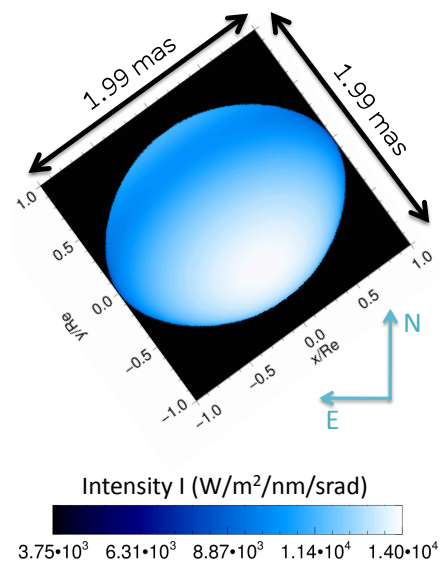


Fig. 11. Intensity map of Achernar corresponding to the best-fit of the CHARRON RVZ model to the VLT/PIONIER *H* band observations. The spatial coordinates indicated in angular milliarcseconds (mas) units and also normalized to the equatorial radius $R_{\text{eq}} = 9.16 R_{\odot}$. The complete list of the measured stellar parameters is given in Table 6.

known that because of gravity darkening, the $V_{\text{eq}} \sin i$ obtained from visible/IR spectroscopy are generally underestimated in fast-rotating stars (Townsend et al. 2004; Frémat et al. 2005). Moreover, the actual $V_{\text{eq}} \sin i$ of Achernar seems to significantly vary in time, as recently shown by Rivinius et al. (2013), who reported $V_{\text{eq}} \sin i$ variations with amplitudes $\lesssim 35$ km s $^{-1}$ that are correlated to the B ζ Be phase transitions. Interestingly, this amplitude of $V_{\text{eq}} \sin i$ variations is on the same order of the differences between the $V_{\text{eq}} \sin i$ values measured in this work and those reported by several other authors, as discussed above.

Finally, Goss et al. (2011) identified a low-amplitude frequency of 0.68037 ± 0.00003 d $^{-1}$ from time-series analysis of photometric light-curves of Achernar. We note that this frequency is relatively close (but still $\sim 2.5\sigma$ above) to the rotation frequency $\nu_{\text{rot}} = 0.644 \pm 0.015$ d $^{-1}$ derived in the present work (uncertainty estimated by properly adding quadratically the relative maximum individual uncertainties on R_{eq} and V_{eq}). Whether or not the measured frequency is related to the rotation of Achernar remains to be further investigated.

3.2. The Be star Achernar (α Eridani)

A&A 569, A10 (2014)

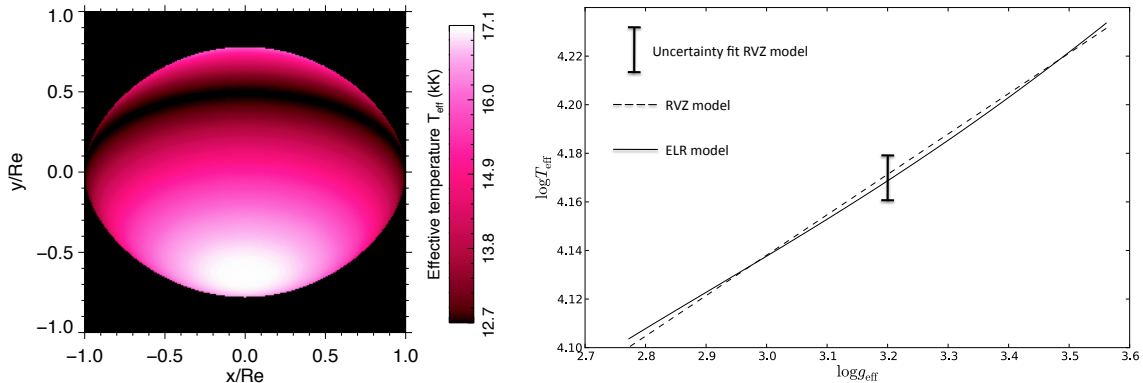


Fig. 12. *Left:* effective temperature map of Achernar corresponding to the best-fit of the CHARRON RVZ model to the VLT/PIONIER H band observations (model parameters in Table 6). The spatial coordinates are normalized to the measured equatorial radius $R_{\text{eq}} = 9.16 R_{\odot}$. The polar and equatorial effective temperatures of Achernar are $T_{\text{p}} = 17\,124$ K (white) and $T_{\text{eq}} = 12\,673$ K (black). *Right:* $\log T_{\text{eff}}$ as a function of $\log g_{\text{eff}}$ of Achernar for the ELR model (solid line from Espinosa Lara & Rieutord 2011). The calculations were performed considering a Roche model with the same stellar parameters as in Table 6, except for the gravity darkening, which is directly obtained from the ELR model. The dashed straight line shows the $\log T_{\text{eff}}$ versus $\log g_{\text{eff}}$ corresponding to the best-fit RVZ model with the measured gravity-darkening coefficient $\beta (=0.166^{+0.012}_{-0.010})$. The vertical bar indicates the uncertainty in T_{eff} associated with the measured uncertainty in this best-fit β value alone. We also note that by fitting a straight line to the ELR model (solid curve) results in an identical $\beta (=0.166)$ as measured with the CHARRON RVZ model, which exactly matches the dashed straight line. Thus, although the ELR model predicts a slightly more complex gravity-darkening relation than the RVZ model (Eq. (3)), these two gravity-darkening models agree within the uncertainties derived from the RVZ model fit to the PIONIER observations.

5.4. Gravity darkening

The gravity-darkening parameter β determined in this work is significantly lower than the von Zeipel law ($\beta = 0.25$), a result in agreement with β values derived from recent interferometric observations of fast-rotating stars (see for example the recent review from van Belle 2012, and references therein).

These low β (<0.25) were explained theoretically by Espinosa Lara & Rieutord (2011), who derived an alternative gravity-darkening law (ELR model hereafter) by relaxing the assumption of barotropicity that leads to the von Zeipel law. The ELR model includes a divergence-free flux vector and the ratio $T_{\text{eff}}^4/g_{\text{eff}}$ is allowed to vary with latitude, leading to an analytical relation between T_{eff} and g_{eff} without the need of assuming a constant β parameter as in Eq. (3). Let us compare in more detail the gravity darkening derived from the best-fit of the CHARRON RVZ model with the prediction from the ELR model. Both models adopt the Roche approximation so that they consider an identical photospheric shape $R(\theta)$. Based on the best-fit parameters in Table 6, Fig. 12 compares the $\log T_{\text{eff}}$ versus $\log g_{\text{eff}}$ relations for the two gravity darkening models. The T_{eff} map of the RVZ model is also illustrated in Fig. 12. As shown in the figure, the two models agree within the parameter uncertainties, but the present observation errors do not yet allow us to probe the small differences in $T_{\text{eff}}(\theta)$ predicted by the models.

Although the detailed $T_{\text{eff}}(\theta)$ cannot be investigated, it is clear that the ELR model reproduces an average $T_{\text{eff}}(\theta)$ dependence that is totally compatible with measurements from the RVZ model, but without the need of using a β parameter. Indeed, by estimating an equivalent β value (e.g., from $\log(T_{\text{eq}}/T_{\text{p}})/\log(g_{\text{eq}}/g_{\text{p}})$), Espinosa Lara & Rieutord (2011, in their Fig. 4) showed a good agreement between their predictions and the β coefficients measured on four fast rotators as a function of flattening ϵ ($\equiv 1 - R_{\text{p}}/R_{\text{eq}}$).

In Fig. 13 we extend this comparison by adding α Lyr (Vega; Monnier et al. 2012) and Achernar (α Eri; present work). These two new stars provide a crucial test for the ELR model since they have, respectively, the lowest and highest flattening in the

sample. Figure 13 thus compares β and ϵ from the ELR model with values measured on six fast rotators (listed from hotter to colder spectral types): α Eri (Achernar, B3-6Vpe; this work), α Leo (Regulus, B8IVn; Che et al. 2011), α Lyr (Vega, A0V; Monnier et al. 2012), α Aql (Altair, A7IV-V; Monnier et al. 2007), α Cep (Alderamin, A7IV; Zhao et al. 2009), β Cas (Caph, F2IV; Che et al. 2011).

Five out of the six stars agree relatively well with the ELR model (in particular Altair and Achernar), considering the observational uncertainties. The only exception is β Cas, and a more detailed study would be required to decide if the discrepancy is due to a bias in the measured flattening related to its low inclination (as discussed by Espinosa Lara & Rieutord 2011) and/or maybe related to the fact that this star is the coldest one in the sample. This agreement between observational and theoretical results is therefore a promising perspective for a more profound understanding of the gravity-darkening effect in rotating stars.

Based on the curve β versus flattening ϵ given in Fig. 13 and derived from the ELR model, we can deduce a linear relation that roughly follows this curve:

$$\beta \simeq 0.25 - 0.328\epsilon. \quad (6)$$

This linear approximation reproduces the curve in Fig. 13 within 1% (3%) for $\epsilon \lesssim 0.27$ (0.30). We recall, however, that the use of a β parameter is neither required nor compatible with the ELR model, which does not describe the gravity darkening by a power law as in Eq. (3).

5.5. Comparison with the VLT/AMBER differential phases

We now compare the best-fit CHARRON model determined from the PIONIER data (Table 6) with the AMBER differential phases, described in Sect. 2.2 and by Domiciano de Souza et al. (2012a). The differential phases computed directly from the PIONIER best-fit model already well reproduce the AMBER observations, resulting in $\chi_{\text{r}}^2 = 1.3$ (DOF = 3808). This χ_{r} is only slightly higher than the 1.2 value found by Domiciano de Souza et al. (2012a) from the same model, but

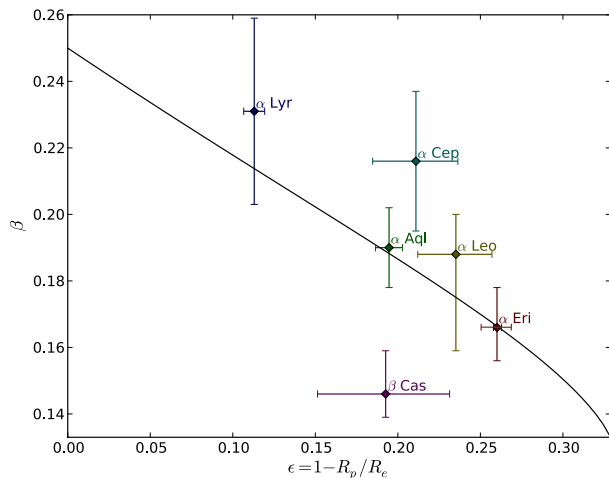


Fig. 13. Gravity-darkening coefficient β estimated from the ELR model (Espinosa Lara & Rieutord 2011) as a function of the rotation flattening ϵ compared with values measured from interferometric observations of six rapidly rotating stars (references in Sect. 5.4), Achernar (α Eri) being the flattest one. The estimate of β is obtained from a fit to the $\log T_{\text{eff}}$ versus $\log g_{\text{eff}}$ curves directly predicted by the ELR model, such as in Fig. 12 (right). The ELR model predictions and interferometric measurements have a good general agreement (see Sect. 5.4 for a more detailed discussion).

with a somewhat different set of parameters. Indeed, for all AMBER baselines and wavelengths considered, the absolute differences between both sets of modeled differential phases are smaller than 0.5° , which is lower than the typical uncertainties in the differential phases for these AMBER observations (median value of 0.6°).

Conversely, the photospheric model parameters derived from the AMBER differential phases (Domiciano de Souza et al. 2012a) are far from reproducing the PIONIER observations, resulting in a 10 times higher χ_r^2 ($=19.2$). Moreover, compared to the best-fit model determined in this work, the model from Domiciano de Souza et al. (2012a) presents a worse agreement with the photometric observations as shown in Table 7 (brighter star in particular because of the higher β and size). Thus, the CHARRON RVZ photospheric model with parameters as in Table 6 provides the best general agreement with the whole set of polarimetric, spectroscopic, photometric, and interferometric (PIONIER and AMBER) observations of Achernar considered in this work.

6. Beyond the photospheric model ?

We have shown in Sect. 3 that the interferometric data analyzed in this work are not influenced by a strong circumstellar disk or by the known binary companion. This conclusion agrees with the good quality of the fit obtained by adopting a single photospheric fast rotator RVZ model in Sect. 4. In spite of this satisfactory result, and relying on the relatively high-precision PIONIER data, we take the analysis a step farther to search for possible more subtle components in the close environment of Achernar and/or indications of small deviations from the adopted fast-rotator RVZ model. To this aim, two complementary approaches were adopted: (1) model-fitting of the RVZ model plus an additional analytical component; and (2) image reconstruction.

6.1. Photospheric physical model plus analytical component

We used the emcee code to fit a model consisting of the photospheric best-fit RVZ model determined in Sect. 4 plus an analytical 2D Gaussian ellipse. The free parameters of the 2D Gaussian ellipse and their initial range of values (initial uniform distribution of values) are

- major axis *FWHM* a_{GE} : 0.5 mas to 20 mas
- minor-to-major-axis ratio r_{GE} : 0.1 to 1
- position angle of the major axis PA_{GE} : 0° to 180°
- flux ratio (relative to the stellar total flux) F_{GE} : 0% to 10%
- horizontal (equatorial direction) shift relative to the center of the star x_{GE} : -15 mas to 15 mas
- vertical (polar direction) shift relative to the center of the star y_{GE} : -15 mas to 15 mas.

This approach is similar to, but more general than, the one adopted by Kervella & Domiciano de Souza (2006) since it allows to simultaneously test different faint circumstellar structures such as a faint companion or a weak polar wind or equatorial disk.

As before, the emcee algorithm explored the entire parameter space (within the above defined boundaries) using 800 walkers in a 200 steps burn-in phase and 150 steps in the final phase. Since the RVZ model already provides a good fit to the data, the parameters of the additional 2D Gaussian ellipse are not expected to be strongly constrained, leading to $\chi_r^2 = 1.79$, which is only slightly lower than the value obtained for the RVZ model alone. Two parameters of the 2D Gaussian ellipse were nevertheless relatively well constrained: $a_{\text{GE}} = 5.2 \pm 2.4$ mas and $F_{\text{GE}} = 0.7\% \pm 0.1\%$. The fit also shows that the position of this possible additional component is roughly centered on the star, with a shift uncertainty smaller than ~ 5 mas for both directions (x_{GE} and y_{GE}). The remaining parameters are poorly constrained by the data.

6.2. Image reconstruction

As a model-independent study of the PIONIER data we also performed an image reconstruction of Achernar using the MIRA⁴ software (Thiébaud 2008). MIRA is based on an iterative process, aimed at finding the image that minimizes a joint criterion under constraints of positivity and normalization,

$$f(x) = f_{\text{data}}(x) + \mu f_{\text{prior}}(x), \quad (7)$$

where x are the set of image pixels, $f_{\text{data}}(x)$ is the penalty function of the measurements, $f_{\text{prior}}(x)$ is a term that enforces additional a priori constraints, and μ (≥ 0) is the hyperparameter, i.e., the weight of the priors.

The hyperparameter has to be chosen as large as possible to maximize the weight of the constraints arising from physical modeling and to ensure the convergence of the reconstruction at a minimal value of the penalty χ^2 . As we have satisfying a model of the target, we used an elliptical Lorentzian a priori ($f_{\text{prior}}(x)$) with (1) the same minor-axis position angle as Achernar, 216.9° ($\equiv 36.9^\circ$ for a centrically-symmetrical ellipse); (2) a major-to-minor axis ratio of 1.3 corresponding to the apparent flattening; and (3) a *FWHM* = 3.2 mas in the major-axis direction, corresponding to a size slightly bigger than Achernar's angular diameter, to avoid missing possible structures close to the photosphere.

To determine the best value of the hyperparameter, we performed several ($\sim 10^3$) independent reconstructions with 200 iterations and random μ values ranging from 1 to 10^9 . In Fig. 14

⁴ Multi-aperture image reconstruction algorithm.

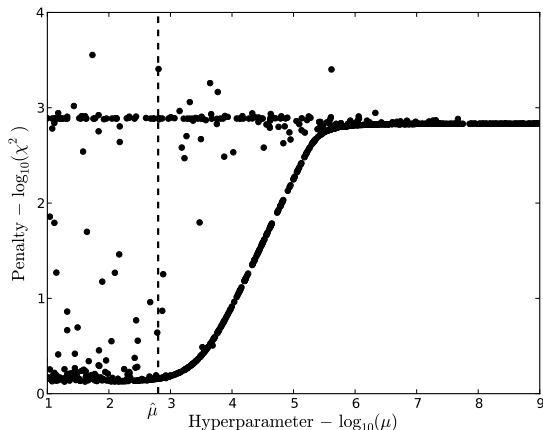


Fig. 14. Penalty factor χ^2 as a function of the hyperparameter μ for a set of reconstructed MIRA images (log scales). Based on this curve, the value $\hat{\mu}$ ($=630$) was chosen for the image reconstruction of Achernar.

(available electronically), we show the distribution of χ^2 for converged reconstructions as a function of μ for each reconstruction. This procedure revealed that there is a plateau of minimum χ^2 ($=1.4$), reached for values of μ lower than $\hat{\mu} \sim 630$.

After determining the parameters of the reconstruction, we followed the procedure described by Millour et al. (2012) to create the reconstructed image of Achernar as the weighted average of several hundred converged reconstructed images,

$$\bar{I}(x) = \frac{\sum_i 1/\chi_i^2 I_i(x - \bar{x}_i)}{\sum_i 1/\chi_i^2}, \quad (8)$$

where each image i was centered on its photocenter position \bar{x}_i before summation. The weight of each reconstruction is $1/\chi_i^2$, with a limit penalty value of $\chi_i^2 \leq 5$ to reject low-quality reconstructed images.

Figure 15 shows the reconstructed image of Achernar, both given by MIRA with a 0.07 mas resolution pixel (over-resolved image) and convolved by a Gaussian beam of $FWHM = 1.6$ mas (diffraction limit of the PIONIER observations). Although this diffraction limit does not provide a highly resolved image of the photosphere, it is enough to investigate the close circumstellar environment. Indeed, the reconstructed MIRA image clearly shows the presence of a compact object (stellar photosphere) without any signature of extended circumstellar component. This is more clearly seen in the right panel of Fig. 15, which shows the subtraction of the MIRA and best-fit CHARRON images, convolved by the 1.6 mas Gaussian beam. The difference between these images is at most 1.5% in modulus (relative to the total flux of the MIRA image) and below $\sim 0.5\%$ almost everywhere.

Both the results from the image reconstruction and from the fit of the RVZ model plus an analytical 2D Gaussian ellipse presented in this section show that no additional component is present in the PIONIER data within $\sim \pm 1\%$ level of intensity. This agrees well with the conclusions based on polarimetric and spectroscopic data and modeling shown in Sect. 3.

7. Conclusions

Based on ESO-VLTI interferometric observations of Achernar obtained in a normal B star phase, we derived its photospheric

parameters by fitting our physical model CHARRON using a MCMC method. A best-fit photospheric model was derived from squared visibilities and phase closures recorded with the PIONIER beam combiner in the H band. This model agrees well with AMBER HR differential phase observations around the Bry line.

The interferometric observations were complemented by spectroscopic, polarimetric, and photometric data to investigate the status of the circumstellar environment of Achernar during the VLTI observing runs, to cross-check our model-fitting results, and to set constraints on the model parameter space (photosphere and possible residual disk). In particular, polarimetry was crucial to constrain the disk density, imposing quite well-defined upper limits.

We note that our photospheric model of Achernar agrees with many observations from distinct techniques: PIONIER V^2 and CP, AMBER differential phases, V - and B -band polarimetry, $H\alpha$ and $H\beta$ line profiles, and $UBJHK$ photometry. Moreover, our results are compatible with the theoretical model of gravity darkening proposed by Espinosa Lara & Rieutord (2011, ELR model), which we also showed to be consistent with previously published results from different fast rotators over a wide range of rotational flattening (Achernar being the flattest one in the sample). Observational validation of gravity-darkening models such as the ELR model is an important step in the understanding of rapidly rotating stars since it has the great advantage of reducing the number of free parameters (β coefficient is not needed anymore). Indeed, by relying on a few input parameters and hypotheses, the ELR model reproduces five out of the six measured gravity-darkening β coefficients, which is motivating and promising for a more profound understanding of this important effect in stellar physics.

Taking advantage of the good quality and uv coverage of the PIONIER observations, we also pushed the analysis a little farther and performed an interferometric image reconstruction that did not reveal any signatures of additional circumstellar components and/or deviations from the photospheric Roche-von Zeipel (RVZ) model within a $\sim \pm 1\%$ level of intensity. This result also agrees with a fit of an additional analytical component to the RVZ model. Although the spatial resolution of the image is rather low (spatial frequencies restricted to the first visibility lobe), this is, to our knowledge, the first reconstructed image of the photosphere of a Be star.

The results of this work thus provide the first determination of the pure photospheric parameters of a Be star in a normal B phase. The measured photospheric parameters are R_{eq} , V_{eq} , i , β , and PA_{rot} . Concerning Achernar specifically, these parameters can be used as a reference input photospheric model for future studies based on modeling that includes circumstellar disk and photosphere.

Acknowledgements. PIONIER is funded by the Université Joseph Fourier (UJF), the Institut de Planétologie et d'Astrophysique de Grenoble (IPAG), the Agence Nationale pour la Recherche (ANR-06-BLAN-0421 and ANR-10-BLAN-0505), and the Institut National des Sciences de l'Univers (INSU PNP and PNPS). The integrated optics beam combiner is the result of a collaboration between IPAG and CEA-LETI based on CNES R&T funding. This research has made use of the SIMBAD database, operated at the CDS, Strasbourg, France, of NASA Astrophysics Data System Abstract Service⁵. We also have used the Jean-Marie Mariotti Center (JMCC) services OIFits Explorer⁶, and SearchCal⁷. This work has made use of the computing facilities (I) of the Mésocentre SIGAMM (hosted by Observatoire de la Côte d'Azur, France), and

⁵ Available at <http://cdsweb.u-strasbg.fr/>

⁶ Available at <http://www.jmmc.fr/oifitsexplorer>

⁷ Available at <http://www.jmmc.fr/searchcal>

3. High spectro-spatial resolution observations of fast rotators in the H-R diagram

A. Domiciano de Souza et al.: The environment of the fast rotating star Achernar. III.

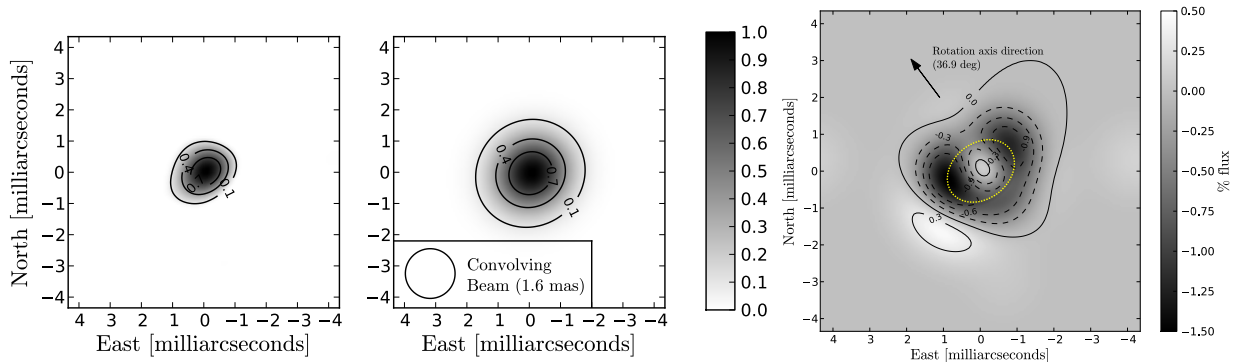


Fig. 15. *Left:* image reconstruction of Achernar obtained by applying the MIRA software to the H band VLT/PIONIER observations. *Middle:* convolution of this reconstructed MIRA image convolved by a Gaussian beam of $FWHM = 1.6$ mas ($=0.61\lambda/B_{\max}$) corresponding to the diffraction limit of the PIONIER observations. *Right:* Reconstructed MIRA image minus the best-fit CHARRON image (Fig. 11) convolved by the Gaussian diffraction limit beam to match the resolution of reconstructed image). The difference between the images is very small, $<1.5\%$ in modulus, relative to the total MIRA image flux), indicating that essentially only the photosphere of Achernar contributes to the PIONIER data, without any additional circumstellar component. The dotted ellipse approximately represents the border of the apparent photosphere of Achernar given by the best-fit CHARRON RVZ model.

(2) of the Laboratory of Astroinformatics (IAG/USP and NAT/Unicisul, Brazil), whose purchase was made possible by the Brazilian agency FAPESP (grant 2009/54006-4) and the INCT-A. We thank the CNRS-PICS (France) program 2010-2012 for supporting our Brazilian-French collaboration and the present work. We acknowledge D. Mary and D. Foreman-Mackey for their enlightening suggestions on MCMC methods and on the emcee code. We also thank E. Alecian and T. Rivinius for providing the reduced HARPS and FEROS visible spectra of Achernar.

References

- Absil, O., Mennesson, B., Le Bouquin, J.-B., et al. 2009, *ApJ*, 704, 150
 Bonneau, D., Clausse, J.-M., Delfosse, X., et al. 2006, *A&A*, 456, 789
 Bordé, P., Coudé du Foresto, V., Chagnon, G., & Perrin, G. 2002, *A&A*, 393, 183
 Carciofi, A. C., & Bjorkman, J. E. 2006, *ApJ*, 639, 1081
 Carciofi, A. C., Magalhães, A. M., Leister, N. V., Bjorkman, J. E., & Levenhagen, R. S. 2007, *ApJ*, 671, L49
 Carciofi, A. C., Domiciano de Souza, A., Magalhães, A. M., Bjorkman, J. E., & Vakili, F. 2008, *ApJ*, 676, L41
 Chauville, J., Zorec, J., Ballereau, D., et al. 2001, *A&A*, 378, 861
 Che, X., Monnier, J. D., Zhao, M., et al. 2011, *ApJ*, 732, 68
 Code, A. D., Bless, R. C., Davis, J., & Brown, R. H. 1976, *ApJ*, 203, 417
 Cohen, M., Walker, R. G., Carter, B., et al. 1999, *AJ*, 117, 1864
 Cutri, R. M., Skrutskie, M. F., van Dyk, S., et al. 2003, *VizieR Online Data Catalog*: II/246
 Domiciano de Souza, A., Vakili, F., Jankov, S., Janot-Pacheco, E., & Abe, L. 2002, *A&A*, 393, 345
 Domiciano de Souza, A., Kervella, P., Jankov, S., et al. 2003, *A&A*, 407, L47
 Domiciano de Souza, A., Hadjara, M., Vakili, F., et al. 2012a, *A&A*, 545, A130
 Domiciano de Souza, A., Zorec, J., & Vakili, F. 2012b, in *SF2A-2012: Proc. Annual meeting of the French Society of Astronomy and Astrophysics*, eds. S. Boissier, P. de Laverny, N. Nardetto, et al. 321
 Espinosa Lara, F., & Rieutord, M. 2011, *A&A*, 533, A43
 Foreman-Mackey, D., Hogg, D. W., Lang, D., & Goodman, J. 2013, *PASP*, 125, 306
 Frémat, Y., Zorec, J., Hubert, A., & Floquet, M. 2005, *A&A*, 440, 305
 Goodman, J., & Weare, J. 2010, *Commun. Appl. Math. Comput. Sci.*, 5, 65
 Goss, K. J. F., Karoff, C., Chaplin, W. J., Elsworth, Y., & Stevens, I. R. 2011, *MNRAS*, 411, 162
 Haguenaer, P., Alonso, J., Bourget, P., et al. 2010, in *SPIE Conf. Ser.*, 7734, 04
 Hanbury Brown, R., Davis, J., & Allen, L. R. 1974, *MNRAS*, 167, 121
 Harmanec, P. 1988, *Bull. Astron. Inst. Czechosl.*, 39, 329
 Haubois, X., Carciofi, A. C., Rivinius, T., Okazaki, A. T., & Bjorkman, J. E. 2012, *ApJ*, 756, 156
 Hog, E., Fabricius, C., Makarov, V. V., et al. 2000, *VizieR Online Data Catalog*: I/259
 Hubeny, I., & Lanz, T. 2011, *Synspec: General Spectrum Synthesis Program*, astrophysics Source Code Library
 Hutchings, J. B., & Stoekley, T. R. 1977, *PASP*, 89, 19
 Jackson, S., MacGregor, K. B., & Skumanich, A. 2004, *ApJ*, 606, 1196
 Jaschek, M., & Egret, D. 1982, in *Be Stars*, eds. M. Jaschek, & H.-G. Groth, IAU Symp., 98, 261
 Jerzykiewicz, M., & Molenda-Zakowicz, J. 2000, *Acta Astron.*, 50, 369
 Johnson, H. L., Mitchell, R. I., Iriarte, B., & Wisniewski, W. Z. 1966, *Communications of the Lunar and Planetary Laboratory*, 4, 99
 Kervella, P., & Domiciano de Souza, A. 2006, *A&A*, 453, 1059
 Kervella, P., & Domiciano de Souza, A. 2007, *A&A*, 474, L49
 Kervella, P., Thévenin, F., Morel, P., Bordé, P., & Di Folco, E. 2003, *A&A*, 408, 681
 Kervella, P., Domiciano de Souza, A., & Bendjoya, P. 2008, *A&A*, 484, L13
 Kurucz, R. L. 1979, *ApJS*, 40, 1
 Lafrasse, S., Mella, G., Bonneau, D., et al. 2010, in *SPIE Conf. Ser.*, 7734
 Le Bouquin, J.-B., Berger, J.-P., Lazareff, B., et al. 2011, *A&A*, 535, A67
 Maeder, A., & Meynet, G. 2000, *ARA&A*, 38, 143
 Magalhães, A. M., Benedetti, E., & Roland, E. H. 1984, *PASP*, 96, 383
 Magalhães, A. M., Rodrigues, C. V., Meade, M., et al. 1996, in *Polarimetry of the Interstellar Medium*, eds. W. G. Roberge & D. C. B. Whittet, *ASP Conf. Ser.*, 97, 202
 Millour, F. A., Vannier, M., & Meilland, A. 2012, in *SPIE Conf. Ser.*, 8445
 Monnier, J. D., Zhao, M., Pedretti, E., et al. 2007, *Science*, 317, 342
 Monnier, J. D., Che, X., Zhao, M., et al. 2012, *ApJ*, 761, L3
 Nazé, Y. 2009, *A&A*, 506, 1055
 Rivinius, T., Baade, D., Townsend, R. H. D., Carciofi, A. C., & Štefl, S. 2013, *A&A*, 559, L4
 Skrutskie, M. F., Cutri, R. M., Stiening, R., et al. 2006, *AJ*, 131, 1163
 Slettebak, A. 1982, *ApJS*, 50, 55
 Thiébaud, E. 2008, in *SPIE Conf. Ser.*, 7013
 Townsend, R. H. D., Owocki, S. P., & Howarth, I. D. 2004, *MNRAS*, 350, 189
 van Belle, G. T. 2012, *A&ARv*, 20, 51
 van Leeuwen, F. 2007, *A&A*, 474, 653
 Vinicius, M. M. F., Zorec, J., Leister, N. V., & Levenhagen, R. S. 2006, *A&A*, 446, 643
 von Zeipel, H. 1924, *MNRAS*, 84, 665
 Zacharias, N., Monet, D. G., Levine, S. E., et al. 2005, *VizieR Online Data Catalog*: I/297
 Zhao, M., Monnier, J. D., Pedretti, E., et al. 2009, *ApJ*, 701, 209

3.2.2 The close CSE of Achernar: wind and residual disk

Because of its $B \leftrightarrow Be$ cyclic variations, Achernar has a dynamic circumstellar environment (CSE) with continuously changing observational signatures on time scales ranging from hours to years. Thus the influence of the CSE on the data can vary depending on the epoch of the observations.

In 2002-2003 we observed Achernar using the VLT/VINCI beam combiner. Squared visibilities V^2 in the H and K bands revealed a strong flattening that cannot be totally explained by the commonly adopted Roche model for fast-rotating stars (Domiciano de Souza et al., 2003).

A subsequent detailed investigation of these data revealed that, in addition to a strong rotational flattening, Achernar also presented detectable CSE components at the epoch of the VLT/VINCI observations:

- Kervella & Domiciano de Souza (2006, A&A paper given hereafter): detection of an elongated structure in the direction of the poles accounting for $4.7 \pm 0.3\%$ of the photospheric flux in the near-IR. This is potentially the first direct evidence of a polar wind or jet accelerated by radiative forces in a gravity darkened star as expected from theory (e.g. Maeder & Desjacques, 2001, and Sect. 2.2.4).
- Carciofi et al. (2008, A&A paper given hereafter): study of the interface between photosphere and circumstellar disk for near-critical rotators. It is shown that a model of photosphere plus a residual (small) equatorial disk for Achernar could explain both (1) the rotational flattening stronger than the Roche limit and (2) the small, but detectable, spectroscopic and polarimetric observations, which cannot be reproduced by a photospheric model alone.

The results from these two papers are also supported by other publications from us (not shown here):

- Kanaan et al. (2008): adopted a "photosphere+disk+wind" model to explain the spectral energy distribution, $H\alpha$ profiles, and the VLT/VINCI V^2 observations. The time variation of the CSE (disk and wind) of Achernar was also investigated. This work was part of the PhD thesis of S. Kanaan (thesis supervisor: Ph. Stee);
- Kervella et al. (2009): VLT/MIDI V^2 observations in the N band taken in 2006. Our analysis indicate the presence of an extended structure in the polar direction contributing to $13.4 \pm 2.5\%$ of the photospheric flux in the thermal IR.

All these works address the important and still poorly known issue concerning the interface between photosphere and CSE of fast-rotating stars, where the exchanges of mass and angular momentum take place leading, for example, to the formation of Be star disks (Be phenomenon). We plan to follow this fascinating research topic in the next years.

The polar wind of the fast rotating Be star Achernar

VINCI/VLTI interferometric observations of an elongated polar envelope

P. Kervella¹ and A. Domiciano de Souza^{2,3}¹ LESIA, CNRS UMR 8109, Observatoire de Paris-Meudon, 5 place Jules Janssen, 92195 Meudon Cedex, France

e-mail: Pierre.Kervella@obspm.fr

² Lab. Univ. d'Astrophysique de Nice (LUAN), CNRS UMR 6525, UNSA, Parc Valrose, 06108 Nice, France³ Observatoire de la Côte d'Azur, CNRS UMR 6203, Département GEMINI, BP 4229, 06304 Nice Cedex 4, France

Received 23 December 2005 / Accepted 20 February 2006

ABSTRACT

Context. Be stars show evidence of mass loss and circumstellar envelopes (CSE) from UV resonance lines, near-IR excesses, and the presence of episodic hydrogen emission lines. The geometry of these envelopes is still uncertain, although it is often assumed that they are formed by a disk around the stellar equator and a hot polar wind.

Aims. We probe the close environment of the fast rotating Be star Achernar at angular scales of a few milliarcseconds (mas) in the infrared, in order to constrain the geometry of a possible polar CSE.

Methods. We obtained long-baseline interferometric observations of Achernar with the VINCI/VLTI beam combiner in the *H* and *K* bands, using various telescope configurations and baseline lengths with a wide azimuthal coverage.

Results. The observed visibility measurements along the polar direction are significantly lower than the visibility function of the photosphere of the star alone, in particular at low spatial frequencies. This points to the presence of an asymmetric diffuse CSE elongated along the polar direction of the star. To our data, we fit a simple model consisting of two components: a 2D elliptical Gaussian superimposed on a uniform ellipse representing the distorted photosphere of the fast rotating star.

Conclusions. We clearly detected a CSE elongated along the polar axis of the star, as well as rotational flattening of the stellar photosphere. For the uniform-ellipse photosphere we derive a major axis of $\theta_{\text{eq}} = 2.13 \pm 0.05$ mas and a minor axis of $\theta_{\text{pol}} = 1.51 \pm 0.02$ mas. The relative near-IR flux measured for the CSE compared to the stellar photosphere is $f = 4.7 \pm 0.3\%$. Its angular dimensions are loosely constrained by the available data at $\rho_{\text{eq}} = 2.7 \pm 1.3$ mas and $\rho_{\text{pol}} = 17.6 \pm 4.9$ mas. This CSE could be linked to free-free emission from the radiative pressure driven wind originating from the hot polar caps of the star.

Key words. techniques: high angular resolution – techniques: interferometric – stars: emission-line, Be – stars: mass-loss – stars: rotation – stars: individual: Achernar

1. Introduction

The southern star Achernar (α Eridani, HD 10144) is the brightest of all Be stars ($V = 0.46$ mag). Depending on the author (and the technique used) the spectral type of Achernar ranges from B3-B4IIIe to B4Ve (e.g., Slettebak 1982; Balona et al. 1987). The estimated projected rotation velocity $v \sin i$ ranges from 220 to 270 km s⁻¹ and the effective temperature T_{eff} from 15 000 to 20 000 K (e.g., Vinicius et al. 2006; Rivinius, priv. comm.; Chauville et al. 2001). The difficulty in deriving these parameters more precisely is a direct consequence of the rapid rotation of Achernar. Such rapid rotation ($\geq 80\%$ of the critical velocity) induces mainly two effects on the star structure: a rotational flattening and a gravity darkening, which can be described by the von Zeipel effect (von Zeipel 1924).

Domiciano de Souza et al. (2003, hereafter D03) measured the apparent rotational flattening of Achernar using the Very Large Telescope Interferometer (VLTI). They showed that the flattening ratio measured on this star cannot be explained in the Roche approximation, especially when taking the von Zeipel effect into account. Recently, this effect was revealed in two other rapidly rotating stars thanks to interferometric observations: Altair (A7V, Ohishi et al. 2004; Domiciano de Souza et al. 2005) and Regulus (B7V, McAlister et al. 2005).

Rapid rotation and gravity darkening seem to be important keys to explaining the two-component circumstellar environment (CSE) of Be stars: (1) a dense (particle densities $N \approx 10^{11} - 10^{12}$ cm⁻³), high mass-loss ($\approx 10^{-8}$ M_{\odot} /yr) and low radial velocity ($\approx 10 - 100$ km s⁻¹) equatorial envelope and (2) a rarefied ($N \approx 10^9$ cm⁻³), low mass-loss ($\approx 10^{-10}$ M_{\odot} /yr) and fast (≈ 1000 km s⁻¹) polar wind (e.g. Damiani Neto & de Freitas Pacheco 1982; Waters et al. 1987, and references therein). This picture of a two-component CSE is based on many observations of Be stars performed in the past few decades. For example, optical/IR data have shown emission lines and IR excesses that essentially probe the denser regions of the CSE (e.g. Waters 1986; Dougherty et al. 1994), while UV resonance lines of highly ionized species can probe regions of lower density (e.g. Snow 1981; Peters 1982). Gehrz et al. (1974) showed that the near-IR excess measured in Be stars is due to free-free radiation.

The disk-like shape of the dense equatorial CSE has been directly measured by interferometric observations in the radio and optical/IR (e.g. Dougherty & Taylor 1992; Stee et al. 1995; Quirrenbach et al. 1997). In a recent work, Tycner et al. (2005) explore the relationship between the angular size of the H α emitting region (measured by interferometry) and the net H α emission measured spectroscopically for seven Be stars. They find an interesting correlation between the two quantities, which they

3.2. The Be star Achernar (α Eridani)

Table 1. Relevant parameters of the calibrators used for VINCI observations of Achernar (continued in Table 2).

Name	α PsA	χ Phe	HR 1318	α Ind	HR 37	HR 2305	δ Phe
HD number	HD 216956	HD 12524	HD 26846	HD 196171	HD 787	HD 44951	HD 9362
m_V	1.2	5.2	4.9	3.1	5.3	5.2	4.0
m_K	1.0	1.3	2.3	0.9	1.8	2.3	1.7
Sp. type	A3V	K5III	K3III	K0III	K5III	K3III	K0IIIb
T_{eff} (K) ^a	8760	3780	6210	4720	3780	4250	4660
$\log g^a$	4.2	1.9	2.2	2.6	1.9	2.4	2.9
$v \sin i$ (km s ⁻¹) ^c	85	–	20	–	2	20	–
θ_{LD} (mas) ^a	2.23 ± 0.07	2.77 ± 0.03	1.86 ± 0.02	3.28 ± 0.03	2.52 ± 0.03	1.81 ± 0.03	2.24 ± 0.02
θ_{UD} (mas) ^b	2.19 ± 0.07	2.69 ± 0.03	1.81 ± 0.02	3.20 ± 0.03	2.45 ± 0.03	1.76 ± 0.03	2.18 ± 0.02

^a From Cohen et al. (1999) or Bordé et al. (2002), except α PsA which angular size was measured by Di Folco et al. (2004). ^b Linear limb darkening coefficients from Claret et al. (1995) or Claret (2000). ^c The projected rotational velocities were taken from the catalogue compiled by Glebocki et al. (2000).

attribute to an optically thick emission proportional to the effective area of the emitting disk. Because the equatorial disks are denser (≈ 100 times) than the polar winds and because the free-free emissivity is proportional to the density squared, the equatorial disk dominates the near-IR continuum emission when it is present.

However, it is still not clear if this free-free radiation comes only from the equatorial envelope or if it can also be formed, at least partially, in the polar wind. Modern high angular resolution techniques have the resolving power and sensitivity required to map the spatial distribution of the near-IR emission. In the present paper we investigate this issue by using all available interferometric observations of Achernar obtained with the VINCI/VLTI near-IR instrument (Sect. 2). These observations were performed during a phase where the equatorial disk was nearly absent. The adopted analytical model is presented in Sect. 3 and our results discussed in Sect. 4.

2. Interferometric observations

2.1. Instrumental setup and observations

The European Southern Observatory's VLTI (Glindemann et al. 2000, 2004) has been in operation on top of the Cerro Paranal, in Northern Chile since March 2001. For the observations reported in this paper, the light coming from two test siderostats (0.35 m aperture) or two Unit Telescopes (8 m aperture) was recombined coherently in VINCI, the VLT INTERferometer Commissioning Instrument (Kervella et al. 2000, 2003). We used either a K band ($\lambda = 2.0\text{--}2.4\ \mu\text{m}$) or H band ($\lambda = 1.4\text{--}1.8\ \mu\text{m}$) filter, depending on the beam combiner. In the K band, we relied on the MONA beam combiner, based on fluoride glass optical fibers, while in the H band, we employed the IONIC integrated optics beam combiner (Berger et al. 2001; Kervella et al. 2003; Lebouquin et al. 2004). A total of nine VLTI baselines were used for this program, including five out of the six possible Unit Telescope baselines. Considering the transmission of the instrument and the average effective temperature of Achernar, the effective wavelength of our observations was $\lambda = 2.175\ \mu\text{m}$ in the K band and $\lambda = 1.631\ \mu\text{m}$ in the H band. The uncertainty on these wavelengths ($\approx 0.2\%$) is negligible compared to the accuracy of our measurements.

2.2. Data processing and calibration

The raw data processing was achieved using a wavelet-based algorithm, integrated in an automated data reduction pipeline (Kervella et al. 2004a). The general principle is similar to the

original FLUOR algorithm (Coudé du Foresto et al. 1997), but instead of the classical Fourier analysis, we implemented a wavelet-based time-frequency analysis (Ségransan et al. 1999). The output of this pipeline is a single value of the squared coherence factor μ^2 for each series of 500 interferograms and the associated bootstrapped error bar. We obtained a total of 49 500 interferograms of Achernar in the K band and 9500 in the H band, among which 32 394 and 3029 were reduced by the pipeline, respectively. The lower proportion of processed interferograms in the H band is explained by the fact that only one interferometric output is available in the IONIC component, instead of two for the MONA beam combiner. In both cases, two photometric outputs are present. This resulted in a total of 99 squared visibility measurements in the K band, and 19 in the H band, with their associated statistical and calibration uncertainties.

We used a number of calibrators taken mainly from the Bordé et al. (2002) catalogue, which is an adaptation of the Cohen et al. (1999) catalogue for interferometric observations. The observations of these stars were used to estimate the point source response of the interferometer immediately before or after the Achernar observations. Their properties are listed in Tables 1 and 2. The choice of the calibrators is an important step in the preparation of interferometric observations, as significant departures of their actual visibilities from the expected model can propagate into biases on the calibrated visibilities of the scientific target. Among the possible reasons for such departures, binarity (or multiplicity) and deviations from sphericity (due, for instance, to fast rotation or gravitational interaction) are the most critical. All stars in the Bordé et al. (2002) catalogue were carefully scrutinized by these authors for the presence of companions, and are currently regarded as single stars. With respect to fast rotation, the values of $v \sin i$ are generally low for all our calibrators. Spectroscopic measurements of the projected rotational velocities are missing for some of our calibrators; but as they are giant stars, we assume that they are small and, therefore, that the deformation of these stars can be neglected.

One of our calibrators, α PsA (Fomalhaut), is a moderately fast rotating dwarf (A3V, $v \sin i \approx 85\ \text{km s}^{-1}$, from Glebocki et al. 2000). We considered carefully the visibilities that were computed using this calibrator, and they show no deviation from the other measurements, in particular those calibrated by δ Phe that were obtained on the same baseline. Moreover, Di Folco et al. (2004) have measured the angular diameter of this star along the same projected baseline azimuth as during our observations of Achernar. Therefore, we do not expect any difference in terms of angular diameter. In any case, we considered a conservative $\pm 0.07\ \text{mas}$ ($\pm 3\%$) uncertainty on the assumed angular diameter of α PsA.

Table 2. Relevant parameters of the calibrators used for VINCI observations of Achernar (continued from Table 1). The references are the same as in Table 1.

Name	ϵ Ind A	α Cet	ν Cet
HD number	HD 209100	HD 18884	HD 12274
m_V	4.7	2.5	4.0
m_K	2.2	-1.7	0.0
Sp. type	K4.5V	M1.5IIIa	K5/M0III
T_{eff} (K)	4500	3730	—
$\log g$	4.5	—	—
$v \sin i$ (km s $^{-1}$)	1	—	—
θ_{LD} (mas) ^a	1.89 ± 0.02	—	—
θ_{UD} (mas) ^b	1.84 ± 0.02	11.6 ± 0.40	5.3 ± 0.5

^a The angular diameter of ϵ Ind A was measured by Kervella et al. (2004b). ^b The uniform disk angular sizes of α Cet and ν Cet were taken from Dyck et al. (1998) and Richichi & Percheron (2005), respectively.

The resulting calibrated squared visibilities are listed in Tables 3a–d. For each measurement, the calibrator is listed. No systematic deviation of the visibility was observed for any of our calibrators at a 1σ level.

3. Model fitting

3.1. Polar and equatorial visibilities

In order to define a plausible model for the light distribution of Achernar, we examine here the shape of the polar and equatorial visibility functions. The orientation of the minor axis of Achernar on the plane of the sky relative to the North was obtained by D03 using a subset of the data discussed in the present paper. Using a simplified analysis of the dependence of the equivalent uniform disk angular diameter with the azimuth of the projected baseline, they obtained an orientation of the minor axis of Achernar (assumed to be the polar axis) of $\alpha_0 = 39 \pm 1^\circ$ east of North.

To visualize the polar visibility function of Achernar, we extracted the interferometric measurements with azimuth angles between 10° and 70° , i.e. $\approx \pm 30^\circ$ from the sky-projected polar axis of the star. As shown in Fig. 2 (left), it appears that the distribution of the measured visibilities does not follow that of a uniform disk, and there is a clear deficit of visibility at low spatial frequencies. Fitting a simple uniform disk model (through a classical least-square minimization) to these data leads to $\theta_{\text{UD}} = 1.78$ mas, but the reduced χ^2 of 6.2 is characteristic of a poor fit. The deficit of visibility at low spatial frequencies is typical of the presence of an extended, incoherent source that is already resolved by the interferometer on the short baselines. In other words, a diffuse and extended envelope appears to be present along the polar axis of the star.

The equatorial visibility function can be evaluated by restricting our sample to the visibility measurements obtained in the azimuth range $\alpha_1 = 129 \pm 30^\circ$. As shown in Fig. 1, we do not have as many measurements at high spatial frequencies along this range of azimuth, due to the limitations in the available VLTI baselines during commissioning. Figure 2 (right) shows the distribution of squared visibilities observed in this azimuth range as a function of the spatial frequency. In this case, the fit of a simple uniform disk model with $\theta_{\text{UD}} = 2.38$ mas produces satisfactory results with a reduced χ^2 of only 0.6. In this case, we conclude that we do not detect any significant diffuse envelope along the equatorial plane of the star.

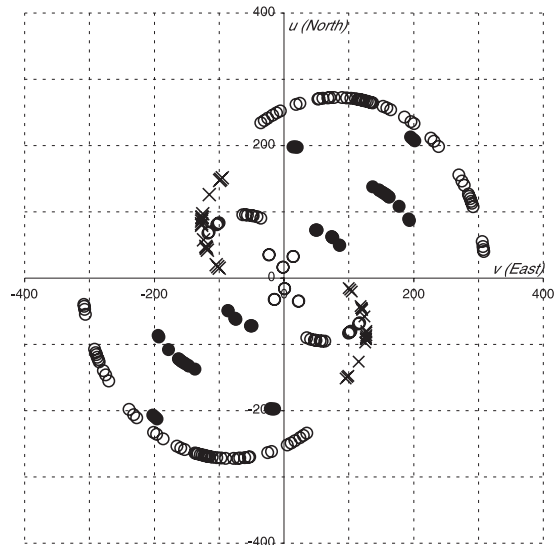


Fig. 1. Coverage of the (u, v) plane for the VINCI observations of Achernar. The K band observations (MONA beam combiner) are represented using circles (open for siderostat observations, solid for the Unit Telescopes), and the H band observations are represented using crosses. The scales are in units of B/λ , expressed in cycles/arcsec.

3.2. Star-envelope model description

As discussed in Sect. 3.1, it appears that a diffuse envelope, confined to the direction of its polar axis, is present around Achernar. In order to study the flux contribution of this envelope, we need to define a simple model to fit the observed visibility data. For this purpose, we considered the following components:

- the stellar photosphere is represented by a uniform ellipse. The parameters are the equatorial and polar angular sizes θ_{eq} and θ_{pol} and the azimuth orientation of the equatorial axis on the sky α_1 ;
- the diffuse envelope is represented by a bidimensional elliptical Gaussian. It is parametrized by its full widths at half maximum (FWHM) along the polar and equatorial axes of the star ρ_{pol} and ρ_{eq} , and its integrated flux relative to the stellar flux f . We make the assumption that its principal axes are aligned with the principal axes of the stellar photosphere.

Using a simple uniform ellipse model is naturally a very simplified approximation of the photospheric light distribution of Achernar. In reality, the rapid rotation of the star causes significant brightening of the polar caps of the star as a consequence of its flattening. Though numerical models can accurately predict the distribution of light on the photosphere of uniformly rotating stars (see e.g. Domiciano de Souza et al. 2002), the underlying Roche approximation is not necessarily verified for Achernar. In particular, Jackson et al. (2004) show that stellar models of Achernar including differential internal rotation result in better agreement with the interferometric profile obtained by D03. Though there are good prospects for differential rotation being constrained observationally by spectro-interferometry (Domiciano de Souza et al. 2004), the current uncertainties on the light distribution of the photosphere lead us to prefer the simple approach of a uniform ellipse. We also make the hypothesis that the axes of the envelope are aligned with the principal axes of the stellar photosphere. Due to the limited coverage of our data set in terms of azimuth angle at intermediate baselines, we

3.2. The Be star Achernar (α Eridani)

1062

P. Kervella and A. Domiciano de Souza: The polar wind of Achernar

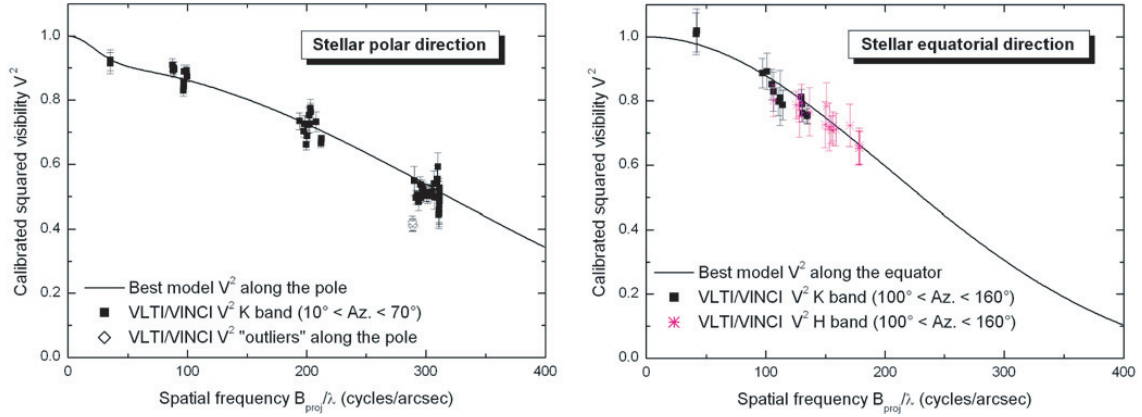


Fig. 2. *Left:* squared visibilities V^2 measured on Achernar and corresponding to projected baseline azimuth angles around the polar direction (values between 10° and 70°). *Right:* V^2 corresponding to projected baseline azimuth angles around the equatorial direction (values between 100° and 160°). The solid squares and crosses represent K and H band data, respectively. The solid curves represent theoretical V^2 along the pole (*left*) and the equator (*right*) obtained from the 2D fit of our two-component model (Sect. 3) to all measured V^2 (Tables 3a–d. Note also the V^2 outliers along the polar direction, which were not included in the fit (see text for details).

Table 3. (a) Squared visibilities of Achernar in the K band from VINCI, ordered by increasing azimuth angle of the projected baseline. The calibrators are named using their HR number, when no Bayer designation is available. The stated Julian date JD_0 is $JD - 2.452 \times 10^6$. The azimuth is counted in degrees clockwise from North ($N = 0$ deg, $E = 90$ deg), and B is the projected baseline in meters. The squared visibilities are followed in subscript by the statistical and calibration uncertainties.

JD_0	Cal.	Stations	B (m)	Az.	V^2 (%)
548.551	α PsA	B3-M0	139.44	7.3	$45.7_{\pm 1.5 \pm 4.1}$
546.558	α PsA	B3-M0	139.48	7.9	$42.7_{\pm 4.4 \pm 3.3}$
548.555	α PsA	B3-M0	139.46	8.7	$46.3_{\pm 1.5 \pm 4.2}$
548.560	α PsA	B3-M0	139.48	10.2	$44.4_{\pm 1.5 \pm 4.0}$
547.595	α PsA	B3-M0	139.61	20.2	$45.9_{\pm 2.1 \pm 3.8}$
545.604	α PsA	B3-M0	139.69	21.2	$50.6_{\pm 1.6 \pm 2.4}$
547.600	α PsA	B3-M0	139.63	21.8	$45.0_{\pm 2.1 \pm 3.7}$
545.608	α PsA	B3-M0	139.70	22.6	$52.6_{\pm 1.6 \pm 2.5}$
547.605	α PsA	B3-M0	139.65	23.3	$46.5_{\pm 2.2 \pm 3.8}$
545.613	α PsA	B3-M0	139.72	24.0	$51.7_{\pm 1.5 \pm 2.5}$
216.589	1318	U1-U3	95.29	24.2	$67.9_{\pm 1.1 \pm 0.5}$
216.592	1318	U1-U3	95.15	24.8	$66.6_{\pm 1.3 \pm 0.5}$
545.622	α PsA	B3-M0	139.72	26.7	$49.7_{\pm 1.5 \pm 2.4}$
545.626	α PsA	B3-M0	139.72	28.0	$48.7_{\pm 2.2 \pm 2.3}$
534.712	χ Phe	U1-U2	44.61	29.6	$87.3_{\pm 1.6 \pm 0.4}$
545.632	α PsA	B3-M0	139.70	29.9	$51.3_{\pm 2.2 \pm 2.4}$
534.714	χ Phe	U1-U2	44.56	30.1	$89.3_{\pm 1.6 \pm 0.4}$
575.637	37, 2305	U1-U3	93.34	31.3	$73.2_{\pm 2.8 \pm 1.3}$
213.654	χ Phe	U1-U3	91.22	36.9	$76.3_{\pm 2.2 \pm 1.6}$
213.655	χ Phe	U1-U3	91.12	37.2	$77.4_{\pm 2.3 \pm 1.6}$
213.658	χ Phe	U1-U3	90.79	37.9	$72.4_{\pm 2.2 \pm 1.5}$
213.660	χ Phe	U1-U3	90.62	38.3	$75.2_{\pm 2.0 \pm 1.6}$
534.749	χ Phe	U1-U2	43.54	38.7	$88.9_{\pm 2.1 \pm 0.4}$
213.663	χ Phe	U1-U3	90.28	39.0	$72.3_{\pm 2.0 \pm 1.5}$
534.750	χ Phe	U1-U2	43.48	39.1	$84.3_{\pm 1.5 \pm 0.4}$
534.752	χ Phe	U1-U2	43.40	39.6	$85.4_{\pm 1.6 \pm 0.4}$
556.635	δ Phe	B3-M0	139.20	39.8	$59.2_{\pm 4.1 \pm 1.7}$
214.664	1318	U1-U3	89.89	39.9	$68.8_{\pm 1.7 \pm 0.5}$
534.755	χ Phe	U1-U2	43.32	40.2	$82.9_{\pm 1.7 \pm 0.4}$
214.667	1318	U1-U3	89.60	40.5	$66.2_{\pm 1.6 \pm 0.5}$
556.642	δ Phe	B3-M0	139.02	41.7	$55.3_{\pm 4.0 \pm 1.6}$
213.675	χ Phe	U1-U3	88.92	41.8	$72.6_{\pm 2.0 \pm 1.5}$
214.675	1318	U1-U3	88.69	42.2	$70.2_{\pm 1.7 \pm 0.5}$
556.646	δ Phe	B3-M0	138.88	42.9	$54.3_{\pm 3.8 \pm 1.6}$
213.691	χ Phe	U1-U3	87.05	45.1	$73.5_{\pm 2.2 \pm 1.5}$

Table 3. (b) Squared visibilities of Achernar in the K band from VINCI (continued from Table 3a).

JD_0	Cal.	Stations	B (m)	Az.	V^2 (%)
533.711	ϵ Ind	U1-U4	129.75	45.7	$41.3_{\pm 1.2 \pm 1.4}$
533.713	ϵ Ind	U1-U4	129.70	46.1	$41.0_{\pm 0.9 \pm 1.4}$
533.715	ϵ Ind	U1-U4	129.64	46.8	$41.0_{\pm 0.9 \pm 1.4}$
533.717	ϵ Ind	U1-U4	129.57	47.4	$42.4_{\pm 0.9 \pm 1.4}$
550.685	δ Phe	B3-M0	137.86	49.2	$49.8_{\pm 3.4 \pm 1.4}$
550.688	δ Phe	B3-M0	137.64	50.3	$53.9_{\pm 3.6 \pm 1.5}$
550.697	δ Phe	B3-M0	137.09	52.5	$51.5_{\pm 1.6 \pm 1.4}$
534.898	χ Phe	U2-U3	39.87	54.7	$89.5_{\pm 2.4 \pm 0.4}$
534.900	χ Phe	U2-U3	39.68	55.0	$89.9_{\pm 1.8 \pm 0.4}$
534.902	χ Phe	U2-U3	39.44	55.4	$89.3_{\pm 1.8 \pm 0.4}$
534.904	χ Phe	U2-U3	39.18	55.9	$91.0_{\pm 1.9 \pm 0.4}$
556.696	δ Phe	B3-M0	135.77	56.9	$50.9_{\pm 2.2 \pm 1.4}$
556.701	δ Phe	B3-M0	135.32	58.2	$50.3_{\pm 2.1 \pm 1.3}$
556.705	δ Phe	B3-M0	134.87	59.5	$51.1_{\pm 2.2 \pm 1.4}$
550.733	δ Phe	B3-M0	133.55	62.6	$52.1_{\pm 2.0 \pm 1.5}$
590.625	δ Phe	B3-M0	133.37	63.0	$51.6_{\pm 0.8 \pm 1.3}$
550.736	δ Phe	B3-M0	133.15	63.5	$52.9_{\pm 1.8 \pm 1.5}$
590.629	δ Phe	B3-M0	132.83	64.2	$49.7_{\pm 0.7 \pm 1.2}$
550.741	δ Phe	B3-M0	132.55	64.7	$53.7_{\pm 1.8 \pm 1.5}$
569.691	δ Phe	B3-M0	132.25	65.3	$49.6_{\pm 1.1 \pm 1.2}$
945.621	α PsA	E0-G0	15.95	65.4	$92.5_{\pm 3.2 \pm 0.1}$
590.634	δ Phe	B3-M0	132.12	65.6	$49.5_{\pm 0.8 \pm 1.2}$
554.735	α PsA	B3-M0	131.85	66.1	$48.4_{\pm 1.9 \pm 2.0}$
569.695	δ Phe	B3-M0	131.58	66.6	$49.7_{\pm 1.1 \pm 1.2}$
945.625	α PsA	E0-G0	15.93	66.7	$91.5_{\pm 3.3 \pm 0.1}$
590.639	δ Phe	B3-M0	131.41	66.9	$50.4_{\pm 0.8 \pm 1.3}$
569.700	δ Phe	B3-M0	130.94	67.8	$49.6_{\pm 1.7 \pm 1.2}$
579.677	δ Phe	B3-M0	130.22	69.1	$54.8_{\pm 4.4 \pm 1.1}$
579.682	δ Phe	B3-M0	129.41	70.4	$49.7_{\pm 4.5 \pm 1.0}$
579.687	δ Phe	B3-M0	128.57	71.8	$48.7_{\pm 4.7 \pm 1.0}$
555.761	δ Phe	B3-M0	127.04	74.1	$48.7_{\pm 1.9 \pm 1.0}$
555.765	δ Phe	B3-M0	126.16	75.4	$49.7_{\pm 3.3 \pm 1.0}$
577.707	δ Phe	B3-M0	125.74	75.9	$50.1_{\pm 3.4 \pm 1.3}$
577.712	δ Phe	B3-M0	124.67	77.4	$49.8_{\pm 3.4 \pm 1.3}$
577.717	δ Phe	B3-M0	123.75	78.6	$50.3_{\pm 3.4 \pm 1.3}$
552.786	α PsA	B3-M0	123.47	79.0	$49.7_{\pm 4.2 \pm 3.6}$
533.781	χ Phe	U2-U4	89.03	84.0	$64.6_{\pm 2.9 \pm 1.2}$
533.783	χ Phe	U2-U4	88.98	84.5	$64.8_{\pm 2.5 \pm 1.2}$
555.798	δ Phe	B3-M0	118.90	84.6	$49.7_{\pm 3.5 \pm 1.0}$

3. High spectro-spatial resolution observations of fast rotators in the H-R diagram

Table 3. (c) Squared visibilities of Achernar in the K band from VINCI (continued from Table 3b).

JD ₀	Cal.	Stations	B (m)	Az.	V^2 (%)
533.786	χ Phe	U2-U4	88.91	85.2	63.6 $_{\pm 2.6}^{\pm 1.1}$
533.788	χ Phe	U2-U4	88.83	85.8	62.9 $_{\pm 2.5}^{\pm 1.1}$
555.802	δ Phe	B3-M0	117.78	85.9	50.3 $_{\pm 2.8}^{\pm 1.0}$
579.754	δ Phe	B3-M0	113.06	91.2	52.6 $_{\pm 4.0}^{\pm 0.8}$
579.759	δ Phe	B3-M0	111.82	92.6	52.0 $_{\pm 4.0}^{\pm 0.8}$
629.580	α Cet	B3-C3	7.37	93.1	98.2 $_{\pm 2.7}^{\pm 0.0}$
579.763	δ Phe	B3-M0	110.48	94.0	52.0 $_{\pm 4.3}^{\pm 0.8}$
629.585	α Cet	B3-C3	7.31	94.7	102.1 $_{\pm 3.4}^{\pm 0.0}$
544.865	χ Phe	B3-M0	108.80	95.8	50.2 $_{\pm 3.8}^{\pm 2.4}$
544.869	α PsA	B3-M0	107.50	97.2	49.5 $_{\pm 3.2}^{\pm 2.4}$
544.873	α PsA	B3-M0	106.17	98.6	48.2 $_{\pm 3.4}^{\pm 2.3}$
535.631	χ Phe	E0-G1	43.57	111.5	88.7 $_{\pm 4.6}^{\pm 0.5}$
535.642	χ Phe	E0-G1	45.32	114.0	89.2 $_{\pm 5.7}^{\pm 0.5}$
538.646	χ Phe	E0-G1	47.10	116.7	85.1 $_{\pm 4.7}^{\pm 0.4}$
538.651	χ Phe	E0-G1	47.74	117.7	82.9 $_{\pm 6.1}^{\pm 0.4}$
535.673	χ Phe	E0-G1	49.58	120.7	79.8 $_{\pm 4.3}^{\pm 0.4}$
535.678	χ Phe	E0-G1	50.24	121.8	80.9 $_{\pm 8.6}^{\pm 0.4}$
662.575	α Cet	E0-G0	18.82	122.1	102.0 $_{\pm 4.3}^{\pm 5.3}$
535.686	χ Phe	E0-G1	51.24	123.6	78.7 $_{\pm 4.6}^{\pm 0.4}$
662.579	ν Cet	E0-G0	18.65	123.6	100.9 $_{\pm 6.0}^{\pm 2.5}$
528.781	χ Phe	E0-G1	58.21	140.2	81.1 $_{\pm 2.5}^{\pm 0.6}$
528.785	χ Phe	E0-G1	58.49	141.1	79.0 $_{\pm 1.8}^{\pm 0.6}$
528.790	χ Phe	E0-G1	58.76	142.1	76.1 $_{\pm 2.4}^{\pm 0.6}$
528.820	χ Phe	E0-G1	60.41	149.0	75.2 $_{\pm 2.2}^{\pm 0.7}$
528.824	χ Phe	E0-G1	60.60	150.0	75.7 $_{\pm 2.8}^{\pm 0.7}$

Table 3. (d) Squared visibilities of Achernar in the H band from VINCI, equipped with the IONIC integrated optics beam combiner.

JD ₀	Cal.	Stations	B (m)	Az.	V^2 (%)
475.861	α Ind	E0-G1	52.48	126.0	70.8 $_{\pm 4.3}^{\pm 1.6}$
475.870	α Ind	E0-G1	53.39	127.8	71.1 $_{\pm 4.8}^{\pm 1.6}$
477.781	α Ind	E0-G1	42.26	109.7	78.7 $_{\pm 3.9}^{\pm 1.7}$
477.785	α Ind	E0-G1	42.98	110.7	77.4 $_{\pm 3.7}^{\pm 1.7}$
479.941	α Ind	E0-G1	59.78	146.1	65.3 $_{\pm 5.2}^{\pm 1.4}$
479.944	α Ind	E0-G1	59.95	146.8	66.0 $_{\pm 5.4}^{\pm 1.4}$
479.949	α Ind	E0-G1	60.19	147.9	65.3 $_{\pm 5.1}^{\pm 1.4}$
482.791	α Ind	E0-G1	45.98	115.0	76.6 $_{\pm 7.3}^{\pm 1.7}$
482.824	α Ind	E0-G1	50.39	122.1	72.5 $_{\pm 7.0}^{\pm 1.6}$
482.827	α Ind	E0-G1	50.80	122.8	78.4 $_{\pm 7.1}^{\pm 1.8}$
483.718	α Ind	E0-G1	34.05	98.7	82.0 $_{\pm 4.4}^{\pm 1.8}$
483.722	α Ind	E0-G1	34.83	99.7	77.5 $_{\pm 4.1}^{\pm 1.7}$
483.727	α Ind	E0-G1	35.78	101.0	80.1 $_{\pm 4.6}^{\pm 1.7}$
483.831	α Ind	E0-G1	51.56	124.2	71.9 $_{\pm 7.2}^{\pm 1.7}$
483.835	α Ind	E0-G1	52.05	125.1	70.9 $_{\pm 3.8}^{\pm 1.7}$
483.839	α Ind	E0-G1	52.51	126.0	72.0 $_{\pm 4.2}^{\pm 1.7}$
484.767	α Ind	E0-G1	43.17	110.9	75.3 $_{\pm 6.4}^{\pm 1.4}$
484.771	α Ind	E0-G1	43.72	111.7	79.3 $_{\pm 5.7}^{\pm 1.4}$
485.887	χ Phe	E0-G1	57.36	137.5	72.3 $_{\pm 6.5}^{\pm 1.2}$

choose this approach in order to reduce the number of fitted parameters, and therefore improve the stability of the convergence of the χ^2 minimization.

3.3. Photospheric visibility function

The visibility function of a uniform ellipse can be derived from the classical visibility function of a circular uniform disk with an angular diameter θ_{UD} :

$$V_{UD}(u, v) = \frac{2 J_1(x)}{x} \quad (1)$$

where $x = \pi \theta_{UD} \sqrt{u^2 + v^2}$, with u and v the spatial frequency coordinates in units of B/λ . In order to obtain the visibility function of the ellipse, we use a rotation of the (u, v) axes and a scaling of the (u, v) variables:

$$u' = u \cos \alpha_1 + v \sin \alpha_1 \quad v' = -u \sin \alpha_1 + v \cos \alpha_1. \quad (2)$$

The visibility of the uniform ellipse with a major axis θ_{eq} , a minor axis θ_{pol} , and a major axis orientation relative to the u axis α_1 is therefore:

$$V_{star}(u, v, \theta_{eq}, \theta_{pol}, \alpha_1) = \frac{2 J_1(x')}{x'} \quad (3)$$

$$\text{where } x' = \pi \sqrt{\theta_{eq}^2 u'^2 + \theta_{pol}^2 v'^2}.$$

3.4. Envelope visibility function

As in Sect. 3.3, we can obtain the visibility function of an elliptical Gaussian brightness distribution from the circularly symmetric case for which we have

$$V_{Gauss}(u, v) = \exp \left[-\frac{(\pi \rho \sqrt{u^2 + v^2})^2}{4 \ln 2} \right] \quad (4)$$

where ρ is the FWHM. In the elliptical case, we therefore obtain

$$V_{env}(u, v, \rho_{eq}, \rho_{pol}, \alpha_1) = \exp \left[-\frac{(\pi \sqrt{\rho_{eq}^2 u'^2 + \rho_{pol}^2 v'^2})^2}{4 \ln 2} \right] \quad (5)$$

with the same expression of u' and v' as in Sect. 3.3, as we assume that the axes of the Gaussian envelope are aligned with the axes of the photosphere. The indexes “eq” and “pol” refer to the equator and pole of the central star.

3.5. Extracted parameters

Combining the visibility expressions presented in Sects. 3.3 and 3.4, we obtain the following expression for our simple model of an elongated ellipse with a superimposed Gaussian envelope:

$$V_{model}(u, v, \theta_{eq}, \theta_{pol}, \rho_{eq}, \rho_{pol}, \alpha_1, f) = \frac{V_{star} + f V_{env}}{1 + f}. \quad (6)$$

To derive the six free parameters of our model, we proceed through a classical χ^2 minimization process, with

$$\chi_{tot}^2(\theta_{eq}, \theta_{pol}, \rho_{eq}, \rho_{pol}, \alpha_1, f) = \sum_i \frac{[V_i^2 - V_{model}(u_i, v_i, \dots)]^2}{\sigma_i^2} \quad (7)$$

where V_i^2 is one of the VINCI squared-visibility measurements, and σ_i^2 its associated total variance. The expression of the reduced χ^2 is:

$$\chi_{red}^2 = \frac{\chi_{tot}^2}{N_{obs} - \text{d.o.f.}} \quad (8)$$

where N_{obs} is the number of individual observations and d.o.f. = 6 the numbers of degrees of freedom, considering that we fit a total of six parameters.

The minimum χ_{red}^2 of 0.79 is reached for the parameters listed in Table 4. This low value is characteristic of a good correspondence of our model to the interferometric data. The best-fit

3.2. The Be star Achernar (α Eridani)

1064

P. Kervella and A. Domiciano de Souza: The polar wind of Achernar

Table 4. Best fit parameters (and corresponding uncertainties) of our simple model consisting in a Gaussian elliptical envelope superimposed on a uniform ellipse representing the central star. The fit was computed on our complete H and K band data set.

θ_{eq}	2.13 ± 0.05 mas	stellar equatorial angular size
θ_{pol}	1.51 ± 0.02 mas	stellar polar angular size
α_1	131.6 ± 1.4 deg	azimuth of the stellar equator
ρ_{eq}	2.7 ± 1.3 mas	envelope FWHM along stellar equator
ρ_{pol}	17.6 ± 4.9 mas	envelope FWHM along stellar pole
f	$4.7 \pm 0.3\%$	relative (envelope to star) near-IR flux

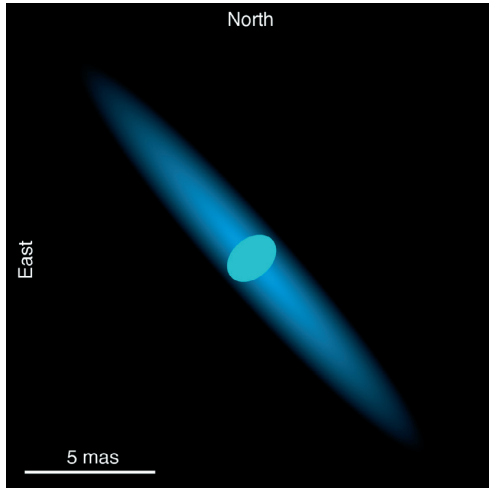


Fig. 3. Graphical representation of the best-fit model intensity distribution of Achernar. The relative flux contributions from the star and the envelope are not to scale. This illustration should not be considered as a true image of the star.

visibility function is a two-dimensional $V^2(u, v)$ map. Figure 2 shows the cuts of this best-fit $V^2(u, v)$ map along the stellar pole and the equator (solid curves). Note that the rapid visibility decrease observed at low spatial frequencies in the polar direction is reproduced well by the presence of the elongated polar envelope in the model.

A graphical representation of the star and its polar envelope based on the best-fit parameters is presented in Fig. 3. We emphasize that this figure is not a true image of the star, but only the representation of the best-fit light distribution with the a priori hypothesis that the star can be described by a uniform ellipse surrounded by an elliptical Gaussian envelope aligned with its principal axes. This intensity distribution reproduces the observed visibilities well, but several others could also fit. In particular, we cannot determine if the envelope is symmetric relative to the star, due to the baseline orientation ambiguity of 180° .

3.6. Excluded data points

In the fitting process, we chose to exclude the four data points obtained on the UT1-UT4 baseline (see Table 3b). With a position angle of ≈ 46 deg for the projected baseline, they correspond to a measurement that is almost aligned with the pole of the star ($\alpha_0 = 41.6 \pm 1.4$ deg). Although they satisfy the data quality criteria that we applied to the other data points, they are located $6-7\sigma$ away from the best-fit model. It should be noted that the 114 remaining data points are in excellent agreement with our

CSE model, and the residuals of the fit present satisfactory statistical properties (see Sect. 3.7).

An instrumental origin for these outliers cannot be formally excluded, especially as these data points were obtained on the very first night of VLTI operations of the UT1-UT4 baseline. However, no particular technical problem was reported, and the other stars observed on this night showed consistent results. As we could not distinguish these measurements from the rest of our data, we chose to publish them all together for the sake of homogeneity. A possible astrophysical cause for these low visibilities would be a stellar eruption that could have suddenly increased the CSE brightness and/or angular extension.

3.7. Comparison with other models and residuals of the fit

In order to assess the level of adequation of our star+CSE model to the data, we also tried to fit them with two simpler models: a circular uniform disk and a uniform ellipse. The residuals for each of the three models are presented in Fig. 4 as a function of the projected baseline azimuth angle. We obtained in the first case a uniform disk angular diameter of $\theta_{\text{UD}} = 1.78$ mas, with the large χ_{red}^2 of 4.9 characteristic of a bad fit. Fitting a uniform ellipse results in the following best-fit values: $\theta_{\text{eq}} = 2.31$ mas, $\theta_{\text{pol}} = 1.68$ mas, and $\alpha_1 = 135.7^\circ$. Again, the χ_{red}^2 of 3.2 shows poor agreement of this model to our data. It thus appears that our star+Gaussian CSE model is a much better fit to our data set ($\chi_{\text{red}}^2 = 0.79$) than the models without CSE.

As shown in Fig. 4 (bottom), the residuals of our star+CSE fit appear to be homogeneous with respect to azimuth angle. Similarly, we do not detect any significant residual either with respect to projected baseline length or with time (Fig. 5). The H and K band data sets do not show any systematic deviation, which justifies a posteriori our combined treatment of these two data sets. Due to the relatively small number of measurements in the H band and their lower accuracy compared to the K band, their influence on the best-fit parameters is very limited. However, they are overall in excellent agreement with the best-fit model, with a specific reduced χ^2 of only 0.2. Considering the limited amount of H band data, we currently cannot investigate the wavelength dependence of the CSE properties, but additional observations with the AMBER instrument of the VLTI in the J and H bands will soon allow such studies. It should be noted that interferometric observations of the bright B0IVpe star γ Cas in the visible have shown that the apparent size of this star can vary considerably with wavelength (Stee et al. 1998). The scatter appears to be slightly larger along the polar direction than along the equator of the star (Fig. 5, top). This could be caused by deviations from our simple star-CSE model on small angular scales. For instance, the presence of clumps in the CSE could create this apparent instability of the visibility function. However, our data set is still too limited to constrain their properties significantly.

4. Nature of the CSE of Achernar

4.1. Total extension

As listed in Table 4, the angular sizes of the axes of the photosphere ellipse (θ_{eq} and θ_{pol}) are well constrained, as is the flux ratio $f = 4.7 \pm 0.3\%$ between the star and the polar envelope. However, the angular dimensions of the envelope itself are poorly constrained. In particular, as visible in Fig. 2, we lack very short baseline measurements to estimate the total extension of the envelope in the polar direction. Considering our data, it could be much more extended than the

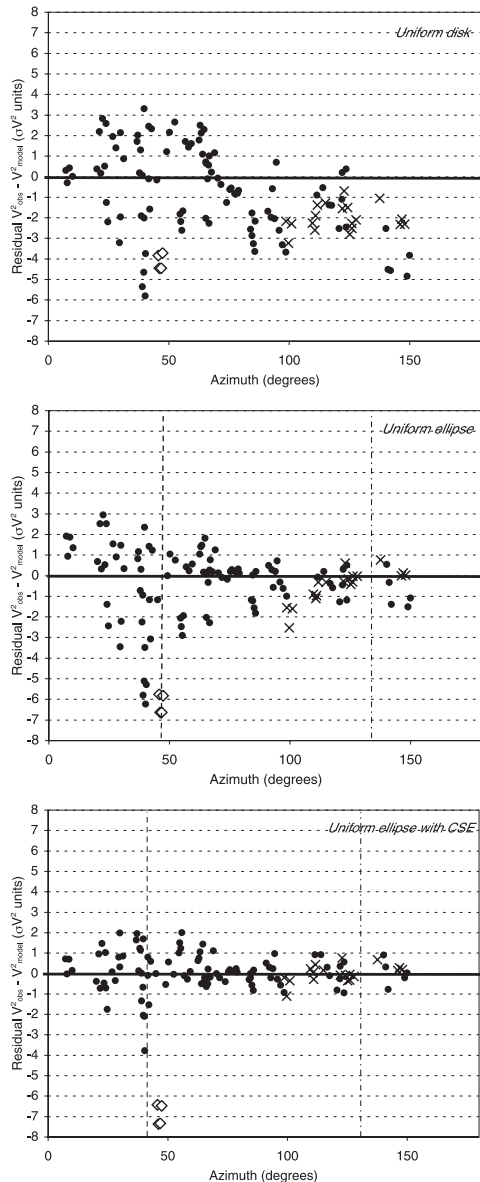


Fig. 4. Residuals of the visibility fit in units of V^2 standard deviation σ , as a function of azimuth angle, for a uniform disk (*top*), a uniform ellipse (*middle*), and our uniform ellipse with CSE model (*bottom*). The H band data are shown with crosses. The four outliers (open diamonds) were not included in the fit. The dashed and dot-dashed lines represent, respectively, the polar and equatorial directions of the models, including a uniform ellipse.

derived $\rho_{\text{pol}} = 17.6 \pm 4.9$ mas, which should be considered as a lower limit. The angular extension of the envelope in the equatorial direction is also rather poorly constrained by our data, but appears to be small, and could be approximately the size of the star itself.

4.2. Photospheric flattening ratio

From the fit of our two-component model, we obtained a photospheric major- over minor-axis ratio of $\theta_{\text{eq}}/\theta_{\text{pol}} = 1.41 \pm 0.04$, while D03 measured a value of 1.56 ± 0.05 , using part of the

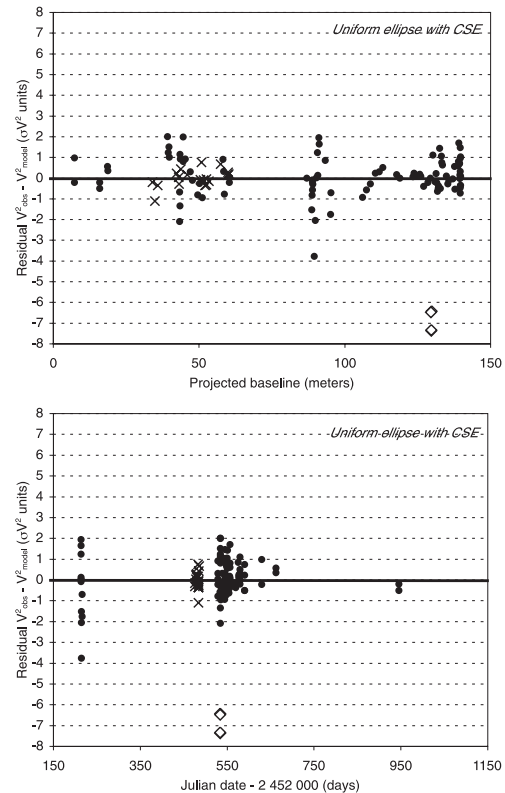


Fig. 5. Residuals of the visibility fit as a function of projected baseline length (*top*) and date of observation (*bottom*). The symbols are the same as in Fig. 4.

current data set. The 2.3σ difference between these two values can be explained by the difference in adopted model between these two approaches. D03 estimated the uniform disk equivalent angular diameter for each available azimuth and fitted an ellipse on the resulting values. In the present work, we directly fitted our two-component model to the visibilities in the (u, v) plane. In addition, D03 used a single-disk model that does not take the presence of the envelope into account.

Both approaches are valid and have their limitations and advantages. The important point where the main objective concerns the study of the flattening of the star is to compare the results to a physically realistic model including (at least) rotational deformation and gravity darkening, as was done by D03. In a future work we intend to perform a complete astrophysical analysis of the available interferometric and spectroscopic data on Achernar, including rotational effects (flattening and gravity darkening) and the CSE, both in the polar and equatorial directions.

4.3. Infrared free-free emission

From the measured flattening ratio, the polar temperature of Achernar could be higher than 20 000 K. In this context, the radiation pressure reaches very high values. As was demonstrated in the case of the luminous blue variable star η Carinae by Van Boekel et al. (2003), a stellar wind ejected from the poles can have a detectable signature in the interferometric visibilities in the near infrared. Recently, Meilland et al. (2006) showed that an elongated polar wind should be included with

3.2. The Be star Achernar (α Eridani)

1066

P. Kervella and A. Domiciano de Souza: The polar wind of Achernar

a thin disk in order to explain the near-IR VLTI/AMBER (e.g., Petrov et al. 2003) observations of α Arae, another Be star that is very similar to Achernar (rotation velocity, spectral type). Although the central stars are similar, one important difference is that α Arae presented hydrogen lines in strong emission during the interferometric observations, while they were absent from the spectrum of Achernar. Both stars show an elongated polar wind responsible for a free-free and free-bound near-IR continuum emission, while only one of them (α Arae) shows a dense equatorial disk (resolved by VLTI/AMBER) where hydrogen emission lines are formed. This indicates that a significant (in terms of size and near-IR emission) polar wind exists independently if the star is in a normal B or in a Be phase; i.e., the polar wind does not seem to be completely related to the existence of a denser equatorial envelope.

In the hypothesis that the observed polar CSE near-IR emission is mostly caused by free-free radiation, we can roughly estimate the mean electron density as $n_e \simeq 2-3 \times 10^{10} \text{ cm}^{-3}$ for the H and K bands. This value was obtained from the free-free emissivity (e.g. Allen 1973) by considering an electron temperature of 20 000 K (the result does not depend strongly on this value) and by using the CSE parameters derived in this work (Table 4).

In a recent paper, Vinicius et al. (2006) estimated the $2.2 \mu\text{m}$ continuum emission based on a residual emission detected in the $H\alpha$ absorption profile measured contemporaneously to the VINCI/VLTI campaign on Achernar. They proposed an explanation for the strong flattening measured on Achernar (Domiciano de Souza et al. 2003) by adopting the hypothesis that the residual $H\alpha$ emission and the associated near-IR continuum emission are formed in the remaining equatorial disk. However, considering the results from the present work, a significant fraction of the near-IR emission appears to originate in the polar envelope.

5. Conclusion

We have detected a diffuse circumstellar envelope around the bright Be star Achernar, which accounts for approximately 5% of the flux of the star in the near-IR (H and K bands). This envelope presents clear asymmetry with a significantly larger extension along the polar direction of the star. The photosphere of the star itself is distorted by the fast rotation with a larger equatorial angular diameter. The elongation of the CSE points to a significant polar wind, most probably powered by the hot temperature at the stellar poles (von Zeipel effect). Its total extension is loosely constrained by our observations, and it could reach large distances from the star. It appears that a complete astrophysical model able to simultaneously explain all observations (spectroscopic and interferometric) of Achernar is required. We are also confident that spectro-interferometric observations of Achernar with the VLTI/AMBER instrument will bring new insight into the gravity darkening, actual shape and relative intensity of the central star and its immediate circumstellar environment.

Acknowledgements. The interferometric measurements were obtained using the VINCI instrument installed at the VLTI. The VLTI is operated by the European Southern Observatory at Cerro Paranal, Chile. These data were obtained

under an unreferenced P70 shared-risk programme and during the technical commissioning of the interferometer. Their processing made use of the wavelet-based technique developed by D. Ségransan (Observatoire de Genève) and integrated into the VINCI pipeline. Observations with the VLTI are only made possible through the efforts of the VLTI team, for which we are grateful. The VINCI public commissioning data reported in this paper were retrieved from the ESO/ST-ECF Archive (Garching, Germany). This research made use of the SIMBAD and VIZIER databases at the CDS, Strasbourg (France), and NASA's Astrophysics Data System Bibliographic Services. We thank Drs. O. Chesneau and J. A. de Freitas Pacheco for their enlightening suggestions.

References

- Allen, C. W. 1973, *Astrophysical quantities* (London: University of London, Athlone Press), 3rd edn.
- Balona, L. A., Engelbrecht, C. A., & Marang, F. 1987, *MNRAS*, 227, 123
- Berger, J.-P., Haguenaer, P., Kern, P., et al. 2001, *A&A*, 376, 31
- Bordé, P., Coudé du Foresto, V., Chagnon, G., & Perrin, G. 2002, *A&A*, 393, 183
- Chauville, J., Zorec, J., Ballereau, D., et al. 2001, *A&A*, 378, 861
- Claret, A., Diaz-Cordovez, J., & Gimenez, A. 1995, *A&AS*, 114, 247
- Claret, A. 2000, *A&A*, 363, 1081
- Cohen, M., Walker, R. G., Carter, B., et al. 1999, *AJ*, 117, 1864
- Coudé du Foresto, V., Ridgway, S., & Mariotti, J.-M. 1997, *A&AS*, 121, 379
- Di Folco, E., Thévenin, F., Kervella, P., et al. 2004, *A&A*, 426, 601
- Damineli Neto, A., & de Freitas-Pacheco, J. A. 1982, *MNRAS*, 198, 659
- Domiciano de Souza, A., Vakili, F., Jankov, S., Janot-Pacheco, E., & Abe, L. 2002, *A&A*, 393, 345
- Domiciano de Souza, A., Kervella, P., Jankov, S., et al. 2003, *A&A*, 407, L47
- Domiciano de Souza, A., Zorec, J., Jankov, S., et al. 2004, *A&A*, 418, 781
- Domiciano de Souza, A., Kervella, P., Jankov, S., et al. 2005, *A&A*, 442, 567
- Dougherty, S. M., & Taylor, A. R. 1992, *Nature*, 359, 808
- Dougherty, S. M., Waters, L. B. F. M., Burki, G., et al. 1994, *A&A*, 290, 609
- Dyck, H. M., van Belle, G. T., & Thompson, R. R. 1998, *AJ*, 116, 981
- Gehrz, R. D., Hackwell, J. A., & Jones, T. W. 1974, *ApJ*, 191, 675
- Glebocki, R., Gnacinski, P., & Stawikowski, A. 2000, *Acta Astron.*, 50, 509
- Gлиндemann, A., Abuter, R., Carbognani, F., et al. 2000, *SPIE*, 4006, 2
- Gлиндemann, A., Albertsen, M., Avila, G., et al. 2004, *SPIE*, 5491, 447
- Jackson, S., MacGregor, K. B., & Skumanich, A. 2004, *ApJ*, 606, 1196
- Kervella, P., Coudé du Foresto, V., Gлиндemann, A., & Hofmann, R. 2000, *SPIE*, 4006, 31
- Kervella, P., Gitton, Ph., Ségransan, D., et al. 2003, *SPIE*, 4838, 858
- Kervella, P., Ségransan, D., & Coudé du Foresto, V. 2004a, *A&A*, 425, 1171
- Kervella, P., Thévenin, F., Di Folco, E., & Ségransan, D. 2004b, *A&A*, 426, 297
- Lebouquin, J.-B., Rousselet-Perraut, K., Kern, P., et al. 2004, *A&A*, 424, 719
- McAlister, H. A., ten Brummelaar, T. A., Gies, D. R., et al. 2005, *ApJ*, 628, 439
- Meilland, A., Stee, Ph., Vannier, M., et al. 2006, *A&A*, submitted
- Ohishi, N., Nordgren, T. E., & Hutter, D. J. 2004, *ApJ*, 612, 463
- Peters, G. J. 1982, *ApJ*, 253, L33
- Petrov, R. G., & Amber Consortium, The 2003, *EAS Publications Series*, Observing with the VLTI, ed. G. Perrin, & F. Malbet, 6, 111
- Quirrenbach, A., Bjorkman, K. S., Bjorkman, J. E., et al. 1997, *ApJ*, 479, 477
- Richichi, A., & Percheron, I. 2005, *A&A*, 434, 1201
- Ségransan, D., Forveille, T., Millan-Gabet, C. P. R., & Traub, W. A. 1999, in *ASP Conf. Ser.*, 194, 290
- Slettebak, A. 1982, *ApJS*, 50, 55
- Stee, Ph., de Araujo, F. X., Vakili, F., et al. 1995, *A&A*, 300, 219
- Stee, Ph., Vakili, F., Bonneau, D., & Mourard, D. 1998, *A&A*, 332, 268
- Snow, T. P. 1981, *ApJ*, 251, 139
- Tycner, C., Lester, J. B., Hajian, A. R., et al. 2005, *ApJ*, 624, 359
- Van Boekel, R., Kervella, P., Schöller, M., et al. 2003, *A&A*, 410, 37
- Vinicius, M. M. F., Zorec, J., Leister, N. V., & Levenhagen, R. S. 2006, *A&A*, 446, 643
- von Zeipel, H. 1924, *MNRAS* 84, 665
- Waters, L. B. F. M. 1986, *A&A*, 162, 121
- Waters, L. B. F. M., Cote, J., & Lamers, H. J. G. L. M. 1987, *A&A*, 185, 206

ON THE DETERMINATION OF THE ROTATIONAL OBLATENESS OF ACHERNAR

A. C. CARCIOFI,¹ A. DOMICIANO DE SOUZA,² A. M. MAGALHÃES,¹ J. E. BJORKMAN,³ AND F. VAKILI²

Received 2007 November 29; accepted 2008 January 31; published 2008 February 22

ABSTRACT

The recent interferometric study of Achernar, leading to the conclusion that its geometrical oblateness cannot be explained by the Roche approximation, has stirred substantial interest in the community, in view of its potential impact on many fields of stellar astrophysics. It is the purpose of this Letter to reinterpret the interferometric observations with a fast-rotating, gravity-darkened central star surrounded by a small equatorial disk, whose presence is consistent with contemporaneous spectroscopic data. We find that we can fit the available data only assuming a critically rotating central star. We identified two different disk models that simultaneously fit the spectroscopic, polarimetric, and interferometric observational constraints: a tenuous disk in hydrostatic equilibrium (i.e., with small scale height) and a smaller, scale height enhanced disk. We believe that these relatively small disks correspond to the transition region between the photosphere and the circumstellar environment and that they are probably perturbed by some photospheric mechanism. The study of this interface between photosphere and circumstellar disk for near-critical rotators is crucial to our understanding of the Be phenomenon and the mass and angular momentum loss of stars in general. This work shows that it is nowadays possible to directly study this transition region from simultaneous multitechnique observations.

Subject headings: polarization — stars: emission-line, Be — stars: individual (Achernar) — techniques: interferometric — techniques: spectroscopic

Online material: color figure

1. INTRODUCTION

Interferometry greatly increased our knowledge of the Be star Achernar (α Eri, HD 10144). Domiciano de Souza et al. (2003, hereafter D03) observed Achernar during fall 2002 with the ESO-VLTI/VINCI instrument (Kervella et al. 2003) in the K band and found that the star is highly oblate. By converting the individual visibilities into equivalent uniform-disk angular diameters, they derived a ratio between the major and minor elongation axis $a/b = 1.56 \pm 0.05$. Later, Kervella & Domiciano de Souza (2006) detected a tenuous polar wind, and very recently Kervella & Domiciano de Souza (2007) found that Achernar has a main-sequence, lower mass companion.

The available interferometric data, together with the abundance of data from the literature, forms a body of information that is probably unrivaled by that of any other Be star. There is, however, much that is still unknown about the star and its circumstellar environment. As pointed out by D03, the determination of the actual stellar oblateness from the interferometric data is not a simple task, since there are so many unknowns involved. In their original work D03, based on simultaneous spectroscopic data, assumed that there was no circumstellar material at the time of the observations and that the observed shape was purely photospheric in origin. Their modeling of the observations with a rotationally deformed, gravity-darkened star, assuming the Roche approximation of uniform rotation and centrally condensed mass, led to the conclusion that the stellar flattening required to explain the observations exceeds that of a critical rigid rotator.

Recent theoretical developments in the theory of differen-

tially rotating stars (e.g., Jackson et al. 2004) show that they can have equatorial radii larger than the Roche limit, which is physically compatible with the interferometric results. However, Vinicius et al. (2006) demonstrated the existence of a tiny yet nonnegligible emission in $H\alpha$ at the time of the VLTI observations, an indication that there was some circumstellar material around Achernar, probably associated with a small rotating disk. Furthermore, Vinicius et al. (2006) showed, from temporal analysis of profile variations of the line He I $\lambda 6678$ Å, that orbiting gas clouds are a very frequent feature of Achernar, even during its quiescent phase.

The presence of this circumstellar material raises the question of how much it can contribute to the observed visibilities. In this Letter we investigate how the presence of a small disk around Achernar may alter the interferometric signal and the effects this may have on the determination of fundamental parameters such as stellar rotation rate and stellar flattening.

2. MODELS

To compute the emergent spectrum of the system we use the computer code HDUST (Carciofi & Bjorkman 2006; Carciofi et al. 2006). This code solves the coupled problem of the non-local thermodynamic equilibrium (NLTE) and radiative equilibrium for arbitrary three-dimensional envelope geometries, using the Monte Carlo method. Given a prescription for the star (rotation rate, shape, flux distribution, effective temperature, luminosity, etc.) and for the circumstellar gas (density and velocity distribution), the code calculates the NLTE hydrogen-level populations and the electron kinetic temperature. Once those quantities are determined, the emergent spectrum (spectral energy distribution, line profiles, polarization, synthetic images, etc.) is calculated.

For the present work, we modified HDUST to treat non-spherical, gravity-darkened stars. We assume the stellar shape to be a spheroid, which is a reasonable approximation for the shape of a rigidly rotating star (Frémat et al. 2005). Given the

¹ Instituto de Astronomia, Geofísica e Ciências Atmosféricas, Universidade de São Paulo, Rua do Matão 1226, Cidade Universitária, São Paulo, SP 05508-900, Brazil.

² Lab. H. Fizeau, CNRS UMR 6525, Université de Nice Sophia Antipolis, Observatoire de la Côte d'Azur, F-06108 Nice cedex 2, France.

³ University of Toledo, Department of Physics and Astronomy, MS 111, 2801 W. Bancroft Street, Toledo, OH 43606.

TABLE 1
 FIXED STELLAR PARAMETERS

Parameter	Value	Reference
R_{pole}	$7.3 R_{\odot}$	This work
T_{pole}	20000 K	This work
Luminosity	$3150 L_{\odot}$	This work
V_{crit}	350 km s^{-1}	Vinicius et al. 2006
Inclination	65°	Carciofi et al. 2007
Distance	44.1 pc	Perryman et al. 1997

stellar rotation rate, $\Omega/\Omega_{\text{crit}}$, the ratio between the equatorial and polar radii is determined from the Roche approximation for the stellar surface equipotentials (Frémat et al. 2005). For the gravity darkening we use the standard von Zeipel flux distribution (von Zeipel 1924), according to which $F(\theta) \propto g_{\text{eff}}(\theta) \propto T_{\text{eff}}^4(\theta)$, where g_{eff} and T_{eff} are the effective gravity and temperature at stellar latitude θ . In HDUST, the star is divided into a number of latitude bins (typically 50) that have an associated T_{eff} and g_{eff} and emit with a spectral shape given by the corresponding Kurucz model atmosphere (Kurucz 1994).

For the disk density distribution we assume the following expression:

$$\rho(\varpi, z) = \frac{\rho_0 R_{\text{eq}}}{\sqrt{2\pi}H} \left(\frac{R_{\text{eq}}}{\varpi}\right)^2 \exp\left(-\frac{z^2}{H^2}\right), \quad (1)$$

which is similar to the density distribution of an isothermal viscous decretion disk in vertical hydrostatic equilibrium (e.g., Carciofi et al. 2006). In the above equation, ϖ is the radial distance in cylindrical coordinates, R_{eq} is the equatorial radius of the star, and ρ_0 is the disk density scale. We write the disk vertical scale height, H , as

$$H = H_0 \left(\frac{\varpi}{R_{\text{eq}}}\right)^{1.5}, \quad (2)$$

where H_0 is the scale height at the base of the disk. For isothermal disks in vertical hydrostatic equilibrium $H_0 = aV_{\text{crit}}^{-1}R_{\text{eq}}$, where a is the sound speed and the critical velocity, $V_{\text{crit}} \equiv (GM/R_{\text{eq}})^{1/2}$, is the Keplerian orbital speed at the stellar surface.

We chose a set of fixed stellar parameters, listed in Table 1. The value for the polar radius came directly from the interferometry, once we fixed the stellar inclination angle to be 65° after the recent work of Carciofi et al. (2007). It is worth noting, however, that the results we show below are little affected if we allow the inclination angle to vary within a reasonable range (say, $\pm 5^{\circ}$). The value for the stellar luminosity was obtained by fitting the available photometric data (see legend of Fig. 1).

Each model of the star plus disk system has four free parameters: (1) the stellar angular rotation rate, $\Omega/\Omega_{\text{crit}}$, (2) the disk density scale, ρ_0 , (3) the disk outer radius, R_d , and (4) the disk scale height, H_0 .

We have two well-known observational constraints, namely, the 2002 interferometric observations (D03) and the 2002 $H\alpha$ line profile (Vinicius et al. 2006, fig. 12). Unfortunately, no contemporaneous measurement of the linear polarization exists, but we can impose, with a reasonable level of confidence, an upper limit for the polarization based on the recent results of Carciofi et al. (2007). In that Letter, the results of a polarization monitoring of Achernar, carried out between 2006 July and November, is reported. Those measurements were taken during a period in which Achernar was active, with a tenuous circum-

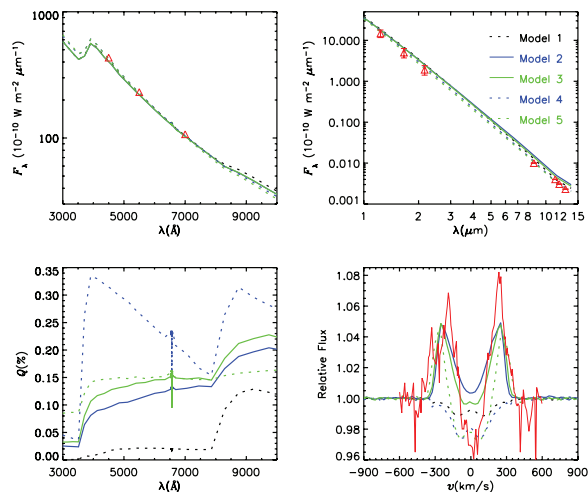


FIG. 1.—Emergent spectrum for models 1–5. *Top left*: Visible SED. The red triangles correspond to *BVR* photometry from the NOMAD catalog (Zacharias et al. 2005), for which no observational errors were available. *Top right*: IR SED. The *JHK* photometry is from the 2MASS catalog (Cutri et al. 2003) and the mid-IR photometry is from Kervella & Domiciano de Souza (2007). The observational errors for the mid-IR data are of the order of 2%. *Bottom left*: Continuum polarization. *Bottom right*: $H\alpha$ emission profile. The red curve corresponds to the residual emission profile of Vinicius et al. (2006).

stellar disk, as indicated by the weak $H\alpha$ emission (Carciofi et al. 2007, fig. 3). We adopt as an upper limit for the polarization in our modeling the lowest value reported in Carciofi et al. (2007), which was 0.12% in the *B* band. As we shall see below, fixing this upper limit for the polarization level has important consequences for the modeling.

3. RESULTS

Our modeling procedure is as follows. For a given set of $\Omega/\Omega_{\text{crit}}$, ρ_0 , R_d , and H_0 we calculate synthetic images in the *K* band, centered at $\lambda = 2.15 \mu\text{m}$, the $H\alpha$ line profile, the continuum polarization, and the spectral energy distribution (SED). The model amplitude visibilities were obtained from the Fourier transform moduli of the model images at $2.15 \mu\text{m}$, normalized by the total *K*-band flux of the synthetic image.

Since the $H\alpha$ emission from 2002 October is very small and the true photospheric profile of Achernar is not known, we model, instead of the observed profile, the residual emission profile of Vinicius et al. (2006, fig. 12). This profile was obtained by subtracting from the 2002 October observations the average profile of the 1999 period, which is believed to be purely photospheric. The equivalent width (EW) of this emission profile is -0.29 \AA .

In Figure 2 we show the visibility curves along the polar and equatorial directions together with the corresponding *K*-band images for five representative models that were chosen to illustrate different aspects of our solution. In Table 2 we list the model parameters, along with some model results, such as the *B*-band polarization level, the $H\alpha$ EW, and the *K*-band flux excess, E_K , which is defined as $F^{\lambda}/F_{\star}^{\lambda} - 1$, where F_{\star}^{λ} is the stellar flux without the disk at wavelength λ .

Let us begin discussing models 1–3, for which the star was assumed to be rotating critically. We have used $\Omega/\Omega_{\text{crit}} = 0.999999$ ($V_{\text{eq}}/V_{\text{crit}} = 0.9993$) instead of 1 to avoid the unphysical situation of having $T_{\text{eff}} = 0$ in the stellar equator.

3. High spectro-spatial resolution observations of fast rotators in the H-R diagram

No. 1, 2008

DETERMINATION OF ROTATIONAL OBLATENESS OF ACHERNAR

L43

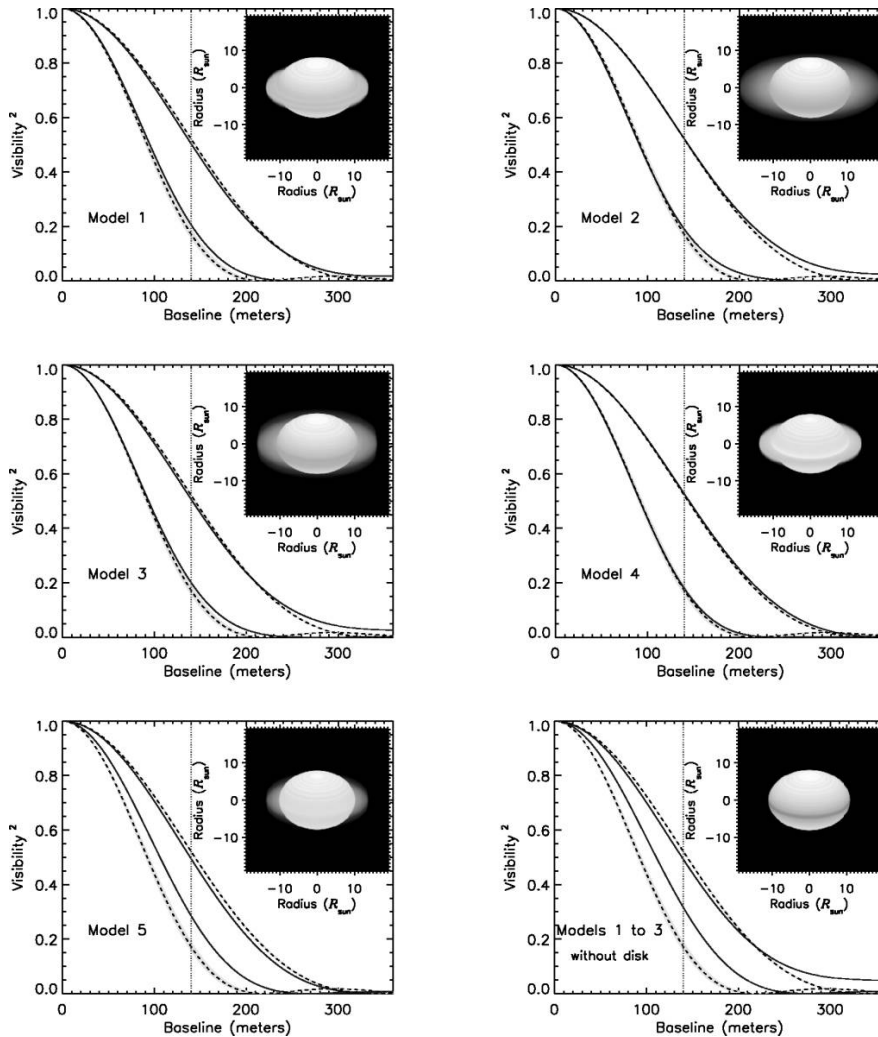


FIG. 2.—Squared visibilities for the models of Table 2 (*solid lines*), along the polar (*upper curves*) and equatorial (*lower curves*) directions. The dashed lines represent the *K*-band visibilities for uniform-disk (UD) angular diameters of 1.62 mas and 2.53 mas derived by D03; the corresponding $\pm 1 \sigma$ uncertainties are shown as light-color bands. These UD diameters indicate the maximum (equatorial direction) and minimum (polar direction) sizes measured on Achernar in the *K* band with VLT/VINCI. The vertical dotted lines indicate the maximum baseline available from the VLT data. The insets show the model image in the *K* band, in logarithmic scale. The bottom right plot shows the squared visibilities for a gravity-darkened Roche star at near-critical velocity (models 1–3) without the disk and indicates, as shown by D03, that such a model does not reproduce the observations. [See the electronic edition of the *Journal for a color version of this figure.*]

Model 1 corresponds to a small and relatively dense disk, with H_0 given by equation (2); i.e., model 1 corresponds to a disk in vertical hydrostatic equilibrium. For this model the visibility curves match very well the observations and the polarization is within the adopted limit, but the $H\alpha$ emission is very weak, as a result of the small disk size.

One way to increase the $H\alpha$ emission is to make the disk larger. For model 2 we adopted a larger value for R_d , but the density had to be decreased in order to keep the polarization within the adopted limit. This model reproduces well both the visibility curves and the $H\alpha$ EW.

Another way of increasing the line emission is to raise the

TABLE 2
MODEL PARAMETERS

Model	$\Omega/\Omega_{\text{crit}}$	ρ_0 (g cm^{-3})	R_d	H (R_\odot)	R_{eq}/R_p	T_p/T_{eq}	$H\alpha$ EW (\AA)	P_B (%)	E_K
1	0.999999	1.0×10^{-11}	13.7	0.45	1.5	5.8	0.10	0.02	0.17
2	0.999999	3.8×10^{-12}	19.1	0.45	1.5	5.8	-0.34	0.10	0.14
3	0.999999	2.6×10^{-12}	16.1	1.1	1.5	5.8	-0.27	0.12	0.12
4	0.992	1.0×10^{-11}	13.7	0.45	1.4	1.8	0.20	0.31	0.15
5	0.992	1.7×10^{-12}	13.7	0.91	1.4	1.8	-0.05	0.15	0.03

disk scale height. If one raises H by a factor of, say, k , the disk density scale must be decreased by a factor $k^{1/2}$ to keep the polarization approximately constant. Model 3 corresponds to our best scale height enhanced model for a critically rotating star. The visibility curves and the $H\alpha$ EW are well reproduced by the model, and the polarization is within the adopted upper limit.

We also studied models with lower values of $\Omega/\Omega_{\text{crit}}$. In this case, our attempts to fit simultaneously the visibility curves, polarization, and $H\alpha$ EW were unsuccessful.

Models 4 and 5 are examples of the results we have obtained for subcritical stars. Model 4 corresponds to a small and dense disk in vertical hydrostatic equilibrium. This model reproduces quite well the visibilities but has too large B -band polarization and no $H\alpha$ emission. A scale height enhanced model with lower density, such as model 5, has better values for polarization and $H\alpha$ EW but does not have enough IR flux in the equator to account for the observed size.

Our lack of success in fitting the observations with subcritical models is a direct result of two physical effects, both related to the presence of gravity darkening. For the critical models 1–3, the bolometric stellar flux at the equator is about 1100 times lower than the flux at the pole. Since the disks are relatively small and the star oblate, light from the pole cannot reach the disk and, as a result, the net scattered flux is small. As $\Omega/\Omega_{\text{crit}}$ decreases, the flux at the equator rises, and the star becomes less oblate. Both mechanisms cause a significant increase in the scattered flux and, thus, in the polarization level.

4. DISCUSSION

The presence of a small disk around Achernar is a realistic possibility to explain the interferometric observations. As shown by D03 (see also Fig. 1), Roche models without a disk cannot account for the observed aspect ratio.

The combined constraints imposed by the interferometry, spectroscopy, and the adopted upper limit for the polarization have allowed us to impose very narrow limits on the model parameters, within our assumption of a rigidly rotating star in the Roche approximation surrounded by a small disk. The main result is that the star must be rotating very close to critical, since all of our models with $\Omega/\Omega_{\text{crit}} < 0.992$ that successfully reproduced both the visibilities and the $H\alpha$ EW (e.g., model 5) had too large polarization levels, for the reasons discussed above.

We have found two critical models that reproduce equally well the observations: a large and dense disk in hydrostatic equilibrium (i.e., geometrically thin; model 2) and a small and more tenuous disk with enhanced scale height (i.e., geometrically thick; model 3). Because of the lack of contemporaneous polarization measurements, the model parameters shown in Table 2 have a degree of uncertainty that is difficult to estimate.

This stresses the importance of having simultaneous multi-technique data.

The current paradigm for Be star disks is that of a geometrically thin viscous Keplerian disk in vertical hydrostatic equilibrium. This paradigm has been corroborated by several recent studies (e.g., Carciofi et al. 2006; Meilland et al. 2007).

When a star is close to critical rotation, the stellar photospheric material near the equator, which is weakly bound to the star because of the strong centrifugal force, can eventually escape the star provided it is given an extra energy by some other mechanism (e.g., stellar pulsation, interaction in a binary system, photospheric activity). This material is likely to have, initially, a very complicated density and velocity distribution. As the gas diffuses outward as a result of viscosity, the density and velocity distributions will tend to relax and become in hydrostatic equilibrium.

Thus, it is reasonable to assume that there is a *transition region* between the photosphere (which is characterized by large densities of the order of 10^{-10} g cm $^{-3}$) and the disk itself, which has densities at least 10 times lower. Many unknowns exist concerning the size and physical properties (e.g., density, temperature, velocity field) of this smooth transition region.

With the available data we were able to narrow down substantially the range of possible values for Achernar's model parameters, but we cannot distinguish yet between model 2 and 3, i.e., between a model in hydrostatic equilibrium and a model with enhanced scale heights that might result from the perturbation of the gas by some photospheric mechanism.

As shown in Figure 1, high-precision spectropolarimetry might add invaluable information, since models 2 and 3 have different values for the size of Balmer and Paschen jumps in polarization. Also, with simultaneous spectrointerferometry and spectropolarimetry one can spatially resolve the velocity field, thus establishing whether the material is in equilibrium or not. The observed residual emission profile (Fig. 1) is indicative of velocity fields more complex than the simple Keplerian rotation that was assumed in this work.

In any case, one important consequence of this work is that we have shown that with current observing techniques and state-of-the-art modeling it is already possible to study the properties of the very inner layers of the disk in Achernar and possibly other nearby Be stars. Future simultaneous spectropolarimetry, spectrointerferometry, and photometry will allow us to study the properties of this region and determine, for instance, the size of the transition region and the point at which the disk becomes in vertical hydrostatic equilibrium.

This work was supported by FAPESP grant 04/07707-3 to A. C. C., FAPESP grant 01/12598-1 to A. M. M., and NSF grant AST 03-07686 to the University of Toledo (J. E. B.). A. M. M. also acknowledges partial support by CNPq.

REFERENCES

- Carciofi, A. C., & Bjorkman, J. E. 2006, *ApJ*, 639, 1081
 Carciofi, A. C., Magalhães, A. M., Leister, N. V., Bjorkman, J. E., & Levenhagen, R. S. 2007, *ApJ*, 671, L49
 Carciofi, A. C., et al. 2006, *ApJ*, 652, 1617
 Cutri, R. M., et al. 2003, The IRSA 2MASS All-Sky Point Source Catalog, <http://irsa.ipac.caltech.edu/applications/Gator/>
 Domiciano de Souza, A., Kervella, P., Jankov, S., Abe, L., Vakili, F., di Folco, E., & Paresce, F. 2003, *A&A*, 407, L47 (D03)
 Frémat, Y., Zorec, J., Hubert, A.-M., & Floquet, M. 2005, *A&A*, 440, 305
 Jackson, S., MacGregor, K. B., & Skumanich, A. 2004, *ApJ*, 606, 1196
 Kervella, P., & Domiciano de Souza, A. 2006, *A&A*, 453, 1059
 ———. 2007, *A&A*, 474, L49
 Kervella, P., et al. 2003, *Proc. SPIE*, 4838, 858
 Kurucz, R. L. 1994, CD-ROM Nos. 19, 20, 21 (Cambridge: SAO)
 Meilland, A., et al. 2007, *A&A*, 464, 59
 Perryman, M. A. C., et al. 1997, *A&A*, 323, L49
 Vinicius, M. M. F., Zorec, J., Leister, N. V., & Levenhagen, R. S. 2006, *A&A*, 446, 643
 von Zeipel, H. 1924, *MNRAS*, 84, 665
 Zacharias, N., Monet, D. G., Levine, S. E., Urban, S. E., Gaume, R., & Wycoff, G. L. 2005, *VizieR Online Data Catalog*, 1297, 0

3.2.3 The binary companion of Achernar: detection and characterization

As part of our program to study Achernar and its close CSE we combined different high angular resolution techniques of direct imaging. We used in particular the VLT imaging instruments VISIR in burst mode (multiple mid-IR short exposure images of 20 – 25 ms allowing a final diffraction limited image) and NACO (near-IR adaptive optics). These observations revealed that Achernar is a binary system, composed by the previously known Be star, and by a, newly discovered, fainter companion ($\sim 20 - 30$ times). We have characterized this companion as being most likely a A1V-A3V star.

The details on the detection and characterization of the companion of Achernar are presented, respectively, in the two A&A papers given below: [Kervella & Domiciano de Souza \(2007\)](#) and [Kervella et al. \(2008\)](#).

Since these works on Achernar, we have continued to follow the binary companion across its orbit, using several high angular resolution techniques (imaging, adaptive optics, aperture masking, interferometry). A future work is being prepared (Kervella, Domiciano de Souza et al., in prep.), where we intend to derive the orbital parameters of the system, providing in particular the orbital period and the masses of each component. The preliminary results indicate masses $\simeq 6 M_{\odot}$ for the primary Be star and $\simeq 2 M_{\odot}$ for the secondary, with an orbital period of $\simeq 7$ years.

This work on Achernar's binary system can bring crucial clues to the study of binary interactions in massive, fast-rotating stars in general, and in Be stars in particular. The interplay between fast-rotation and binarity of massive stars is closely linked to questions concerning their chemical evolution, ionizing fluxes, mass and momentum losses, and final stages of evolution.

LETTER TO THE EDITOR

The environment of the fast rotating star Achernar

High-resolution thermal infrared imaging with VISIR in BURST mode

P. Kervella¹ and A. Domiciano de Souza^{2,3}¹ LESIA, Observatoire de Paris, CNRS, UPMC, Université Paris Diderot, 5 place Jules Janssen, 92195 Meudon Cedex, France
e-mail: Pierre.Kervella@obspm.fr² Lab. Univ. d'Astrophysique de Nice (LUAN), CNRS UMR 6525, UNSA, Parc Valrose, 06108 Nice, France³ Observatoire de la Côte d'Azur, CNRS UMR 6203, Département GEMINI, BP 4229, 06304 Nice Cedex 4, France

Received 31 August 2007 / Accepted 19 September 2007

ABSTRACT

Context. It is expected that Be stars are surrounded by circumstellar envelopes, and that a significant fraction have companions. Achernar (α Eri) is the nearest Be star, and is thus a favourable target to search for their signatures using high resolution imaging.

Aims. We aim at detecting circumstellar material or companions around Achernar at distances of a few tens of AU.

Methods. We obtained diffraction-limited thermal IR images of Achernar using the BURST mode of the VLT/VISIR instrument.

Results. The images obtained in the *PAH1* band show a point-like secondary source located 0.280'' north-west of Achernar. Its emission is 1.8% of the flux of Achernar in this band, but is not detected in the *PAH2*, *SiC* and *NeII* bands.

Conclusions. The flux from the detected secondary source is compatible with a late A spectral type main sequence companion to Achernar. The position angle of this source (almost aligned with the equatorial plane of Achernar) and its projected linear separation (12.3 AU at the distance of Achernar) favor this interpretation.

Key words. stars: individual: Achernar – methods: observational – techniques: high angular resolution – stars: emission-line, Be

1. Introduction

The southern star Achernar (α Eridani, HD 10144) is the brightest and nearest of all Be stars ($V = 0.46$ mag). Depending on the author (and the technique used) its spectral type ranges from B3-B4IIIe to B4Ve (e.g., Slettebak 1982; Balona et al. 1987). The estimated projected rotation velocity $v \sin i$ ranges from 220 to 270 km s⁻¹ and the effective temperature T_{eff} from 15 000 to 20 000 K (see e.g., Vinicius et al. 2006; Rivinius, priv. comm.; Chauville et al. 2001). It has been the subject of a renewed interest since its distorted photosphere was resolved by means of near-IR long-baseline interferometry (Domiciano de Souza et al. 2003). Further interferometric observations revealed the polar wind ejected from the hot polar caps of the star (Kervella & Domiciano 2006), due to the von Zeipel effect (von Zeipel 1924).

Our observations aim at studying two aspects of the close environment of Achernar: the circumstellar envelope at distances of up to a few tens of AU, and binarity. Mid-infrared (hereafter MIR) imaging is perfectly suited for these two objectives. Firstly, this wavelength range corresponds to where a circumstellar envelope becomes optically thick (assuming the emission is caused by free-free radiation, following for instance Panagia & Felli 1975). Secondly, the contrast between Achernar and a cool companion will be significantly reduced.

We hereafter present the result of our imaging campaign with the VLT/VISIR instrument, to explore the environment of this star at angular distances of ≈ 0.1 to $10''$.

2. Observations

2.1. Instrumental setup: the BURST mode of VISIR

We used the VISIR instrument (Lagage et al. 2004), installed at the Cassegrain focus of the Melipal telescope (UT3) of the VLT (Paranal, Chile). VISIR is a MIR imager, that also provides a slit spectrometer. As it is a ground-based instrument, its sensitivity is severely limited by the high thermal background of the atmosphere, compared for instance to the Spitzer space telescope, but its resolving power is ten times higher, thanks to the 8 m diameter of the primary mirror. VISIR is therefore very well suited for our programme to search for the presence of circumstellar material and companions within a few tens of AU of Achernar.

However, under standard conditions at Paranal (median seeing of 0.8'' at 0.5 μm), the 8 m telescope is not diffraction limited in the MIR (seeing $\approx 0.4''$ vs. 0.3'' diffraction). Instead of a pure Airy diffraction pattern, several moving speckles and tip-tilt usually degrade the quality of the image (see e.g. Tokovinin et al. 2007). To overcome this limitation, a specific mode of the instrument, called the BURST mode, was introduced by Doucet et al. (2007a,b). Its principle is to acquire very short exposures ($\Delta t \lesssim 50$ ms), in order to keep the complete integration within a fraction of the coherence time (≈ 300 ms at Paranal in the MIR). The detector is therefore read very quickly, and the resulting images freeze the turbulence. It is subsequently possible to select the best images that present a single speckle ("lucky imaging"), and are thus diffraction-limited. The details of this selection

3. High spectro-spatial resolution observations of fast rotators in the H-R diagram

L50

P. Kervella and A. Domiciano de Souza: Thermal infrared imaging of Achernar

Table 1. Log of the observations of Achernar and its PSF calibrator, δ Phe using the BURST mode of VISIR. MJD is the modified Julian date of the middle of the exposures on the target, minus 54 012. The Detector Integration Time (DIT) is given in milliseconds for one BURST image. θ is the seeing in the visible ($\lambda = 0.5 \mu\text{m}$) as measured by the observatory DIMM sensor, in arcseconds. The airmass (AM) is the average airmass of the observation.

#	MJD*	Star	Filter	DIT	N exp.	θ (")	AM
A	0.0669	α Eri	PAH1	20	1200 \times 14	0.9	1.64
B	0.0844	δ Phe	PAH1	20	1200 \times 14	1.0	1.43
C	0.0965	δ Phe	NeII	25	960 \times 14	1.1	1.37
D	0.1201	α Eri	NeII	25	960 \times 14	1.0	1.36
E	0.1319	α Eri	PAH1	20	1200 \times 14	0.6	1.32
F	0.1482	δ Phe	PAH1	20	1200 \times 14	0.6	1.18
G	0.1604	δ Phe	PAH2	20	1200 \times 14	0.6	1.16
H	0.1877	α Eri	PAH2	20	1200 \times 14	0.8	1.21
I	0.1997	α Eri	PAH1	20	1200 \times 14	0.8	1.20

procedure are given in Sect. 2.3. The BURST mode was already applied successfully to the observation of the nucleus of NGC 1068 (Poncelet et al. 2007).

2.2. Observations log

We observed Achernar during the first half of the night of October 3–4, 2006. A series of BURST mode observations of this star and δ Phe was obtained in three filters: PAH1, PAH2 and NeII (central wavelengths $\lambda = 8.59, 11.25$ and $12.81 \mu\text{m}$). They were followed by classical VISIR imaging observations of Achernar and δ Phe in the PAH1, SiC ($\lambda = 11.85 \mu\text{m}$) and NeII filters, in order to provide a reference for processing using the standard instrument pipeline.

The detailed transmission curves of the filters can be found in the VISIR instrument manual, available from the ESO web site¹. The images obtained on the targets were chopped and nodded in a North-South and East-West direction by offsetting the M2 mirror and the telescope itself (resp.) in order to remove the fluctuating thermal background in the post-processing. The chopping and nodding amplitudes were both set to $8''$ on the sky, and the periods were 4 and 90 s, respectively. The pixel scale was set to the smallest scale available on VISIR ($0.075''/\text{pixel}$), in order to sample as well as possible the $\approx 0.3''$ FWHM diffraction pattern of the telescope. The Achernar observations were interspersed every 40–50 min with a PSF reference star, observed with the same instrumental setup. The journal of the VISIR BURST mode observations is given in Table 1. During the observations, the seeing quality in the visible varied from average ($1.1''$) to excellent ($0.6''$).

The PSF reference star, δ Phe (HD 9362, G9III), was chosen in the Cohen et al. (1999) catalogue of spectrophotometric standards for infrared wavelengths. In addition to being a stable star, previous interferometric observations in the near-IR with the VINCI instrument (see in particular Thévenin et al. 2005; Kervella & Domiciano de Souza 2006) have confirmed that δ Phe is indeed single. Another advantage of choosing our PSF star in this catalogue is that its flux is absolutely calibrated, and it therefore provides a convenient photometric reference to estimate accurately the absolute flux of the observed object. δ Phe is located relatively close to Achernar on the sky (8.2°), and therefore at a similar airmass. It is also of comparable brightness in the MIR (9.5 Jy at $12 \mu\text{m}$ vs. ≈ 16 Jy for Achernar).

¹ <http://www.eso.org/instruments/visir>

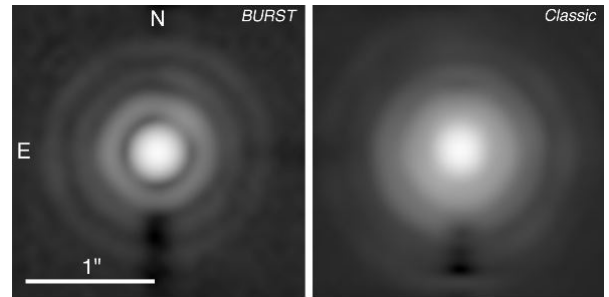


Fig. 1. Comparison of the BURST (image A in Table 1) and Classic (image L in Table 2) images of Achernar in the PAH1 filter. The two images were obtained in the same seeing conditions.

Table 2. Log of the observations of Achernar and δ Phe using the classical imaging mode of VISIR. The columns are the same as in Table 1, except the “Total” column, giving the total integration time on target.

#	MJD*	Star	Filter	DIT	Total (s)	θ (")	AM
J	0.2085	α Eri	SiC	25	640	0.7	1.19
K	0.2188	α Eri	NeII	25	650	0.7	1.19
L	0.2292	α Eri	PAH1	20	650	0.7	1.19
M	0.2445	δ Phe	SiC	25	640	0.7	1.10
N	0.2474	δ Phe	NeII	25	650	0.6	1.11
O	0.2518	δ Phe	PAH1	20	650	0.6	1.11

2.3. Raw data processing

One drawback of the BURST mode is that it produces a very large quantity of data: almost 20 Gbytes for our half-night of observations. However, the basic MIR data reduction to remove the instrument signature and the thermal background from the images is simple, and the data quantity is quickly brought to a more manageable volume. The fluctuations of the thermal background were removed through the classical subtraction of the chopped and nodded images, in order to produce data cubes of more than 10 000 images covering $6.8 \times 6.8''$. After a precentering at the integer pixel level, the images were sorted based on their maximum intensity, used as a proxy of the Strehl ratio. The 5000 best images of each cube were then resampled up by a factor 10 using a cubic spline interpolation, and the star image was subsequently centered using Gaussian fitting, at a precision level of a few milliarseconds. The field of view was trimmed to $2.25 \times 2.25''$ to reduce the computing time. The resulting cubes were eventually averaged to obtain the master images of Achernar and δ Phe used in the image analysis process described below.

Our classical (non-BURST) VISIR images were processed using the standard VISIR pipeline. This mode differs from the BURST mode in the sense that the images obtained within one chopping cycle (every 90 s) are averaged together immediately after acquisition in order to reduce the data rate. As a result, the atmospheric tip-tilt and higher order perturbations degrade the image quality. The main advantage of this mode is that the processing is less computer intensive.

2.4. BURST vs. classical mode images

As expected, the classical mode images present a significantly degraded effective resolution compared to the BURST mode images (Fig. 1), although the seeing conditions were excellent in both cases (visible seeing $\approx 0.7''$). The full-width at half-maximum (hereafter FWHM) of the classical mode image

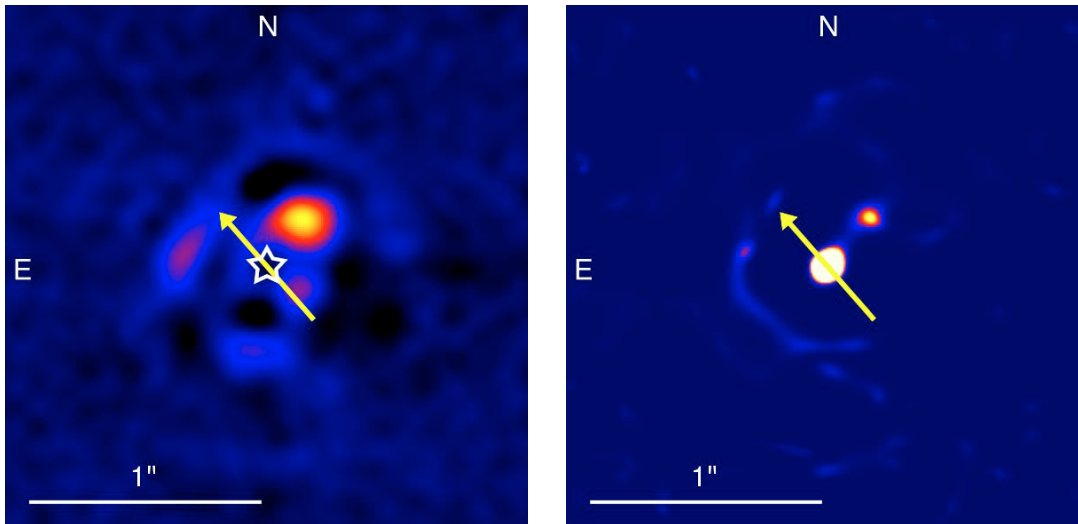


Fig. 2. *Left:* average of the three PSF subtracted images of Achernar in the *PAH1* filter (AB, EF and IF pairs). The position of Achernar is marked with a “star” symbol. *Right:* average deconvolved image of Achernar (without PSF subtraction). In both images, the orientation of the polar axis of Achernar (Kervella & Domiciano 2006) is represented by an arrow.

is $0.285''$, while it is only $0.217''$ for the BURST image. As already demonstrated by Doucet et al. (2007a), this clearly shows that the BURST mode is perfectly suited for the most demanding observing programs in terms of angular resolution.

3. Image analysis

3.1. PSF subtraction and image deconvolution

To analyse the images of Achernar, we used two distinct methods: PSF subtraction and Lucy-Richardson deconvolution. Provided the seeing conditions are comparable between Achernar and the calibrator (a condition verified during our observations), these two methods give access to the close environment of the star. The images were processed pairwise with the following Achernar-PSF combinations (see Table 1): A-B (*PAH1*), D-C (*NeII*), E-F (*PAH1*), H-G (*PAH2*), I-F (*PAH1*).

Firstly, we directly subtracted the normalized PSF image obtained on the calibrator star from the image of Achernar. The normalization factor between the two images was computed using a two-parameter linear least squares fit (slope and zero point) on the central 375×375 mas (50×50 pixels on our resampled images). A higher degree fit was also tried to account for a possible non-linearity of the detector, but no difference was noticeable between the two fitting methods. The average of the three subtracted *PAH1* images is presented in Fig. 2 (left), and the *NeII* and *PAH2* images are shown in Fig. 3. This procedure does not work well with the classical (non-BURST) images, due to the degraded image quality. We thus employed the classical mode images only for photometry.

Secondly, we deconvolved the three Achernar images using their associated PSF calibrator images as the “dirty beam” and the classical Lucy deconvolution algorithm (200 iterations). The average of the three resulting deconvolved images in the *PAH1* band is presented in Fig. 2 (right). The deconvolved images in the *NeII* and *PAH2* bands do not show any source in the field around Achernar.

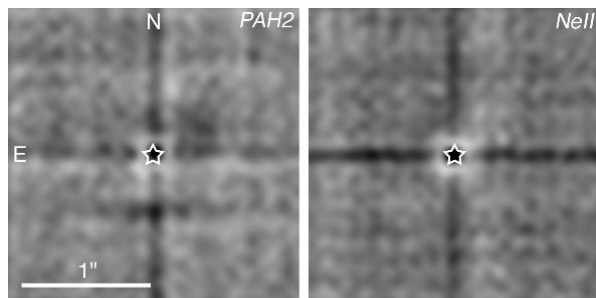


Fig. 3. Residual of the subtraction of the PSF calibrator image from the images of Achernar obtained using the *PAH2* (D-C) and *NeII* (H-G) filters ($\lambda = 11.25$ and $12.81 \mu\text{m}$, respectively). The vertical and horizontal dark lines are artefacts from the detector.

3.2. Photometry of Achernar

We obtained photometry of Achernar and δ Phe using an aperture of $0.6''$ in diameter. In order to absolutely calibrate the flux of Achernar in the four filters used for the present observations, we used as reference the spectrophotometric template of δ Phe from Cohen et al. (1999). The irradiance of δ Phe was read from this template at the average wavelength of each filter, and multiplied by the ratio of the measured aperture photometry of Achernar and δ Phe. The results are presented in Table 3.

3.3. Northwestern emission

An emitting region in the northwest quadrant, hereafter referred to as “source B”, is visible in the subtracted and deconvolved *PAH1* images (Fig. 2). A Gaussian fit to the deconvolved image of Achernar gives the following relative position of source B from Achernar along the right ascension and declination directions: $\Delta\alpha = -0.184''$, $\Delta\delta = +0.211''$, giving an angular separation of $0.280''$ and a position angle $\phi = -41.1^\circ$ (counted negatively from North towards West, for which $\phi = -90^\circ$). At the distance of Achernar (44 pc, ESA 1997) this corresponds to a linear projected separation of 12.3 AU. The measured azimuth is

3. High spectro-spatial resolution observations of fast rotators in the H-R diagram

L52

P. Kervella and A. Domiciano de Souza: Thermal infrared imaging of Achernar

Table 3. Measured irradiance of Achernar.

Filter	λ (μm)	10^{-13} W/m ² / μm	Jy
<i>PAH1</i>	8.59	9.99	23.7
<i>PAH2</i>	11.25	4.01	16.8
<i>SiC</i>	11.85	3.06	14.4
<i>NeII</i>	12.81	2.31	12.5

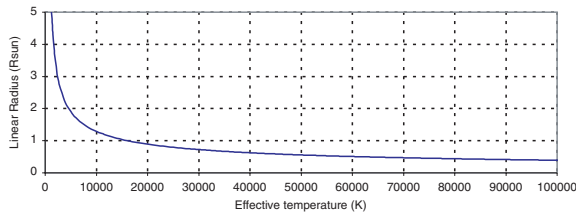


Fig. 4. Linear radius of the companion of Achernar, as a function of its effective temperature.

close to that of the equatorial plane of Achernar: $\phi_{\text{eq}} = -48.4^\circ$ (Kervella & Domiciano de Souza 2006).

The *FWHM* of source B on the subtracted image (Fig. 2) is $\sigma(\alpha) = 0.243''$, $\sigma(\delta) = 0.170''$. This extension is comparable to the *FWHM* of the image of Achernar ($0.217''$), and therefore compatible with a point-like source. This is confirmed by the point-like appearance of the source in the deconvolved image (Fig. 2). The peak intensity of source B on the subtracted image reaches 1.95% of that of Achernar, and an integration over a $0.22''$ diameter circular aperture gives a flux ratio of 1.79%. Considering the photometry of Achernar presented in Sect. 3.2, the absolute flux from source B is therefore $\approx 1.9 \times 10^{-14}$ W/m²/ μm , or 0.4 Jy, in the *PAH1* band.

4. Discussion

The nature of source B cannot be established as we have only *PAH1* photometry, but Fig. 4 gives the linear radius of the stars that could produce the flux observed in the *PAH1* band, as a function of their effective temperature. An interesting possibility is that source B could be an evolved helium star (e.g. a planetary nebula nucleus variable) with $T_{\text{eff}} \approx 10^5$ K and $R \approx 0.4 R_\odot$. Future imaging and spectroscopy will provide a more secure identification, but for the present discussion, we make the hypothesis that it is a main sequence (MS) star. At the distance of Achernar, a MS star with an apparent flux of 0.4 Jy ($m_N \approx 5.2$, $M_N \approx 2.0$) has an effective temperature of ≈ 7500 K (spectral type $\approx A7V$), and a mass of $\approx 2 M_\odot$. Its extrapolated magnitude in the *V* band is $m_V \approx 5.8$, giving a contrast of $\Delta m_V = 5.4$ magnitudes with Achernar. The apparent position of this source, almost orthogonal to the polar axis of Achernar, is a clue that its orbit is probably coplanar with the equatorial plane of the star. In turn, this indicates that the polar axis of Achernar could be almost in the plane of the sky. The non-detection of source B in the *PAH2* and *NeII* filters can be explained by the higher noise in these images and the decreasing flux of the source with increasing wavelength. The residual noise in the PSF subtracted images in the *PAH1*, *PAH2* and *NeII* bands correspond to 5σ point-source detection limits of 0.05, 0.31 and 0.59 Jy, respectively, while the expected fluxes of an *A7V* star are 0.42, 0.25 and 0.20 Jy in the same filters. A 5σ detection in the *PAH2* and *NeII* bands thus appears difficult.

Statistically, the presence of a companion around a massive star like Achernar is not unexpected: about two-thirds of the stars

in this mass range ($M_{\alpha \text{ Eri}} \approx 6 M_\odot$) have at least one companion (Preibisch et al. 2001; see also Vanbeveren et al. 1998). It is also interesting to remark that the estimated binary frequency for Cepheids, a state into which Achernar will evolve in the future, is also around two-third (Szabados 2003). The detected companions to these supergiants are typically A-type dwarfs, a scenario compatible with the secondary source we detected.

The spectral type and rotational velocity of α Ara (B3Ve, $v \sin i \approx 250\text{--}300 \text{ km s}^{-1}$; Yudin 2001; Chauville et al. 2001) make it an interesting analogue of Achernar, though with a higher absolute flux in the MIR. Interferometric observations with the VLTI/MIDI (Chesneau et al. 2005) MIR instrument showed that α Ara is surrounded by a truncated circumstellar disk. This points at the presence of a stellar companion orbiting at a distance of $\approx 30 R_*$. The detected source B is located much further away, but the presence of companions in both cases could be an indication that the Be phenomenon is linked to binarity.

5. Conclusion

We presented high resolution thermal infrared images of the close environment of Achernar. A point-like source is identified at an angular distance of $0.280''$ from Achernar, contributing for 1.8% of the flux of Achernar in the *PAH1* band. This source is not detected in our longer wavelength images, probably due to their insufficient sensitivity. Its location, close to Achernar and almost in the equatorial plane of the star, indicates that it is likely to be a physical companion orbiting Achernar. The measured flux corresponds to that of an *A7V* star (similar to Altair, for instance). A secure identification requires further observations, that will also determine if source B indeed shares the proper motion of Achernar ($\approx 97 \text{ mas/yr}$).

Acknowledgements. We wish to thank the VISIR instrument team at Paranal, and in particular Dr. L. Vanzi, for making the BURST mode available to us in visitor mode, on a very short notice. Based on observations made with ESO Telescopes at Paranal Observatory under programs 078.D-0295(A) and (B). This research used the SIMBAD and VIZIER databases at the CDS, Strasbourg (France), and NASA's ADS bibliographic services.

References

- Balona, L. A., Engelbrecht, C. A., & Marang, F. 1987, MNRAS, 227, 123
- Chauville, J., Zorec, J., Ballereau, D., et al. 2001, A&A, 378, 861
- Chesneau, O., Meilland, A., Rivinius, T., et al. 2005, A&A, 435, 275
- Cohen, M., Walker, R. G., Carter, B., et al. 1999, AJ, 117, 1864
- Domiciano de Souza, A., Kervella, P., Jankov, S., et al. 2003, A&A, 407, L47
- Doucet, C., Lagage, P. O., & Pantin, E. 2007, Proc. of the VIRA conference, Paris, 20–22 March 2006, in press [arXiv:astro-ph/0610322]
- Doucet, C., Habart, E., Pantin, E., et al. 2007, A&A, 470, 625
- ESA 1997, The Hipparcos Catalogue, ESA SP-1200
- Kervella, P., & Domiciano de Souza, A. 2006, A&A, 453, 1059
- Lagage, P. O., Pel, J. W., Authier, M., et al. 2004, The ESO Messenger, 117, 12
- Meilland, A., Stee, Ph., Vannier, M., et al. 2006, A&A, 464, 59
- Panagia, N., & Felli, M. 1975, A&A, 39, 1
- Poncellet, A., Doucet, C., Perrin, G., Sol, H., & Lagage, P. O. 2007, A&A, 472, 823
- Preibisch, Th., Weigelt, G., & Zinnecker, H. 2001, Proc. IAU Symp., 200, 69
- Slettebak, A. 1982, ApJS, 50, 55
- Szabados, L. 2003, IBVS, 5394, 1
see also <http://www.konkoly.hu/CEP/intro.html>
- Thévenin, F., Kervella, P., Pichon, B., et al. 2005, A&A, 436, 253
- Tokovinin, A., Sarazin, M., & Smette, A. 2007, MNRAS, 378, 701
- Vanbeveren, D., De Loore, C., & Van Rensbergen, W. 1998, A&ARv, 9, 63
- Vinicius, M. M. F., Zorec, J., Leister, N. V., & Levenhagen, R. S. 2006, A&A, 446, 643
- von Zeipel, H. 1924, MNRAS, 84, 665
- Yudin, R. V. 2001, A&A, 368, 912

L E

The close-in companion of the fast rotating Be star Achernar^{***}P. Kervella¹, A. Domiciano de Souza², and Ph. Bendjoya²¹ LESIA, Observatoire de Paris, CNRS UMR 8109, UPMC, Université Paris Diderot, 5 place Jules Janssen, 92195 Meudon, France
e-mail: Pierre.Kervella@obspm.fr² Lab. H. Fizeau, CNRS UMR 6525, Univ. de Nice-Sophia Antipolis, Observatoire de la Côte d’Azur, 06108 Nice Cedex 2, France

Received 11 March 2008 / Accepted 16 April 2008

ABSTRACT

Context. The Be stars are massive dwarf or subgiant stars that present temporary emission lines in their spectrum, and particularly in the $H\alpha$ line. The mechanism triggering these Be episodes is currently unknown, but binarity could play an important role.

Aims. Previous observations with the VLT/VISIR instrument (Kervella & Domiciano de Souza 2007, A&A, 474, L49) revealed a faint companion to Achernar, the brightest Be star in the sky. The present observations are intended to characterize the physical nature of this object.

Methods. We obtained near-IR images and an H -band spectrum of Achernar B using the VLT/NACO adaptive optics systems.

Results. Our images clearly show the displacement of Achernar B over a portion of its orbit around Achernar A. Although there are not enough data to derive the orbital parameters, they indicate a period of about 15 yr. The projected angular separation of the two objects in December 2007 was less than $0.15''$, or 6.7 AU at the distance of Achernar.

Conclusions. From its flux distribution in the near- and thermal-infrared, Achernar B is most likely an A1V–A3V star. Its orbital period appears similar to the observed pseudo-periodicity of the Be phenomenon of Achernar. This indicates that an interaction between A and B at periastron could be the trigger of the Be episodes.

Key words. stars: individual: Achernar – techniques: high angular resolution – stars: emission-line, Be – stars: binaries: close

1. Introduction

As the brightest ($m_V = 0.46$) and nearest Be star in the sky, Achernar (α Eri, HD 10144) has been the focus of a lot of interest over the past decades. Its very fast rotation velocity $v \sin i$ is estimated between 220 to 270 km s^{-1} and its effective temperature between 15 000 to 20 000 K (Vinicius et al. 2006). Achernar was chosen as the subject of the first VLTI observations, which revealed its extraordinarily distorted interferometric profile (Domiciano de Souza et al. 2003). Different possibilities have been proposed recently to explain the exceptionally high flattening ratio of the photosphere of the star (Jackson et al. 2004; Carciofi et al. 2008). Further interferometric observations have revealed the presence of the stellar wind emitted by the overheated poles of the star (Kervella & Domiciano de Souza 2006), resulting in a slight revision of its flattening ratio. A model of the envelope of Achernar has recently been presented by Meilland (2007). Last year, we discovered a close-in faint companion to Achernar, from diffraction-limited thermal IR imaging with VLT/VISIR (Kervella & Domiciano de Souza 2007). The present Letter reports the follow-up adaptive optics observations in the near-IR domain to characterize this companion, hereafter referred to as Achernar B.

2. Observations

2.1. Imaging

We observed Achernar at several epochs in the second half of 2007 using the Nasmyth Adaptive Optics System (NAOS, Rousset et al. 2003) of the Very Large Telescope (VLT), coupled to the CONICA infrared camera (Lenzen et al. 1998), abbreviated as NACO. Table A.1 gives the list of the observations of Achernar and the standard star δ Phe (HD 9362). We selected the smallest available pixel scale of 13.26 ± 0.03 mas/pix (Masciadri et al. 2003), giving a field of view of $13.6'' \times 13.6''$. Due to the brightness of Achernar, we employed narrow-band filters at wavelengths 1.094 ± 0.015 , 1.644 ± 0.018 , and 2.166 ± 0.023 μm (hereafter abbreviated as 1.09, 1.64, and 2.17) together with a neutral density filter (labeled “ND2_short”), with a transmission of about 1.5%. The raw images were processed using the Yorick¹ and IRAF² software packages in a standard way, except that we did not subtract the negligible sky background. Examples of the images of Achernar A and B and δ Phe are presented in Fig. 1.

2.1.1. Astrometry

To obtain the position of B, we first prepared the images by subtracting a 180° rotated version of each image to itself. This

* Based on observations collected at the European Southern Observatory, Chile under ESO Program 279.D-5064(A).

** Appendix A is only available in electronic form at <http://www.aanda.org>

¹ <http://yorick.sourceforge.net/>

² IRAF is distributed by the NOAO, which are operated by the Association of Universities for Research in Astronomy, Inc., under cooperative agreement with the National Science Foundation.

3. High spectro-spatial resolution observations of fast rotators in the H-R diagram

L14

P. Kervella et al.: The close-in companion of the fast rotating star Achernar

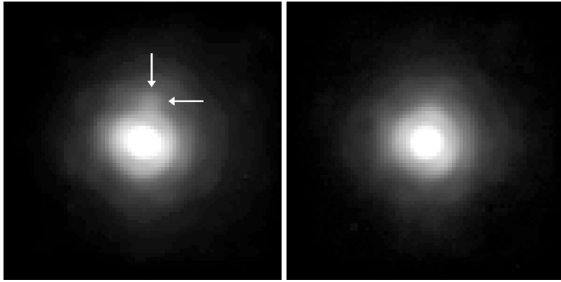


Fig. 1. NACO images of Achernar A and B (*left*) and δ Phe (*right*) in the $2.17 \mu\text{m}$ filter obtained on 22 December 2007. The arrows indicate the position of Achernar B. The field of view is $1''$, and the grey scale is normalized for both images to the central part of the PSF.

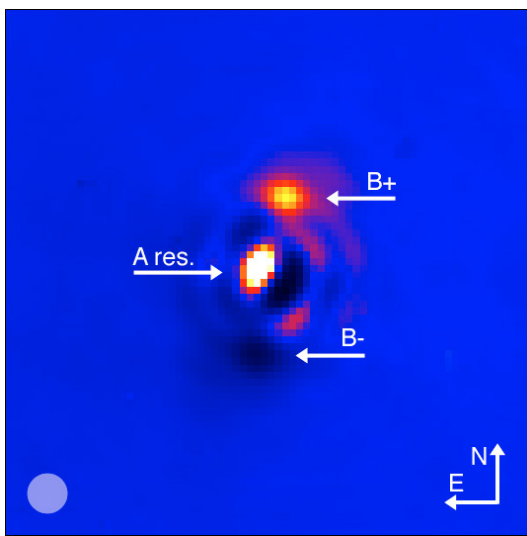


Fig. 2. Result of the subtraction of a 180° rotated version of the image of the Achernar system presented in Fig. 1 (*left*) from itself. The “B+” and “B-” arrows point at the positions of the positive and negative images of Achernar B, and the “A res.” arrow indicates the A subtraction residuals. The aperture used for photometry is shown in the *lower left* corner, and the field of view is $1''$ on each side.

removes the contribution of Achernar A and mainly leaves a pair of positive and negative images of B, corrected from the PSF wing leaks from A (Fig. 2). We then directly measured the position of Achernar B relative to A using a Gaussian fit procedure on these images. Although Achernar B is clearly visible at all three wavelengths, the Gaussian fit converged essentially in the K band where the high Strehl ratio (compared to the $1.09 \mu\text{m}$ images in particular) results in a better separation of the two objects. The formal fitting error is below ± 0.1 pixel, but we estimate the true uncertainty to ± 0.5 pixel ($0.066''$), due to the presence of residual speckles from Achernar A close to B. The pixel scale and detector orientation introduce negligible systematic uncertainties (Masciadri et al. 2003; Chauvin et al. 2005).

Between epochs 2006.760 (Kervella & Domiciano 2007) and 2007.975, we measured an apparent displacement of B relative to A of $\rho_B = 161 \pm 10$ mas along an azimuth of $\alpha = +113^\circ$ (Fig. 3 and Table 1). According to the *Hipparcos* catalog (ESA 1997), the amplitude of Achernar A’s proper motion on the sky over 1.2 yr is $\rho_{\text{pm}} = 116$ mas along an azimuth of $\alpha_{\text{pm}} = +115^\circ$. If B was a background source, we would expect an apparent

Table 1. Position of Achernar B relative to Achernar A.

Epoch	λ (μm)	$\Delta\alpha^a$	$\sigma(\alpha)$	$\Delta\delta^a$	$\sigma(\delta)$	R_p^b
2006.760 ^c	11.25	-184.0	7.5	211.0	7.5	12.3
2007.488	2.17	-95.9	6.6	178.6	6.6	8.9
2007.824	2.17	-46.9	6.6	165.8	6.6	7.6
2007.975	2.17	-35.3	6.6	148.2	6.6	6.7

^a Differential coordinates and uncertainties in milliarcseconds (mas).

^b Projected A–B separation in AU.

^c From Kervella & Domiciano de Souza (2007).

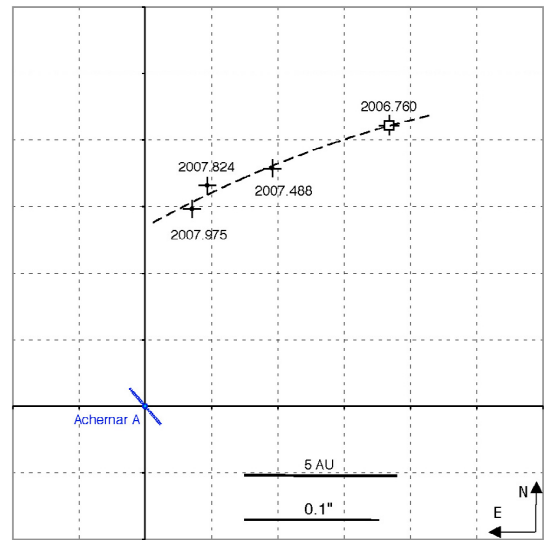


Fig. 3. Position of Achernar B relative to A for four epochs. The open square indicates the VISIR observation (Kervella & Domiciano 2007), and the dots represent the new NACO epochs. The dashed curve is a simple quadratic fit through the data points intended to guide the eye. The segment over Achernar A indicates its projected rotation axis and polar wind as measured by Kervella & Domiciano (2006). The apparent angular sizes of Achernar A and its polar wind are approximately represented to scale.

displacement *opposite* in azimuth to A’s proper motion. As B is clearly comoving with A, we can rule out the possibility that it is a background source. As a remark, the parallactic oscillation of the position of Achernar A is small ($\pi = 22.68 \pm 0.57$ mas) compared to the observed displacements, but the presence of B could have affected the *Hipparcos* proper motion and parallax measurement of Achernar. The other epochs listed in Table A.1 give astrometric positions compatible with the trajectory shown in Fig. 3, although with lower accuracy due to poor seeing conditions.

2.1.2. Photometry

For the photometric calibration of our images, we observed a standard star immediately before or after Achernar, δ Phe (HD 9362, G9III) in the same narrow-band filters. It was chosen in the Cohen et al. (1999) catalogue of spectrophotometric standards for infrared wavelengths. Due to the small separation of the Achernar A–B pair, PSF fitting is not possible for measuring the photometry of B. We therefore proceeded in three steps:

1. We measured classical aperture photometry of Achernar relative to δ Phe, using a large aperture of $1.2''$ in radius.

3.2. The Be star Achernar (α Eridani)

2. As for the astrometry measurement, we subtracted a 180° rotated version of each image to itself to remove the contribution of Achernar A and leave a positive and a negative image of B, along with limited residuals from A (Fig. 2).
3. We obtained aperture photometry of B from the subtracted images using an aperture radius of 0.040'' (shown in Fig. 2).

This procedure has ensured that we obtain properly referenced photometry for Achernar A (the influence of B is negligible at step 1), that we can transfer to B at step 3. Step 2 is necessary because B is located inside the wings of the PSF of A. This subtraction is efficient thanks to the good circular symmetry of the PSF produced by NACO. At step 3, we measure the photometry of A and B over the same aperture and within the same images. This allows us to avoid the problem of the variable Strehl ratio of adaptive optics images. The conversion of the measured narrow-band magnitudes to standard *JHK* band magnitudes requires taking the position of the quasi-monochromatic wavelengths within the bands and the shape of the observed spectra into account. Starting from the narrow-band fluxes measured on Achernar and δ Phe, we used the Pickles (1998)³ reference spectra corresponding to their spectral types (B3V and G9III) to recover the corresponding broadband flux ratio. The filter profiles were taken from Bessell & Brett (1988). From the October–December 2007 observations, we derived magnitudes of: $m_J(A) = 0.58_{\pm 0.14}$, $m_H(A) = 0.80_{\pm 0.11}$, $m_K(A) = 0.81_{\pm 0.11}$. These values generally agree with the *JHK* magnitudes of Achernar from the 2MASS (Skrutskie et al. 2006; 0.82 $_{\pm 0.25}$, 0.87 $_{\pm 0.32}$, 0.88 $_{\pm 0.33}$) and Ducati (2002; 0.79, 0.86, 0.88) catalogs, although systematically brighter by 0.1–0.2 mag, particularly in the *J* band. This may be due our narrow-band filters corresponding to the emission lines sometimes present in the spectrum of Achernar. As we may slightly overestimate the brightness of Achernar, we quadratically added an uncertainty of 0.1 mag.

From the magnitudes of Achernar A, the small-aperture photometry obtained at step 3 gives the following broadband magnitudes for Achernar B: $m_J(B) = 4.23_{\pm 0.36}$, $m_H(B) = 4.29_{\pm 0.22}$, $m_K(B) = 4.61_{\pm 0.27}$. The magnitude differences measured between A and B in the three narrow-band filters are: $\Delta m_{1.09} = 3.64_{\pm 0.47}$, $\Delta m_{1.64} = 3.50_{\pm 0.19}$, $\Delta m_{2.17} = 3.80_{\pm 0.25}$, corresponding to an average contrast of ≈ 30 between the two stars in the near-infrared. These magnitudes of B are averages over the October–December 2007 observations (epoch 2007.8) and the error bars contain the statistical uncertainty and the dispersion of all the measurements. The magnitudes at the other epochs (list of the observations in Table A.1) show a marginally significant brightening of B by $-0.7_{\pm 0.4}$ mag in the *K* band between 2007.488 and 2007.975 as it approaches A.

2.2. Spectroscopy

For the spectroscopic observations, we used the S27_3_SH mode of NACO, featuring a slit width of 86 mas on the sky, a spectral resolution of 1500 over the *H* band (dispersion of 0.34 nm/pixel), and an angular pixel scale of 27 mas/pixel. As shown in Fig. 4, the slit was centered on Achernar B. Although most of the light fed into the slit comes from the companion, it is not excluded that Achernar A may contribute with part of the *H* band spectrum. Details on the 3 recorded ABBA sequences are given in Table A.1. Observations were performed using the classical IR NACO sequence where the spectrum is

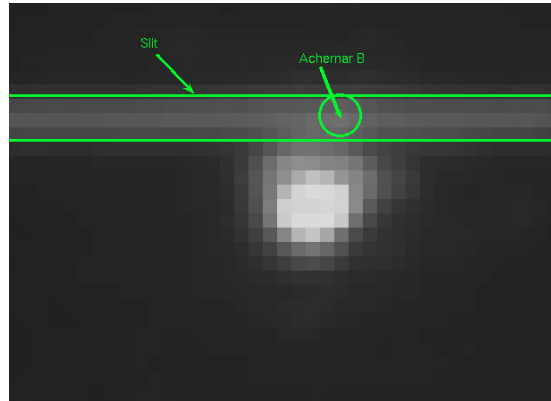


Fig. 4. Position of the NACO slit relative to Achernar A and B.

recorded with the target positioned at two different slit positions, i.e. the ABBA observing sequence. For the data reduction we applied two different procedures: (1) the classical spectral reduction procedure using the IRAF packages for dark and flat field corrections, and (2) the A-B, B-A procedure. Because the sky background is negligible and the target is rather bright, both procedures give identical results. In the last step, IRAF was used to obtain 1D spectra from weighted averages of 2D spectra and to perform the wavelength calibration. Figure 5 shows the continuum-normalized average spectrum derived from our 12 observations. The atmospheric absorption lines were corrected using the transmission by Lord (1992), but some residuals are visible in particular around $\lambda = 1.66 \mu\text{m}$ (CH_4 and water vapor lines). The absorption lines from the Brackett transitions 11 to 23 of hydrogen are clearly visible in the spectrum and marked by vertical lines.

3. Discussion

The *Hipparcos* parallax of Achernar ($\pi = 22.68 \pm 0.57$ mas; ESA 1997) corresponds to a distance modulus of $\mu = 3.22 \pm 0.06$ mag. The absolute magnitudes of B in the *JHK* and thermal infrared *N* band (average of the PAH1 and PAH2 magnitudes, see Appendix A) are therefore: $M_J = 1.00_{\pm 0.37}$, $M_H = 1.07_{\pm 0.22}$, $M_K = 1.39_{\pm 0.28}$, and $M_N = 1.88_{\pm 0.12}$. The *JHK* absolute magnitudes suggest a spectral type around A1V, slightly fainter than Vega and slightly brighter than Sirius, which have respective magnitudes of $M_{JHK} \approx 0.55$ and 1.56. The *N* band absolute magnitude of Achernar B is also very similar to that of Sirius ($M_N = 1.62$). It thus does not appear to present an infrared excess that would betray a Vega-like dusty envelope. Because Vega itself presents a significant excess in this band ($M_N = 0.55$) due to the presence of dust, it is not comparable.

Our NACO *H* band spectrum of B presents a lot of similarity with early A-type star spectra, as shown in Fig. 5. This is confirmed by the computation of linear Pearson cross-correlation coefficients between our normalized spectrum and the reference *H* band spectra from Ranade et al. (2004)⁴ and Pickles (1998)⁵. As shown in Fig. 6, the spectral types A0V–A4V give the best correlation with our observation. As shown by Meyer et al. (1998)⁶, the equivalent width (*EW*) of the 11–4 Brackett line at

⁴ http://vo.iucaa.ernet.in/~voi/NIR_Header.html

⁵ <http://www.ifa.hawaii.edu/users/pickles/AJP/hilib.html>

⁶ <ftp://ftp.noao.edu/catalogs/medresIR/>

³ <http://www.ifa.hawaii.edu/users/pickles/AJP/hilib.html>

3. High spectro-spatial resolution observations of fast rotators in the H-R diagram

L16

P. Kervella et al.: The close-in companion of the fast rotating star Achernar

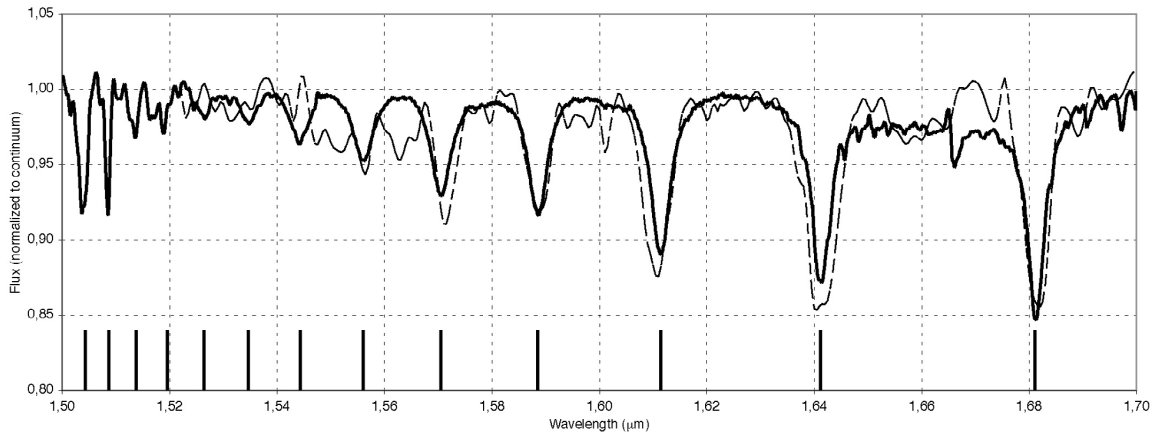


Fig. 5. Average spectrum of Achernar B (solid curve) compared to the H band spectrum of HR 2763 (λ Gem, A3V, dashed curve) from Ranade et al. (2004). The positions of the Brackett transitions 11-4 to 23-4 of hydrogen are marked with vertical lines.

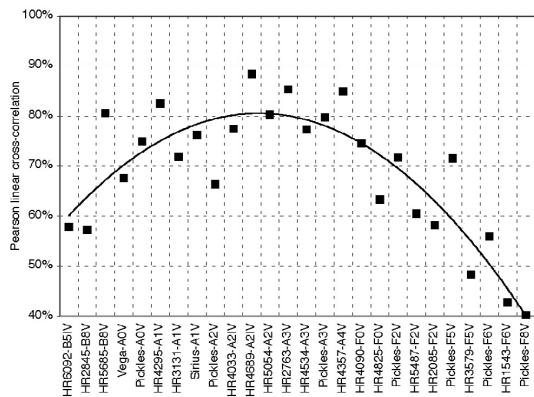


Fig. 6. Cross-correlation between our spectrum of B and reference spectra from Ranade et al. (2004), Meyer et al. (1998), and Pickles (1998).

1.681 μm offers a possibility to test the effective temperature, although it is not monotonic. An integration normalized to the pseudo-continuum between 1.670 and 1.690 μm gives an equivalent width of 0.675 nm ($=2.4 \text{ cm}^{-1}$). From Fig. 7 in Meyer et al. (1998), this gives $\log T_{\text{eff}} \approx 3.9\text{--}4.1$, also compatible with an early A-type star. Such a star has an approximate mass of $\approx 2 M_{\odot}$ (Kervella et al. 2003).

Although we cannot derive the full parameters of Achernar B's orbit from our limited astrometry, the combination of its estimated mass ($\approx 2 M_{\odot}$), the mass of A ($\approx 6.7 M_{\odot}$; Vinicius et al. 2006, see also Harmanec 1988) and the maximum apparent A-B separation ($r_{\text{AB}} \approx 12.3 \text{ AU}$) allow us to roughly estimate its period. From Kepler's third law and by assuming an elliptic orbit, we have $T^2 = a^3/M$ where a is the semi-major axis in AU, T the period in years, and M the total mass in M_{\odot} . Assuming that a is equal to the observed maximum separation of 12.3 AU, we obtain a minimum period of $T = 14$ to 15 yr.

4. Conclusion

From our photometry and spectroscopy, Achernar B is most probably an A1V-A3V star. Our data are currently insufficient for deriving its full orbit, but its minimum period is ≈ 15 yr. Its fast orbital motion should allow the derivation of reliable

parameters within a few years. The periodic approach of the companion could be the cause of the observed ≈ 15 yr pseudo-periodicity of the Be episodes of Achernar (Vinicius et al. 2006). The passage of B at periastron within a few AUs of A could extract material from the equator of A, where the effective gravity is very low. The next such passage should happen around 2010 (Meilland 2007). Achernar appears similar to the B0.2IVe star δ Sco, which has a 1.5 mag fainter companion on a highly eccentric 10.6 yr orbit (Bedding 1993; Miroshnichenko et al. 2001). This suggests that the presence of companions around Be stars should be examined carefully, as it may play a key role in triggering the Be phenomenon.

Acknowledgements. This research made use of the SIMBAD and VIZIER databases at the CDS, Strasbourg (France), and NASA's Astrophysics Data System Bibliographic Services. We also received the support of PHASE, the high angular resolution partnership between ONERA, Observatoire de Paris, the CNRS, and University Denis Diderot Paris 7.

References

- Bedding, T. R. 1993, *AJ*, 106, 1068
 Bessell, M. S., & Brett, J. M. 1988, *PASP*, 100, 1134
 Carciofi, A. C., Domiciano de Souza, A., Magalhães, A. M., Bjorkman, J. E., & Vakili, F. 2008, *ApJ*, 676, L41
 Chauvin, G., Lagrange, A.-M., Lacombe, F., et al. 2005, *A&A*, 430, 1027
 Cohen, M., Walker, R. G., Carter, B., et al. 1999, *AJ*, 117, 1864
 Domiciano de Souza, A., Kervella, P., Jankov, S., et al. 2003, *A&A*, 407, L47
 Domiciano de Souza, A., Kervella, P., Bendjoya, Ph., & Niccolini, G. 2008, *A&A*, 480, L29
 Ducati, J. R. 2002, *NASA Ref. Pub.*, 1294
 The Hipparcos and Tycho Catalogues 1997, *ESA SP-1200*
 Jackson, S., MacGregor, K. B., & Skumanich, A. 2004, *ApJ*, 606, 1196
 Harmanec, P. 1988, *Bull. Astron. Inst. Czechoslovakia*, 39, 329
 Kervella, P., Thévenin, F., Morel, P., et al. 2003, *A&A*, 408, 681
 Kervella, P., & Domiciano de Souza, A. 2006, *A&A*, 453, 1059
 Kervella, P., & Domiciano de Souza, A. 2007, *A&A*, 474, L49
 Lenzen, R., Hofmann, R., Bizenberger, P., & Tusche, A. 1998, *SPIE*, 3354, 606
 Lord, S. D. 1992, *NASA Technical Memor.*, 103957
 Masciadri, E., Brandner, W., Bouy, H., et al. 2003, *A&A*, 411, 157
 Meilland, A. 2007, Ph.D. Thesis, Université de Nice-Sophia Antipolis
 Meyer, M. R., Edwards, S., Hinkle, K. H., & Srom, S. E. 1998, *ApJ*, 508, 397
 Miroshnichenko, A. S., Fabregat, J., Bjorkman, K. S., et al. 2001, *A&A*, 377, 485
 Pickles, A. J. 1998, *PASP*, 110, 863
 Ranade, A., Gupta, R., Ashok, N. M., & Singh, H. P. 2004, *BASI*, 32, 311
 Rousset, G., Lacombe, F., Puget, F., et al. 2003, *Proc. SPIE*, 4839, 140
 Skrutskie, R. M., Cutri, R., Stiening, M. D., et al. 2006, *AJ*, 131, 1163
 Vinicius, M. M. F., Zorec, J., Leister, N. V., & Levenhagen, R. S. 2006, *A&A*, 446, 643

3.2. The Be star Achernar (α Eridani)

P. Kervella et al.: The close-in companion of the fast rotating star Achernar, *Online Material p 1*

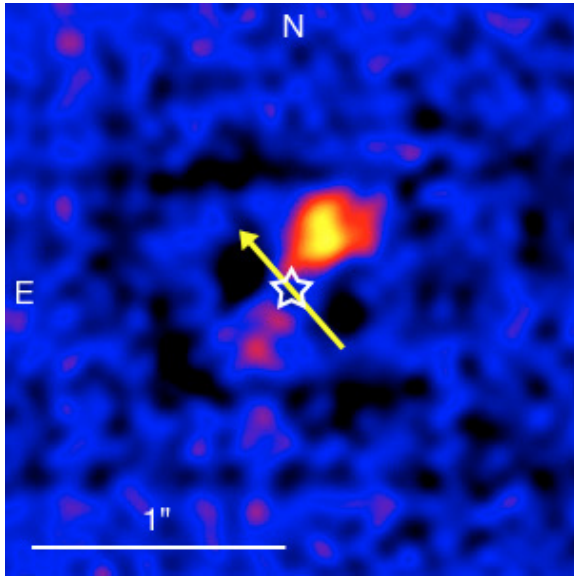


Fig. A.1. Residual of the subtraction of the VISIR PAH2 image of η Ser from the image of Achernar in the same band. The contribution of Achernar B is clearly visible. The arrow indicates the rotation axis of Achernar A.

Appendix A: Thermal infrared imaging at $11.25 \mu\text{m}$

Kervella & Domiciano de Souza (2007) did not detect Achernar B in the $11.25 \mu\text{m}$ images (PAH2 band) of the system obtained with the VLT/VISIR instrument in BURST mode. A re-analysis of these observations has shown that the reason for this non-detection was the introduction of noise during the normalization and subtraction of the PSF reference star (δ Phe). For our VISIR program on the B[e] star MWC300 (Domiciano de Souza et al. 2008), we obtained BURST mode images of another PSF calibrator (η Ser) 3.4 h before the observations of Achernar (under similar seeing conditions). Since η Ser is brighter than δ Phe, we could obtain a cleaner PSF-subtracted image of Achernar B, as presented in Fig. A.1. From this image, aperture photometry over a $0.22''$ diameter gives a flux ratio of 1.74% between Achernar B and A (the ratio of peak intensities is 2.14%). From the 16.8 Jy absolute flux derived by Kervella & Domiciano de Souza (2007) for A, the contribution from B is therefore 0.3 Jy at $11.25 \mu\text{m}$. This value is comparable to the 0.4 Jy flux derived by Kervella & Domiciano de Souza (2007) at $8.59 \mu\text{m}$.

Table A.1. Log of the NACO observations of Achernar and δ Phe.

Date / UT	Star	Filt.	$\Delta t \times N^a$	$\sigma (")^b$	AM ^c
<i>Imaging</i>					
2007-06-27T08:48:52	α Eri	2.17	2×5	0.102	1.46
2007-08-01T10:07:20	α Eri	2.17	2×5	0.082	1.19
2007-08-09T09:51:54	α Eri	2.17	2×5	0.088	1.20
2007-10-27T04:41:17	α Eri	2.17	2×30	0.091	1.20
2007-10-27T04:46:27	α Eri	1.64	2×22	0.092	1.20
2007-10-27T04:50:06	α Eri	1.09	2×20	0.141	1.20
2007-10-27T05:45:31	δ Phe	2.17	4×8	0.094	1.19
2007-10-27T05:48:24	δ Phe	1.64	4×6	0.096	1.20
2007-10-27T05:50:22	δ Phe	1.09	4×5	0.122	1.20
2007-10-28T03:01:11	α Eri	2.17	1.5×40	0.083	1.21
2007-10-28T03:04:21	α Eri	1.64	1.5×30	0.084	1.20
2007-10-28T03:07:18	α Eri	1.09	1.5×27	0.104	1.20
2007-10-28T03:37:24	δ Phe	2.17	3×9	0.084	1.10
2007-10-28T03:39:15	δ Phe	1.64	3×8	0.090	1.10
2007-10-28T03:44:21	δ Phe	1.09	3×7	0.102	1.10
2007-11-01T00:09:42	α Eri	2.17	0.4×150	0.096	1.54
2007-11-01T00:12:42	α Eri	1.64	0.4×110	0.103	1.53
2007-11-01T00:15:35	α Eri	1.09	0.4×100	0.175	1.51
2007-11-07T02:22:55	α Eri	2.17	0.4×150	0.093	1.21
2007-11-07T02:25:12	α Eri	1.64	0.4×110	0.097	1.20
2007-11-07T02:28:02	α Eri	1.09	0.4×100	0.132	1.20
2007-11-07T02:37:56	δ Phe	2.17	1×25	0.089	1.11
2007-11-07T02:39:46	δ Phe	1.64	1×22	0.094	1.10
2007-11-07T02:41:25	δ Phe	1.09	1×20	0.119	1.10
2007-12-22T01:39:46	α Eri	2.17	1.2×50	0.073	1.23
2007-12-22T01:44:21	α Eri	1.64	1.2×37	0.071	1.24
2007-12-22T01:46:51	α Eri	1.09	1.2×34	0.087	1.24
2007-12-22T02:26:40	δ Phe	2.17	1×25	0.076	1.23
2007-12-22T02:31:48	δ Phe	1.64	1×22	0.070	1.24
2007-12-22T02:34:57	δ Phe	1.09	5×4	0.093	1.25
<i>Spectroscopy</i>					
2007-10-27T05:22:23	α Eri	H	0.5×100	1.28	1.23
2007-10-27T05:23:26	α Eri	H	0.5×100	1.28	1.23
2007-10-27T05:24:20	α Eri	H	0.5×100	1.26	1.24
2007-10-27T05:25:24	α Eri	H	0.5×100	1.23	1.24
2007-10-28T03:20:30	α Eri	H	0.5×100	1.25	1.19
2007-10-28T03:21:33	α Eri	H	0.5×100	1.17	1.19
2007-10-28T03:22:27	α Eri	H	0.5×100	1.20	1.19
2007-10-28T03:23:31	α Eri	H	0.5×100	1.19	1.19
2007-12-22T02:04:11	α Eri	H	1.0×50	0.91	1.26
2007-12-22T02:05:14	α Eri	H	1.0×50	0.91	1.26
2007-12-22T02:06:08	α Eri	H	1.0×50	0.83	1.27
2007-12-22T02:07:10	α Eri	H	1.0×50	0.85	1.27

^a The exposure times Δt are given in seconds. N is the number of individual exposures.

^b For the imaging observations, $\sigma (")$ is the FWHM of the star image as measured on the images themselves, and for the spectroscopic observations, we list the observatory seeing in the visible.

^c AM is the airmass.

3.2.4 Beyond the diffraction limit of optical/IR interferometers: angular diameter and rotation parameters of Achernar from differential phases

Being the closest and brightest star in the sky, Achernar is an ideal target to test alternative high angular and spectral resolution techniques. Differential interferometry (spectro-interferometry) is a self-calibrated and essentially seeing-independent technique. This allows differential interferometry to be used even in cases where visibility amplitudes $|V|$ (fringe contrast) are unavailable and/or when the star is partially or poorly resolved so that $|V| \simeq 1$. The target can be partially resolved down to a few times the diffraction limit of the instrument.

Such super-resolution potential combined to spectral resolution is ideal for measuring sizes, rotation velocities, and orientation of rotating stars (e.g. Chelli & Petrov, 1995; Domiciano de Souza et al., 2004a; Le Bouquin et al., 2009). Some basic equations of differential interferometry are given in Sect. 1.2.

In the A&A paper given hereafter, we demonstrate this super-resolution capability of differential interferometry by measuring, from real observations, the equatorial size, rotation velocity, and orientation of Achernar based only on VLTI/AMBER differential phases centered on the Br γ line (Domiciano de Souza et al., 2012). Two PhD students contributed to this work as part of their thesis:

- M. Hadjara (thesis supervisors: A. Domiciano de Souza and F. Vakili) - reduction of most of the VLTI/AMBER data;
- D. Moser Faes (thesis supervisors: A. Domiciano de Souza and A. C. Carciofi) - work on spectroscopic and polarimetric data.

By adopting the same strategy from Domiciano de Souza et al. (2012) a second paper was published in A&A (not shown here), as the main scientific result of the PhD thesis of M. Hadjara (Hadjara et al., 2014). The physical parameters of four fast-rotating stars were measured from VLTI/AMBER differential phases alone, namely, Achernar, Altair, δ Aquilae, and Fomalhaut. These observations are part of our VLTI/AMBER GTO program *Calibrating Stellar Rotation across the H-R Diagram* (P.I.: A. Domiciano de Souza).

Beyond the diffraction limit of optical/IR interferometers^{★,★★,★★★}**I. Angular diameter and rotation parameters of Achernar from differential phases**A. Domiciano de Souza¹, M. Hadjara^{1,2}, F. Vakili¹, P. Bendjoya¹, F. Millour¹, L. Abe¹, A. C. Carciofi³, D. M. Faes^{1,3}, P. Kervella⁴, S. Lagarde¹, A. Marconi⁵, J.-L. Monin⁶, G. Niccolini¹, R. G. Petrov¹, and G. Weigelt⁷¹ Laboratoire J.-L. Lagrange, UMR 7293, Observatoire de la Côte d'Azur (OCA), Université de Nice-Sophia Antipolis (UNS), Centre National de la Recherche Scientifique (CNRS), Campus Valrose, 06108 Nice Cedex 2, France
e-mail: Armando.Domiciano@oca.eu² Centre de Recherche en Astronomie, Astrophysique et Géophysique (CRAAG), Route de l'Observatoire, BP 63, Bouzareah 16340, Alger, Algérie³ Instituto de Astronomia, Geofísica e Ciências Atmosféricas, Universidade de São Paulo (USP), Rua do Matão 1226, Cidade Universitária, São Paulo 05508-900, Brazil⁴ LESIA, Observatoire de Paris, CNRS UMR 8109, UPMC, Université Paris Diderot, 5 Place Jules Janssen, 92195 Meudon, France⁵ INAF-Osservatorio Astrofisico di Arcetri, Largo E. Fermi 5, 50125 Firenze, Italy⁶ UJF-Grenoble 1 / CNRS-INSU, Institut de Planétologie et d'Astrophysique de Grenoble (IPAG) UMR 5274, 38041 Grenoble, France⁷ Max-Planck-Institut für Radioastronomie, Auf dem Hügel 69, 53121 Bonn, Germany

Received 6 January 2012 / Accepted 26 July 2012

ABSTRACT**Context.** Spectrally resolved long-baseline optical/IR interferometry of rotating stars opens perspectives to investigate their fundamental parameters and the physical mechanisms that govern their interior, photosphere, and circumstellar envelope structures.**Aims.** Based on the signatures of stellar rotation on observed interferometric wavelength-differential phases, we aim to measure angular diameters, rotation velocities, and orientation of stellar rotation axes.**Methods.** We used the AMBER focal instrument at ESO-VLTI in its high-spectral resolution mode to record interferometric data on the fast rotator Achernar. Differential phases centered on the hydrogen Br γ line (K band) were obtained during four almost consecutive nights with a continuous Earth-rotation synthesis during ~ 5 h/night, corresponding to $\sim 60^\circ$ position angle coverage per baseline. These observations were interpreted with our numerical code dedicated to long-baseline interferometry of rotating stars.**Results.** By fitting our model to Achernar's differential phases from AMBER, we could measure its equatorial radius $R_{\text{eq}} = 11.6 \pm 0.3 R_\odot$, equatorial rotation velocity $V_{\text{eq}} = 298 \pm 9 \text{ km s}^{-1}$, rotation axis inclination angle $i = 101.5 \pm 5.2^\circ$, and rotation axis position angle (from North to East) $\text{PA}_{\text{rot}} = 34.9 \pm 1.6^\circ$. From these parameters and the stellar distance, the equatorial angular diameter \mathcal{D}_{eq} of Achernar is found to be $2.45 \pm 0.09 \text{ mas}$, which is compatible with previous values derived from the commonly used visibility amplitude. In particular, \mathcal{D}_{eq} and PA_{rot} measured in this work with VLTI/AMBER are compatible with the values previously obtained with VLTI/VINCI.**Conclusions.** The present paper, based on real data, demonstrates the super-resolution potential of differential interferometry for measuring sizes, rotation velocities, and orientation of rotating stars in cases where visibility amplitudes are unavailable and/or when the star is partially or poorly resolved. In particular, we showed that differential phases allow the measurement of sizes up to ~ 4 times smaller than the diffraction-limited angular resolution of the interferometer.**Key words.** stars: rotation – stars: individual: Achernar – methods: observational – methods: numerical – techniques: interferometric**1. Introduction**

By combining high angular and high spectral resolution, differential interferometry (DI; i.e., the measurement of wavelength-differential phases or wavelength-differential visibilities) yields physical parameters of sources with important wavelength-dependent spatial structures, even in cases where

these sources are only poorly or partially resolved by the telescope (single-aperture) or the interferometer (multi-aperture).

Because they are self-calibrated and essentially seeing-independent, DI observables are usually more reliable than absolute visibility amplitude, which is the classical observable used to measure stellar angular diameters. Moreover, visibility amplitudes below ≈ 0.7 (well-resolved objects) are typically required to attain useful constraints (a few percent) on the angular diameters. This demands access to relatively long baselines (≈ 100 – 300 m) for optical/IR interferometers in order to measure angular diameters of ≈ 0.5 – 2 mas, a typical range of values for many bright stars. These observational constraints are relaxed in DI, where more precise and accurate stellar parameters can be measured for stars only slightly to partially resolved,

* Based on observations performed at ESO, Chile under AMBER-consortium GTO programme ID 084.D-0456.

** Full Fig. 5 is available in electronic form at <http://www.aanda.org>

*** The FITS tables of the reduced data are only available at the CDS via anonymous ftp to cdsarc.u-strasbg.fr (130.79.128.5) or via <http://cdsarc.u-strasbg.fr/viz-bin/qcat?J/A+A/545/A130>

corresponding to relatively high visibility amplitudes ≈ 0.6 – 0.9 . Recently, [Le Bouquin et al. \(2009\)](#) used DI to measure the position angle (orientation on the plane of the sky) of the rotation axis of the fast rotator Fomalhaut.

[Chelli & Petrov \(1995\)](#) performed a theoretical study showing that DI can be used to measure stellar angular diameters, rotation velocities, and position angle of rotation axes. However, their study was based on a model of rotating spherical stars with homogeneous effective temperature and gravity, implying a constant local photospheric profile. Such formalism is thus more adapted to slowly rotating stars. It cannot be applied for fast rotators because the effective temperature and gravity, as well as the local profile, vary over the rotationally distorted stellar surface due to rotational flattening and gravity-darkening (also called von Zeipel effect; [von Zeipel 1924](#)). To interpret DI observations of rapidly rotating stars, it is thus necessary to use models including these two physical effects caused by high rotation velocities. In this work, we use our model for fast rotators CHARRON (Code for High Angular Resolution of Rotating Objects in Nature; [Domiciano de Souza et al. 2012, 2002](#)) to interpret differential phases of the rapidly rotating star Achernar (α Eridani). The observations were performed with the ESO VLTI/AMBER beam combiner ([Petrov et al. 2007](#)) centered on the hydrogen Br γ line (K band).

Achernar is a fast rotating Be star ($V_{\text{eq}} \sin i \approx 225 \text{ km s}^{-1}$ from spectroscopy; e.g., [Vinicius et al. 2006](#)) presenting a strong rotational flattening directly measured from VLTI/VINCI interferometry ([Domiciano de Souza et al. 2003; Kervella & Domiciano de Souza 2006](#)), which indicates that its rotation rate is close to the critical limit. Differential rotation ([Jackson et al. 2004](#)) and/or a small residual disk ([Carciofi et al. 2008](#)) are additional effects invoked to explain the very strong flattening observed on Achernar. In any case, the rapid stellar rotation is mainly responsible for this flattening.

Because Achernar is bright and well-studied with an angular diameter interferometrically measured, it is an ideal target to investigate, from real observations, how differential phases can be used to measure sizes, rotation velocities, and orientation of rotating stars. In this work, we thus interpret AMBER differential phases of Achernar under the hypothesis that its strong geometrical deformation is essentially due to a fast (near-critical) uniform rotation. This hypothesis is supported by the fact that the Br γ line observed with AMBER is in clear absorption; also, linear polarimetry obtained at the Pico dos Dias Observatory, Brazil, produced a null result within the observational errors ($P \lesssim 0.01\%$; [Faes & Carciofi 2012](#), priv. comm.) Both observables, obtained at contemporaneous epochs, indicate that Achernar had no disk (or a very tenuous one at most) during our AMBER observations.

Our model for fast rotators is briefly presented in Sect. 2 while the observations and data reduction are described in Sect. 3. The data analysis followed by the discussion and conclusions of this study are presented in Sects. 4 and 5.

2. Differential phase modeling for fast rotating stars

We investigate here the dependence of the differential phase ϕ_{diff} , close to and within the Br γ line, on the relevant physical parameters of a model for fast rotating stars.

Thanks to the Van Cittert-Zernike theorem (e.g., [Born & Wolf 1980](#)), the interferometric observables can be derived from the monochromatic intensity maps of the studied object. In the

present work, these intensity maps are computed with the numerical program CHARRON ([Domiciano de Souza et al. 2012](#)). This code is an IDL¹-based, faster (~ 0.5 min per model) version of the interferometry-oriented code for rotating stars presented by [Domiciano de Souza et al. \(2002\)](#).

The ϕ_{diff} obtained with the AMBER data reduction algorithm are related to the object's Fourier phase ϕ_{obj} by (e.g., [Millour et al. 2011, 2006](#))

$$\phi_{\text{diff}}(u, v) = \phi_{\text{obj}}(u, v) - a(u, v) - b(u, v)/\lambda, \quad (1)$$

where the spatial frequency coordinates u and v depend on the wavelength λ , the projected baseline length B_{proj} and the baseline position angle PA (from north to east; $u = B_{\text{proj}} \sin(\text{PA})/\lambda$ and $v = B_{\text{proj}} \cos(\text{PA})/\lambda$). The parameters a and b correspond to an offset and a slope, given in appropriate units.

The high spectral resolution mode of AMBER ($\lambda/\Delta\lambda \approx 10^4$) leads to a velocity resolution of $\approx 30 \text{ km s}^{-1}$. Projected equatorial rotational velocities $V_{\text{eq}} \sin i$ above $\sim 150 \text{ km s}^{-1}$ would ensure that observations show ~ 10 individual ϕ_{diff} values inside Br γ . In such cases, rapid rotation effects need to be accounted for when modeling phase signatures in order to be consistent with the physics of the studied star.

Many previous works have shown that the geometrical flattening and gravity-darkening are the main consequences of fast rotation measured by interferometry. Based on these works, the model of a uniformly rotating, gravity-darkened star in the Roche approximation was adopted in the present study ([Domiciano de Souza et al. 2002](#)). The most relevant physical parameters defining the model are: the rotation axis inclination angle i , the equatorial rotation velocity V_{eq} (or alternatively $V_{\text{eq}} \sin i$), the equatorial radius R_{eq} , the stellar mass M , the mean stellar effective temperature on the stellar surface \bar{T}_{eff} , and the gravity-darkening coefficient β . This set of input parameters defines the co-latitudinal (θ) dependent surface radius $r(\theta)$, the local effective gravity $g(\theta)$, the local effective temperature $T(\theta)$, the geometrical flattening (ratio of equatorial to polar radii) $R_{\text{eq}}/R_{\text{p}} = 1 + V_{\text{eq}}^2 R_{\text{eq}}/2GM$, the stellar surface area S , the luminosity $L = S \sigma \bar{T}_{\text{eff}}^4$ (σ is the Stefan-Boltzmann constant), among other quantities. The local effective temperature and gravity are related by the von Zeipel law: $T(\theta) \propto g(\theta)^\beta$.

Two additional geometrical parameters required for calculating interferometric observables are the distance d and the position angle of the sky-projected rotation axis PA_{rot} . Further details on the adopted fast rotator model are given by [Domiciano de Souza et al. \(2002\)](#).

To study the dependence of ϕ_{diff} on the model parameters, we define a reference stellar model similar to Achernar: $R_{\text{eq}} = 11 R_{\odot}$, $d = 50 \text{ pc}$, $V_{\text{eq}} \sin i = 250 \text{ km s}^{-1}$, $i = 60^\circ$, $M = 6.1 M_{\odot}$, $\bar{T}_{\text{eff}} = 15000 \text{ K}$, $\text{PA}_{\text{rot}} = 0^\circ$ (north direction), $\beta = 0.25$ (theoretical value for radiative stellar envelopes; [von Zeipel 1924](#)). These parameters correspond to V_{eq} equal to 90% of the critical velocity V_{crit} , $R_{\text{eq}}/R_{\text{p}} = 1.4$ and an equatorial angular diameter $\mathcal{D}_{\text{eq}} = 2R_{\text{eq}}/d = 2 \text{ mas}$. To be compatible with the AMBER observations presented in Sect. 3, the simulations were performed around the hydrogen Br γ line, considering an uncertainty in ϕ_{diff} of $\sigma_\phi = 0.5^\circ$, $B_{\text{proj}} = 75 \text{ m}$ and 150 m , $\text{PA} = 45^\circ$ and 90° , and $\lambda/\Delta\lambda = 12000$.

Figures 1 to 3 show several plots comparing ϕ_{diff} from the reference model with those from models where the input parameters have been varied one by one. The characteristic s-shaped signature of rotation is seen at all ϕ_{diff} curves inside Br γ . Our

¹ Interactive Data Language.

3.2. The Be star Achernar (α Eridani)

A. Domiciano et al.: Beyond the diffraction limit of optical/IR interferometers. I.

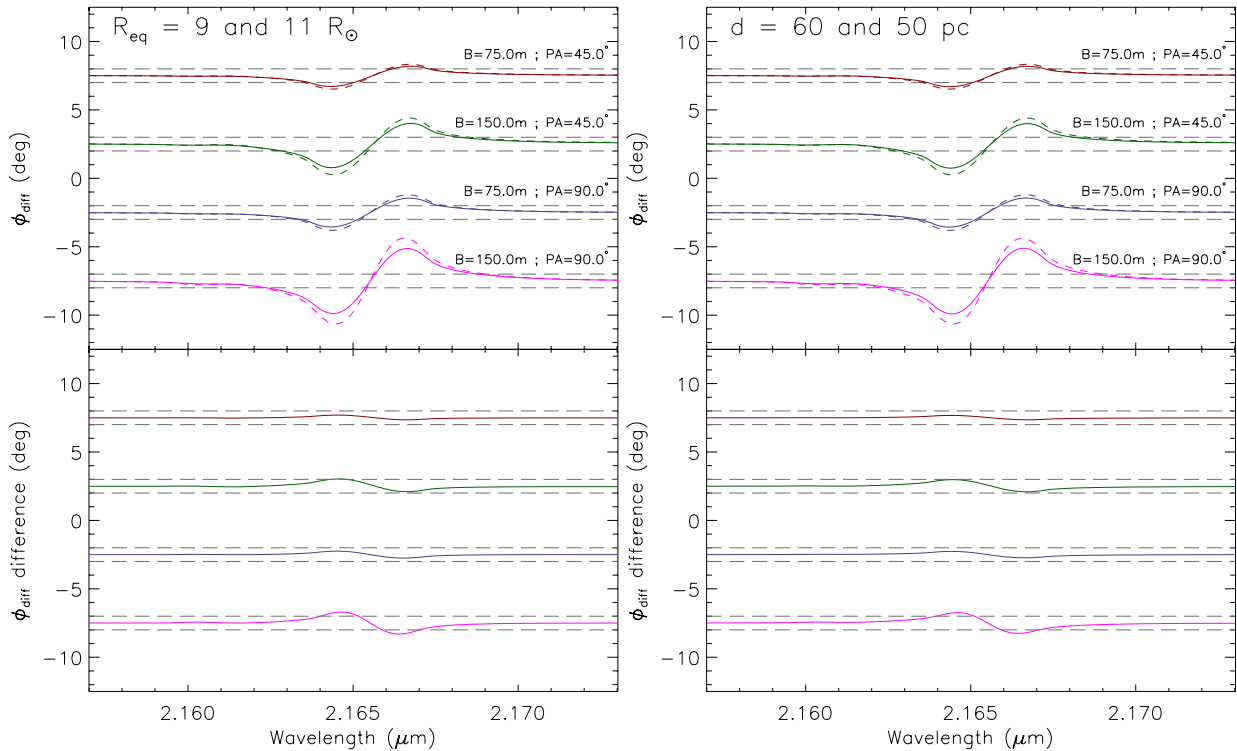


Fig. 1. *Top:* dependence of simulated differential phases ϕ_{diff} on R_{eq} and on d (solid line: tested model; dashed line: reference model as described in Sect. 2). The parameters of the tested model are identical to those of the reference model, except that $R_{\text{eq}} = 9 R_{\odot}$ (*left*) and $d = 60$ pc (*right*). The values of the tested and reference models differ by $\approx 20\%$; they are indicated in the upper left part of the figures. All ϕ_{diff} models were calculated across the Br γ line with a spectral resolution of 12 000 at four projected baselines ($B_{\text{proj}} = 75$ m and 150 m, and PA = 45° and 90°), which are typical values attained with VLT/AMBER. These wavelengths and baselines result in visibility amplitudes between 0.6 and 0.9 for the studied stellar models, corresponding to a partially resolved star. The horizontal dashed gray lines indicate the typical error bar of AMBER ϕ_{diff} ($\sigma_{\phi} = \pm 0.5^\circ$). The ϕ_{diff} signature of stellar rotation appears as an s-shaped curve well visible inside Br γ , with an amplitude higher than σ_{ϕ} at all baselines. *Bottom:* difference between ϕ_{diff} of the tested and reference models (solid minus dashed curves in the *top* panel). The continuum of all curves is equal to zero, but they were shifted for better readability.

simulations indicate that ϕ_{diff} is mostly sensitive to R_{eq} and d (defining the equatorial angular diameter \mathcal{D}_{eq}), and to $V_{\text{eq}} \sin i$ (or V_{eq}). For the adopted σ_{ϕ} and stellar model, these parameters can be determined within a $\approx 20\%$ precision for a few observations, with the longest baselines at different PA. Figures 2 and 3 show that ϕ_{diff} is also sensitive to i , $\overline{T}_{\text{eff}}$, and β , but to a lesser extent when compared to R_{eq} , d , and $V_{\text{eq}} \sin i$.

The strong dependence of ϕ_{diff} on PA_{rot} can equally be seen in Figs. 1 to 3, which show that, for a given baseline, the amplitude of the s-shaped ϕ_{diff} inside the line is stronger for PA = 90° (perpendicular to PA_{rot}) and weaker for PA = 45° (45° from PA_{rot}). Indeed, for uniform rotation, the ϕ_{diff} amplitude decreases to zero when PA is parallel to PA_{rot} . This indicates that only the angular sizes in the equatorial directions are constrained directly from ϕ_{diff} data alone and, consequently, this interferometric observable is not strongly sensitive to the apparent flattening of the star.

Of course, the uncertainties of the model parameters mentioned above are only indicative values. The actual precisions of the model parameters depend on the available baselines, observation errors, and parameter values. In the next section, we analyze real VLT/AMBER observations using CHARRON and the results from the simulations presented above.

3. VLT/AMBER observations and data reduction

VLT/AMBER observations of Achernar in high spectral resolution ($\lambda/\Delta\lambda \approx 12\,000$) centered on the Br γ line were carried out from October 25th to November 1th, 2009, during four nights with a different Auxiliary Telescope (AT) triplet configuration in each night (D0-H0-K0, D0-H0-G1, A0-G1-K0, and E0-G0-H0), providing good (u, v) coverage (Fig. 4). The calibrator δ Phe was observed interleaved with Achernar's observations. δ Phe is a bright ($K = 1.7$) K0IIIb single star with a K band uniform-disk angular diameter of $\mathcal{D}_{\text{UD}} = 2.180 \pm 0.023$ mas (Bordé et al. 2002). Previous works showed that it is a trustable interferometric calibrator (e.g., Kervella & Domiciano de Souza 2006). The fringe tracker FINITO was used, providing a good locking ratio and fringe tracking performance. Individual exposure times ranged from 360 ms to 735 ms. The seeing varied from $0.8''$ to $1.2''$. The log of the observations with details on the dates, times, and baselines is given in Table 1.

Data were reduced with amdlib software (version 3.1; Chelli et al. 2009; Tatulli et al. 2007). We adopted a frame selection based on fringe SNR and kept the 50% best frames. Data were calibrated using a dedicated script from Millour et al. (2008). Wavelength calibration was performed by fitting a Gaussian function to the line center of the AMBER spectra and correcting to the rest wavelength of Br γ .

3. High spectro-spatial resolution observations of fast rotators in the H-R diagram

A&A 545, A130 (2012)

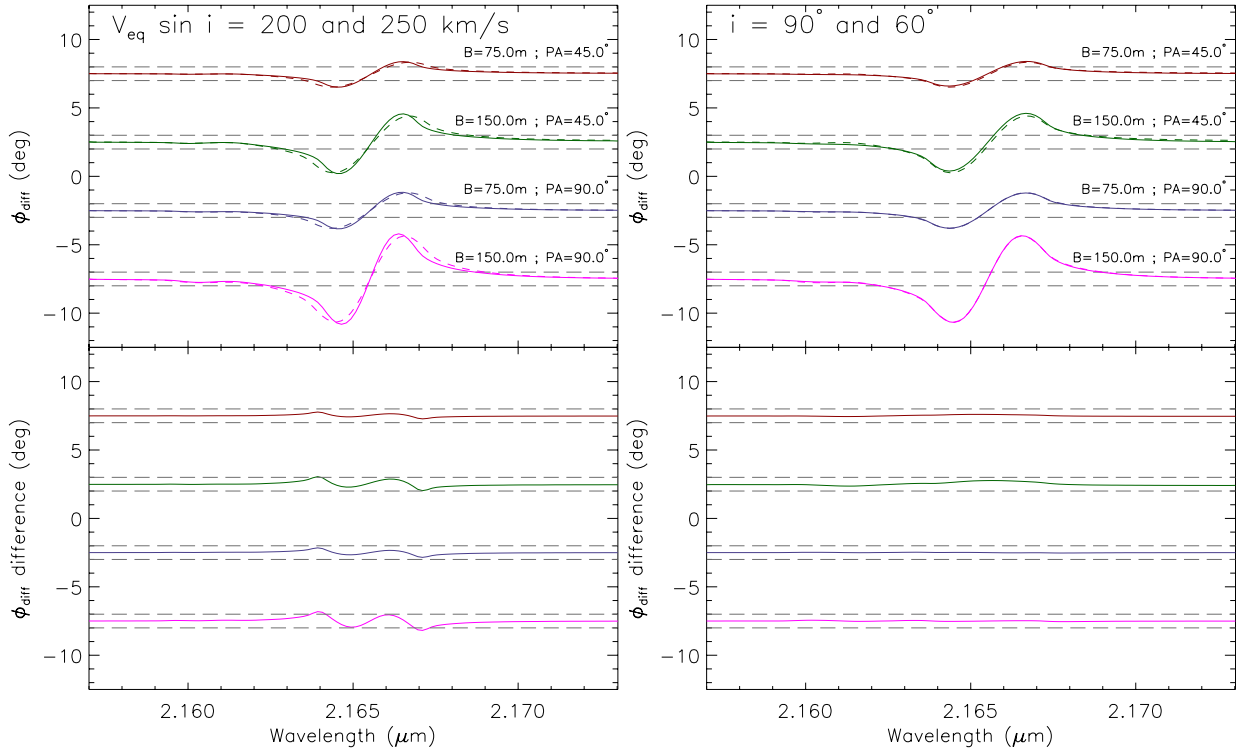


Fig. 2. Similar to Fig. 1 but for the dependence of ϕ_{diff} on $V_{\text{eq}} \sin i$ and i . The left panel shows that ϕ_{diff} in Br γ is sensitive to a variation of 20% in $V_{\text{eq}} \sin i$ ($= 200 \text{ km s}^{-1}$ for the tested model). The right panel shows that ϕ_{diff} also depends on i (changing from 60° to 90°), but to a lesser extent when compared to R_{eq} , d , and $V_{\text{eq}} \sin i$.

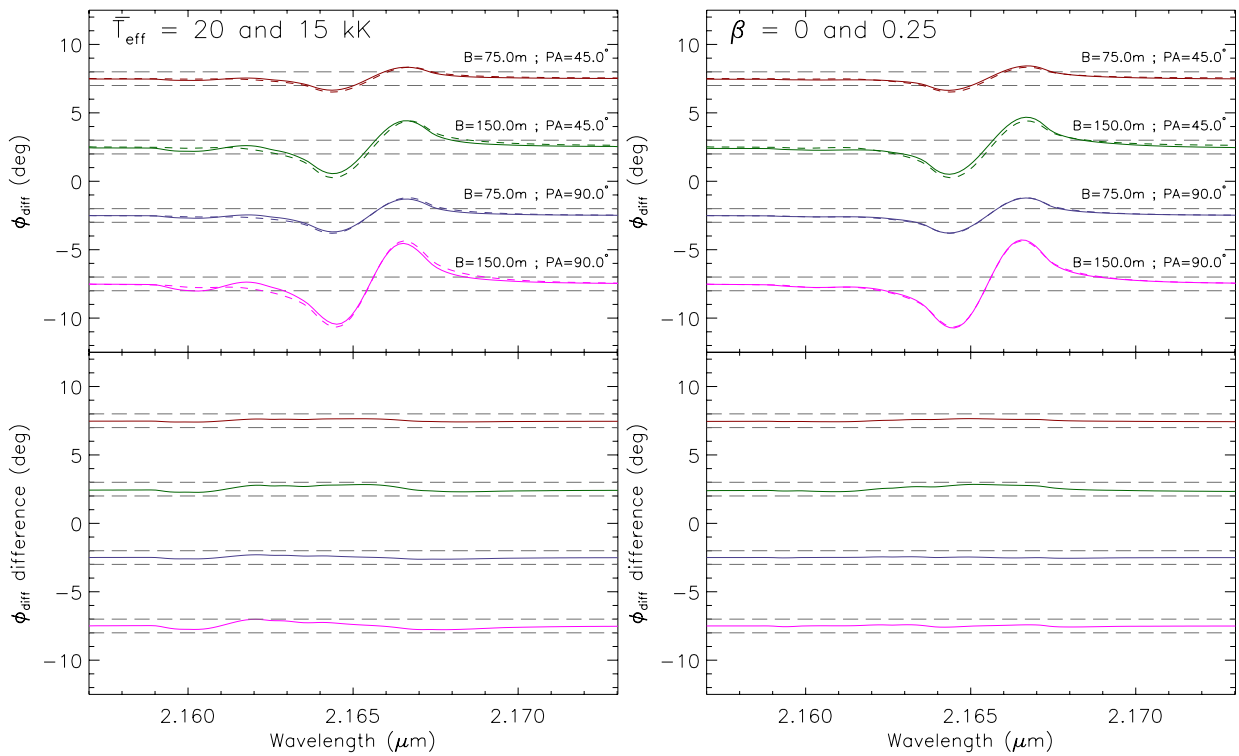


Fig. 3. Similar to Fig. 1 but for the dependence of ϕ_{diff} on \bar{T}_{eff} and β . \bar{T}_{eff} changed from 15 000 K to 20 000 K, and β changed from 0.25 (von Zeipel value) to 0.0 (no gravity-darkening). ϕ_{diff} in Br γ is not strongly sensitive to these parameters.

3.2. The Be star Achernar (α Eridani)

A. Domiciano et al.: Beyond the diffraction limit of optical/IR interferometers. I.

Table 1. Log of the 28 VLTI/AMBER observations of Achernar with details on the dates, times, and baseline triplets.

Object	Date and time	Baseline length	Baseline PA
		B_{proj} (m)	PA ($^{\circ}$)
Observations with AT triplet D0-H0-K0:			
δ Phe	2009-10-25T01:51	63, 31, 94	48, 48, 48
Achernar	2009-10-25T02:10	64, 32, 96	50, 50, 50
δ Phe	2009-10-25T02:27	64, 32, 96	55, 55, 55
δ Phe	2009-10-25T03:59	63, 32, 95	73, 73, 73
Achernar	2009-10-25T04:15	63, 31, 94	76, 76, 76
δ Phe	2009-10-25T04:32	62, 31, 93	79, 79, 79
Achernar	2009-10-25T04:50	61, 31, 92	84, 84, 84
δ Phe	2009-10-25T05:11	60, 30, 90	86, 86, 86
Achernar	2009-10-25T05:28	60, 30, 89	92, 92, 92
δ Phe	2009-10-25T05:48	58, 29, 87	93, 93, 93
Achernar	2009-10-25T06:04	57, 29, 86	99, 99, 99
δ Phe	2009-10-25T06:21	55, 27, 83	100, 100, 100
Observations with AT triplet G1-D0-H0:			
δ Phe	2009-10-25T23:53	44, 60, 63	-85, 22, -20
Achernar	2009-10-26T00:11	45, 62, 58	-93, 24, -20
Achernar	2009-10-26T01:01	51, 63, 60	-83, 35, -14
δ Phe	2009-10-26T01:18	56, 62, 65	-71, 42, -10
Achernar	2009-10-26T01:38	55, 64, 60	-76, 44, -9
δ Phe	2009-10-26T01:58	60, 63, 66	-66, 50, -5
Achernar	2009-10-26T02:29	60, 64, 61	-67, 55, -3
δ Phe	2009-10-26T03:14	66, 64, 66	-54, 65, 4
Achernar	2009-10-26T03:29	65, 64, 61	-56, 67, 5
δ Phe	2009-10-26T03:52	68, 63, 65	-49, 72, 8
Achernar	2009-10-26T04:09	67, 63, 60	-49, 76, 10
δ Phe	2009-10-26T04:27	70, 62, 65	-43, 79, 12
Achernar	2009-10-26T04:45	68, 62, 60	-43, 83, 15
δ Phe	2009-10-26T05:04	71, 61, 64	-37, 85, 16
Achernar	2009-10-26T05:22	69, 60, 59	-36, 91, 19
δ Phe	2009-10-26T05:43	71, 58, 63	-30, 93, 20
Achernar	2009-10-26T06:01	70, 57, 57	-29, 99, 24
δ Phe	2009-10-26T06:18	71, 56, 61	-24, 100, 24
Observations with AT triplet K0-G1-A0:			
δ Phe	2009-10-30T03:11	85, 88, 128	-155, -71, -112
Achernar	2009-10-30T03:32	80, 87, 127	-151, -70, -108
δ Phe	2009-10-30T03:54	83, 90, 126	-149, -63, -104
Achernar	2009-10-30T04:15	77, 89, 124	-145, -62, -100
δ Phe	2009-10-30T04:35	81, 90, 123	-144, -56, -97
Achernar	2009-10-30T04:55	75, 90, 121	-139, -54, -92
δ Phe	2009-10-30T06:00	73, 90, 110	-134, -39, -81
Achernar	2009-10-30T06:20	67, 90, 110	-128, -36, -73
δ Phe	2009-10-30T06:40	69, 89, 102	-130, -31, -72
Achernar	2009-10-30T07:00	62, 90, 104	-123, -27, -63
δ Phe	2009-10-30T07:20	63, 88, 93	-127, -22, -62
Achernar	2009-10-30T07:42	55, 90, 97	-117, -18, -52
δ Phe	2009-10-30T07:59	57, 87, 85	-123, -13, -52
Achernar	2009-10-30T08:16	50, 89, 92	-113, -10, -42
δ Phe	2009-10-30T08:32	51, 86, 78	-121, -5, -41
Achernar	2009-10-30T08:56	43, 89, 87	-107, -1, -29
Observations with AT triplet H0-G0-E0:			
δ Phe	2009-11-01T00:22	31, 15, 46	-145, -145, -145
Achernar	2009-11-01T00:50	32, 16, 47	-141, -141, -141
δ Phe	2009-11-01T01:08	31, 16, 47	-135, -135, -135
Achernar	2009-11-01T01:25	32, 16, 48	-133, -133, -133
δ Phe	2009-11-01T01:47	32, 16, 48	-127, -127, -127
Achernar	2009-11-01T02:04	32, 16, 48	-125, -125, -125
δ Phe	2009-11-01T02:22	32, 16, 48	-120, -120, -120
Achernar	2009-11-01T02:40	32, 16, 48	-117, -117, -117
δ Phe	2009-11-01T02:59	32, 16, 48	-113, -113, -113
Achernar	2009-11-01T03:16	32, 16, 48	-110, -110, -110
δ Phe	2009-11-01T03:34	32, 16, 48	-106, -106, -106
Achernar	2009-11-01T03:50	31, 16, 47	-103, -103, -103

Notes. The calibration star is δ Phe.

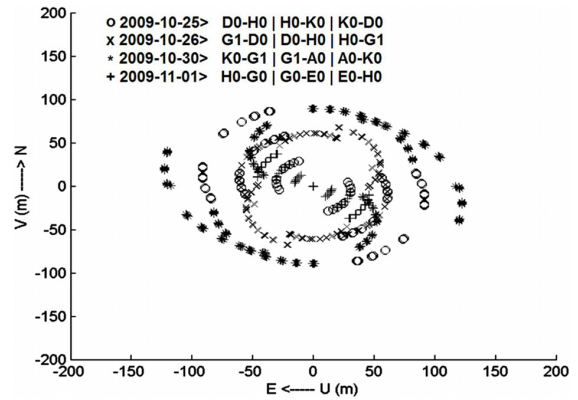


Fig. 4. Used VLTI baselines and (u, v) coverage of our VLTI/AMBER observations of Achernar. Earth-rotation synthesis spanning ~ 5 h/night provided this good (u, v) coverage.

After this initial data reduction, we obtain several VLTI/AMBER spectro-interferometric observables: source spectra, absolute and differential visibilities, differential phases, and closure phases. A high-frequency beating in wavelength was present in the calibrated data of all measurements (spectrum, visibilities, phases) due to a dichroic plate in the VLTI optical train in front of AMBER, routing the H band light to the IRIS image-tracker camera. Since this beating appears in a narrow frequency range in the wave-number domain, we removed it by applying a Fourier filtering to that specific wave-number domain. Moreover, a low-frequency beating was also present in our data due to the polarizing prisms of AMBER. This second beating was removed by subtracting a single sine wave fitted to the continuum close to $\text{Br } \gamma$.

Once the described data reduction steps are done, the differential phases ϕ_{diff} show a clear signal in the $\text{Br } \gamma$ line region corresponding to the expected s-shaped signature caused by stellar rotation (Fig. 5). Unfortunately, the commonly used visibility amplitudes could not be reliably calibrated due to a very chaotic transfer function. Additionally, no clear stellar signal was present in the $\text{Br } \gamma$ line region in the differential visibilities. Finally, the closure phases are compatible with zero within the observational errors at all AT triplets and wavelengths ($\text{Br } \gamma$ line included), not revealing any strong signatures of stellar rotation and/or asymmetries in the intensity distribution. At each AT triplet, the wavelength-averaged closure phase is always $< 0.8^{\circ}$ (in absolute value), with a corresponding standard deviation several (~ 3 – 10) times higher. Such lack of stellar signatures in the closure phases is in agreement with (1) the Achernar's inclination angle i being close to 90° (centrally-symmetric object; see Sect. 4) and with (2) the closure phases being less sensitive to the spatial intensity distribution than the differential phases for partially resolved objects. This last point is a consequence of the fact that, for poorly resolved objects, the closure phase is a third-order term of the Fourier transform of the spatial intensity distribution, while the differential phase is a first-order term (e.g., Lachaume 2003).

We thus concentrate hereafter our data analysis on the differential phase ϕ_{diff} alone, which is the only available spectro-interferometric observable presenting a signal-to-noise ratio high enough to constrain the physical parameters of Achernar with a model-fitting algorithm. Most model-fitting algorithms, including the Levenberg-Marquardt algorithm used in the next section, assume that all data points are independent. To be

3. High spectro-spatial resolution observations of fast rotators in the H-R diagram

A&A 545, A130 (2012)

consistent with this assumption, we did not use the ϕ_{diff} observations at all wavelengths. Instead, we used only each third point (one wavelength over three), which ensures that all observations are independent with respect to the finite resolution of the AMBER spectrograph.

Our final data set consists of 84 ($=28 \times 3$ baselines) $\phi_{\text{diff}}(\lambda)$ curves centered on Br γ (from 2.159 to 2.172 μm) and presents ≈ 45 ϕ_{diff} points for each of the 84 individual projected baselines. The median uncertainty of this data set is $\sigma_{\phi, \text{median}} = 0.6^\circ$.

4. Stellar parameters from VLTI/AMBER ϕ_{diff}

The VLTI/AMBER ϕ_{diff} observations of Achernar were analyzed with the numerical model CHARRON presented in Sect. 2. A χ^2 minimization was performed using an IDL implementation of the Levenberg-Marquardt (LM) algorithm (Markwardt 2009, and references therein).

The free parameters for the model-fitting are R_{eq} , V_{eq} , i , and PA_{rot} . Based on measurements from previous works and on the results of Sect. 2, the remaining model parameters were held fixed, namely:

- $d = 44.1$ pc. For a consistent comparison of our results with previous works, we adopted the HIPPARCOS distance $d = 44.1$ pc from Perryman et al. (1997), instead of the more recent value of $d = 42.7$ pc from van Leeuwen (2007).
- $\beta = 0.20$. Since Achernar is a hot B star with a mostly radiative envelope, the gravity-darkening parameter β should be close to 0.25. Recent interferometric observations of fast rotators (Che et al. 2011) and theoretical works (Claret 2012) suggest that the value $\beta = 0.20$ would be more adapted to Achernar's spectral type. Gravity-darkening models from Espinosa Lara & Rieutord (2011) also indicate that $\beta < 0.25$ for fast rotators. Based on these works and on our results showing that ϕ_{diff} is not strongly sensitive to β (Fig. 3), this parameter was fixed to 0.20 throughout the data analysis.
- $M = 6.1 M_{\odot}$. Value from Harmanec (1988), which was adopted by Domiciano de Souza et al. (2003) for Achernar.
- $\bar{T}_{\text{eff}} = 15000$ K. We adopt the value given by Vinicius et al. (2006), corresponding to the apparent temperature of Achernar. As shown in Fig. 3, ϕ_{diff} does not depend strongly on \bar{T}_{eff} .

Figure 5 show the best-fit ϕ_{diff} , together with the corresponding observations. The best-fit values of the free parameters found with the LM algorithm are given in Table 2. The uncertainties of the parameters estimated by the LM algorithm are $\sim 1\%$. However, previous works have shown that the LM errors derived from the fit of spectro-interferometric data are often too optimistic and should be considered as lower limits (e.g., Niccolini et al. 2011; Domiciano de Souza et al. 2011). To obtain a more realistic estimation of the parameter uncertainties, we applied a Monte Carlo method, which consists in the analysis of artificial data sets generated from the real observations (Press et al. 2002). These artificial data sets have a random Gaussian distribution with a standard deviation given by the observed σ_{ϕ} and an average value given by the observed ϕ_{diff} . By generating 300 artificial ϕ_{diff} data sets and by performing a LM model-fit on each of these data sets, we determined the histogram distribution of each fitted parameter, which allowed us to estimate its uncertainty. The limits of the parameter distribution defining the uncertainties of the best-fit parameters given in Table 2 were chosen to correspond to the 68% confidence level of the commonly used standard deviation for normal distributions. We also present in Table 2 several stellar parameters derived from the best-fit parameters.

Table 2. Parameters and uncertainties estimated from a Levenberg-Marquardt fit of our model to the VLTI/AMBER ϕ_{diff} observed on Achernar.

Best-fit parameter	Best-fit value and error
Equatorial radius R_{eq}	$11.6 \pm 0.3 R_{\odot}$
Equatorial rotation velocity V_{eq}	$298 \pm 9 \text{ km s}^{-1}$
Rotation-axis inclination angle i	$101.5 \pm 5.2^\circ$
Rotation-axis position angle PA_{rot}	$34.9 \pm 1.6^\circ$
Fixed parameter	Value
Distance d	44.1 pc
Mass M	$6.1 M_{\odot}$
Surface mean temperature \bar{T}_{eff}	15 000 K
Gravity-darkening coefficient β	0.20
Derived parameter	Value and error
Equatorial angular diameter \mathcal{D}_{eq}	$2.45 \pm 0.09 \text{ mas}$
Equatorial-to-polar radii $R_{\text{eq}}/R_{\text{p}}$	1.45 ± 0.04
$V_{\text{eq}} \sin i$	$292 \pm 10 \text{ km s}^{-1}$
$V_{\text{eq}}/V_{\text{crit}}$	0.96 ± 0.03
Polar temperature T_{pol}	$18\,013_{-171}^{+141} \text{ K}$
Equatorial temperature T_{eq}	$9955_{-2339}^{+1115} \text{ K}$
Luminosity $\log L/L_{\odot}$	3.654 ± 0.028

Notes. The minimum reduced χ^2 of the fit is $\chi_{\text{min,r}}^2 = 1.22$. The HIPPARCOS distance $d = 44.1 \pm 1.1$ pc from Perryman et al. (1997) was adopted to convert from linear to angular sizes.

5. Discussion and conclusions

The stellar parameters derived from the Achernar's ϕ_{diff} mostly agree with those from previous results. Our equatorial angular diameter $\mathcal{D}_{\text{eq}} = 2.45 \pm 0.09$ mas (or, alternatively, R_{eq}) is between the values reported by Kervella & Domiciano de Souza (2006, $\mathcal{D}_{\text{eq}} = 2.13 \pm 0.05$ mas) and by Domiciano de Souza et al. (2003, $\mathcal{D}_{\text{eq}} = 2.53 \pm 0.06$ mas), which were based on VLTI/VINCI observations. The relatively small differences between these three values can be explained, at least partially, by the fact that different approaches and models were used to interpret the interferometric observations. In particular, the smaller \mathcal{D}_{eq} from Kervella & Domiciano de Souza (2006) is due to the use of a uniform brightness ellipse model, which is known to give smaller angular sizes than more realistic models, such as the one used in this work. The comparison with previous works also suggests that the uncertainty of \mathcal{D}_{eq} derived from ϕ_{diff} is of the same order as the uncertainties attained from visibility amplitudes.

The PA_{rot} derived here is $\approx 6^\circ$ smaller than the values reported in these two previous works, meaning that these results agree within $\approx 3-4$ sigma. The fact that the AMBER (u, v) coverage is more complete than the VLTI/VINCI (u, v) coverage suggests that the PA_{rot} from the present work is probably somewhat more accurate.

The derived $V_{\text{eq}} \sin i$ is larger than those obtained in other works based on spectroscopic data (e.g., Vinicius et al. 2006). These differences can be explained by gravity-darkening, which tends to decrease the $V_{\text{eq}} \sin i$ estimated from spectroscopy alone (e.g., Frémat et al. 2005). In any case, the derived rotation rate ($V_{\text{eq}}/V_{\text{crit}} = 0.96 \pm 0.03$) agrees with the value reported by Carciofi et al. (2008), who obtained a lower limit for the rotational speed of $V_{\text{eq}}/V_{\text{crit}} > 0.93$, based on interferometric, spectroscopic, and polarimetric data.

3.2. The Be star Achernar (α Eridani)

A. Domiciano et al.: Beyond the diffraction limit of optical/IR interferometers. I.

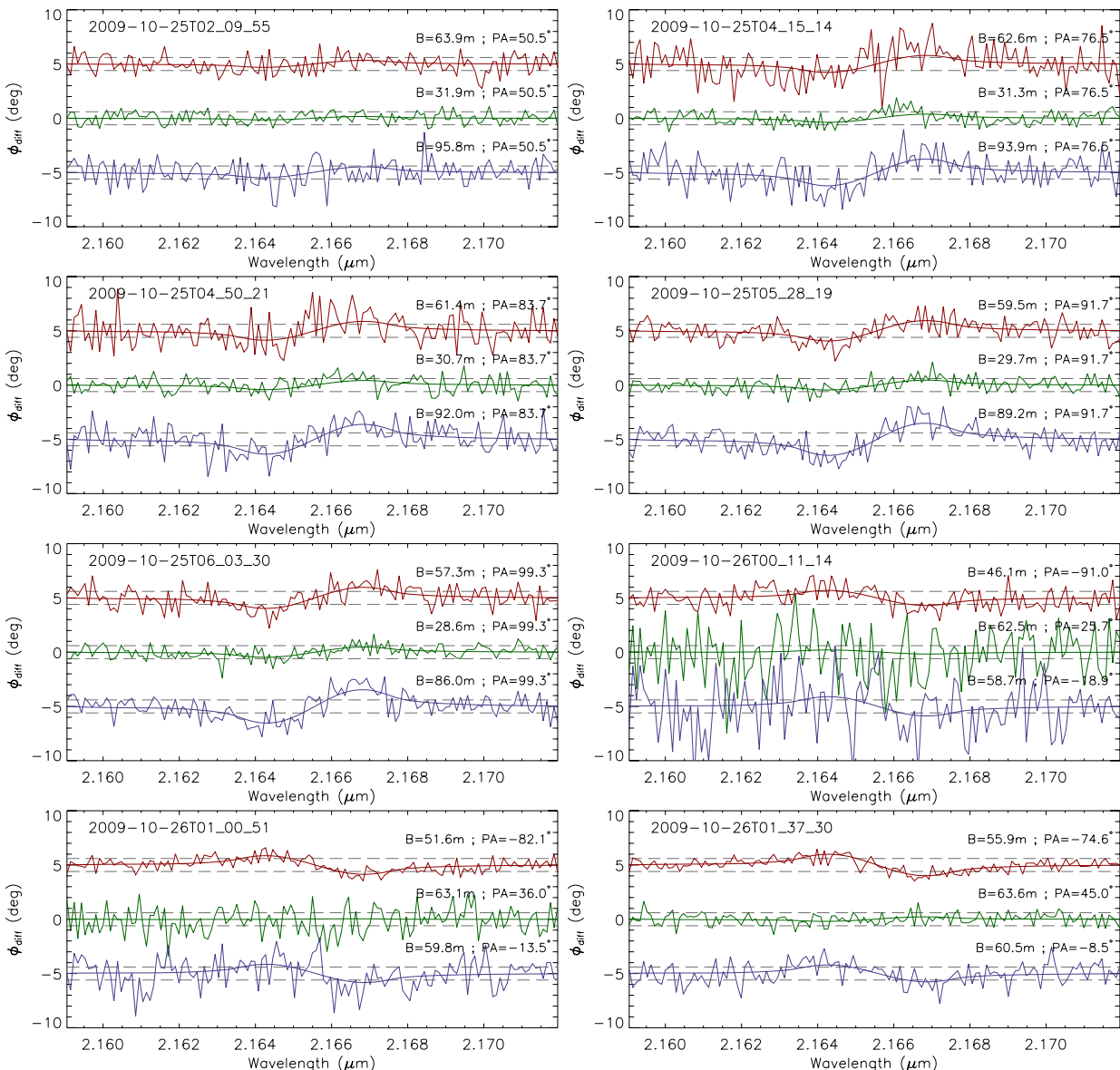


Fig. 5. The 84 VLTI/AMBER $\phi_{\text{diff}}(\lambda)$ measured on Achernar around Br γ at 28 different observing times (format YYYY-MM-DDTHH_MM_SS) and, for each time, three different projected baselines and baseline position angles, as indicated in the plots. The dashed gray horizontal lines indicate the median $\pm\sigma_\phi = \pm 0.6^\circ$ of all observations. The smooth curves superposed to the observations are the best-fit ϕ_{diff} obtained with a uniform-rotation, gravity-darkened Roche model, as described in Sect. 4. All the observed ϕ_{diff} points are shown here, even if the fit has been performed using only each third wavelength point (cf. Sect. 4). All ϕ_{diff} curves are equal to zero in the continuum, but they were shifted for better readability. The other panels are available in the electronic edition.

The measured $i (=101.5 \pm 5.2^\circ)$ is compatible with previous results, suggesting that $65^\circ \leq i \leq 115^\circ$ (Vinicius et al. 2006; Carciofi et al. 2007). We note that, although $i = 101.5^\circ$ and $i = 78.5^\circ (= 180^\circ - 101.5^\circ)$ are indistinguishable from spectroscopic observations, they have different ϕ_{diff} signatures when gravity-darkening is present. The measured inclination close to 90° (nearly a centrally-symmetric intensity distribution) is totally consistent with the observed closure phases, which show values compatible with zero within the error bars.

Following Vinicius et al. (2006), a somewhat higher \bar{T}_{eff} value could be adopted in our models, since this quantity is dependent on the rotation rate of the star and on the inclination angle i . We have thus checked the robustness of our results by

performing an additional model-fitting fixing $\bar{T}_{\text{eff}} = 16000$ K, which corresponds to the average effective temperature of the visible stellar hemisphere given by Vinicius et al. (2006). In agreement with what was expected from Fig. 3, the values of the parameters obtained from the best fits with $\bar{T}_{\text{eff}} = 15000$ K (Table 2) and with $\bar{T}_{\text{eff}} = 16000$ K are compatible within the parameter uncertainties.

Finally, we also checked that compatible results, within uncertainties, are obtained from a fit performed over all wavelengths, instead of one-third of the $\phi_{\text{diff}}(\lambda)$ points.

The present work shows that ϕ_{diff} can be used to measure several parameters in fast rotators, in particular \mathcal{D}_{eq} (or R_{eq}),

3. High spectro-spatial resolution observations of fast rotators in the H-R diagram

A&A 545, A130 (2012)

PA_{rot} , V_{eq} , and i . This is very useful, notably in cases when the visibility amplitude is too high (partially resolved objects), when it is poorly determined (large errors), and/or when it cannot be calibrated (as in the case of Achernar's data). By analyzing VLTI/AMBER ϕ_{diff} of Achernar, we have shown, using real observations, that the combination of high spatial and high spectral resolution allows one to go beyond diffraction-limited angular resolution of the interferometer, commonly defined as $\lambda/B_{\text{proj}}^{\text{max}}$. The equatorial angular diameter of Achernar of $\mathcal{D}_{\text{eq}} = 2.45 \pm 0.09$ mas was measured from ϕ_{diff} alone on B_{proj} between $B_{\text{proj}}^{\text{min}} \simeq 15$ m and $B_{\text{proj}}^{\text{max}} \simeq 128$ m at $\lambda \simeq 2.2 \mu\text{m}$. The derived \mathcal{D}_{eq} is therefore $\simeq 1.5$ times smaller than the maximum available diffraction-limited angular resolution. Furthermore, our observations show that the Achernar's diameter is already resolved at shorter baselines, with a clear signature of rotation seen (ϕ_{diff} amplitudes $\gtrsim \sigma_{\phi}$) at B_{proj} above $\simeq 45$ m (Fig. 5). Therefore, in these observations with $B_{\text{proj}} \simeq 45$ m, the measured diameter is even $\simeq 4$ times smaller than the corresponding diffraction-limited resolution of 10 mas.

This super-resolution capacity provided by ϕ_{diff} can be further improved if the observational uncertainties are smaller than those attained in the present work. In such cases, the angular diameters of even smaller and slower rotators can be measured, thanks to this powerful technique. The results obtained in this work from VLTI/AMBER differential phases open new perspectives to measure angular sizes of faint and/or angularly small stars, beyond the diffraction limit of optical/IR interferometers.

Acknowledgements. This research has made use of the SIMBAD database, operated at the CDS, Strasbourg, France, of NASA Astrophysics Data System Abstract Service, and of the Jean-Marie Mariotti Center Aspro service². A.D.S. and A.C.C. thank the CNRS-PICS program for supporting our Brazilian-French collaboration and the present work. This research received the support of PHASE, the high angular resolution partnership between ONERA, Observatoire de Paris, CNRS, and University Denis Diderot Paris 7. A.C.C. acknowledges support from CNPq (grant 308985/2009-5) and Fapesp (grant 2010/19029-0). M.H. acknowledges the CRAAG and the EII/OPTICON Fizeau program for supporting his PhD thesis. We acknowledge the anonymous referee for her/his constructive comments and suggestions that helped us to improve this work.

References

- Bordé, P., Coudé du Foresto, V., Chagnon, G., & Perrin, G. 2002, A&A, 393, 183
- Born, M., & Wolf, E. 1980, Principles of Optics Electromagnetic Theory of Propagation, Interference and Diffraction of Light, 6th edn.
- Carciofi, A. C., Domiciano de Souza, A., Magalhães, A. M., Bjorkman, J. E., & Vakili, F. 2008, ApJ, 676, L41
- Carciofi, A. C., Magalhães, A. M., Leister, N. V., Bjorkman, J. E., & Levenhagen, R. S. 2007, ApJ, 671, L49
- Che, X., Monnier, J. D., Zhao, M., et al. 2011, ApJ, 732, 68
- Chelli, A., & Petrov, R. G. 1995, A&AS, 109, 401
- Chelli, A., Utrera, O. H., & Duvert, G. 2009, A&A, 502, 705
- Claret, A. 2012, A&A, 538, A3
- Domiciano de Souza, A., Bendjoya, P., Niccolini, G., et al. 2011, A&A, 525, A22
- Domiciano de Souza, A., Kervella, P., Jankov, S., et al. 2003, A&A, 407, L47
- Domiciano de Souza, A., Vakili, F., Jankov, S., Janot-Pacheco, E., & Abe, L. 2002, A&A, 393, 345
- Domiciano de Souza, A., Zorec, J., & Vakili, F. 2012, SF2A Proc., in press
- Espinosa Lara, F., & Rieutord, M. 2011, A&A, 533, A43
- Frémat, Y., Zorec, J., Hubert, A., & Floquet, M. 2005, A&A, 440, 305
- Harmanec, P. 1988, Bull. Astron. Inst. Czechoslovakia, 39, 329
- Jackson, S., MacGregor, K. B., & Skumanich, A. 2004, ApJ, 606, 1196
- Kervella, P., & Domiciano de Souza, A. 2006, A&A, 453, 1059
- Lachaume, R. 2003, A&A, 400, 795
- Le Bouquin, J., Absil, O., Benisty, M., et al. 2009, A&A, 498, L41
- Markwardt, C. B. 2009, in Astronomical Data Analysis Software and Systems XVIII, eds. D. A. Bohlender, D. Durand, & P. Dowler, ASP Conf. Ser., 251
- Millour, F., Vannier, M., Petrov, R. G., et al. 2006, in EAS Publ. Ser. 22, eds. M. Carillet, A. Ferrari, & C. Aime, 379
- Millour, F., Petrov, R. G., Vannier, M., & Kraus, S. 2008, in SPIE Conf. Ser., 7013, 41
- Millour, F., Meilland, A., Chesneau, O., et al. 2011, A&A, 526, A107
- Niccolini, G., Bendjoya, P., & Domiciano de Souza, A. 2011, A&A, 525, A21
- Perryman, M. A. C., Lindgren, L., Kovalevsky, J., et al. 1997, A&A, 323, L49
- Petrov, R. G., Malbet, F., Weigelt, G., et al. 2007, A&A, 464, 1
- Press, W., Teukolsky, S., Vetterling, W., & Flannery, B. 2002, Numerical Recipes in C: The art of scientific computing, 2nd edn. (Cambridge University Press)
- Tatulli, E., Millour, F., Chelli, A., et al. 2007, A&A, 464, 29
- van Leeuwen, F. 2007, A&A, 474, 653
- Vinicius, M. M. F., Zorec, J., Leister, N. V., & Levenhagen, R. S. 2006, A&A, 446, 643
- von Zeipel, H. 1924, MNRAS, 84, 665

Pages 9 to 10 are available in the electronic edition of the journal at <http://www.aanda.org>

² Available at <http://www.jmmc.fr/aspro>

3.2. The Be star Achernar (α Eridani)

A. Domiciano et al.: Beyond the diffraction limit of optical/IR interferometers. I.

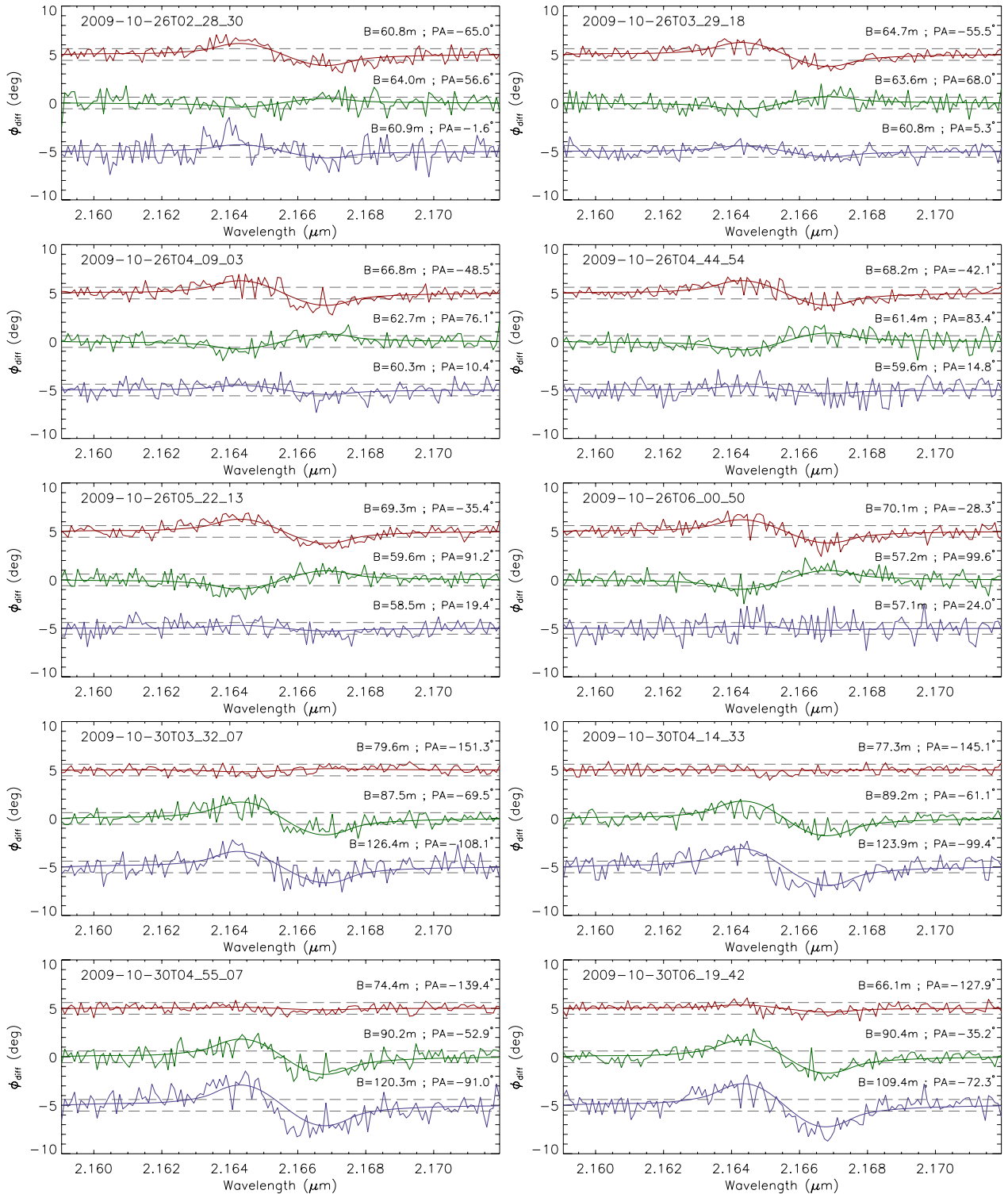


Fig. 5. continued.

3. High spectro-spatial resolution observations of fast rotators in the H-R diagram

A&A 545, A130 (2012)

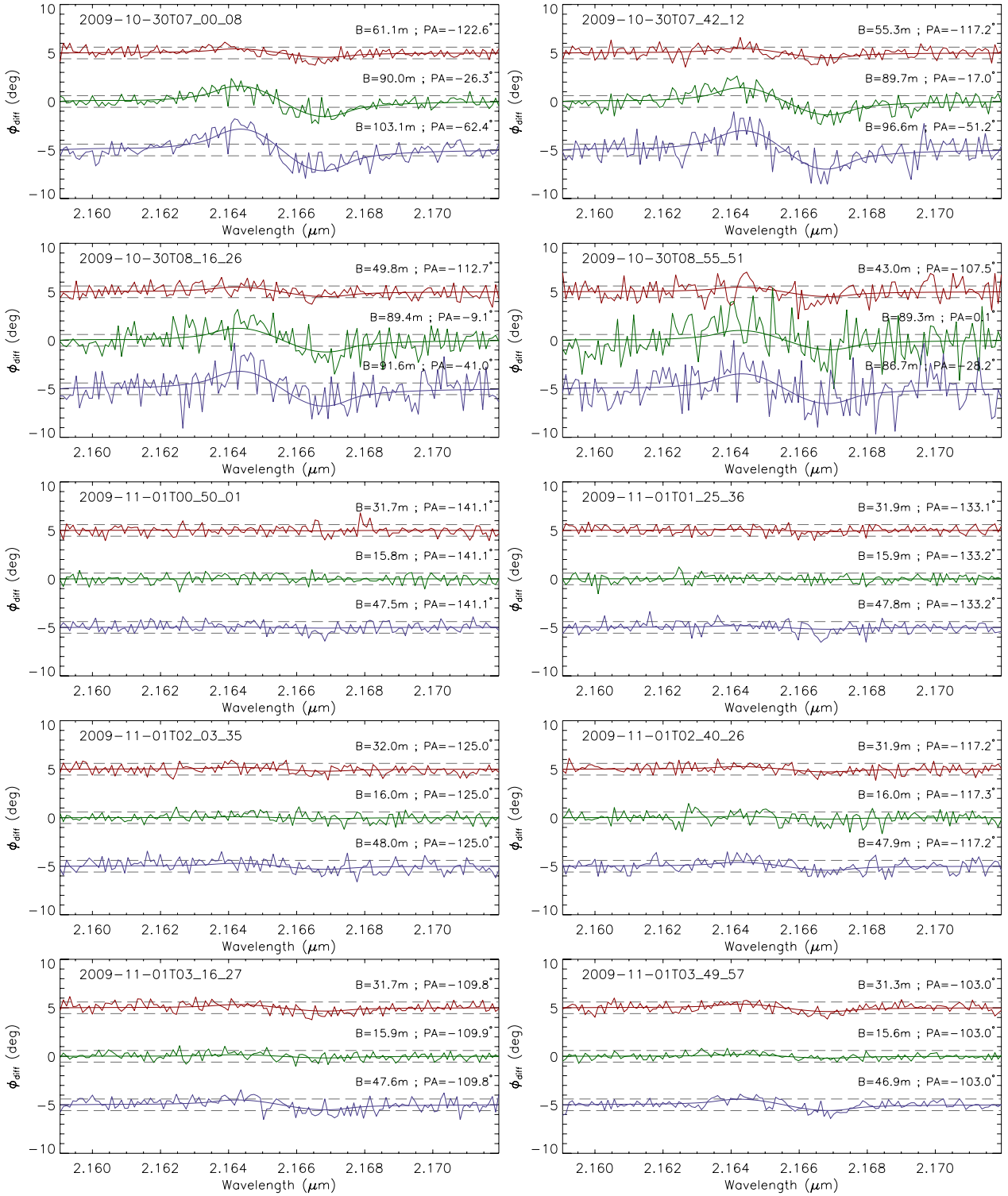


Fig. 5. continued.

3.3 The supergiant B[e] star CPD-57° 2874

The galactic sgB[e] star [CPD-57° 2874](#) was the first to be studied simultaneously with OLBI in the near- and mid-IR with the ESO beam-combiners VLT/AMBER and VLT/MIDI ([Domiciano de Souza et al., 2007](#)). This work, given hereafter, was published in the 2007 A&A Special feature dedicated to the first results of the VLT/AMBER beam combiner (*AMBER: Instrument description and first astrophysical results*)³. These results were also published as part of the ESO Press Release 29/05⁴.

These observations allowed us to spatially resolve CPD-57° 2874, revealing an elongated CSE where the size of the emitting region increases from near- to mid-IR. The spectrally resolved VLT/AMBER observations also revealed a significant increase of the CSE size in the Br γ line compared to the size in the adjacent continuum. The observations are well reproduced by an analytical model composed by a 2-D elliptical Gaussian with FWHM varying linearly with wavelength in the continuum. The increase of the size of the region emitting in Br γ , with respect to the close continuum, is well modeled by a Gaussian law.

Following this first work on CPD-57° 2874, the initial VLT/MIDI observations were complemented with additional ones, and the total set was re-analyzed with our ray-tracing radiative transfer code FRACS (Sect. 2.5.2). The adopted CSE model is the one described in Sect. 2.4. Thanks to the use of FRACS and a CSE model we could constrain several physical parameters (and corresponding uncertainties) of CPD-57° 2874, namely, the inner dust radius, the relative flux contribution of the central source and of the dusty CSE, the dust temperature profile, and the disk inclination. These results are published in the second A&A paper given hereafter ([Domiciano de Souza et al., 2011](#)).

This interferometric-based work on CPD-57° 2874 is probably the first direct evidence of a non-spherical sgB[e] CSE.

³http://www.aanda.org/index.php?option=com_content&view=article&id=216

⁴<http://www.eso.org/public/news/eso0538/>

AMBER: Instrument description and first astrophysical results

AMBER/VLTI and MIDI/VLTI spectro-interferometric observations of the B[e] supergiant CPD–57° 2874[★]**Size and geometry of the circumstellar envelope in the near- and mid-IR**A. Domiciano de Souza^{1,4}, T. Driebe¹, O. Chesneau², K.-H. Hofmann¹, S. Kraus¹, A.S. Miroshnichenko^{1,3}, K. Ohnaka¹, R.G. Petrov⁴, T. Preisbisch¹, P. Stee², G. Weigelt¹, F. Lisi⁵, F. Malbet⁶, and A. Richichi⁷¹ Max-Planck-Institut für Radioastronomie, Auf dem Hügel 69, 53121 Bonn, Germany² Laboratoire Gemini, UMR 6203 Observatoire de la Côte d'Azur/CNRS, BP 4229, 06304 Nice Cedex 4, France³ Dept. of Physics and Astronomy, PO Box 26170, University of North Carolina at Greensboro, Greensboro, NC 27402 6170, USA⁴ Laboratoire Universitaire d'Astrophysique de Nice, UMR 6525 Université de Nice – Sophia Antipolis/CNRS, Parc Valrose, 06108 Nice Cedex 2, France⁵ INAF-Osservatorio Astrofisico di Arcetri, Istituto Nazionale di Astrofisica, Largo E. Fermi 5, 50125 Firenze, Italy⁶ Laboratoire d'Astrophysique de Grenoble, UMR 5571 Université Joseph Fourier/CNRS, BP 53, 38041 Grenoble Cedex 9, France⁷ European Southern Observatory, Karl Schwarzschild Strasse 2, 85748 Garching, Germany

Received 31 August 2005 / Accepted 17 October 2005

ABSTRACT

We present the first high spatial and spectral resolution observations of the circumstellar envelope (CSE) of a B[e] supergiant (CPD–57° 2874), performed with the Very Large Telescope Interferometer (VLTI). Spectra, visibilities and closure phase were obtained using the beam-combiner instruments AMBER (near-IR interferometry with three 8.3 m Unit Telescopes or UTs) and MIDI (mid-IR interferometry with two UTs). The interferometric observations of the CSE are well fitted by an elliptical Gaussian model with FWHM diameters varying linearly with wavelength. Typical diameters measured are $\approx 1.8 \times 3.4$ mas or $\approx 4.5 \times 8.5$ AU (adopting a distance of 2.5 kpc) at $2.2 \mu\text{m}$, and $\approx 12 \times 15$ mas or $\approx 30 \times 38$ AU at $12 \mu\text{m}$. The size of the region emitting the Br γ flux is $\approx 2.8 \times 5.2$ mas or $\approx 7.0 \times 13.0$ AU. The major-axis position angle of the elongated CSE in the mid-IR ($\approx 144^\circ$) agrees well with previous polarimetric data, hinting that the hot-dust emission originates in a disk-like structure. In addition to the interferometric observations we also present new optical (*UBVR_cI_c*) and near-IR (*JHKL*) broadband photometric observations of CPD–57° 2874. Our spectro-interferometric VLTI observations and data analysis support the non-spherical CSE paradigm for B[e] supergiants.

Key words. techniques: high angular resolution – techniques: interferometric – infrared: stars – stars: early-type – stars: emission-line, Be – stars: mass-loss

1. Introduction

Supergiant B[e] (sgB[e]) stars are luminous ($\log L/L_\odot > 4.0$) post-main sequence objects showing the B[e] phenomenon (Lamers et al. 1998): (1) strong Balmer emission lines; (2) low-excitation emission lines of Fe II, [Fe II], and [O I]; and (3) strong near/mid-infrared (IR) excess due to hot circumstellar dust. Spectroscopic and polarimetric observations suggest that sgB[e] stars have non-spherical circumstellar envelopes (CSE; e.g., Zickgraf et al. 1985; Magalhães 1992). Zickgraf et al. (1985) proposed an empirical model of the sgB[e] CSE that consists of a hot and fast line-driven wind in the polar regions, and a slow, much cooler and denser wind (by a factor of 10^2 – 10^3) in the equatorial region, where dust could be formed. Rapid rotation of the central star seems to play a key role in the origin of the CSE, but a complete explanation of its formation mechanism is still unknown.

To investigate these crucial questions concerning the origin, geometry and physical structure of the sgB[e] CSE, it is

necessary to combine several observing techniques. In particular, the high spatial resolution provided by optical/IR long-baseline interferometry allows us to directly probe the vicinity of these complex objects. In this paper we present the first direct multi-wavelength measurements of the close environment of a Galactic sgB[e] star, namely CPD–57° 2874 (WRAY 15-535; IRAS 10136-5736), using the VLTI with its instruments AMBER and MIDI.

CPD–57° 2874 is a poorly-studied object for which McGregor et al. (1988) suggested a distance of $d = 2.5$ kpc, assuming that it belongs to the Carina OB association. A high reddening and the presence of CO emission bands at 2.3 – $2.4 \mu\text{m}$ makes it compatible with the sgB[e] class. Zickgraf (2003) obtained high-resolution optical spectra exhibiting double-peaked emission lines that are suggestive of a flattened CSE geometry, typical for sgB[e] stars. However, the physical parameters of neither the star nor its CSE have been studied in detail yet.

2. Interferometric observations and data reduction**2.1. AMBER/VLTI (near-IR)**

CPD–57° 2874 was observed on 2005 February 25 using the AMBER/VLTI instrument (e.g., Petrov et al. 2007) to

[★] Based on observations collected at the European Southern Observatory, Paranal, Chile, within the AMBER science demonstration time programme 074.A-9026 and the MIDI open time programme 074.D-0101.

3.3. The supergiant B[e] star CPD-57° 2874

Table 1. AMBER and MIDI observation log for CPD-57° 2874.

AMBER ($2.09 \leq \lambda \leq 2.24 \mu\text{m}$)				
3 Unit telescopes				
Night	t_{obs} (UTC)	UT baseline	B_p (m)	PA (°)
2005-02-26	03:41:21	UT2-UT3	43.5	37.8
		UT3-UT4	59.8	98.8
		UT2-UT4	89.4	73.6
MIDI ($7.9 \leq \lambda \leq 13.5 \mu\text{m}$)				
2 Unit telescopes				
Night	t_{obs} (UTC)	UT baseline	B_p (m)	PA (°)
2004-12-29	05:52:12	UT2-UT3	45.2	18.5
		UT2-UT3	43.9	35.1
2004-12-31	06:04:03	UT3-UT4	54.8	79.6
		UT3-UT4	60.9	104.8

combine the light from the 8.3 m Unit Telescopes UT2, UT3 and UT4. With an exposure time of 85 ms, 3000 spectrally dispersed interferograms (frames) were recorded on the target and calibrator (HD 90393). This allowed us to obtain spectra as well as wavelength-dependent visibilities and a closure phase in the K band with a spectral resolution of $R = 1500$ between 2.09 and 2.24 μm (including the Br γ line).

Data reduction was performed with the *amdlib* software (Millour et al. 2004; Tatulli et al. 2007). We checked the consistency of our results by selecting a fixed percentage of frames from the target and calibrator data sets, based on the fringe contrast signal-to-noise ratio. By keeping 50%, 30%, and 10% of the frames with the best SNR, we found that the derived quantities were stable (differences $\leq 4\%$). Moreover, we also found good agreement between the results from the *amdlib* software and our own software based on a power spectrum analysis.

2.2. MIDI/VLTI (mid-IR)

We also observed CPD-57° 2874 with the MIDI/VLTI instrument (Leinert et al. 2004) on 2004 December 28 and 30. The N-band spectrum as well as spectrally dispersed fringes have been recorded between 7.9 and 13.5 μm with a spectral resolution of $R = 30$, allowing us to study the wavelength dependence of the apparent size of CPD-57° 2874 in the mid-IR. In total, 4 data sets have been obtained using the UT2-UT3-47 m and UT3-UT4-62 m baselines. Several calibrator stars were observed: HD 37160, HD 50778, HD 94510 and HD 107446.

Data reduction was performed with the MIA (Leinert et al. 2004) and EWS (Jaffe 2004) packages. While MIA follows the classical power spectrum analysis, in the EWS software the fringes are coherently added after correction for the instrumental and atmospheric delay in each scan. The visibilities derived with both softwares agree within the uncertainties of $\approx 10\%$.

The logs of the AMBER and MIDI observations are given in Table 1, while Fig. 1 shows the projected baseline lengths (B_p) and corresponding position angles (PA) used. In Table 2 we list the uniform disc diameters θ_{UD} and observation log for the calibrators. Calibrated visibilities from both AMBER and MIDI observations were obtained using the known uniform disk diameters of the calibrator stars (Richichi et al. 2005), which were observed during the same nights as CPD-57° 2874.

3. Photometric observations

In addition to the VLTI data we present new broadband photometric observations of CPD-57° 2874. Optical (*UBVR_cI_c*) and near-IR (*JHKL*) photometric observations were obtained

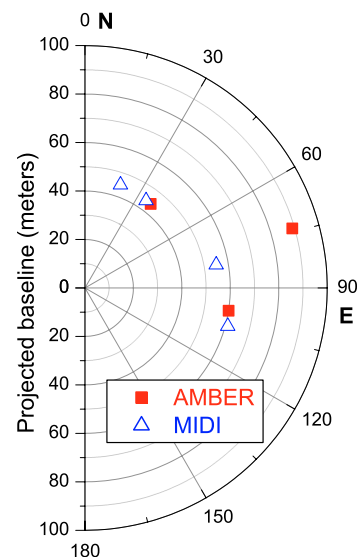


Fig. 1. Projected baselines and corresponding position angles for the AMBER and MIDI observations of CPD-57° 2874 (see also Table 1).

Table 2. Uniform disc diameters and observation log for the calibrators.

AMBER ($2.09 \leq \lambda \leq 2.24 \mu\text{m}$)			
3 Unit telescopes			
Calibrator HD number	θ_{UD} (mas)	Night	t_{obs} (UTC)
90393	0.77 ± 0.01	2005-02-26	04:38:04
MIDI ($7.9 \leq \lambda \leq 13.5 \mu\text{m}$)			
2 Unit telescopes			
Calibrator HD number	θ_{UD} (mas)	Night	t_{obs} (UTC)
37160	2.08 ± 0.20	2004-12-29	04:12:26
			05:29:32
50778	3.95 ± 0.22	2004-12-29	06:13:08
		2004-12-31	02:15:59
94510	2.16 ± 0.11	2004-12-29	07:47:21
		2004-12-31	06:31:19
			07:41:22
107446	4.54 ± 0.23	2004-12-31	07:19:17

quasi-simultaneously on 1997 July 10 at the South African Astronomical Observatory (SAAO). Additional near-IR observations were obtained on 1997 June 15 and December 28. The 0.75-m telescope with a single-element InSb photometer (Carter 1990) was used in the near-IR, while the 0.5-m telescope with a GaAs photometer (Menziés et al. 1991) was used in the optical region.

The data are presented in Table 3. The errors in the tabulated magnitudes and colors are not greater than 0.02 mag. A number of standard stars were observed during the same nights for calibration.

Our photometric results are very close to previously published observations of the star. Drilling (1991) obtained 3 *UBV* observations in 1972–1976 ($V = 10.20$; $B - V = 1.66$, $U - B = 0.41$ mag; the colon indicates either a variability suspicion or an uncertainty of over 0.08 mag), and McGregor et al. (1988) obtained near-IR observations on 1983 May 15 ($J = 5.77$, $H = 4.99$, $K = 4.02$ mag). The 2MASS data obtained on 2000 January 18 (Cutri et al. 2003) are very similar ($J = 5.76$, $H = 4.96$, $K = 4.3 \pm 0.3$ mag). However, the near-IR

Table 3. Photometry of CPD–57° 2874 obtained at SAAO.

JD	V	$U - B$	$B - V$	$V - R_c$	$V - I_c$	J	H	K	L
2 450 000+									
615.29						5.76	4.87	4.02	2.73
640.21						5.80	4.88	4.03	2.74
640.23	10.08	0.30	1.65	1.23	2.39				
811.57						5.74	4.86	4.02	2.73

fluxes from Swings & Allen (1972) are very different: $K = 5.44$, $H - K = 0.33$, $K - L \sim 0.7$ mag. Also, Wackerling (1970) quotes $m_{\text{vis}} = 8.6$ mag and $m_{\text{pg}} = 10.2$ mag¹. This information is not sufficient to conclude whether any brightness changes occurred in the early 1970s, but it indicates that the optical and near-IR fluxes have been stable for the last 30 years.

Analysis of the available photometric and spectroscopic data for the object and its neighborhood allows us to put some constraints on the basic parameters of the underlying star and the distance toward it, an issue that has never been carefully addressed. The observed set of emission lines in the optical region (H I, He I, Fe II; Zickgraf 2003; McGregor et al. 1988; Carlson & Henize 1979, and others) suggests that the star has an early B spectral type, which in combination with the large optical colour-indices implies a high reddening (see Table 3). However, the presence of a significant amount of gas and dust in the object’s CSE makes uncertain whether the entire reddening is interstellar. On the other hand, this is most likely the case, because the observed $U - B$ and $B - V$ colour-indices are in agreement with the interstellar reddening slope for the stars in the object’s direction ($E(U - B)/E(B - V) = 0.74 \pm 0.06$). If we ignore the possible impact of the CSE gas on the object’s SED, then dereddening with the above colour-index ratio gives $E(B - V) = 1.85$ mag and the spectral type $B1 \pm 1$ (also in agreement with the spectral line content). Moreover, strong diffuse interstellar bands (at $\lambda 5780 \text{ \AA}$ and $\lambda 5797 \text{ \AA}$) are present in the spectrum, and their strengths are consistent with the $E(B - V)$ (Herbig 1993).

Adopting the typical galactic total-to-selective interstellar extinction ratio $A_V/E(B - V) = 3.1$ for early-type stars, we get $A_V = 5.8$ mag and the intrinsic visual brightness $V_0 = 4.3$ mag. Such a brightness, in combination with the high reddening, implies a high stellar luminosity. Since a few nearby A-type stars of 9–10 mag have negligible reddenings, there is almost no interstellar extinction in the object’s direction closer than ~ 1 kpc. Even at such a distance, CPD–57° 2874 would be a supergiant ($\log L/L_\odot \sim 5$). An upper limit for the distance (~ 3 kpc) is set by the Humphreys-Davidson luminosity limit ($\log L/L_\odot \sim 6$, Humphreys & Davidson 1979). Thus, the most probable range for the object’s distance is 2.5 ± 0.5 kpc. It is difficult to constrain it better due to the unknown contribution of the CSE gas to the star’s brightness, possible anomalous extinction by the CSE dust, and the absence of high-resolution spectroscopic data that show photospheric lines and allow us to measure their radial velocities. The distance determination using galactic kinematic models and available radial velocities of the emission lines is uncertain, because the line profiles are double-peaked. The interstellar extinction law in the object’s direction indicates a patchy structure of dust in the line of sight and hampers further improvement of the above distance estimate.

Summarizing the above discussion, we adopt the following parameters for CPD–57° 2874: $d = 2.5 \pm 0.5$ kpc, $T_{\text{eff}} = 20\,000 \pm 3\,000$ K, $A_V = 5.8$ mag. They lead to an estimate for the star’s radius of $R_\star = 60 \pm 15 R_\odot$.

¹ m_{pg} means photographic magnitude, which is usually considered a rough analog of the B -band photometry.

4. Results

Figures 2 and 3 show the spectra and visibilities obtained with AMBER and MIDI, respectively. CPD–57° 2874 is resolved in both spectral regions at all projected baselines B_p and position angles PA. As a zero-order size estimate these figures also show the uniform disk angular diameters θ_{UD} obtained from the visibilities at each spectral channel. The size of the region emitting the Bry line is larger than the region emitting the near-IR continuum. Moreover, the mid-IR sizes are much larger than those in the near-IR.

The AMBER observations also reveal a zero closure phase (Fig. 4) at all wavelengths (within the noise level of a few degrees). This is a strong indication that the near-IR emitting regions (continuum and Bry line) have an approximately centrally-symmetric intensity distribution.

Since sgB[e] stars are thought to have non-spherical winds, we expect an elongated shape for their CSE projected onto the sky, unless the star is seen close to pole-on. Hereafter, we show that both AMBER and MIDI observations can indeed be well reproduced by an elliptical Gaussian model for the CSE intensity distribution, corresponding to visibilities of the form:

$$V(u, v) = \exp \left\{ \frac{-\pi^2 (2a)^2}{4 \ln 2} [u^2 + (Dv)^2] \right\} \quad (1)$$

where u and v are the spatial-frequency coordinates, $2a$ is the major-axis FWHM of the intensity distribution (image plane), and D is the ratio between the minor and major axes FWHM ($D = 2b/2a$). Since, in general, $2a$ forms an angle α with the North direction (towards the East), u and v should be replaced in Eq. (1) by $(u \sin \alpha + v \cos \alpha)$ and $(u \cos \alpha - v \sin \alpha)$, respectively. A preliminary analysis of V at each individual wavelength λ showed that D and α can be considered independent on λ within a given spectral band (K or N). On the other hand, the CSE size varies with λ , as seen from the θ_{UD} curves in Figs. 2 and 3.

4.1. Size and geometry in the K band

We interpret the AMBER observations in terms of an elliptical Gaussian model (Eq. (1)) with a chromatic variation of the size. The $\theta_{\text{UD}}(\lambda)$ curves in Fig. 2 suggest a linear increase of the size within this part of the K band. In addition, the AMBER visibilities decrease significantly inside Bry, indicating that the line-forming region is more extended than the region responsible for the underlying continuum. Based on these considerations, we adopted the following expression for the major-axis FWHM:

$$2a(\lambda) = 2a_0 + C_1(\lambda - \lambda_0) + C_2 \exp \left[-4 \ln 2 \left(\frac{\lambda - \lambda_{\text{Bry}}}{\Delta\lambda} \right)^2 \right] \quad (2)$$

where $2a_0$ is the major-axis FWHM at a chosen reference wavelength $\lambda_0 (= 2.2 \mu\text{m})$, and C_1 is the slope of $2a(\lambda)$. The size-increase within Bry is modeled by a Gaussian with an amplitude C_2 and FWHM $\Delta\lambda$, centered at $\lambda_{\text{Bry}} = 2.165 \mu\text{m}$. Figure 2 shows a rather good fit of this model to the observed visibilities in both the continuum and inside Bry. The parameters derived from the fit are listed in Table 4.

3.3. The supergiant B[e] star CPD-57° 2874

84

A. Domiciano de Souza et al.: AMBER/VLTI and MIDI/VLTI observations of the sgB[e] CPD-57° 2874

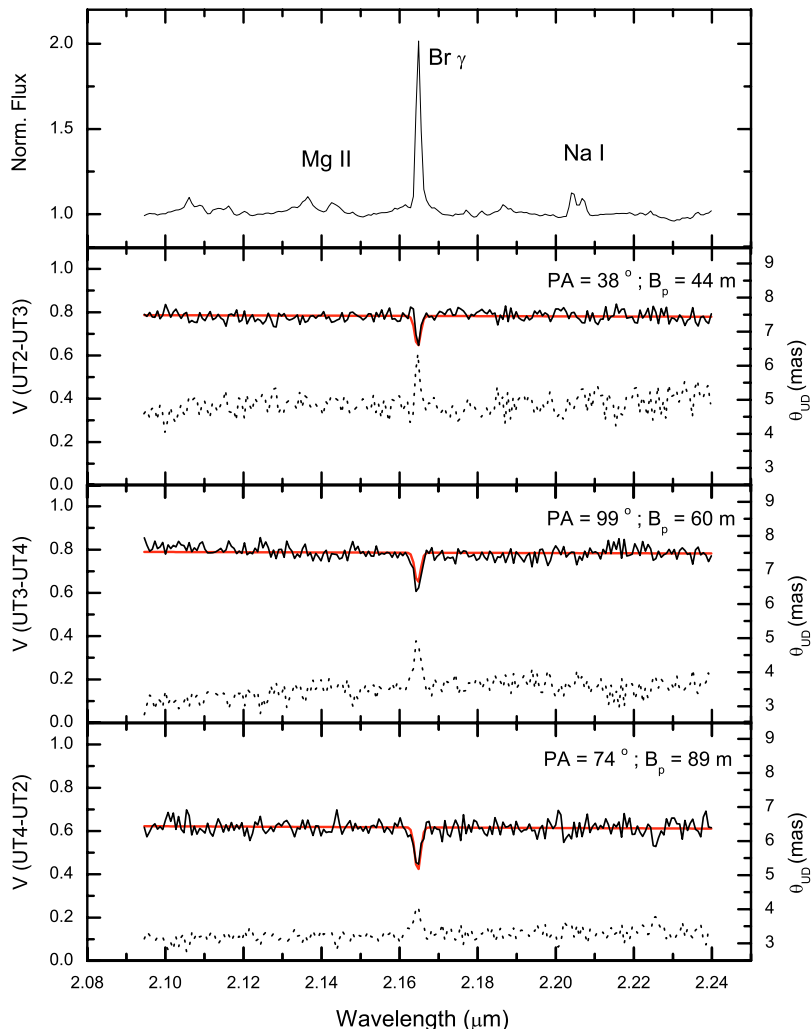


Fig. 2. AMBER/VLTI observations of CPD-57° 2874 obtained around Br γ with spectral resolution $R = 1500$. The normalized flux is shown in the top panel and the visibilities V for each baseline (30% best frames) are given in the other panels (the corresponding projected baselines B_p and position angles PA are indicated). The errors in V are $\approx \pm 5\%$. The dotted lines are the uniform disk angular diameters θ_{UD} (to be read from the scales on the right axis), computed from V at each λ as a zero-order size estimate. The visibilities obtained from the elliptical Gaussian model fit the observations quite well (smooth solid lines; Eqs. (1) and (2), and Table 4). In contrast to the Br γ line, the Mg II and Na I lines do not show any clear signature in the visibilities.

Table 4. Model parameters and χ^2_{red} (reduced chi-squared) derived from the fit of an elliptical Gaussian (Eqs. (1) and (2)) to the AMBER/VLTI and MIDI/VLTI visibilities. Angular sizes (in mas) correspond to FWHM diameters. The errors of the fit parameters include the calibration errors of the instrumental transfer function ($\approx 5\%$), estimated from all calibrator stars observed.

Instrument	λ_0 (μm)	Major axis $2a_0$ (mas)	C_1 (mas/ μm)	Position angle α	$D = 2b/2a$	Minor axis $2b_0$ (mas)	Br γ : C_2 (mas) ^a	Br γ : $\Delta\lambda$ ($10^{-3} \mu\text{m}$)	χ^2_{red}
AMBER	2.2	3.4 ± 0.2	1.99 ± 0.24	$173^\circ \pm 9^\circ$	0.53 ± 0.03	1.8 ± 0.1	1.2 ± 0.1	1.8 ± 0.2	0.7
MIDI (<10 μm)	8.0	10.1 ± 0.7	2.58 ± 0.41	$145^\circ \pm 6^\circ$	0.76 ± 0.11	7.7 ± 1.0			0.1
MIDI (>10 μm)	12.0	15.3 ± 0.7	0.45 ± 0.22	$143^\circ \pm 6^\circ$	0.80 ± 0.10	12.2 ± 1.1			0.1

^a Corresponding to a FWHM major axis $2a = 4.5 \pm 0.3$ mas and minor axis $2b = D * 2a = 2.4 \pm 0.1$ mas at the center of the Br γ line ($\lambda_{Br\gamma} = 2.165 \mu\text{m}$).

4.2. Size and geometry in the N band

Similar to the analysis of the AMBER visibilities, we interpret the MIDI observations of CPD-57° 2874 in terms of an elliptical Gaussian model (Eq. (1)) with a size varying linearly with λ as given in Eq. (2) (for the analysis of the MIDI data the parameter C_2 is set to zero). Additionally, since the θ_{UD} curves show a stronger λ -dependence between 7.9 and 9.8 μm compared to

the region between 10.2 and 13.5 μm (see Fig. 3), we performed an independent fit for each of these two spectral regions. The adopted elliptical Gaussian model also provides a good fit to the MIDI visibilities as shown in Fig. 3. The parameters corresponding to the fit in the two spectral regions within the N band are listed in Table 4.

To illustrate our results the model parameters given in Table 4 can be visualized in Fig. 5.

3. High spectro-spatial resolution observations of fast rotators in the H-R diagram

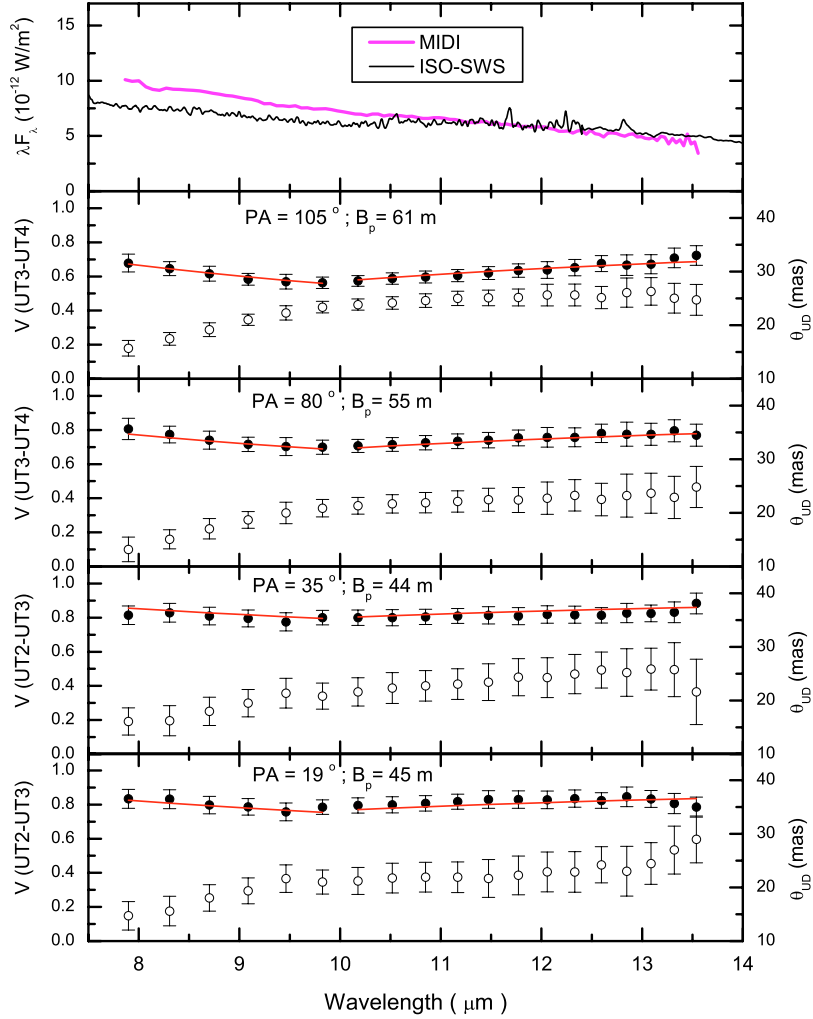


Fig. 3. MIDI/VLTI observations of CPD-57° 2874 obtained in the mid-IR with spectral resolution $R = 30$. This figure is organized as Fig. 2, but here V and θ_{UD} are shown as filled and open circles, respectively. The MIDI and ISO-SWS (Sloan et al. 2003) spectra (*top panel*) do not show any clear evidence of a silicate feature around $10\ \mu\text{m}$. The MIDI visibilities are well fitted with an elliptical Gaussian model (solid lines; Eqs. (1) and (2), and Table 4).

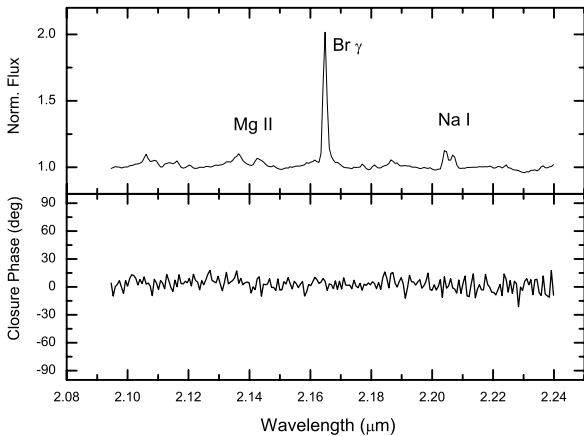


Fig. 4. AMBER/VLTI closure phase for CPD-57° 2874 obtained around Br γ with spectral resolution $R = 1500$. Within the noise level ($\approx \pm 10^\circ$) the closure phase is zero both in the continuum and in the Br γ line. This strongly suggests that the CSE has an approximately centrally-symmetric projected intensity distribution in the near-IR.

5. Discussion and conclusions

Our analysis of the VLTI spectro-interferometric data presented in Sect. 4 supports the hypothesis of a non-spherical CSE for sgB[e] stars.

In particular, the MIDI observations suggest that the hot-dust emission originates in an elongated structure (probably in an equatorial disk), which is in agreement with previous polarization measurements from Yudin & Evans (1998). After correction for the interstellar polarization, Yudin (private communication) estimated an intrinsic polarization position angle $\approx 45^\circ - 55^\circ$. Interestingly, within the error bars this angle is perpendicular to the major-axis PA we derived from the MIDI data ($\alpha \approx 144^\circ$; see Table 4), as is expected from a disk-like dusty CSE. Under the disk hypothesis, the measured mid-IR flattening ($D \approx 0.76 - 0.80$; see Table 4) allows us to estimate an intermediate viewing angle for the non-spherical CSE ($i \sim 30^\circ - 60^\circ$).

The contemporaneous recording of the AMBER and MIDI data enables us to compare the CSE structure in the near- and mid-IR. As shown in Table 4, the size, flattening and orientation of the elliptical Gaussian model significantly changes from the

3.3. The supergiant B[e] star CPD-57° 2874

86

A. Domiciano de Souza et al.: AMBER/VLTI and MIDI/VLTI observations of the sgB[e] CPD-57° 2874

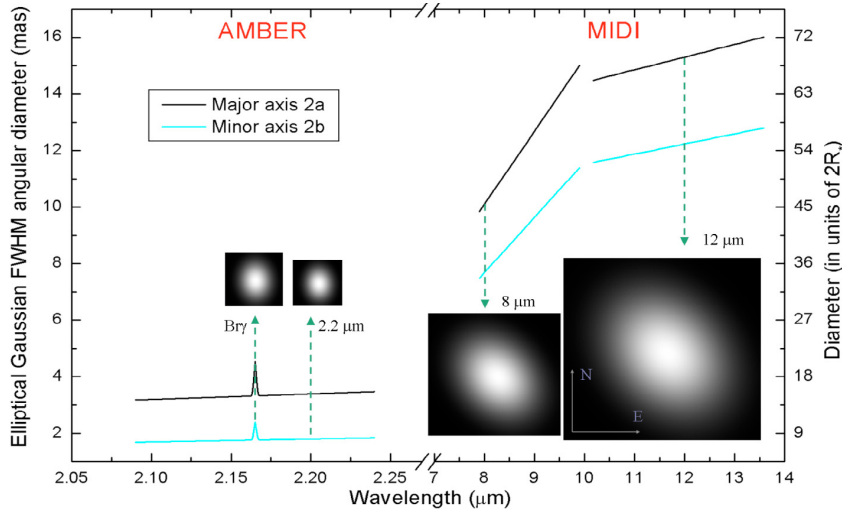


Fig. 5. Size and orientation of the CSE derived from the fit of an elliptical Gaussian model (Eqs. (1) and (2)) to the AMBER/VLTI and MIDI/VLTI visibilities (the corresponding fit parameters are listed in Table 4). The scale in the right is given in stellar diameters ($2R_*$), where the radius R_* is estimated to be $60 \pm 15 R_\odot$ (Sect. 3).

K to the N band. For example, the region emitting the mid-IR flux ($2a \geq 10 \text{ mas} = 25 \text{ AU}$ at $\lambda \geq 8 \mu\text{m}$)² is more than 2.5 times larger than the region emitting the near-IR continuum flux ($2a \approx 3.4 \text{ mas} = 8.5 \text{ AU}$ at $\lambda \approx 2.2 \mu\text{m}$).

If we correct the influence of the continuum on the visibility measured in Bry (Malbet et al. 2007), we estimate the size (minor \times major axes) of the region responsible for the pure Bry emission to be $\approx 2.8 \times 5.2 \text{ mas}$ (or $\approx 7.0 \times 13.0 \text{ AU}$). This size is $\approx 55\%$ larger than that of the underlying near-IR continuum, but more than 2 times smaller than the mid-IR emitting region ($\lambda \geq 8 \mu\text{m}$). Near-IR diameters of $\sim 10 \text{ AU}$ correspond to $\sim 36 R_*$ (assuming $R_* = 60 R_\odot$; see Sect. 3). This measurements are compatible with the theoretical CSE diameters computed by Stee & Bittar (2001) for a classical Be star, although our data show a larger difference between the Bry and continuum sizes.

The differences in flattening and position angle of the elliptical models fitted to the AMBER and MIDI data are in agreement with the two-component CSE paradigm suggested for sgB[e] stars (Zickgraf et al. 1985). The mid-IR flux is probably solely due to dust emission from an equatorial disk. In contrast, the near-IR continuum flux distribution probably results from a complex interplay among the radiation from the central star, the tail of hot-dust emission ($T_{\text{dust}} \approx 1500 \text{ K}$), and the free-free and free-bound emission from the fast polar wind and the disk-wind interaction. The Bry emission does not necessarily follow the same geometry.

A detailed investigation of the CSE geometry in the near-IR (continuum and Bry) requires additional interferometric observations covering a larger range of baselines and position angles. In addition, we believe that further MIDI observations at baselines longer than $\approx 80 \text{ m}$ should be performed to obtain higher spatial resolution of the innermost parts of the dusty CSE. This would allow one to investigate more deeply how close to the hot central star ($T_{\text{eff}} \approx 20000 \text{ K}$) the dust is formed.

Moreover, the combination of interferometric resolution, multi-spectral wavelength coverage and relatively high spectral resolution now available from the VLTI requires development of interferometry-oriented and physically-consistent models for sgB[e] stars. We hope that the present work will motivate the

development of such models, as well as open the door for new spectro-interferometric observations of these complex and intriguing objects.

Acknowledgements. A.D.S. acknowledges the Max-Planck-Institut für Radioastronomie for a postdoctoral fellowship. We are indebted to Dr. R. V. Yudin for his calculations on the intrinsic polarization vector. The preparation and interpretation of AMBER observations benefit from the tools developed by the Jean-Marie Mariotti Center for optical interferometry (JMMC) and from the databases of the Centre de Données Stellaires (CDS) and of the Smithsonian/NASA Astrophysics Data System (ADS). The data reduction software `amdlib` and the user-friendly interface `ammyorick` used in this work is available on the AMBER site <http://amber.obs.ujfgrenoble.fr>.

References

- Carlson, E. D., & Henize, K. G. 1979, *Vistas Astron.*, 23, 213
 Carter, B. C. 1990, *MNRAS*, 242, 1
 Cutri, R. M., Scruskie, M. F., Van Dyk, S., et al. 2003, The 2MASS All-Sky Catalog of Point Sources, University of Massachusetts and Infrared Processing and Analysis Center, IPAC/California Institute of Technology
 Drilling, J. S. 1991, *ApJS*, 76, 1033
 Herbig, G. H. 1993, *ApJ*, 407, 142
 Humphreys, R. M., & Davidson, K. 1979, *ApJ*, 232, 409
 Jaffe, W. 2004, *Proc. SPIE*, 5491, 715
 Lamers, H. J. G. L. M., Zickgraf, F., de Winter, D., Houziaux, L., & Zorec, J. 1998, *A&A*, 340, 117
 Leinert, Ch., van Boekel, R., Waters, L. B. F. M., et al. 2004, *A&A*, 423, 537
 Magalhães, A. M. 1992, *ApJ*, 398, 286
 Malbet, F., Benisty, M., de Wit, W.-J., et al. 2007, *A&A*, 464, 43
 McGregor, P. J., Hyland, A. R., & Hillier, D. J. 1988, *ApJ*, 324, 1071
 Menzies, J. W., Marang, F., Laing, J. D., Coulson, I. M., & Engelbrecht, C. A. 1991, *MNRAS*, 248, 642
 Millour, F., Tatulli, E., Chelli, A., et al. 2004, *Proc. SPIE*, 5491, 1222
 Petrov, R. G., Malbet, F., Weigelt, G., et al. 2007, *A&A*, 464, 1
 Richichi, A., Percheron, I., & Khristoforova, M. 2005, *A&A*, 431, 773
 Sloan, G. C., Kraemer, K. E., Price, S. D., & Shipman, R. F. 2003, *ApJS*, 147, 379
 Stee, P., & Bittar, J. 2001, *A&A*, 367, 532
 Swings, J.-P., & Allen, D. A. 1972, *PASP*, 84, 523
 Tatulli E., Millour, F., Chelli, A., et al. 2007, *A&A*, 464, 29
 Wackerling, L. R. 1970, *Mem. RAS*, 73, 153
 Yudin, R. V., & Evans, A. 1998, *A&AS*, 131, 401
 Zickgraf, F.-J. 2003, *A&A*, 408, 257
 Zickgraf, F.-J., Wolf, B., Stahl, O., Leitherer, C., & Klare, G. 1985, *A&A*, 143, 421

² Adopting a distance $d = 2.5 \text{ kpc}$; see Sect. 3.

Fast ray-tracing algorithm for circumstellar structures (FRACS)

II. Disc parameters of the B[e] supergiant CPD-57° 2874 from VLT/MIDI data^{*,**}A. Domiciano de Souza¹, P. Bendjoya¹, G. Niccolini¹, O. Chesneau¹, M. Borges Fernandes^{1,2},
A. C. Carciofi³, A. Spang¹, P. Stee¹, and T. Driebe^{4,5}¹ Laboratoire H. Fizeau, UMR CNRS 6525, Université de Nice-Sophia Antipolis (UNS), Observatoire de la Côte d'Azur (OCA), Campus Valrose, 06108 Nice Cedex 2, France

e-mail: Armando.Domiciano@obs-azur.fr

² Observatório Nacional, Rua General José Cristino, 77, 20921-400 São Cristóvão, Rio de Janeiro, Brazil³ Instituto de Astronomia, Geofísica e Ciências Atmosféricas, Universidade de São Paulo (USP), Rua do Matão 1226, Cidade Universitária, São Paulo, SP - 05508-900, Brazil⁴ Max-Planck-Institut für Radioastronomie, Auf dem Hügel 69, 53121 Bonn, Germany⁵ Deutsches Zentrum für Luft- und Raumfahrt, Raumfahrt-Agentur, Königswinterer Strasse 522-524, 53227 Bonn, Germany

Received 10 June 2010 / Accepted 15 September 2010

ABSTRACT

Context. B[e] supergiants are luminous, massive post-main sequence stars exhibiting non-spherical winds, forbidden lines, and hot dust in a disc-like structure. The physical properties of their rich and complex circumstellar environment (CSE) are not well understood, partly because these CSE cannot be easily resolved at the large distances found for B[e] supergiants (typically ≥ 1 kpc).

Aims. From mid-IR spectro-interferometric observations obtained with VLT/MIDI we seek to resolve and study the CSE of the Galactic B[e] supergiant CPD-57° 2874.

Methods. For a physical interpretation of the observables (visibilities and spectrum) we use our ray-tracing radiative transfer code (FRACS), which is optimised for thermal spectro-interferometric observations.

Results. Thanks to the short computing time required by FRACS (< 10 s per monochromatic model), best-fit parameters and uncertainties for several physical quantities of CPD-57° 2874 were obtained, such as inner dust radius, relative flux contribution of the central source and of the dusty CSE, dust temperature profile, and disc inclination.

Conclusions. The analysis of VLT/MIDI data with FRACS allowed one of the first direct determinations of physical parameters of the dusty CSE of a B[e] supergiant based on interferometric data and using a full model-fitting approach. In a larger context, the study of B[e] supergiants is important for a deeper understanding of the complex structure and evolution of hot, massive stars.

Key words. stars: individual: CPD-57° 2874 – methods: observational – methods: numerical – techniques: high angular resolution – techniques: interferometric – stars: emission-line, Be

1. Introduction

The B[e] stars form a heterogeneous group composed of objects at different evolutionary stages, but with many similar observational signatures characterising the so-called “B[e] phenomenon”: simultaneous presence of hydrogen emission lines, low-excitation forbidden and permitted metallic lines in emission, and a significant infrared (IR) excess mainly caused by hot circumstellar dust. Another common property of B[e] stars is the presence of a non-spherical circumstellar environment (hereafter CSE, e.g. Zickgraf 2003).

Lamers et al. (1998) defined five B[e] sub-classes, one of which contains unclassified stars. Miroshnichenko (2007) proposed an additional B[e] sub-class (the FS CMa stars) to explain at least part of the unclassified B[e]-type stars as binaries at a

phase of ongoing or recently ended rapid mass transfer and dust formation.

One of the B[e] sub-classes is composed of luminous ($\log(L_*/L_\odot) \geq 4$) post-main sequence objects: the B[e] supergiant stars (hereafter sgB[e]). Previous spectroscopic and polarimetric observations of sgB[e] (e.g. Zickgraf et al. 1985; Magalhães 1992) show that the wind of these massive and luminous stars is composed of two distinct components: (1) a wind of low density and high velocity and (2) a wind of high density and low velocity. Zickgraf et al. (1985) proposed a picture where the sgB[e] winds consist of a hot and fast radiation-driven polar wind and a slow, much cooler and denser (by a factor of 10^2 or 10^3) equatorial wind. This disc-like structure provides a natural explanation for the existence of dust around those objects, because the presence of dust requires regions of sufficiently high density and low kinetic temperatures. One possible explanation for this two-component CSE is that rapid rotation of the central star leads to the formation of an equatorial disc because of the combination of rotation-induced bi-stability and rotation-induced wind compression (Lamers & Pauldrach 1991; Bjorkman 1998; Pelupessy et al. 2000). Other mechanisms, such as binarity, are evoked to explain the disc-like CSE, but in any case, rapid rotation seems to play a key

* Based on VLT/MIDI observations collected at the European Southern Observatory (ESO), Paranal, Chile under ESO Programmes 074.D-0101 and 078.D-0213. Also based on observations at the ESO 2.2-m telescope, La Silla, Chile, under agreement with the Observatório Nacional-MCT (Brazil).

** Figure 5 is only available in electronic form at <http://www.aanda.org>

3.3. The supergiant B[e] star CPD-57° 2874

A&A 525, A22 (2011)

role in the origin of these discs (e.g. Meynet & Maeder 2006). Owing to their physical characteristics (fast rotation, disc-like CSE, high luminosity, evolutionary status), it has also been suggested (Vink et al. 2009) that sgB[e] might share evolutionary links with rapidly rotating O-stars and long-duration gamma-ray bursts (GRBs).

Because of the large distances of sgB[e] (≥ 1 kpc for the closest ones), the geometry and physical structure (e.g. density and temperature distribution) of their CSE could be only quite recently directly probed, thanks to modern high angular resolution (HAR) techniques. For example, Domiciano de Souza et al. (2008) used ESO's VLT/VISIR instrument to directly measure the typical size of the dusty CSE of the sgB[e] MWC 300 from diffraction-limited mid-IR images. Among HAR techniques, optical/IR long baseline interferometry (OLBI) provides the highest resolving power, allowing the study of sgB[e] CSEs at angular resolutions ~ 1 – 10 milliarcsec (mas). For example, Millour et al. (2009) combined adaptive optics (VLT/NACO) and OLBI (VLT/AMBER and VLT/MIDI) to detect a companion around the sgB[e] HD87643 and to perform an extensive study of the dusty CSE of the binary system.

In the examples above as well as in most works based on HAR data of sgB[e], two different strategies are commonly adopted to interpret the observations: (1) geometrical analytical modelling and (2) radiative transfer modelling (e.g. using the Monte Carlo approach). The geometrical analytical models have the advantage to be very fast to calculate, allowing a full model-fitting (for example a χ^2 minimisation) and error estimate of the model parameters (mostly geometrical parameters of the CSE). However, these simple models do not give access to physical parameters of the targets such as temperature and density distributions, optical depths, etc. On the other hand, most radiative transfer models present a consistent description of the physical conditions of the CSE. However, because these models are quite complex, they demand a lot of computing time, which prevents one from exploring a large domain of the parameter space and also from obtaining a good estimate of the uncertainties on the fitted parameters. In this work we adopt a third approach for the data modelling, which tries to keep the advantages of the other approaches, without the drawbacks. To this aim we use our *fast ray-tracing algorithm for circumstellar structures* (FRACS), which is based on a parametrised CSE combined to a simplified radiative transfer (no scattering). A complete description of this algorithm is given in Niccolini et al. (2010, hereafter Paper I).

In the present paper we apply FRACS to study the CSE of the Galactic sgB[e] CPD-57° 2874 (also named Hen 3-394, WRAY 15-535) based on mid-IR spectro-interferometric observations performed with ESO's VLT/MIDI beam-combiner instrument. Previous near- and mid-IR interferometric observations of CPD-57° 2874 directly revealed an elongated CSE that is compatible with a disc-like structure formed by gas and dust (Domiciano de Souza et al. 2007, hereafter DS07). However, because only a limited number (four) of baselines was available and since the authors adopted simple analytical models, only geometrical parameters could be derived from this first analysis of CPD-57° 2874. As shown below, the use of FRACS allowed us to confirm the previous results and, most importantly, to derive physical parameters for this Galactic sgB[e].

In Sect. 2 we give the log of the VLT/MIDI observations and describe the data reduction procedure. In Sect. 3 we provide a new distance estimate of CPD-57° 2874 obtained from spectroscopic observations with FEROS. A short reminder of the ray-tracing code FRACS is presented in Sect. 4, followed by the results obtained from a model-fitting analysis of the VLT/MIDI

Table 1. Summary of VLT/MIDI observations of CPD-57° 2874: data set index, date, Coordinated Universal Time (UTC) of observation, baseline configuration, projected baseline length and position angle.

#	Date	t_{obs} (UTC)	UT config.	B_{proj} (m)	PA (°)
1	2004-11-01	08:51:55	UT2-UT4	85.1	37.8
2 ^(a)	2004-12-29	05:52:12	UT2-UT3	45.2	18.6
3 ^(a)	2004-12-29	07:26:06	UT2-UT3	43.9	35.1
4 ^(a)	2004-12-31	06:04:03	UT3-UT4	54.8	79.6
5 ^(a)	2004-12-31	08:02:48	UT3-UT4	60.9	104.8
6	2006-11-09	07:15:36	UT1-UT4	129.7	8.6
7	2006-12-13	08:35:55	UT1-UT3	93.8	28.6
8	2006-12-31	08:13:05	UT1-UT4	125.8	63.5
9	2006-12-31	08:59:06	UT1-UT4	121.8	72.5
10	2007-01-05	08:35:09	UT1-UT3	88.1	42.8

Notes. ^(a) Data previously used by DS07.

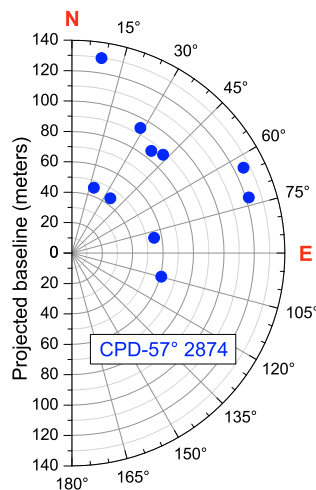


Fig. 1. uv-Plane coverage: projected baselines (length and position angle) for the VLT/MIDI observations of CPD-57° 2874 (further details are given in Table 1).

observations (Sect. 5). A discussion of the results and the conclusions of this work are presented in Sects. 6 and 7, respectively.

2. VLT/MIDI observations

The interferometric observations of CPD-57° 2874 were performed with MIDI, the mid-infrared 2-telescope beam-combiner instrument of ESO's VLT (Leinert et al. 2004). All four 8.2 m unit telescopes (UTs) were used. The N-band spectrum as well as spectrally dispersed fringes have been recorded between $\lambda \approx 7.5 \mu\text{m}$ and $\lambda \approx 13.5 \mu\text{m}$ with a spectral resolution of $R \approx 30$ using a prism. In total, $n_B = 10$ data sets have been obtained with projected baselines (B_{proj}) ranging from ≈ 40 m to ≈ 130 m, and baseline position angles (PA) between $\approx 8^\circ$ and $\approx 105^\circ$ (from North to East). A summary of the VLT/MIDI observations of CPD-57° 2874 is given in Table 1, and the corresponding uv-plane coverage is shown in Fig. 1.

The MIDI data were reduced with the MIA+EWS data reduction package, which includes two different sub-packages: the MIA package developed at the Max-Planck-Institut für Astronomie, and the EWS package developed at the Leiden Observatory¹.

¹ The MIA+EWS software package is available at <http://www.mpia-hd.mpg.de/MIDISOFT/> and <http://www.strw.leidenuniv.nl/~nevec/MIDI/index.html>

3. High spectro-spatial resolution observations of fast rotators in the H-R diagram

A. Domiciano de Souza et al.: FRACS modelling - disc parameters of CPD-57° 2874 from VLTI/MIDI.II.

Table 2. Observation log and angular diameters of calibrators (values from DS07) used to derive the calibrated N-band visibilities of CPD-57° 2874.

Date	t_{obs} (UTC)	UT config.	Calibrator	\mathcal{D}_{UD} (mas)
2004-11-01	09:28:16	UT2-UT4	HD 94510	2.16 ± 0.11
2004-12-29	04:12:26	UT2-UT3	HD 37160	2.08 ± 0.20
2004-12-29	05:29:32	UT2-UT3	HD 37160	2.08 ± 0.20
2004-12-29	06:13:08	UT2-UT3	HD 50778	3.95 ± 0.22
2004-12-29	07:47:21	UT2-UT3	HD 94510	2.16 ± 0.11
2004-12-31	02:15:59	UT3-UT4	HD 50778	3.95 ± 0.22
2004-12-31	03:04:33	UT3-UT4	HD 50778	3.95 ± 0.22
2004-12-31	06:31:19	UT3-UT4	HD 94510	2.16 ± 0.11
2004-12-31	07:19:17	UT3-UT4	HD 107446	4.54 ± 0.23
2004-12-31	07:41:22	UT3-UT4	HD 94510	2.16 ± 0.11
2006-11-09	07:45:21	UT1-UT4	HD 94510	2.16 ± 0.11
2006-12-13	02:04:34	UT1-UT3	HD 23249	2.33 ± 0.01
2006-12-13	08:10:27	UT1-UT3	HD 94510	2.16 ± 0.11
2006-12-13	08:54:41	UT1-UT3	HD 94510	2.16 ± 0.11
2006-12-31	06:58:10	UT1-UT4	HD 94510	2.16 ± 0.11
2006-12-31	07:44:55	UT1-UT4	HD 94510	2.16 ± 0.11
2006-12-31	08:37:22	UT1-UT4	HD 94510	2.16 ± 0.11
2007-01-05	08:08:04	UT1-UT3	HD 94510	2.16 ± 0.11

While MIA is based on the power spectrum analysis, which measures the total power of observed fringes (Leinert et al. 2004), EWS coherently adds the fringes after correction for optical path differences (instrumental as well as atmospheric delays) in each scan (Jaffe et al. 2004). The data reduction results obtained with the MIA and EWS packages agree well within the uncertainties.

The instrumental transfer function at each spectral channel was obtained from the observations of calibrator stars with known uniform-disc diameters (\mathcal{D}_{UD}). The calibrators used in the data reduction and the adopted angular diameters and uncertainties are listed in Table 2. The calibrated visibilities were calculated from the ratio of the targets' raw visibilities and the average transfer function derived from the calibrator measurements of the corresponding night (Fig. 3). The error of the calibrated MIDI visibilities is of the order of $\approx 5\text{--}10\%$ and includes the raw visibility error as well as the error of the transfer function. The uncertainties on the calibrator angular diameter are negligible compared to the standard deviation of the transfer function. Usually, $\approx 3\text{--}5$ calibrator measurements per night were available (Table 2). In the few cases where only one suitable calibrator observation was available we assumed a typical transfer function error of 5% to estimate the errors on the final calibrated visibilities.

VLTI/MIDI also provides spectral fluxes of CPD-57° 2874 in the N-band. On average, all fluxes are compatible within $\approx 10\%$ with those previously presented by DS07 (MIDI and ISO-SWS spectra). We here considered the VLTI/MIDI spectrum used by DS07 with an uncertainty of 20% (Fig. 4). This larger uncertainty ensures a complete agreement between the observed MIDI and ISO fluxes at all wavelengths. We note that the mid-IR spectrum of CPD-57° 2874 does not show any clear evidence of an important silicate feature around $10\ \mu\text{m}$.

3. FEROS observations and distance estimate

In addition to our mid-IR interferometric observations, we obtained high-resolution optical spectra of CPD-57° 2874. The spectra were recorded with the high-resolution Fiber-fed Extended Range Optical Spectrograph (FEROS), attached to the

Table 3. Equivalent widths (EW) of the Na absorption lines ($\lambda\lambda$ 5890 Å, 5896 Å), obtained from our FEROS data.

Line	5890 Å		5896 Å	
	abs. comp. 1	abs. comp. 2	abs. comp. 1	abs. comp. 2
W(Å)	0.11	0.80	0.05	0.70

Notes. The relative uncertainty of these measurements is about 20%.

2.2-m telescope at ESO in La Silla (Chile). FEROS is a bench-mounted Echelle spectrograph with fibers, covering a sky area of $\approx 2'' \times 2''$ and a wavelength range from 3600 Å to 9200 Å. Its spectral resolution is $R \approx 55\,000$ (around 6000 Å). We have adopted its complete automatic online reduction, which includes the heliocentric correction. The FEROS spectra were obtained on 2008 December 21. We recorded two exposures of 1000 s with S/N of ~ 60 in the 5500 Å region.

These observations were used to estimate the distance of CPD-57° 2874. A previous distance estimate of $d = 2.5$ kpc has been proposed by McGregor et al. (1988), assuming that this star belongs to the Carina OB association.

From our FEROS high-resolution spectra it is possible to estimate the distance of CPD-57° 2874, based on the statistical relation cited by Allen (1973). This relation uses the equivalent widths of interstellar Na lines. In our data, each Na line is composed of two absorption components. However, owing to the lack of data from different epochs, it is impossible to see any temporal changes, which would allow us to derive a possible circumstellar contamination. We have therefore assumed that both Na components are of interstellar origin. The measured equivalent widths are given in Table 3. Our estimated distance for CPD-57° 2874 is $d = 1.7$ kpc with an uncertainty of 0.7 kpc. This large error is firstly due to a possible contamination from the circumstellar emission component and the saturation of the absorption one, and secondly to a systematic error caused by the statistical relation used. Within the error bars, our distance estimate is roughly compatible with the result of McGregor et al. (1988). We have considered both distances in our analysis: 1.7 and 2.5 kpc.

4. Description of the model FRACS

Here we present a short description of our numerical model FRACS and the parametrisation adopted to describe a sgB[e]. A full description of FRACS is given in Paper I.

FRACS is based on the ray-tracing technique using quadtree meshes for the grid and the full symmetries of the problem to hand to significantly decrease the computing time necessary to obtain monochromatic images (calculated with 300×300 pixels) within seconds. Complex visibilities and fluxes can be directly derived from these monochromatic images. FRACS neglects scattering, an approximation well suited to interpret spectro-interferometric observations in the thermal IR. Indeed, compared to absorption of light from dust, scattering can be neglected in the IR and beyond (Paper I; Lamers & Cassinelli 1999).

To analyse the VLTI/MIDI data of CPD-57° 2874 we adopted the same parametrised description of a sgB[e] (central star and dusty CSE) as given in Paper I. Below we summarise the main equations of this description in axis-symmetric spherical coordinates, and define the free parameters used in the model-fitting.

3.3. The supergiant B[e] star CPD-57° 2874

A&A 525, A22 (2011)

We assume the specific intensity from the central regions of the star to be a power-law with spectral index α and level $I_{\lambda_0}^s$ at a fiducial wavelength $\lambda_0 = 10 \mu\text{m}$:

$$I_{\lambda}^s = I_{\lambda_0}^s \left(\frac{\lambda_0}{\lambda}\right)^{\alpha}. \quad (1)$$

This emission from the central region includes a contribution from the stellar photosphere and from the continuum radiation (free-free and free-bound) of the circumstellar ionised gas. The spectral index α is sensitive to the nature of the central source. Panagia & Felli (1975) and Felli & Panagia (1981) give theoretical values for the spectral index for spherical envelopes: $\alpha \simeq 4$ for a blackbody and $\alpha \simeq 2.6$ for a fully ionised gas (free-free emission) with an electron density proportional to r^{-2} . Their estimates are valid within the Rayleigh-Jeans domain of the spectrum, which fits to our case when we consider the hot central parts of a sgB[e] in the mid-IR.

A radius $R_s = 54 R_{\odot}$ was adopted for the central region. This value is used simply as a scaling factor and to convert $I_{\lambda_0}^s$ to the observed $10 \mu\text{m}$ flux from the central region:

$$F_{\lambda_0}^s = \pi \left(\frac{R_s}{d}\right)^2 I_{\lambda_0}^s. \quad (2)$$

We note that at distances of a few kpc the central regions of a sgB[e] are not resolved by VLT/MIDI and can thus be considered as point sources.

For the gas number density we adopt the bi-modal distribution used by Carciofi et al. (2010) to study another B[e] star. Similar density distribution descriptions were adopted for Be stars (e.g. Stee et al. 1995). The adopted distribution is motivated by the two-wind scenario proposed by Zickgraf et al. (1985) and assumes a fast polar wind, a slow equatorial outflow, and a latitude-dependent mass loss rate. The number density of dust grains is therefore given by

$$n(r, \theta) = n_{\text{in}} \left(\frac{R_{\text{in}}}{r}\right)^2 \left(\frac{1 + A_2}{1 + A_1}\right) \frac{1 + A_1 (\sin \theta)^m}{1 + A_2 (\sin \theta)^m}, \quad (3)$$

where (r, θ) are the radial coordinate and co-latitude, and n_{in} is the dust grain number density at $\theta = 90^\circ$ and at $r = R_{\text{in}}$, which is the inner dust radius where dust starts to survive. Dust is confined between R_{in} and the outer dust radius R_{out} . The value of R_{out} cannot be determined from the VLT/MIDI data and has been fixed to a high value: 750 AU (the exact value does not affect our results).

The parameter A_1 controls the ratio between the equatorial and polar mass loss rates. More precisely, $(1 + A_1)$ specifies the ratio between the mass loss rate per unit solid angle in the equator and the pole. In the bi-modal scenario, the poles are assumed to be much less dense than the equator, therefore A_1 must have a large value ($\gtrsim 10$). Our models indicate that for a wide range of values this parameter does not have a strong influence on the results because it can always be compensated by n_{in} (see also discussion in Paper I). Therefore, we have arbitrarily fixed $(1 + A_1)$ to 50.

The parameter A_2 indicates how much faster the polar wind is compared to the slow equatorial wind. $(1 + A_2)$ is the equatorial to polar terminal velocity, i.e., $v_{\infty}(90^\circ)/v_{\infty}(0^\circ)$. This parameter is also quite uncertain and in principle can assume values ranging from ~ 1 to ~ 100 . We kept A_2 as a free parameter, although it is not well constrained from the observations as shown in the next sections.

Finally, parameter m controls how fast the mass loss (and consequently the density) drops from the equator to the pole.

Defining the disc opening angle $\Delta\theta_d$ as the latitudinal range within which the mass loss rate is higher than half its equatorial value, we have

$$\Delta\theta_d = 2 \arccos\left(\frac{A_1 - 1}{2A_1}\right)^{\frac{1}{m}} \simeq 2 \arccos\left(\frac{1}{2}\right)^{\frac{1}{m}}. \quad (4)$$

High m values correspond to thinner regions of high density around the equator. These dense, slowly flowing disc-like regions around the equatorial plane of sgB[e] stars provide favourable conditions for dust to form and survive. Different approaches exist to define regions of dust formation (e.g. Carciofi et al. 2010). Here we adopt the relatively simple assumption where dust is allowed to exist only within the disc opening angle, i.e., at co-latitudes between $90^\circ - 0.5\Delta\theta_d$ and $90^\circ + 0.5\Delta\theta_d$.

The dust grain opacity was calculated in the Mie theory (Mie 1908) for silicate dust and for a dust size distribution following the commonly adopted MRN (Mathis et al. 1977) power-law $\propto a^{-3.5}$, where a is the dust grain radius. The Mie absorption cross sections are computed from the optical indices of astronomical silicate (Draine & Lee 1984; see also Paper I). One possibility to reproduce the absence of a silicate feature in the N-band spectrum of CPD-57° 2874 is to have relatively large grain sizes. We thus used grain radii ranging from $a = 0.5$ to $50 \mu\text{m}$, which can relatively well reproduce the observed spectrum (Fig. 4). We checked that ignoring scattering remains a valid assumption for this dust distribution with large grains. By neglecting the dust albedo the visibilities and fluxes are affected by only a few percent ($\lesssim 3.5\%$) within the N-band (further details in Paper I).

The temperature structure of the dusty CSE is given by

$$T(r) = T_{\text{in}} \left(\frac{R_{\text{in}}}{r}\right)^{\gamma}, \quad (5)$$

where T_{in} is the dust temperature at the disc inner radius R_{in} , i.e., the dust sublimation temperature. To be consistent with our choice of dust composition we require that $T_{\text{in}} \leq 1500$ K. The coefficient γ is expected to assume values $\lesssim 1$.

Finally, because OLBI is sensitive to the projection of the object's intensity distribution onto the sky, there are two angles related to this projection:

- the inclination of the disc plane towards the observer i (0° for pole-on view and 90° for equator-on view);
- the position angle (from North to East) of the maximum elongation of the sky-projected disc PA_d . This angle is defined for $i \neq 0^\circ$.

Thus, the 10 free parameters (n_{free}) of the model are: $I_{\lambda_0}^s$, α , T_{in} , γ , R_{in} , i , PA_d , A_2 , n_{in} , and m .

5. Model-fitting with FRACS

Here we use FRACS with the parametrised sgB[e] description defined in the last section in order to interpret the VLT/MIDI observations of CPD-57° 2874 through a model-fitting procedure.

To ensure spectrally independent observations for the model-fitting we decided to consider one data point every $\simeq 0.5 \mu\text{m}$ between $8 \mu\text{m}$ and $13 \mu\text{m}$. This step approximately corresponds to twice the used spectral resolution width ($\Delta\lambda = \lambda/R$). Additionally, to avoid poor visibility calibration owing to the Earth signature of ozone around $9.6 \mu\text{m}$ we have not included observations in this spectral region in our analysis. Finally, the

3. High spectro-spatial resolution observations of fast rotators in the H-R diagram

A. Domiciano de Souza et al.: FRACS modelling - disc parameters of CPD-57° 2874 from VLTI/MIDI.II.

same spectral sampling ($n_\lambda = 10$ wavelengths points) was adopted for the VLTI/MIDI visibilities and spectrum. This choice also provides faster calculations because it is not necessary to compute model images at too many wavelengths.

We have performed a χ^2 minimisation simultaneously on the VLTI/MIDI visibilities and fluxes using a Levenberg-Marquardt (LM) algorithm (Markwardt 2008). In order to treat the visibilities and fluxes on the same level (similar weights) we have minimised a χ^2 like quantity defined as (see further details in Paper I):

$$\chi^2 = \sum_{j=1}^{n_\lambda} \sum_{k=1}^{n_B} \left[\left(\frac{V_{j,k}^{\text{obs}} - V_{j,k}}{\sigma_{V,j,k}} \right)^2 + \left(\frac{F_j^{\text{obs}} - F_j}{\sigma_{F,j}} \right)^2 \right], \quad (6)$$

where $V_{j,k}^{\text{obs}}$ and $V_{j,k}$ are the observed and modelled visibility modulus wavelength index j and for baseline index k , F_j^{obs} and F_j are the observed and modelled mid-IR fluxes. $\sigma_{V,j,k}$ and $\sigma_{F,j}$ are the estimated errors on the visibilities and fluxes.

The starting parameter values for the fit were determined from physical considerations of the CSE and from the previous results from DS07. Below we consider the reduced χ^2 defined by $\chi_r^2 = \chi^2 / (2n_B n_\lambda - n_{\text{free}})$, where $n_{\text{free}} = 10$. The LM algorithm stops when the relative decrease in χ_r^2 is less than 10^{-3} . For the CPD-57° 2874 data, the LM algorithm reaches the χ_r^2 minimum ($\chi_{\text{min},r}^2$) in a few hours ($\approx 2-3$ h) on a single CPU.

Figure 2 shows the intensity map of the model corresponding to $\chi_{\text{min},r}^2$ (best-fit model) for our distance estimate of 1.7 kpc, which also corresponds to the lowest $\chi_{\text{min},r}^2$. The visibilities and fluxes for the best-fit model are shown, together with the observations, in Figs. 3 and 4. These plots show that the model well reproduces most observations within their uncertainties for both adopted distances (1.7 and 2.5 kpc). In particular the slightly curved shape of the visibilities is well reproduced by FRACS. The models indicate that this curved shape is probably caused by the combined fact (1) that the intensity maps have different relative contributions from the central source and from the dusty CSE at different wavelengths, (2) that the optical properties of the adopted dust grains are wavelength-dependent even if there is no strong silicate feature seen in the spectrum, and (3) that the angular resolution significantly changes along the observed wavelengths.

The model parameters at $\chi_{\text{min},r}^2$ and their uncertainties are listed in Table 4. The derived parameters are almost independent of the adopted distance, except of course for those scaling with the distance. The uncertainties of the parameters have been estimated from χ_r^2 maps calculated with 21×21 points for each pair of free parameters (45 pairs) and centred on the $\chi_{\text{min},r}^2$ position. All 45 χ_r^2 maps are shown in Fig. 5 for $d = 1.7$ kpc. These maps show that the χ_r^2 space presents a well defined $\chi_{\text{min},r}^2$, without showing several local minima in the parameter domain explored. Additionally, they provide visual and direct information on the behaviour of the model parameters in the vicinity of $\chi_{\text{min},r}^2$, revealing, for instance, potential correlations between certain parameters.

We have estimated the parameter uncertainties in a conservative way by searching for the maximum parameter extension in all χ_r^2 maps corresponding to $\chi_{\text{min},r}^2 + \Delta\chi^2$, where $\Delta\chi^2 = 1$ (see contours in Fig. 5). This choice of $\Delta\chi^2$ sets a lower limit confidence region of $\approx 60\%$ to the parameter uncertainties. This limit results from two extreme assumptions about the data:

- data points per baseline are completely dependent (correlated): because the same set of stars is used to calibrate all

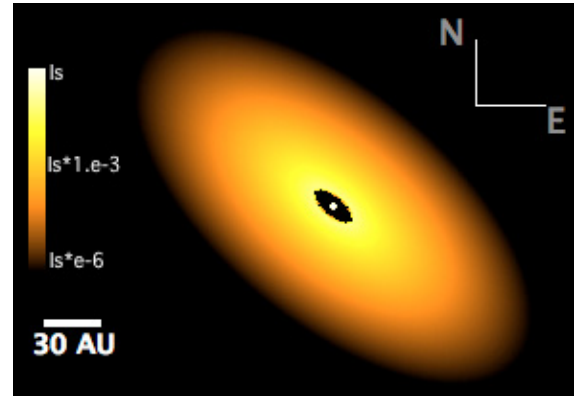


Fig. 2. Intensity map of CPD-57° 2874 at $10 \mu\text{m}$ for the best-fit FRACS model obtained for a distance $d = 1.7$ kpc (see Table 4). The image scale is in log of the specific intensity I_λ^s .

visibilities of a given baseline, we can consider a limiting case where all these visibilities are correlated. This assumption implies that only 10 independent visibility observations are available (this corresponds to the number of baselines). The flux at each spectral channel can still be considered to be independent. This pessimistic assumption leads to the lower limit of $\approx 60\%$ to the formal confidence level for $\Delta\chi^2 = 1$, corresponding to only 20 independent observations (10 baselines and 10 fluxes),

- all data points are completely independent (uncorrelated): an upper limit of $\approx 100\%$ of formal confidence level is obtained if we assume that all data points are independent. Then the uncertainties derived from $\Delta\chi^2 = 1$ are very conservative (overestimated).

Hence the parameter uncertainties given in Table 4 correspond to a confidence level of at least 60%, but most probably they are somewhat overestimated.

In the next section we present a physically motivated discussion of the derived model parameters of CPD-57° 2874.

6. Discussion

6.1. Geometrical parameters (PA_d , R_{in} , and i)

Let us first compare the derived geometrical parameters (PA_d , R_{in} , and i) with those previously obtained by DS07 from elliptical Gaussian models fitted on a sub-set of the VLTI/MIDI data used here.

The geometrical parameter PA_d can be directly compared with the major-axis position angle of the ellipse previously determined by DS07 ($\approx 143^\circ - 145^\circ$). As expected, the two estimates of PA_d are identical within their error bars.

Because the bulk of the thermal IR emission comes from the internal regions of the disc, one can expect the inner dust angular radius (R_{in}/d) to be comparable to (or slightly smaller than) the major-axis half width at half maximum ($HWHM$) of an elliptical Gaussian. Indeed, the R_{in}/d derived here agrees with the major-axis $HWHM$ ($= 0.5FWHM$) given by DS07: $4.5 < HWHM$ (mas) < 8.0 .

Domiciano de Souza et al. (2007) estimated a CSE viewing angle $i \sim 30^\circ - 60^\circ$ from the minor- to major-axis ratio of the fitted elliptical Gaussian model. This estimate agrees fairly well with the more precise determination of this parameter given here.

3.3. The supergiant B[e] star CPD-57° 2874

A&A 525, A22 (2011)

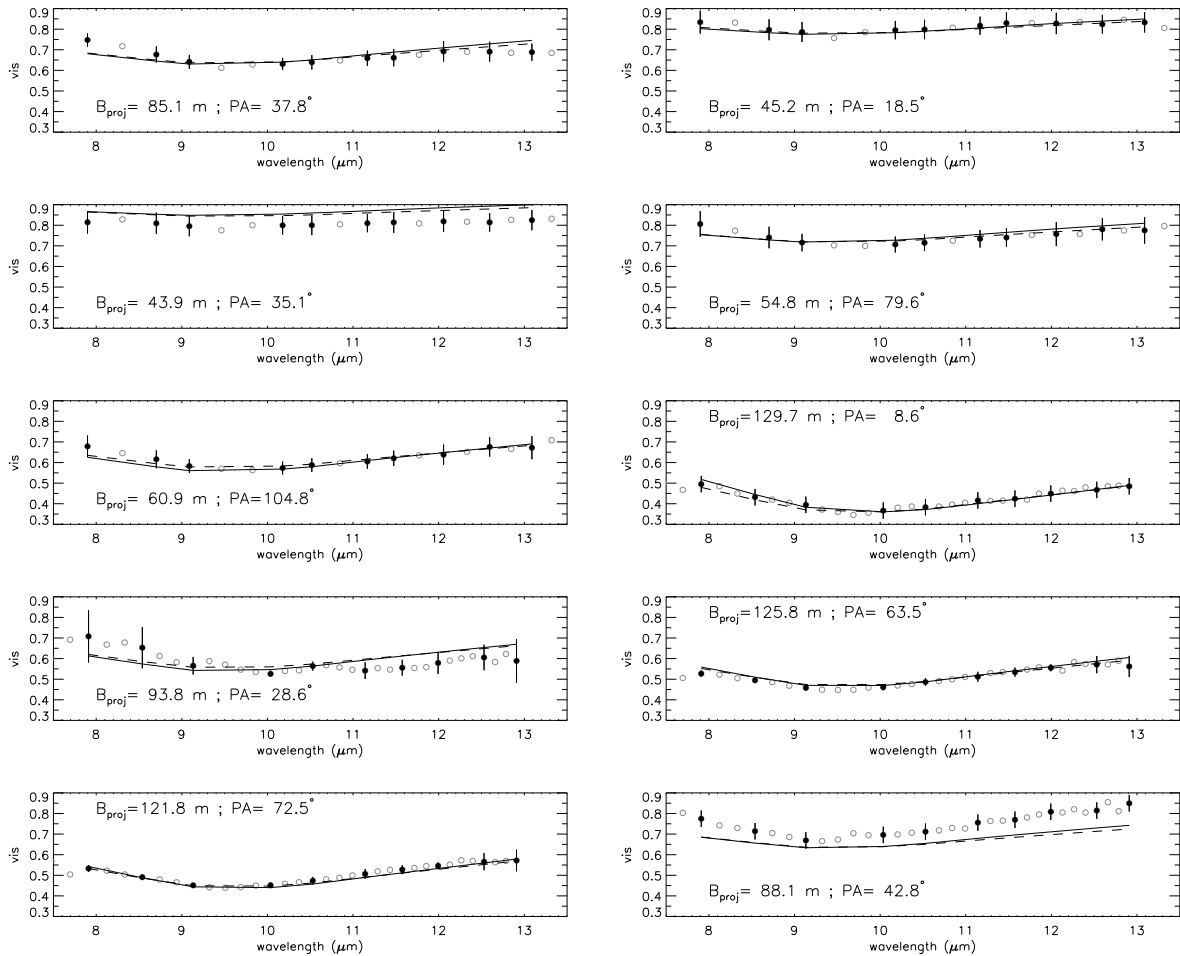


Fig. 3. VLT/MIDI visibilities of CPD-57° 2874 (circles) and the best-fit FRACS visibilities obtained from a χ^2 minimisation for a distance $d = 1.7$ kpc (solid curve) and $d = 2.5$ kpc (dashed curve). The model-fitting was performed simultaneously on the visibilities and spectral flux. The visibilities effectively used for the fit are shown as filled circles together with the corresponding visibility error bars. The good quality of this fit is reflected by a reduced χ^2_{\min} of ≈ 0.55 for both distances (see details in Table 4).

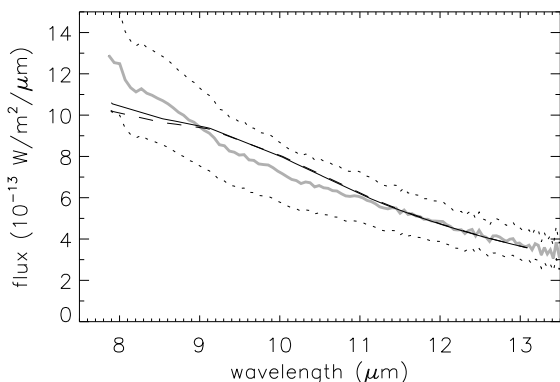


Fig. 4. VLT/MIDI flux of CPD-57° 2874 (thick solid grey curve) and the $\pm 20\%$ adopted uncertainty (dots). The thin solid and dashed curves are the best-fit model fluxes for assumed distances of $d = 1.7$ kpc and $d = 2.5$ kpc, respectively. The wavelengths used for the fit are those from Fig. 3.

The comparison of these parameters shows on one hand that the geometrical parameters obtained with FRACS agree with

those obtained from a simpler approach using analytical models. On the other hand, this comparison clearly shows that, at the cost of somewhat higher but similar computing times, FRACS gives us access to physical parameters of CPD-57° 2874 that cannot be extracted from simple geometrical analytical models.

6.2. Continuum emission from the central source ($I_{\lambda_0}^s$ and α)

In contrast to what may be initially expected, we show below that the central source (star and continuum emission components such as free-free, free-bound) contributes to almost half of the total mid-IR radiation of CPD-57° 2874. The total $10 \mu\text{m}$ flux of the best model for $d = 1.7$ kpc is $F_{\text{tot}} = 7.9 \times 10^{-13} \text{ W m}^{-2} \mu\text{m}^{-1}$ (see Fig. 4). The contribution of the dust CSE alone to the $10 \mu\text{m}$ flux computed with FRACS is $F_d = 4.4 \times 10^{-13} \text{ W m}^{-2} \mu\text{m}^{-1}$. It follows therefore that the $10 \mu\text{m}$ flux from the CSE is $\approx 56\% F_{\text{tot}}$ and from the central source is $\approx 44\% F_{\text{tot}}$. Similar results are obtained for $d = 2.5$ kpc.

We note that in the particular case of CPD-57° 2874 where $i \approx 60^\circ$ and where the dust is confined in a relatively narrow disc (opening angle $\sim 7^\circ$), these relative flux contributions can be directly obtained from $F_{\lambda_0}^s$ (derived from $I_{\lambda_0}^s$; see Table 4).

3. High spectro-spatial resolution observations of fast rotators in the H-R diagram

A. Domiciano de Souza et al.: FRACS modelling - disc parameters of CPD-57° 2874 from VLTI/MIDI.II.

Table 4. Best-fit model parameters and uncertainties derived for CPD-57° 2874 from a χ^2 minimisation.

Adopted distance	$d = 1.7$ kpc		$d = 2.5$ kpc	
	$\chi^2_{\min,r} = 0.54$		$\chi^2_{\min,r} = 0.56$	
Model parameters	value	error	value	error
$I_{\lambda_0}^s$ ($10^5 \text{ W m}^{-2} \mu\text{m}^{-1} \text{ str}^{-1}$)	2.2	+0.7 -0.7	4.2	+1.8 -1.4
α	2.4	+1.3 -1.2	2.4	+1.4 -1.4
T_{in} (K) ^(a)	1498	+1042 -427	1500	+1050 -535
γ	1.02	+0.71 -0.29	0.86	+0.43 -0.24
R_{in} (AU)	12.7	+3.6 -2.9	14.4	+5.1 -4.0
i (°)	61.3	+10.8 -18.2	59.6	+11.8 -21.2
PA_d (°)	140.3	+12.3 -14.0	139.4	+13.7 -15.1
A_2 ^(b)	-0.98	-	-0.98	-
n_{in} (m^{-3}) ^(b)	0.30	-	0.33	-
m ^(b)	332	-	377	-
Other derived parameters	value	error	value	error
$F_{\lambda_0}^s$ ($10^{-13} \text{ W m}^{-2} \mu\text{m}^{-1}$) ^(c)	3.5	+1.1 -1.1	6.8	+2.8 -2.3
R_{in}/d (mas)	7.5	+2.1 -1.7	5.8	+2.0 -1.6
$\Delta\theta_d$ (°)	7.5	-	7.0	-

Notes. The uncertainties were estimated from the χ_r^2 maps. ^(a) To be physically consistent with the adopted dust composition the upper limit for T_{in} is 1500 K, even though the χ_r^2 maps were allowed to explore higher temperature values. ^(b) Not well constrained. ^(c) Observed mid-IR flux from the central region at $\lambda_0 = 10 \mu\text{m}$ (Eq. (2)).

This is valid if there is no absorption of the central regions by the CSE.

Although the uncertainties on the spectral index α are relatively high ($\approx 50\%$), the derived value (≈ 2.4) suggests an important contribution of free-free continuum radiation from the central regions (Felli & Panagia 1981).

6.3. Temperature structure of the dusty CSE (T_{in} and γ)

The dust temperature at the inner radius T_{in} is found to be ≈ 1500 K (the imposed upper limit for the fit), which is consistent with the definition of T_{in} itself and with the chosen silicate dust composition. The large upper limit uncertainties in T_{in} and the fact that the best-fit T_{in} is 1500 K for $d = 2.5$ kpc indicate that a T_{in} slightly higher than 1500 K could still be compatible with the observations. A higher T_{in} value is consistent with, for instance, different dust compositions. However, we prefer to keep our choice of dust composition and to have a relatively large upper limit uncertainty in T_{in} , since the present observations do not provide strong constraints on the exact dust composition.

The derived value for the coefficient of the temperature profile γ indicates an almost linear decrease of the disc temperature as a function of r . The steepness of this temperature profile lies between those expected for a non irradiated, adiabatically cooling disc ($T \propto r^{-4/3}$) and a reprocessing disc ($T \propto r^{-3/4}$) (cf. Porter 2003). This implies that a non negligible part of the reprocessed radiation from the inner parts of the disc escapes without being re-absorbed, so that the disc cools down faster than highly optically thick discs, without of course reaching the limit of a purely adiabatic cooling.

6.4. Parameters related to the density law (n_{in} , A_2 , and m)

Our results suggest that the observed mid-IR visibilities and fluxes cannot strongly constrain each individual parameter related to the density law: n_{in} , A_2 , and m . The χ^2 maps show a

significant correlation between these three parameters, indicating that they are degenerated for the available VLTI/MIDI observations. Even if their uncertainties are significant, the values of these parameters at χ_{\min}^2 suggest

- a low inner density n_{in} corresponding to relatively low CSE optical depth in the mid-IR ($\lesssim 0.2$ along the line of sight around $10 \mu\text{m}$);
- a polar-to-equatorial terminal velocity ratio $v_{\infty}(0^\circ)/v_{\infty}(90^\circ) = 1/(1 + A_2) \approx 50$, compatible with the values found in the literature (e.g. Zickgraf 2003);
- a high value for m , translating into a quite narrow opening angle ($\leq 10^\circ$) for the dust disc.

Because n_{in} , A_2 , and m are not well constrained, we fitted the observations by fixing these parameters to their values in Table 4 in order to investigate their influence on the remaining parameters. We have also fixed the T_{in} to 1500 K. The fit was performed for $d = 1.7$ kpc, starting from slightly different values from those in Table 4. The χ^2 and values obtained for the free parameters ($I_{\lambda_0}^s$, α , γ , R_{in} , i , PA_d) are essentially the same as in Table 4 (differences are only a small fraction of the parameter uncertainties). We have also checked that the uncertainties on the other parameters are not affected by the fact that n_{in} , A_2 , and m are not well constrained.

6.5. Data analysis from a model with fewer free parameters

Thanks to the data analysis performed here we found that some parameters of the sgB[e] model adopted for CPD-57° 2874 cannot be well constrained from the available VLTI/MIDI data. Of course this is not necessarily a general conclusion because it depends on the nature of the studied target and on the spectro-interferometric data available.

The results from our analysis of CPD-57° 2874 indicate that it is justified to consider a simplified version of the model described in Sect. 4. As shown in the previous section, the parameters related to the density law are the less constrained by the data. Let us thus consider an alternative density law where the number density of dust grains is given by

$$n(r, \theta) = \begin{cases} n_{\text{in}} \left(\frac{R_{\text{in}}}{r}\right)^2 & 90^\circ - 0.5\Delta\theta_d \leq \theta \leq 90^\circ + 0.5\Delta\theta_d \\ 0 & \theta < 90^\circ - 0.5\Delta\theta_d \text{ and } \theta > 90^\circ + 0.5\Delta\theta_d. \end{cases} \quad (7)$$

The parameters A_1 , A_2 , and m are not present in this simpler density prescription. Only n_{in} and $\Delta\theta_d$ are necessary to define the density structure. Based on our previous results we have also fixed T_{in} to 1500 K. The number of free parameters is thus reduced from 10 to 8, namely, $I_{\lambda_0}^s$, α , γ , R_{in} , i , PA_d , n_{in} , and $\Delta\theta_d$.

Following the previous procedure we have performed a χ^2 minimisation on the visibilities and fluxes using a LM algorithm. The results are shown in Table 5. Note that the best-fit parameters completely agree (well within the uncertainties) with the previous values obtained with the initial model (Table 4).

Only n_{in} shows an important difference compared to the previously tested model. Contrarily to the previous density law (Eq. (3)), the new one (Eq. (7)) assumes that the density is constant along a given r inside the dust disc. In order to obtain similar fluxes and optical depths as before, n_{in} has to be somewhat smaller than the previous value.

Table 5 also provides the parameter uncertainties estimated with the LM algorithm, which are smaller than those estimated from the χ_r^2 maps (given in Table 4). These smaller errors appear because all data points are assumed to be independent and no

3.3. The supergiant B[e] star CPD-57° 2874

A&A 525, A22 (2011)

Table 5. Best-fit model parameters derived for CPD-57° 2874 from a χ^2 minimisation using a model with fewer free parameters than the initial one (cf. Sect. 6.5).

Adopted distance	$d = 1.7$ kpc		$d = 2.5$ kpc	
	$\chi^2_{\min,r} = 0.54$		$\chi^2_{\min,r} = 0.56$	
Reduced χ^2_{\min}				
Model parameters	value	error	value	error
		LM		LM
$I_{\lambda_0}^s$ ($10^5 \text{ W m}^{-2} \mu\text{m}^{-1} \text{ str}^{-1}$)	2.1	+0.1 -0.1	4.2	+0.1 -0.1
α	2.4	+0.2 -0.2	2.4	+0.2 -0.2
γ	0.92	+0.07 -0.07	0.85	+0.05 -0.05
R_{in} (AU)	11.0	+2.0 -2.0	13.9	+2.4 -2.4
i (°)	60.5	+1.5 -1.5	59.3	+1.5 -1.5
PA_d (°)	139.8	+1.0 -1.0	139.3	+1.0 -1.0
n_{in} (m^{-3})	0.09	+0.06 -0.06	0.11	+0.07 -0.07
$\Delta\theta_d$ (°)	7.5	+4.4 -4.4	5.9	+4.4 -4.4

Notes. Uncertainties were estimated from the Levenberg-Marquardt (LM) algorithm and can be considered as lower limits to the errors on the derived parameters (see discussion in the text).

covariance matrix is used in the error estimations. The estimated errors from LM in Table 5 can then be considered as lower limits, while the errors from the χ^2_r maps can be considered as upper limits to the parameter uncertainties (see discussion in Sect. 5).

7. Conclusions

The dusty CSE of the Galactic sgB[e] CPD-57° 2874 was spatially resolved thanks to mid-IR spectro-interferometric observations performed with the VLTI/MIDI instrument. Several physical parameters and corresponding uncertainties of this star were derived from a χ^2 minimisation and from the analysis of χ^2 maps. The physical quantities derived include the inner dust radius, relative flux contribution of the central source and of the dusty CSE, dust temperature profile, and disc inclination (refer to Table 4 and Sect. 6 for details).

To our knowledge, this is the first direct determination of physical parameters of the dusty CSE of a B[e] supergiant based on interferometric data and using a model-fitting approach from a χ^2 minimisation. This was possible thanks to FRACS, which adopts a parametrised description of the central object and of the dusty CSE combined to a simplified radiative transfer (no scattering). Its main advantage is computation speed (<10 s per monochromatic image with 300×300 pixels). Because it is fast, FRACS allows us (1) to explore a large parameter space domain for a true global χ^2 minimisation and (2) to more realistically estimate the uncertainties on the best-fit parameters. We would like to recall that contrarily to a model such as FRACS, simple geometrical models do not allow a simple and direct access to physical parameters and uncertainties of the dusty CSE.

Future complementary observations could be included to measure new CSE parameters and/or to reduce the uncertainties and the correlations on some parameters that were not strongly constrained by the VLTI/MIDI observations alone. Consistently with the domain of validity of FRACS, these complementary data should be obtained at wavelengths above the near-IR, where the dust starts to contribute to a significant amount of the stellar flux (UV to visible observations cannot be consistently modelled by FRACS). For example, the closure phase information from

the MATISSE beam combiner (second generation instrument on VLTI, (Lopez et al. 2009; Wolf et al. 2009) could inform on the disc inclination and opening angle, which are parameters that can influence the symmetry of the mid-IR intensity distribution. Also, near-future interferometric observations in the millimetre with ALMA will be more sensitive than MIDI and MATISSE to the thermal emission from the colder regions of the dusty CSE. Thus, these observations will probably better constrain the temperature profile of the dust and also provide direct information on the structure and actual size of the CSE, allowing also for mass estimates. Moreover, this information on the colder dust is very important for the study of the evolutionary history of sgB[e] stars (e.g. mass and angular momentum losses, chemical enrichment and interaction with the close interstellar medium).

Acknowledgements. This research used the SIMBAD and VIZIER databases at the CDS, Strasbourg (France), and NASA's ADS bibliographic services. M.B.F. acknowledges financial support from the Programme National de Physique Stellaire (PNPS-France) and the Centre National de la Recherche Scientifique (CNRS-France). M.B.F. also acknowledges Conselho Nacional de Desenvolvimento Científico e Tecnológico (CNPq-Brazil) for the post-doctoral grant. We thank the CNRS for financial support through the collaboration program PICS France-Brazil. We also thank the referee for his useful and constructive comments, which helped us to improve the quality of this work.

References

- Allen, C. W. 1973, in *Astrophysical Quantities*, University of London (The Athlone Press), 266
- Bjorkman, J. E. 1998, B[e] stars, 233, 189
- Carciofi, A. C., Miroshnichenko, A. S., & Bjorkman, J. E. 2010, *ApJ*, 721, 1079
- Domiciano de Souza, A., Driebe, T., Chesneau, O., et al. 2007, *A&A*, 464, 81
- Domiciano de Souza, A., Kervella, P., Bendjoya, P., & Niccolini, G. 2008, *A&A*, 480, L29
- Draine, B. T., & Lee, H. M. 1984, *ApJ*, 285, 89
- Felli, M., & Panagia, N. 1981, *A&A*, 102, 424
- Jaffe, W. J. 2004, in *New Frontiers in Stellar Interferometry*, ed. W. A. Traub, Bellingham, WA: The International Society for Optical Engineering, Proc. SPIE Conf., 5491, 715
- Lamers, H. J. G. L. M., & Pauldrach, A. W. A. 1991, *A&A*, 244, L5
- Lamers, H. J. G. L. M., Zickgraf, F.-J., de Winter, D., Houziaux, L., & Zorec, J. 1998, *A&A*, 340, 117
- Lamers, H. J. G. L. M., & Cassinelli, J. P. 1999, *Introduction to Stellar Winds*, ed. J. P. Lamers, H. J. G. L. M., & Cassinelli
- Leinert, Ch., van Boekel, R., Waters, L. B. F. M., et al. 2004, *A&A*, 423, 537
- Lopez, B., Lagarde, S., Wolf, S., et al. 2009, *Science with the VLT in the ELT Era*, 353
- Magalhães, A. M. 1992, *ApJ*, 398, 286
- Markwardt, C. B. 2008, in *Proc. Astronomical Data Analysis Software and Systems XVIII*, Quebec, Canada, ASP Conf. Ser., ed. D. Bohlender, P. Dowler, & D. Durand, 411, 251
- Mathis, J. S., Rumpl, W., & Nordsieck, K. H. 1977, *ApJ*, 217, 425
- McGregor, P. J., Hyland, A. R., & Hillier, D. J. 1988, *ApJ*, 324, 1071
- Meynet, G., & Maeder, A. 2006, *Stars with the B[e] Phenomenon*, 355, 27
- Mie, G. 1908, *Ann. Phys.*, 25, 377
- Millour, F., Chesneau, O., Borges Fernandes, M., et al. 2009, *A&A*, 507, 317
- Miroshnichenko, A. S. 2007, *ApJ*, 667, 497
- Niccolini, G., Bendjoya, P., & Domiciano de Souza, A. 2010, *A&A*, 525, A21 (Paper I)
- Panagia, N., & Felli, M. 1975, *A&A*, 39, 1
- Pelupessy, I., Lamers, H. J. G. L. M., & Vink, J. S. 2000, *A&A*, 359, 695
- Stee, P., de Araujo, F. X., Vakili, F., et al. 1995, *A&A*, 300, 219
- Vink, J. S., Davies, B., Harries, T. J., Oudmaijer, R. D., & Walborn, N. R. 2009, *A&A*, 505, 743
- Wolf, S., Lopez, B., Jaffe, W., et al. 2009, *Science with the VLT in the ELT Era*, 359
- Zickgraf, F.-J. 2003, *A&A*, 408, 257
- Zickgraf, F.-J., Wolf, B., Stahl, O., Leitherer, C., & Klare, G. 1985, *A&A*, 143, 421

3. High spectro-spatial resolution observations of fast rotators in the H-R diagram

A. Domiciano de Souza et al.: FRACS modelling - disc parameters of CPD-57° 2874 from VLTI/MIDI.II.

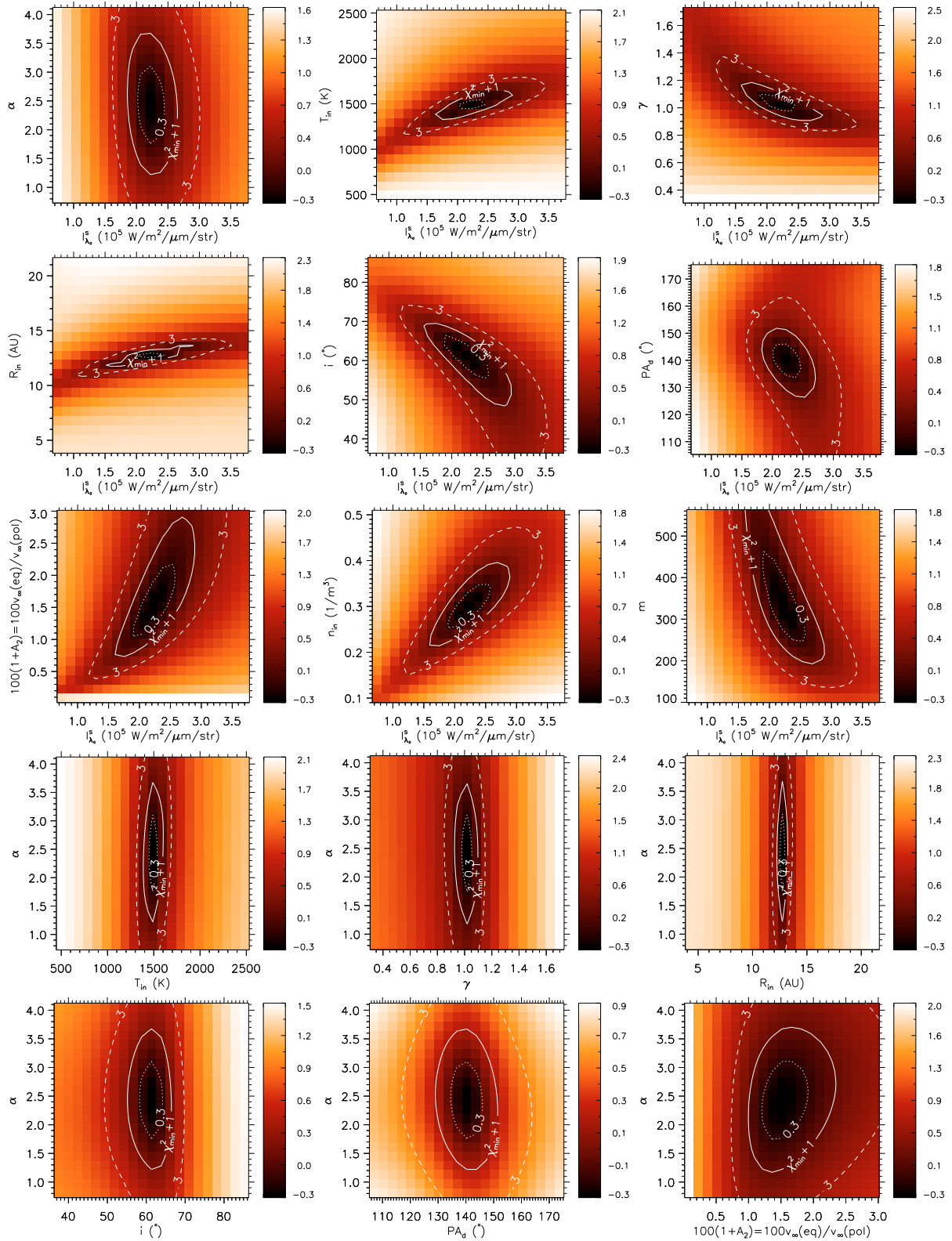


Fig. 5. Reduced χ^2 maps from VLTI/MIDI observations of CPD-57° 2874 for all 45 combinations of free parameters of our model (FRACS). The maps are centered on the $\chi^2_{\text{min},r}$ ($=0.54$) position and correspond to the distance of 1.7 kpc. Contours are drawn for $\chi^2_{\text{min},r} + \Delta\chi^2$, with $\Delta\chi^2 = 0.3, 1, 3$. The parameters are ordered as in Table 4. The map scale is given in logarithmic units. Details on the model-fitting procedure are given in Sect. 5.

3.3. The supergiant B[e] star CPD-57° 2874

A&A 525, A22 (2011)

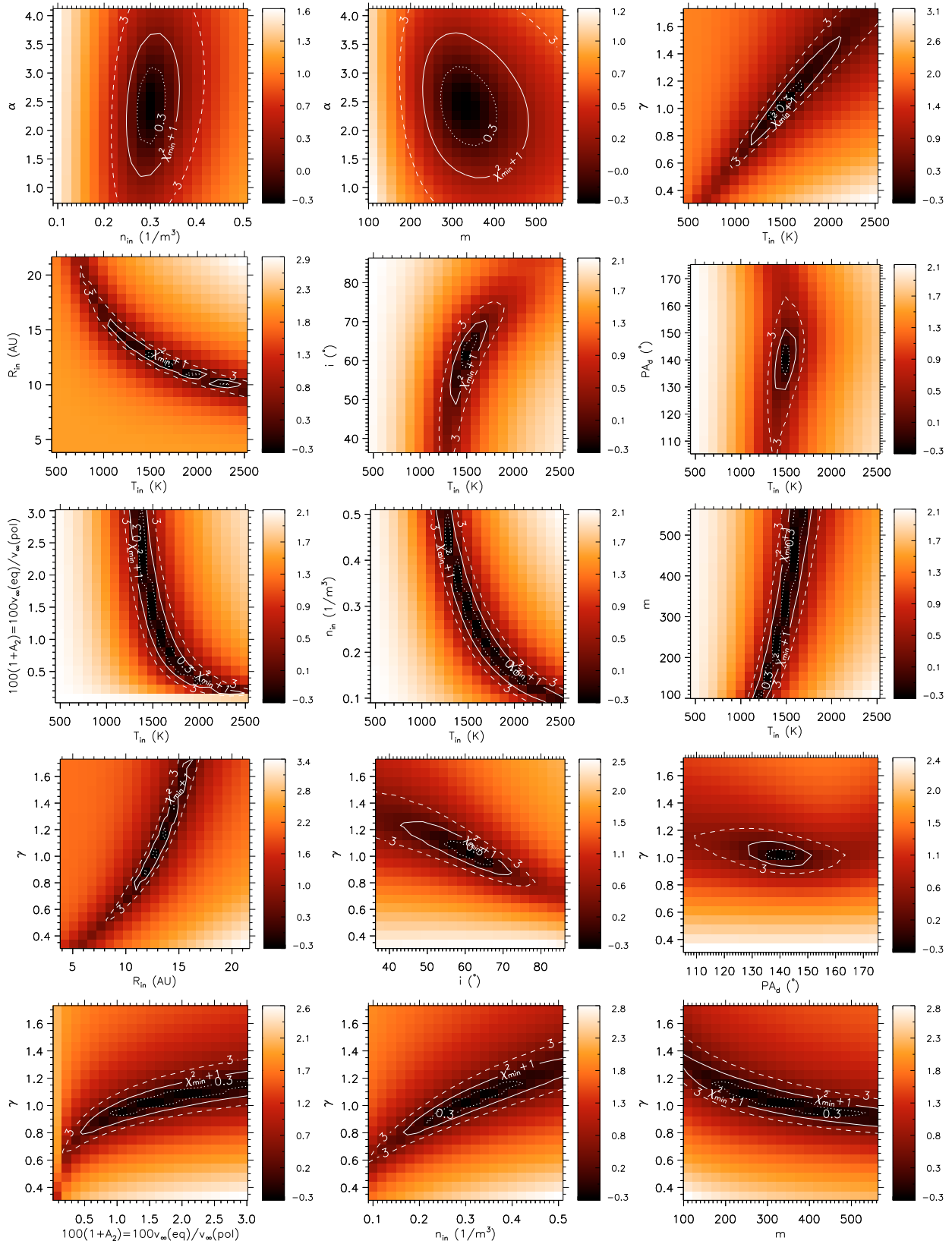


Fig. 5. continued.

3. High spectro-spatial resolution observations of fast rotators in the H-R diagram

A. Domiciano de Souza et al.: FRACS modelling - disc parameters of CPD-57° 2874 from VLTI/MIDI.II.

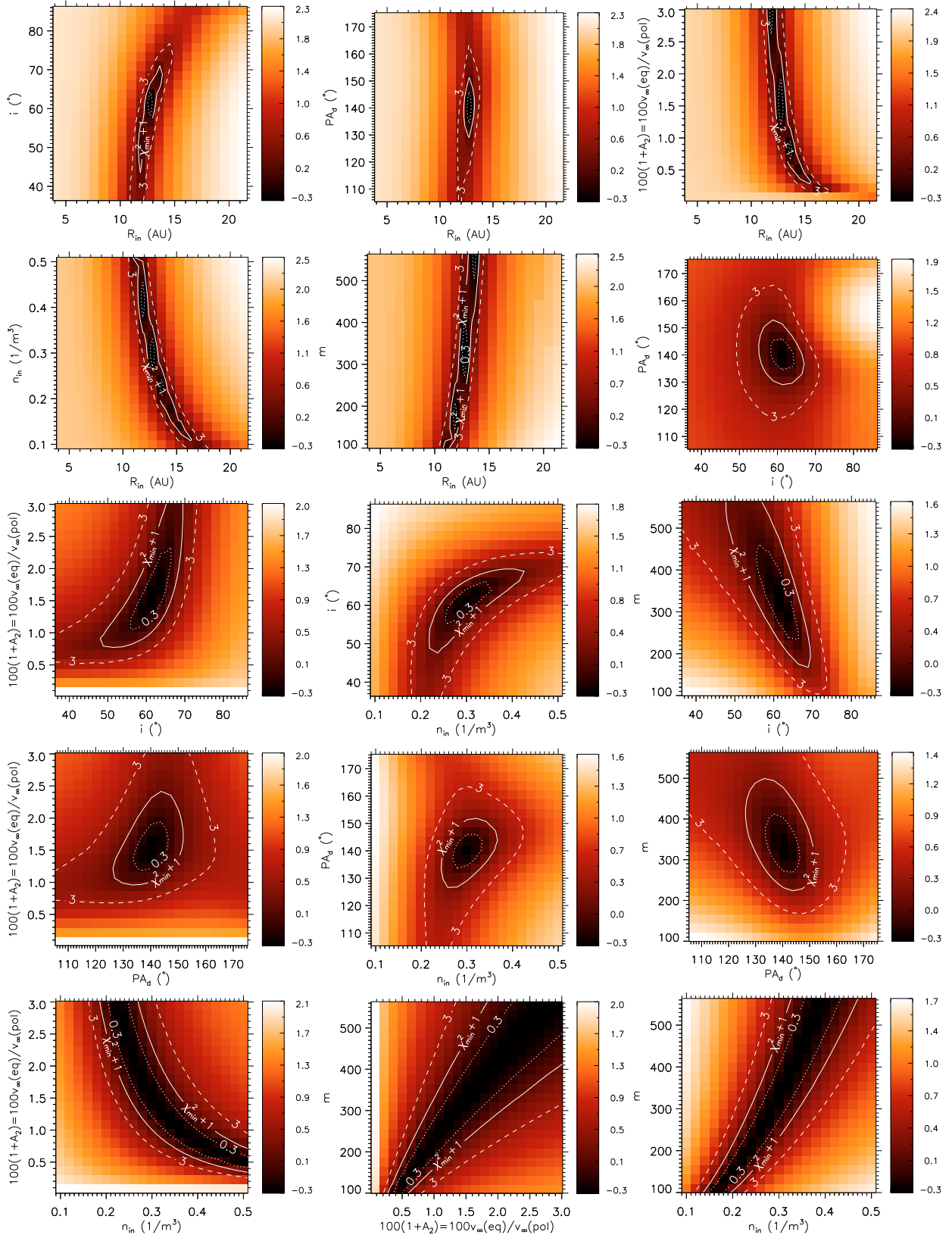


Fig. 5. continued.

CHAPTER 4

PERSPECTIVES

We give below a non-exhaustive list of future projects based on or motivated by the results obtained in the present work.

Stellar rotation

- The results from [Domiciano de Souza et al. \(2012, Sect. 3.2.4\)](#) demonstrated from real observations that interferometric differential phases (differential interferometry) allow to measure the angular diameter, the orientation (position angle of the rotation axis projected onto the sky), and the projected rotation velocity of fast-rotating stars. Based on this work we proposed additional programs to study fast rotators from differential phases: (1) fast-rotating debris-disk stars (VLTI/AMBER GTO program¹; seven stars observed and data reduced), (2) Pleiades cluster (observations with the CHARA/VEGA beam combiner).
- The results presented in this study showed that a deeper understanding of stellar gravity darkening requires observational determination of the β coefficient over a broader range of rotation flattening and on single late-type stars (colder than $T_{\text{eff}} \sim 10\,000$ K). These observations would provide important constraints on the gravity-darkening models proposed by (1) [Claret \(1998, 2000, 2012\)](#) and (2) [Espinosa Lara & Rieutord \(2011, 2012\)](#), which predict different dependences of β on the stellar flattening, T_{eff} , and convection (see also discussion in Sect. 2.2.2).
- Comparative study of different laws for differential rotation (e.g. from [Zorec et al., 2011](#); [Reiners & Royer, 2004](#); [Zahn, 1992](#)) and gravity darkening (e.g. from [Espinosa Lara & Rieutord, 2011](#); [Claret, 2012](#); [Maeder, 1999](#)). This study will also allow to develop the optimal strategies of observation and data analysis in order to measure differential rotation as well as to improve and expand the measurements of gravity darkening across the H-R diagram. Examples of results based on OLBI already achieved on this topic are given by [Domiciano de Souza et al. \(2004a\)](#), [Domiciano de Souza et al. \(2004b\)](#), and those presented in Chapter 3. Work in collaboration with M. Rieutord, J. Zorec, F. Espinosa Lara, A. Claret, D. Reese, among others.

¹Calibrating Stellar Rotation across the H-R Diagram; P.I.: A. Domiciano de Souza.

- Collaboration to the **ESTER**² project to study the structure and evolution of fast-rotating stars. One of the next steps on the ESTER project is to create two-dimensional stellar models for a large range of masses being able to deal simultaneously with fast rotation and with time evolution. Collaboration with M. Rieutord, F. Espinosa Lara, P. Kervella, and others.

Achernar

- The binary companion of Achernar: determination of orbit, period, masses, and fluxes (luminosities) of both stars, as well as the distance of the system. Investigation of a possible relation with episodic emission phases. This work is the continuation of the results presented in Sect. 3.2.3 and is performed in collaboration mainly with P. Kervella, and many others; it is based on observations with VLT/NACO, VLT/VISIR, VLT/AMBER, and different spectroscopic data from our team or publicly available.
- Evolution and structure of Achernar's disk (a new Be phase started in 2012-2013). For this project we have already VLT/AMBER DDT³ observations performed in 2013 and an open time proposal is accepted for 2014. This work is part of the PhD thesis of D. Moser Faes (double thesis USP-OCA; thesis supervisors: A. C. Carciofi and A. Domiciano de Souza). A first work on the evolution of the disk of Achernar was already performed during the PhD thesis of S. Kanaan (thesis supervisor: Ph. Stee) with the main results published by [Kanaan et al. \(2008\)](#).

Circumstellar environments: Be, sgB[e], protoplanetary disks

- Extension of the grid of sgB[e] models presented in Sect. 2.4.1, in order to include additional luminosities, temperatures, densities, CSE velocity fields (e.g. rotation laws), among others. This work is being carried in collaboration with M. Borges Fernandes and A. C. Carciofi.
- Spectro-interferometric study of sgB[e] stars: (1) GG Car (Domiciano de Souza, Carciofi, Borges Fernandes, et al.; order of authors to be defined yet; A&A paper in preparation based on VLT/MIDI observations; poster contribution to be published in the proceedings of the IAU 307: Domiciano de Souza et al. 2014), (2) HD50138 (collaboration with L. Ellerbroek, M. Benisty, K. Perraut, A. C. Carciofi, M. Borges Fernandes, and others; e.g. [Borges Fernandes et al., 2009, 2011](#)), (3) survey and imaging of sgB[e] stars as part of the GTO-OCA of the next generation VLT beam-combiner MATISSE⁴ (work in collaboration with A. Meilland, F. Millour, Ph. Stee, G. Niccolini, and others). The physical interpretation of these observations will be partially performed using FRACS (Sect. 2.5.2) and the HDUST grid of sgB[e] models (Sect. 2.4.1). Some important questions to be addressed in this high angular resolution study of sgB[e] stars include (1) the role of binarity, (2) the observational signatures allowing to discriminate between sgB[e] and Herbig B[e], and (3) the velocity field law of the CSE disk (Keplerian, outflow, hybrid behavior).

²Evolution STellaire en Rotation Rapide (P.I.: M. Rieutord)

³Director's Discretionary Time.

⁴Multi AperTure mid-Infrared SpectroScopic Experiment (P.I.: B. Lopez - OCA, France).

-
- Creation of a grid of Be star models, similar to the grid of sgB[e] described in Sect. 2.4.1. Work in collaboration with A. C. Carciofi and D. Moser Faes (part of his PhD thesis). The Be models will be calculated for a large range of disk densities, sizes, mass losses, and temperatures of central star. Images, SED, and spectral lines will be delivered with the grid of models at wavelengths (visible, IR, mm) corresponding to modern spectrographs and interferometers.
 - Study of protoplanetary disks (gas and dust) in young stellar objects (Herbig Ae/Be, debris disks, and T Tauri stars) in the context of astrobiology. This project is the result of the combination of the expertise on high angular resolution, radiative transfer, and organic chemistry from several collaborators in France (e.g. G. Niccolini, Ph. Bendjoya, O. Suarez, N. Nardetto, A. Domiciano de Souza) and Brazil (e.g. E. Janot-Pacheco, C. Lage, , A. C. Carciofi). The main objective is to use radiative transfer models of protoplanetary disks to interpret high angular resolution observations in search for simultaneous presence of atomic and molecular lines of astrobiological interest (in particular hydrogen, CO, PAH, H₂O, and others). We intend to ask for observations on present (VLT/AMBER, VLT/MIDI, CHARA/VEGA, ALMA) and future interferometers/instruments, in particular VLT/MATISSE. The radiative transfer codes to be used for data analysis are HDUST and FRACS.

Numerical models

- Different upgrades can be introduced in CHARRON depending on the requirements from future observations and projects. For example, inclusion of (1) additional differential-rotation laws, (2) stellar spots and oscillations to be studied by spectro-interferometry, (3) binary interaction (including gravitational deformation, mutual illumination). It is also planned to create a parallel version of CHARRON in order to speed up the model-fitting procedures using MCMC techniques (cf. Sect. 3.2.1).
- A new version of FRACS will be developed in collaboration with G. Niccolini and Ph. Bendjoya. We intend to implement atomic (starting with hydrogen), gas continuum opacities (free-free and free-bound), and molecular lines (e.g. CO, PAH, H₂O). The detection and study of these molecules is important in the context of astrobiology (exo-biochemistry) in protoplanetary disks, as discussed above. FRACS will also be upgraded in order to include different CSE velocity fields (e.g. keplerian rotation, decretion disks). This project aims in particular at the scientific exploitation of VLT(I) (AMBER, MIDI, MATISSE, SPHERE, VISIR) and ALMA in the field of Be, sgB[e], and protoplanetary disks, notably in programs on astrobiology. Because FRACS is fast, it can be easily used in model fitting, such as MCMC methods (e.g. used by the emcee code), allowing to estimate the relevant parameters of the model and their uncertainties. This information can be used for example as inputs to more complex (and time consuming) radiative transfer codes (e.g. HDUST).

APPENDIX A

ROCHE SURFACE

We derive below the equation of the stellar surface for the Roche model by solving Eq. 2.12, which is a (depressed) cubic equation on $R(\theta)$. It is straightforward to express this equation as

$$R(\theta)^3 + pR(\theta) + q = 0, \quad (\text{A.1})$$

where

$$p = -\frac{2GM}{R_p \Omega^2 \sin^2 \theta} = -\frac{2R_c^3}{R_p} \left(\frac{\Omega_c}{\Omega \sin \theta} \right)^2 \quad (\text{A.2})$$

and

$$q = -p(\theta)R_p = \frac{2GM}{\Omega^2 \sin^2 \theta} = 2R_c^3 \left(\frac{\Omega_c}{\Omega \sin \theta} \right)^2, \quad (\text{A.3})$$

where we have also used Eq. 2.14. Note that $p < 0$, which means that all three roots of the cubic equation are real.

Let us now follow two distinct ways to solve the foregoing cubic equation by making

$$R(\theta) = A \sin(\theta) \quad \text{and} \quad R(\theta) = A \cos(\theta). \quad (\text{A.4})$$

Substituting individually each of these two relations into Eq. A.1 leads to

$$4 \sin^3(\theta) + \frac{4q}{A^2} \sin(\theta) + \frac{4q}{A^3} = 0 \quad (\text{A.5})$$

and

$$4 \cos^3(\theta) + \frac{4q}{A^2} \cos(\theta) + \frac{4q}{A^3} = 0 \quad (\text{A.6})$$

where

$$A = 2\sqrt{-\frac{p}{3}}. \quad (\text{A.7})$$

Compare each term of Eqs. A.5 and A.6 respectively with those from the following trigonometric identities¹:

$$4 \sin^3(\theta) - 3 \sin(\theta) + \sin(3\theta) = 0 \quad (\text{A.8})$$

and

$$4 \cos^3(\theta) - 3 \cos(\theta) - \cos(3\theta) = 0 \quad (\text{A.9})$$

¹These identities can be derived from the development of $\sin(3\theta) = \sin(2\theta)\cos(\theta) + \sin(\theta)\cos(2\theta)$ and $\cos(3\theta) = \cos(2\theta)\cos(\theta) - \sin(\theta)\sin(2\theta)$.

A. Roche surface

From these comparisons it can be shown that

$$\sin(3\theta) = -\frac{3q}{2p} \sqrt{\frac{-3}{p}} \quad (\text{A.10})$$

and

$$\cos(3\theta) = \frac{3q}{2p} \sqrt{\frac{-3}{p}}. \quad (\text{A.11})$$

Finally, resolving the two previous equations for θ and substituting them back into Eq. A.4, together with Eqs. A.2 and A.3, leads to

$$R(\theta) = R_p \frac{\sin \left[\frac{1}{3} \arcsin \left(\frac{\Omega}{\Omega_c} \sin \theta \right) + \frac{2\pi}{3} k \right]}{\frac{1}{3} \left(\frac{\Omega}{\Omega_c} \sin \theta \right)}, \quad k = 0, 1, 2 \quad (\text{A.12})$$

and

$$R(\theta) = R_p \frac{\cos \left[\frac{1}{3} \arccos \left(-\frac{\Omega}{\Omega_c} \sin \theta \right) + \frac{2\pi}{3} k \right]}{\frac{1}{3} \left(\frac{\Omega}{\Omega_c} \sin \theta \right)}, \quad k = 0, 1, 2. \quad (\text{A.13})$$

The two different formulations above correspond to identical three real solutions (for different values of k), i.e., $R(\theta)$ for $k = 0, 1, 2$ in Eq. A.12 are identical to $R(\theta)$ for $k = 2, 0, 1$ in Eq. A.13. Note that for $k > 2$ or $k < 0$ (k integer) one recovers the same three solutions above (for $k = 0, 1, 2$) cycled over 2π .

By examining the different solutions above one finds that only one is physically acceptable, while the two others lead to unphysical results: $R(\theta = 0) \rightarrow \infty$ and $R(\theta) < 0$. The only physical solution is thus obtained for $k = 0$ in Eq. A.12 and $k = 2$ in Eq. A.13, which correspond to the expressions given in Eq. 2.18.

BIBLIOGRAPHY

Abney, W. D. W. 1877, MNRAS, 37, 278

1 citation on page [1](#),

[\[ADS\]](#)

Aufdenberg, J. P., Mérand, A., Coudé du Foresto, V., Absil, O., Di Folco, E., Kervella, P., Ridgway, S. T., Berger, D. H., ten Brummelaar, T. A., McAlister, H. A., Sturmman, J., Sturmman, L., & Turner, N. H. 2006, ApJ, 645, 664

1 citation on page [5](#),

[\[ADS\]](#)

Balona, L. A., Engelbrecht, C. A., & Marang, F. 1987, MNRAS, 227, 123

1 citation on page [78](#),

[\[ADS\]](#)

Bjorkman, J. E. & Carciofi, A. C. 2005, in Astronomical Society of the Pacific Conference Series, Vol. 337, The Nature and Evolution of Disks Around Hot Stars, ed. R. Ignace & K. G. Gayley, 75

2 citations on 2 pages [33](#) and [35](#),

Bodenheimer, P. & Ostriker, J. P. 1973, ApJ, 180, 159

1 citation on page [1](#),

[\[ADS\]](#)

Borges Fernandes, M., Kraus, M., Chesneau, O., Domiciano de Souza, A., de Araújo, F. X., Stee, P., & Meilland, A. 2009, A&A, 508, 309

1 citation on page [148](#),

[\[ADS\]](#)

Borges Fernandes, M., Meilland, A., Bendjoya, P., Domiciano de Souza, A., Niccolini, G., Chesneau, O., Millour, F., Spang, A., Stee, P., & Kraus, M. 2011, A&A, 528, A20

1 citation on page [148](#),

[\[ADS\]](#)

Born, M. & Wolf, E. 1980, Principles of Optics: Electromagnetic Theory of Propagation, Interference and Diffraction of Light, 6th edn. (Pergamon Press Ltd.)

1 citation on page [7](#),

BIBLIOGRAPHY

- Carciofi, A. C. 2011, in IAU Symposium, Vol. 272, Active OB Stars: Structure, Evolution, Mass Loss, and Critical Limits, ed. Neiner, C., Wade, G., Meynet, G. & Peters, G., 325–336
4 citations on 2 pages [33](#) and [35](#),
- Carciofi, A. C. & Bjorkman, J. E. 2006, ApJ, 639, 1081
2 citations on 2 pages [36](#) and [62](#),
[\[ADS\]](#)
- Carciofi, A. C., Bjorkman, J. E., Otero, S. A., Okazaki, A. T., Štefl, S., Rivinius, T., Baade, D., & Haubois, X. 2012, ApJ, 744, L15
1 citation on page [36](#),
[\[ADS\]](#)
- Carciofi, A. C., Domiciano de Souza, A., Magalhães, A. M., Bjorkman, J. E., & Vakili, F. 2008, ApJ, 676, L41
3 citations on 3 pages [3](#), [78](#), and [95](#),
[\[ADS\]](#)
- Carciofi, A. C., Magalhães, A. M., Leister, N. V., Bjorkman, J. E., & Levenhagen, R. S. 2007, ApJ, 671, L49
1 citation on page [78](#),
[\[ADS\]](#)
- Carciofi, A. C., Miroshnichenko, A. S., & Bjorkman, J. E. 2010, ApJ, 721, 1079
2 citations on page [36](#),
[\[ADS\]](#)
- Che, X., Monnier, J. D., Zhao, M., Pedretti, E., Thureau, N., Mérand, A., ten Brummelaar, T., McAlister, H., Ridgway, S. T., Turner, N., Sturmman, J., & Sturmman, L. 2011, ApJ, 732, 68
7 citations on 4 pages [5](#), [18](#), [22](#), and [23](#),
[\[ADS\]](#)
- Chelli, A. & Petrov, R. G. 1995, A&AS, 109, 401
1 citation on page [118](#),
[\[ADS\]](#)
- Chesneau, O. 2009, New A Rev., 53, 279
1 citation on page [37](#),
[\[ADS\]](#)
- Claret, A. 1998, A&AS, 131, 395
4 citations on 4 pages [17](#), [20](#), [22](#), and [147](#),
[\[ADS\]](#)
- . 2000, A&A, 359, 289
6 citations on 5 pages [17](#), [20](#), [22](#), [23](#), and [147](#),
[\[ADS\]](#)

BIBLIOGRAPHY

- . 2012, *A&A*, 538, A3
6 citations on 5 pages [17](#), [20](#), [22](#), [23](#), and [147](#),
[\[ADS\]](#)
- Clement, M. J. 1974, *ApJ*, 194, 709
1 citation on page [14](#),
[\[ADS\]](#)
- Connon Smith, R. & Worley, R. 1974, *MNRAS*, 167, 199
1 citation on page [17](#),
[\[ADS\]](#)
- de Wit, W. J., Oudmaijer, R. D., & Vink, J. S. 2014, *Advances in Astronomy*, 2014, 1
1 citation on page [37](#),
[\[ADS\]](#)
- Domiciano de Souza, A., Bendjoya, P., Niccolini, G., Chesneau, O., Borges Fernandes, M., Carciofi, A. C., Spang, A., Stee, P., & Driebe, T. 2011, *A&A*, 525, A22
2 citations on 2 pages [45](#) and [129](#),
[\[ADS\]](#)
- Domiciano de Souza, A. & Carciofi, A. C. 2012, in *Astronomical Society of the Pacific Conference Series*, Vol. 464, *Astronomical Society of the Pacific Conference Series*, ed. T. Carciofi, A. C. & Rivinius, 149
1 citation on page [39](#),
- Domiciano de Souza, A., Driebe, T., Chesneau, O., Hofmann, K., Kraus, S., Miroshnichenko, A. S., Ohnaka, K., Petrov, R. G., Preisbisch, T., Stee, P., Weigelt, G., Lisi, F., Malbet, F., & Richichi, A. 2007, *A&A*, 464, 81
1 citation on page [129](#),
[\[ADS\]](#)
- Domiciano de Souza, A., Hadjara, M., Vakili, F., Bendjoya, P., Millour, F., Abe, L., Carciofi, A. C., Faes, D. M., Kervella, P., Lagarde, S., Marconi, A., Monin, J.-L., Niccolini, G., Petrov, R. G., & Weigelt, G. 2012, *A&A*, 545, A130
5 citations on 3 pages [78](#), [118](#), and [147](#),
[\[ADS\]](#)
- Domiciano de Souza, A., Kervella, P., Jankov, S., Abe, L., Vakili, F., di Folco, E., & Paresce, F. 2003, *A&A*, 407, L47
5 citations on 4 pages [3](#), [5](#), [78](#), and [95](#),
[\[ADS\]](#)
- Domiciano de Souza, A., Kervella, P., Jankov, S., Vakili, F., Ohishi, N., Nordgren, T. E., & Abe, L. 2005, *A&A*, 442, 567
3 citations on 3 pages [5](#), [17](#), and [65](#),
[\[ADS\]](#)

BIBLIOGRAPHY

- Domiciano de Souza, A., Kervella, P., Moser Faes, D., Dalla Vedova, G., Mérand, A., Le Bouquin, J.-B., Espinosa Lara, F., Rieutord, M., Bendjoya, P., Carciofi, A. C., Hadjara, M., Millour, F., & Vakili, F. 2014, *A&A*, 569, A10
10 citations on 5 pages [5](#), [18](#), [23](#), [78](#), and [79](#),
[\[ADS\]](#)
- Domiciano de Souza, A., Vakili, F., Jankov, S., Janot-Pacheco, E., & Abe, L. 2002, *A&A*, 393, 345
2 citations on 2 pages [16](#) and [44](#),
[\[ADS\]](#)
- Domiciano de Souza, A., Zorec, J., Jankov, S., Vakili, F., Abe, L., & Janot-Pacheco, E. 2004a, *A&A*, 418, 781
2 citations on 2 pages [118](#) and [147](#),
[\[ADS\]](#)
- Domiciano de Souza, A., Zorec, J., Vakili, F., Jankov, S., & Abe, L. 2004b, in *SF2A-2004: Semaine de l'Astrophysique Francaise*, ed. F. Combes, 285
1 citation on page [147](#),
- Eddington, A. S. 1925, *The Observatory*, 48, 73
1 citation on page [17](#),
[\[ADS\]](#)
- . 1926, *The Internal Constitution of the Stars* (Cambridge University Press)
1 citation on page [31](#),
- Ekström, S., Meynet, G., Maeder, A., & Barblan, F. 2008, *A&A*, 478, 467
1 citation on page [14](#),
[\[ADS\]](#)
- Espinosa Lara, F. & Rieutord, M. 2011, *A&A*, 533, A43
13 citations on 8 pages [17](#), [18](#), [20](#), [22](#), [23](#), [30](#), [79](#), and [147](#),
[\[ADS\]](#)
- . 2012, *A&A*, 547, A32
2 citations on 2 pages [20](#) and [147](#),
[\[ADS\]](#)
- Faes, D. M. 2015, PhD thesis, IAG-Universidade de Sao Paulo (Brazil), Lab. Lagrange-Université de Nice Sophia Antipolis (France)
1 citation on page [62](#),
- Foreman-Mackey, D., Hogg, D. W., Lang, D., & Goodman, J. 2013, *PASP*, 125, 306
1 citation on page [78](#),
[\[ADS\]](#)
- Glatzel, W. 1998, *A&A*, 339, L5
2 citations on 2 pages [30](#) and [32](#),
[\[ADS\]](#)

BIBLIOGRAPHY

- Goodman, J. & Weare, J. 2010, *Communications in Applied Mathematics and Computational Science*, 5, 65
1 citation on page [78](#),
- Goss, K. J. F., Karoff, C., Chaplin, W. J., Elsworth, Y., & Stevens, I. R. 2011, *MNRAS*, 411, 162
1 citation on page [78](#),
[\[ADS\]](#)
- Hadjara, M., Domiciano de Souza, A., Vakili, F., Jankov, S., Millour, F., Meilland, A., Khorrami, Z., Chelli, A., Baffa, C., Hofmann, K.-H., Lagarde, S., & Robbe-Dubois, S. 2014, *A&A*, 569, A45
1 citation on page [118](#),
[\[ADS\]](#)
- Hanbury Brown, R., Davis, J., & Allen, L. R. 1967, *MNRAS*, 137, 375
1 citation on page [2](#),
[\[ADS\]](#)
- Huang, W. & Gies, D. R. 2006, *ApJ*, 648, 580
1 citation on page [4](#),
[\[ADS\]](#)
- Hubeny, I. & Lanz, T. 2011, *Synspec: General Spectrum Synthesis Program*, *astrophysics Source Code Library*
3 citations on 3 pages [24](#), [44](#), and [62](#),
- Jackson, S., MacGregor, K. B., & Skumanich, A. 2004, *ApJ*, 606, 1196
1 citation on page [3](#),
[\[ADS\]](#)
- . 2005, *ApJS*, 156, 245
1 citation on page [14](#),
[\[ADS\]](#)
- James, R. A. 1964, *ApJ*, 140, 552
1 citation on page [1](#),
[\[ADS\]](#)
- Kanaan, S., Meilland, A., Stee, P., Zorec, J., Domiciano de Souza, A., Frémat, Y., & Briot, D. 2008, *A&A*, 486, 785
2 citations on 2 pages [95](#) and [148](#),
[\[ADS\]](#)
- Kervella, P. & Domiciano de Souza, A. 2006, *A&A*, 453, 1059
3 citations on 3 pages [5](#), [78](#), and [95](#),
[\[ADS\]](#)
- . 2007, *A&A*, 474, L49
2 citations on 2 pages [78](#) and [108](#),
[\[ADS\]](#)

BIBLIOGRAPHY

- Kervella, P., Domiciano de Souza, A., & Bendjoya, P. 2008, *A&A*, 484, L13
2 citations on 2 pages [78](#) and [108](#),
[\[ADS\]](#)
- Kervella, P., Domiciano de Souza, A., Kanaan, S., Meilland, A., Spang, A., & Stee, P. 2009, *A&A*, 493, L53
1 citation on page [95](#),
[\[ADS\]](#)
- Kippenhahn, R. 1977, *A&A*, 58, 267
2 citations on 2 pages [17](#) and [22](#),
[\[ADS\]](#)
- Kopal, Z. 1987, *Ap&SS*, 133, 157
2 citations on 2 pages [16](#) and [19](#),
[\[ADS\]](#)
- Kraus, M., Oksala, M. E., Nickeler, D. H., Muratore, M. F., Borges Fernandes, M., Aret, A., Cidale, L. S., & de Wit, W. J. 2013, *A&A*, 549, A28
1 citation on page [37](#),
[\[ADS\]](#)
- Kraus, S., Monnier, J. D., Che, X., Schaefer, G., Touhami, Y., Gies, D. R., Aufdenberg, J. P., Baron, F., Thureau, N., ten Brummelaar, T. A., McAlister, H. A., Turner, N. H., Sturmman, J., & Sturmman, L. 2012, *ApJ*, 744, 19
1 citation on page [34](#),
[\[ADS\]](#)
- Kurucz, R. L. 1979, *ApJS*, 40, 1
3 citations on 3 pages [24](#), [44](#), and [62](#),
[\[ADS\]](#)
- Lamers, H. J. G. & Pauldrach, A. W. A. 1991, *A&A*, 244, L5
2 citations on 2 pages [30](#) and [32](#),
[\[ADS\]](#)
- Lamers, H. J. G. L. M., Zickgraf, F.-J., de Winter, D., Houziaux, L., & Zorec, J. 1998, *A&A*, 340, 117
1 citation on page [36](#),
[\[ADS\]](#)
- Langer, N. 1997, in *Astronomical Society of the Pacific Conference Series*, Vol. 120, *Luminous Blue Variables: Massive Stars in Transition*, ed. A. Nota & H. Lamers, 83–89
1 citation on page [30](#),
- Le Bouquin, J., Absil, O., Benisty, M., Massi, F., Mérand, A., & Stefl, S. 2009, *A&A*, 498, L41
1 citation on page [118](#),
[\[ADS\]](#)

BIBLIOGRAPHY

- Lee, U., Osaki, Y., & Saio, H. 1991, *MNRAS*, 250, 432
1 citation on page [33](#),
[\[ADS\]](#)
- Lucy, L. B. 1967, *ZAp*, 65, 89
2 citations on 2 pages [17](#) and [19](#),
[\[ADS\]](#)
- Maeder, A. 1999, *A&A*, 347, 185
8 citations on 6 pages [17](#), [22](#), [30](#), [31](#), [32](#), and [147](#),
[\[ADS\]](#)
- Maeder, A. 2009, *Physics, formation and evolution of rotating stars*, 1st edn., *Astronomy and Astrophysics Library* (Springer-Verlag)
7 citations on 6 pages [2](#), [12](#), [14](#), [19](#), [30](#), and [31](#),
- Maeder, A. & Desjacques, V. 2001, *A&A*, 372, L9
1 citation on page [95](#),
[\[ADS\]](#)
- Maeder, A. & Meynet, G. 2000a, *A&A*, 361, 159
4 citations on 2 pages [30](#) and [32](#),
[\[ADS\]](#)
- . 2000b, *ARA&A*, 38, 143
1 citation on page [2](#),
[\[ADS\]](#)
- . 2012, *Reviews of Modern Physics*, 84, 25
2 citations on 2 pages [2](#) and [4](#),
[\[ADS\]](#)
- McAlister, H. A., ten Brummelaar, T. A., Gies, D. R., Huang, W., Bagnuolo, Jr., W. G., Shure, M. A., Sturmman, J., Sturmman, L., Turner, N. H., Taylor, S. F., Berger, D. H., Baines, E. K., Grundstrom, E., Ogden, C., Ridgway, S. T., & van Belle, G. 2005, *ApJ*, 628, 439
1 citation on page [5](#),
[\[ADS\]](#)
- Meilland, A., Millour, F., Kanaan, S., Stee, P., Petrov, R., Hofmann, K.-H., Natta, A., & Perraut, K. 2012, *A&A*, 538, A110
1 citation on page [34](#),
[\[ADS\]](#)
- Meilland, A., Stee, P., Vannier, M., Millour, F., Domiciano de Souza, A., Malbet, F., Martayan, C., Paresce, F., Petrov, R. G., Richichi, A., & Spang, A. 2007, *A&A*, 464, 59
1 citation on page [34](#),
[\[ADS\]](#)

BIBLIOGRAPHY

- Meynet, G. & Maeder, A. 2000, *A&A*, 361, 101
2 citations on 2 pages [2](#) and [3](#),
[\[ADS\]](#)
- Meynet, G. & Maeder, A. 2006, in *Astronomical Society of the Pacific Conference Series*, Vol. 355, *Stars with the B[e] Phenomenon*, ed. M. Kraus & A. S. Miroshnichenko, 27
4 citations on 2 pages [2](#) and [32](#),
- Millour, F., Meilland, A., Chesneau, O., Stee, P., Kanaan, S., Petrov, R., Mourard, D., & Kraus, S. 2011, *A&A*, 526, A107
1 citation on page [8](#),
[\[ADS\]](#)
- Millour, F., Meilland, A., Stee, P., & Chesneau, O. 2013, in *Lecture Notes in Physics*, Berlin Springer Verlag, Vol. 857, *Lecture Notes in Physics*, Berlin Springer Verlag, ed. J.-P. Rozelot & C. Neiner, 149
1 citation on page [37](#),
- Millour, F., Vannier, M., Petrov, R. G., Chesneau, O., Dessart, L., & Stee, P. 2006, in *EAS Publications Series*, Vol. 22, *EAS Publ. Series*, ed. M. Carillet, A. Ferrari, & C. Aime, 379–388
1 citation on page [8](#),
- Monnier, J. D., Che, X., Zhao, M., Ekström, S., Maestro, V., Aufdenberg, J., Baron, F., Georgy, C., Kraus, S., McAlister, H., Pedretti, E., Ridgway, S., Sturmman, J., Sturmman, L., ten Brummelaar, T., Thureau, N., Turner, N., & Tuthill, P. G. 2012, *ApJ*, 761, L3
2 citations on 2 pages [5](#) and [23](#),
[\[ADS\]](#)
- Monnier, J. D., Zhao, M., Pedretti, E., Thureau, N., Ireland, M., Muirhead, P., Berger, J.-P., Millan-Gabet, R., Van Belle, G., ten Brummelaar, T., McAlister, H., Ridgway, S., Turner, N., Sturmman, L., Sturmman, J., & Berger, D. 2007, *Science*, 317, 342
4 citations on 4 pages [5](#), [18](#), [23](#), and [65](#),
[\[ADS\]](#)
- Niccolini, G., Bendjoya, P., & Domiciano de Souza, A. 2011, *A&A*, 525, A21
1 citation on page [45](#),
[\[ADS\]](#)
- Ohishi, N., Nordgren, T. E., & Hutter, D. J. 2004, *ApJ*, 612, 463
3 citations on 2 pages [17](#) and [65](#),
[\[ADS\]](#)
- Ostriker, J. P. & Mark, J. 1968, *ApJ*, 151, 1075
1 citation on page [14](#),
[\[ADS\]](#)

BIBLIOGRAPHY

Peterson, D. M., Hummel, C. A., Pauls, T. A., Armstrong, J. T., Benson, J. A., Gilbreath, G. C., Hindsley, R. B., Hutter, D. J., Johnston, K. J., Mozurkewich, D., & Schmitt, H. 2006a, *ApJ*, 636, 1087

2 citations on 2 pages [5](#) and [65](#),

[\[ADS\]](#)

Peterson, D. M., Hummel, C. A., Pauls, T. A., Armstrong, J. T., Benson, J. A., Gilbreath, G. C., Hindsley, R. B., Hutter, D. J., Johnston, K. J., Mozurkewich, D., & Schmitt, H. R. 2006b, *Nature*, 440, 896

2 citations on 2 pages [5](#) and [18](#),

[\[ADS\]](#)

Petrov, R. G., Malbet, F., Weigelt, G., Antonelli, P., Beckmann, U., Bresson, Y., Chelli, A., Dugué, M., Duvert, G., Gennari, S., Glück, L., Kern, P., Lagarde, S., Le Coarer, E., Lisi, F., Millour, F., Perraut, K., Puget, P., Rantakyö, F., Robbe-Dubois, S., Roussel, A., Salinari, P., Tatulli, E., Zins, G., Accardo, M., Acke, B., Agabi, K., Altariba, E., Arezki, B., Aristidi, E., Baffa, C., Behrend, J., Blöcker, T., Bonhomme, S., Busoni, S., Cassaing, F., Clausse, J., Colin, J., Connot, C., Delboulbé, A., Domiciano de Souza, A., Driebe, T., Feautrier, P., Ferruzzi, D., Forveille, T., Fossat, E., Foy, R., Fraix-Burnet, D., Gallardo, A., Giani, E., Gil, C., Glentzlin, A., Heiden, M., Heining, M., Hernandez Utrera, O., Hofmann, K., Kamm, D., Kiekebusch, M., Kraus, S., Le Contel, D., Le Contel, J., Lesourd, T., Lopez, B., Lopez, M., Magnard, Y., Marconi, A., Mars, G., Martinot-Lagarde, G., Mathias, P., Mège, P., Monin, J., Mouillet, D., Mourard, D., Nussbaum, E., Ohnaka, K., Pacheco, J., Perrier, C., Rabbia, Y., Rebattu, S., Reynaud, F., Richichi, A., Robini, A., Sacchetti, M., Schertl, D., Schöller, M., Solscheid, W., Spang, A., Stee, P., Stefanini, P., Tallon, M., Tallon-Bosc, I., Tasso, D., Testi, L., Vakili, F., von der Lühe, O., Valtier, J., Vannier, M., & Ventura, N. 2007, *A&A*, 464, 1

1 citation on page [8](#),

[\[ADS\]](#)

Porter, J. M. 1999, *A&A*, 348, 512

1 citation on page [33](#),

[\[ADS\]](#)

Pringle, J. E. 1981, *ARA&A*, 19, 137

1 citation on page [33](#),

[\[ADS\]](#)

Reiners, A. & Royer, F. 2004, *A&A*, 415, 325

1 citation on page [147](#),

[\[ADS\]](#)

Rieutord, M. 2006, in *EAS Publications Series*, Vol. 21, *EAS Publications Series*, ed. B. Rieutord, M. & Dubrulle, 275–295

2 citations on 2 pages [17](#) and [18](#),

Rieutord, M. 2015, *Fluid Dynamics: An Introduction*, *Graduate Texts in Physics* (Springer)

1 citation on page [11](#),

BIBLIOGRAPHY

- Rivinius, T., Carciofi, A. C., & Martayan, C. 2013, *A&A Rev.*, 21, 69
3 citations on 3 pages [24](#), [33](#), and [34](#),
[\[ADS\]](#)
- Roxburgh, W. 1970, in *IAU Colloq. 4: Stellar Rotation*, ed. A. Slettebak, 9
1 citation on page [2](#),
- Schlesinger, F. 1911, *MNRAS*, 71, 719
1 citation on page [1](#),
[\[ADS\]](#)
- Secchi, A. 1866, *Astronomische Nachrichten*, 68, 63
1 citation on page [33](#),
[\[ADS\]](#)
- Shajn, G. & Struve, O. 1929, *MNRAS*, 89, 222
1 citation on page [1](#),
[\[ADS\]](#)
- Shakura, N. I. & Sunyaev, R. A. 1973, *A&A*, 24, 337
1 citation on page [35](#),
[\[ADS\]](#)
- Slettebak, A. 1970, in *IAU Colloq. 4: Stellar Rotation*, ed. A. Slettebak, 3
1 citation on page [4](#),
- Slettebak, A. 1976, in *IAU Symposium, Vol. 70, Be and Shell Stars*, ed. A. Slettebak, 123
1 citation on page [1](#),
- Slettebak, A. 1982, *ApJS*, 50, 55
1 citation on page [4](#),
[\[ADS\]](#)
- Stee, P. & Meilland, A. 2012, in *Astronomical Society of the Pacific Conference Series, Vol. 464, Circumstellar Dynamics at High Resolution*, ed. A. C. Carciofi & T. Rivinius, 167
1 citation on page [33](#),
- Strittmatter, P. A. 1969, *ARA&A*, 7, 665
1 citation on page [2](#),
[\[ADS\]](#)
- Struve, O. 1931a, *The Observatory*, 54, 80
1 citation on page [1](#),
[\[ADS\]](#)
- . 1931b, *ApJ*, 73, 94
2 citations on 2 pages [1](#) and [33](#),
[\[ADS\]](#)

BIBLIOGRAPHY

Thiébaud, E. 2008, in Society of Photo-Optical Instrumentation Engineers (SPIE) Conference Series, Vol. 7013, Society of Photo-Optical Instrumentation Engineers (SPIE) Conference Series

1 citation on page [79](#),

Townsend, R. H. D. 1997, MNRAS, 284, 839

1 citation on page [44](#),

[\[ADS\]](#)

van Belle, G. T. 2012, A&A Rev., 20, 51

2 citations on 2 pages [2](#) and [5](#),

[\[ADS\]](#)

van Belle, G. T., Ciardi, D. R., ten Brummelaar, T., McAlister, H. A., Ridgway, S. T., Berger, D. H., Goldfinger, P. J., Sturmman, J., Sturmman, L., Turner, N., Boden, A. F., Thompson, R. R., & Coyne, J. 2006, ApJ, 637, 494

1 citation on page [5](#),

[\[ADS\]](#)

van Belle, G. T., Ciardi, D. R., Thompson, R. R., Akeson, R. L., & Lada, E. A. 2001, ApJ, 559, 1155

4 citations on 4 pages [3](#), [5](#), [16](#), and [65](#),

[\[ADS\]](#)

van Leeuwen, F. 2007, A&A, 474, 653

1 citation on page [78](#),

[\[ADS\]](#)

Vinicius, M. M. F., Zorec, J., Leister, N. V., & Levenhagen, R. S. 2006, A&A, 446, 643

3 citations on 2 pages [3](#) and [78](#),

[\[ADS\]](#)

von Zeipel, H. 1924, MNRAS, 84, 665

6 citations on 4 pages [1](#), [17](#), [18](#), and [19](#),

[\[ADS\]](#)

Zahn, J.-P. 1992, A&A, 265, 115

3 citations on 3 pages [22](#), [31](#), and [147](#),

[\[ADS\]](#)

Zhao, M., Monnier, J. D., Pedretti, E., Thureau, N., Mérand, A., ten Brummelaar, T., McAlister, H., Ridgway, S. T., Turner, N., Sturmman, J., Sturmman, L., Goldfinger, P. J., & Farrington, C. 2009, ApJ, 701, 209

3 citations on 2 pages [5](#) and [23](#),

[\[ADS\]](#)

Zickgraf, F.-J., Wolf, B., Stahl, O., Leitherer, C., & Klare, G. 1985, A&A, 143, 421

3 citations on 2 pages [36](#) and [37](#),

[\[ADS\]](#)

BIBLIOGRAPHY

Zorec, J., Frémat, Y., Domiciano de Souza, A., Delaa, O., Stee, P., Mourard, D., Cidale, L., Martayan, C., Georgy, C., & Ekström, S. 2011, A&A, 526, A87

2 citations on 2 pages [3](#) and [147](#),

[\[ADS\]](#)